Barrier properties and analysis of defects of plasma polymerized hexamethyldisilazane-based films

Von der Fakultät Energie-, Verfahrens- und Biotechnik
der Universität Stuttgart
zur Erlangung der Würde eines Doktors der
Naturwissenschaften (Dr. rer. nat) genehmigte Abhandlung

Vorgelegt von
Mariagrazia Troia
aus Andria, Italien

Hauptberichter:	Prof. Dr. Thomas Hirth
Mitberichter:	Prof. Dr. Marc Kreutzbruck
Tag der mündlichen Prüfung:	26th November 2019

Institut für Grenzflächenverfahrenstechnik
und Plasmatechnologie
der Universität Stuttgart
2019

″おめでとう″

庵野 秀明

Contents

Index of figures

Index of tables

Index of symbols

Symbol	Description
A	Area (Chapter 6), integrated area of absorbance peaks (Appendix A1)
$\bar{a}$	Acceleration
B	Magnetic field
C_{Su}	Sutherland constant
c	Speed of light (Chapter 6), concentration (elsewhere)
$[c]$	Concentration
D	Diffusion coefficient
d_p	Diameter of the permeated pore (Chapter 3), penetration depth (Chapter 6)
E	Electric field
E_B	Binding energy
E_k	Kinetic energy
e	Elementary charge (Chapter 3), Euler's number (elsewhere)
f	Frequency
F	Faraday constant
$\bar{F}$	Lorentz force
h	Lateral size of a defect along the y-axis
k	Elastic constant (Section 6.2.1), equilibrium constant (elsewhere)
k_B	Boltzmann constant
K_n	Knudsen number
j	Electron current (Chapter 4), flux in [mol s^{-1} m^{-2}] (elsewhere)
L	Plasma dimension (Chapter 4), defects separation (Chapter 7)
M	Molecular weight
m	Mass
N	Number of atoms in a molecule
n	Defect density (Chapter 3), Planck constant (Chapter 4), refractive index (Chapter 6)

Symbol	Description
n_c	Cut-off electron density
n_i	Density of particles *i*
P	Pressure (Chapter 6), permeability coefficient (elsewhere)
p	Partial pressure
q	Electric charge (Chapter 4)
R	Ideal gas constant
R^2	Coefficient of determination
r	Radius
r_L	Larmor radius
S	Oversaturation (Chapter 6), solubility (elsewhere)
s	Defects elongation (Chapter 7), solubility coefficient (elsewhere)
T	Temperature
t	Time
U	Electrolytic cell potential
$\overline{v}$	Velocity
v_D	Drift velocity
w	Lateral size of a defect along the x-axis
X	Ionization degree (Chapter 4), concentration in [ppm] (Chapter 6)
y_o	Initial film thickness
Z	Number of vibration for a molecular bond
Z_i	Electric charge of particle *i*
ΔG	Gibbs free energy variation
ΔH	Enthalpy variation
ΔS	Entropy variation
Δy	Variation of film thickness
ε_o	Vacuum permittivity
ε_p	Effective porosity
η	Viscosity
θ	Tilting angle
λ	Wavelength
λ_D	Debye length
λ_f	Mean free path between collisions
μ	Permeand mobility (Chapter 3), reduced mass (Chapter 6)
μ_p	Defect tortuosity
ν	Frequency of electromagnetic radiation
$\overline{\nu}$	Wavenumber

Symbol	Description
π	Archimedes' constant
σ	Cross section (Chapter 3), standard deviation (elsewhere)
Φ	Thickness fraction (Chapter 3), work function (Chapter 6)
ϕ	Volume fraction
φ	Gas flow
χ	Fraction of trans isomers
ω	Angular frequency
ω_c	Cyclotron frequency
AMOLED	Active Matrix Organic Light Emitting Device
ATR	Attenuated Total Reflectance
BEOLED	Bottom Emitting Organic Light Emitting Device
DSC	Differential Scanning Calorimetry
ESCA	Electron Spectroscopy for Chemical Analyses
FOLED	Flexible Organic Light Emitting Device
FTIR	Fourier Transform InfraRed
FWHM	Full Width at Half Maximum
HMDSN	HexaMethylDiSilazaNe
HMDSO	HexaMethylDiSilOxane
ILT	Ideal Laminate Theory
IR	InfraRed
LED	Light Emitting Device
MFC	Mass Flow Controller
OLED	Organic Light Emitting Diode
OTR	Oxygen Transmission Rate
PECVD	Plasma Enhanced Chemical Vapor Deposition
PET	Polyethylene terephthalate
SEM	Scanning Electron Microscopy
UV	UltraViolet
VUV	Vacuum UltraViolet
XPS	X-ray Photoelectron Spectroscopy

Abstract

A great variety of commercially available goods, e. g. food products, require a degree of protection against gases and vapors. Electronic devices whose active layers are based on organic materials in particular demand extremely low oxygen transmission rates in order to attain adequate lifetimes. In order to do so, an encapsulation of the device by means of a barrier becomes necessary. In case of flexible devices, such as organic light emitting devices (OLEDs), conventional encapsulation methods relying on stiff glass lids cannot be employed. Plasma-enhanced chemical vapor deposition (PECVD) methods on the other hand have been proven to be successful in obtaining thin films (in the range of tens or hundreds of nanometers) which combine good barrier performances with flexibility and other favorable mechanical properties.

In the current work, thin silica-like (SiO_x) films have been deposited on polyethylene terephthalate (PET) through a low-pressure microwave plasma and a gaseous feed consisting of hexamethyldisilazane (HMDSN) and oxygen, with the aim of providing flexible oxygen barrier layers with additional properties as transparency, colorlessness, good adhesion to the substrate and resilience. Operational parameters such as the gas feed composition, microwave power and deposition time have been investigated and optimized, thus obtaining inorganic barriers with an optimal thickness in the 50 to 100 nm range and with a barrier improvement, when compared to the uncoated substrates, up to a factor of 100. The defects in the barriers have been investigated by means of a concurrently developed non-destructive method for their localization and identification, based on the precipitation of calcium carbonate crystallites on top of them, which allows the defect to be later retrieved and investigated by means of microscopy methods. Further analyses of the transmission rates have been carried out at different temperatures in order to investigate the permeation mechanisms through the bulk and the defects. The films, when compared to barriers deposited via the common precursor hexamethyldisiloxane (HMDSO), obtained in the same experimental setup, showed consistently better properties in a wider range of conditions, proving HMDSN to be a better precursor for thin films with barrier applications.

Multilayer systems, based on the combination of SiO_x films and an intermediate organic layer optimized in parallel to the barriers, have been developed, tested and used successfully for the encapsulation of flexible Organic Light Emitting Device (OLED) prototypes printed on polymers.

Kurzfassung

Zahlreiche im Handel erhältliche Produkte wie z.B. Nahrungsmmittel müssen vor Gasen und Dämpfen geschützt werden. Um speziell bei elektronischen Bauteilen, deren aktive Schichten aus empfindlichen organischen Materialien bestehen, eine ausreichende Lebensdauer zu gewährleisten, muss die Sauerstoffdurchlässigkeit stark reduziert werden. Zu diesem Zweck wird eine Verkapselung der Bauteile durch eine Barriereschicht erforderlich. Insbesondere bei flexiblen organischen Leuchtdioden (OLEDs) können konventionelle Verkapselungsmethoden wie z.B. das Aufbringen einer dünnen steifen Glasplatte nicht verwendet werden, ohne die Flexibilität dieser Geräte stark zu beeinträchtigen. Die Plasma Enhanced Chemical Vapor Deposition (PECVD)-Methode hat sich bereits als erfolgreich erwiesen, um dünne Schichten im Bereich von einigen Nanometern bis zu einigen 100 nm herzustellen. Diese Schichten besitzen sehr gute Barriereeigenschaften und weisen weitere vorteilhafte mechanische Eigenschaften wie eine hohe Flexibilität auf.

In der aktuellen Arbeit wurden dünne quarzähnliche (SiO_x) Schichten mittels eines Niederdruck-Mikrowellen-Plasmaverfahren aus einer Gasmischung von Hexamethyldisilazan (HMDSN) und Sauerstoff auf Polyethylenterephtalate (PET)-Folien mit einer Dicke von 23 µm abgeschieden. Ziel war es, flexible Sauerstoffbarrierenschichten mit zusätzlichen Eigenschaften wie Transparenz, Farblosigkeit, gute Haftung und Stabilität, zu erhalten. Die Betriebsparameter wie Gasmischungsverhältnis, Mikrowellenleistung und Abscheidungsdauer wurden untersucht und optimiert. Es konnten anorganische Barrierenschichten mit einer optimalen Schichtdicke von 50 bis 100 nm abgeschieden werden, die gegenüber dem unbeschichteten PET eine um den Faktor 100 niedrigere Sauerstoffdurchlässigkeit aufweisen.

Die Defekte (Pinholes) in den Barriereschichten wurden mittels einer im Rahmen der Arbeit entwickelten zerstörungsfreien Lokalisierungs- und Identifizierungsmethode untersucht. Sie basiert auf der Ausfällung von Kalziumkarbonatkristallen auf den Defekten. Diese Methode ermöglicht ebenfalls das nachfolgende Wiederauffinden und die detaillierte Untersuchung der Defekte durch optische Mikroskopie und Rasterelektronenmikroskopie. Weitere Permeationsanalysen bei verschiedenen Temperaturen wurden durchgeführt, um die Permeationsmechanismen durch die PET-Folie und die Defekte zu untersuchen. Im Vergleich mit dem weit verbreiteten Precursor Hexamethyldisiloxan (HMDSO) zeigten die HMDSN-basierten Schichten wesentlich bessere Barriereeigenschaften über einen weiten Bereich von

von experimentellen Betriebsparametern.

Mehrschichtsbarrieresysteme basierend auf SiO_x-Schichten und organischen Pufferschichten wurden entwickelt, getestet und für die Verkapselung von flexiblen, auf Polymeren gedruckten OLED Prototypen erfolgreich eingesetzt.

Chapter 1

Introduction and statement of the objectives

A great variety of commercially available products require a degree of protection against external gases and liquids, chiefly among them oxygen and water vapor. Electronic devices whose active layers are based on organic materials in particular demand extremely low oxygen transmission rates in order to attain adequate lifetimes. In order to do so, an encapsulation of the device by means of a barrier layer becomes necessary. Glass lids several times thicker than such devices, sealed with epoxy resins, are widely employed for this purpose. This kind of encapsulation cannot however be applied if the aim is also to retain the inherent flexibility, lightness and thinness that organic devices like organic LEDs can offer when compared to their inorganic counterparts. The relative harshness of the epoxy resin curing step alone, and the resulting ultraviolet irradiation, are enough to destroy the active layer of the devices.

Thin inorganic films deposited from volatile precursors by means of plasma-aided processes, on the other hand, have been widely investigated and already employed as barriers in food packaging and other similar fields. Such layers combine transparency, thinness, lightness, and superior adhesion and flexibility, when compared to films obtained by conventional deposition methods, all of which is also desirable for the encapsulation of organic devices. The deposition process itself, being carried out through low-temperature plasmas, is 'mild' enough not to endanger the substrates, quick, efficient, reproducible, tunable and easily up-scalable in case of large-area industrial applications. For the latter, the reduced amount of reagents required makes it also environment-friendly and cost-effective, too.

The capacity of films in the sub-micrometric scale to mimic their macroscopic counterparts, their related oxygen barrier properties included, is however limited by the presence of defects extending along their entire bulk. Through such nanometric spaces the permeand molecules can travel almost unhindered and, provided the density of such defects to be high enough, the barrier properties of the whole thin film result to be severely compromised or, at worst, almost completely nullified.

Hence in the current work a low-pressure, microwave-based plasma reactor has been employed for the deposition of silica-like (SiO_x) films with the principal aim to obtain thin barrier layers against oxygen. The reactor employed and its configuration allow areas much larger than the proper plasma to be treated, while at the same time providing mild operating conditions suited for the encapsulation of sensitive electronic devices even in case of prolonged deposition steps.

The main aim is therefore that the thusly obtained films must first and foremost present a suitable chemical composition that allows them to act as barriers against oxygen, but also possess, when possible, further favorable properties that would make an encapsulation of flexible light-emitting devices feasible: they need to be transparent and colorless, to exhibit good adhesion to their substrate and to be able to undergo repeated bending without compromising their mechanical stability. In order to meet the above-mentioned requirements, an optimization of a wide range of operating parameters, including the composition of the plasma feed, the operating power and the duration of the deposition step, has been performed.

Furthermore, for the purposes of encapsulating very sensitive devices, the precursor for the polymerization of the barriers should not contain oxygen atoms. In the current work the monomer of choice has been therefore the organosilicone hexamethyldisilazane (HMDSN), which is relatively seldom used in plasma-assisted processes for the purpose of obtaining silica-like films. Another aim of the work has therefore been to compare the deposited films and their barrier performances with those produced by means of more widespread, conventional and oxygen-containing organosilicone precursors, in order to ascertain whether and to what extent silazanes may prove to be more suitable for the intended encapsulation purposes. The comparison has been focused in particular on the commonly-used hexamethyldisiloxane (HMDSO) monomer, whose similar molecular structure differs only in an oxygen atom in lieu of an amino group.

As part of the aforementioned optimization process of the oxygen barriers, moreover, a simultaneous and thorough investigation of the presence of defects, their nature, size and spacing in the thin layers, their density and most importantly the effect they have in limiting the barrier performances has been rendered necessary. In order to do so, a method for the localization and identification of such defects, that at the same time preserves the integrity of the investigated barriers and allows them to be further tested afterwards, has become necessary. Since most of the currently available defects localization methods are destructive in nature, an entirely new, non-destructive test has been designed and developed. The aim in this case has been to first verify its feasibility, validity and reproducibility, and then later to successfully employ it for the analysis of the plasma-deposited barriers in order to further characterize them.

Once a set of optimized operating conditions leading to the best possible barriers have been reached, the aim has been to first develop and investigate a multilayer system incorporating several of the single optimized barriers, in order to further abate the amount of permeated oxygen, and then later to test whether it would be possible to successfully treat and encapsulate sensitive electronic devices in the current reactor set-up without destroying their integrity in the process.

The layout and general structure of the current work is better detailed in the following. Furthermore, a schematic representation of it, explicitly referencing the chapters in which the single sub-sections of the work have been investigated, is presented below in Figure 1.1.

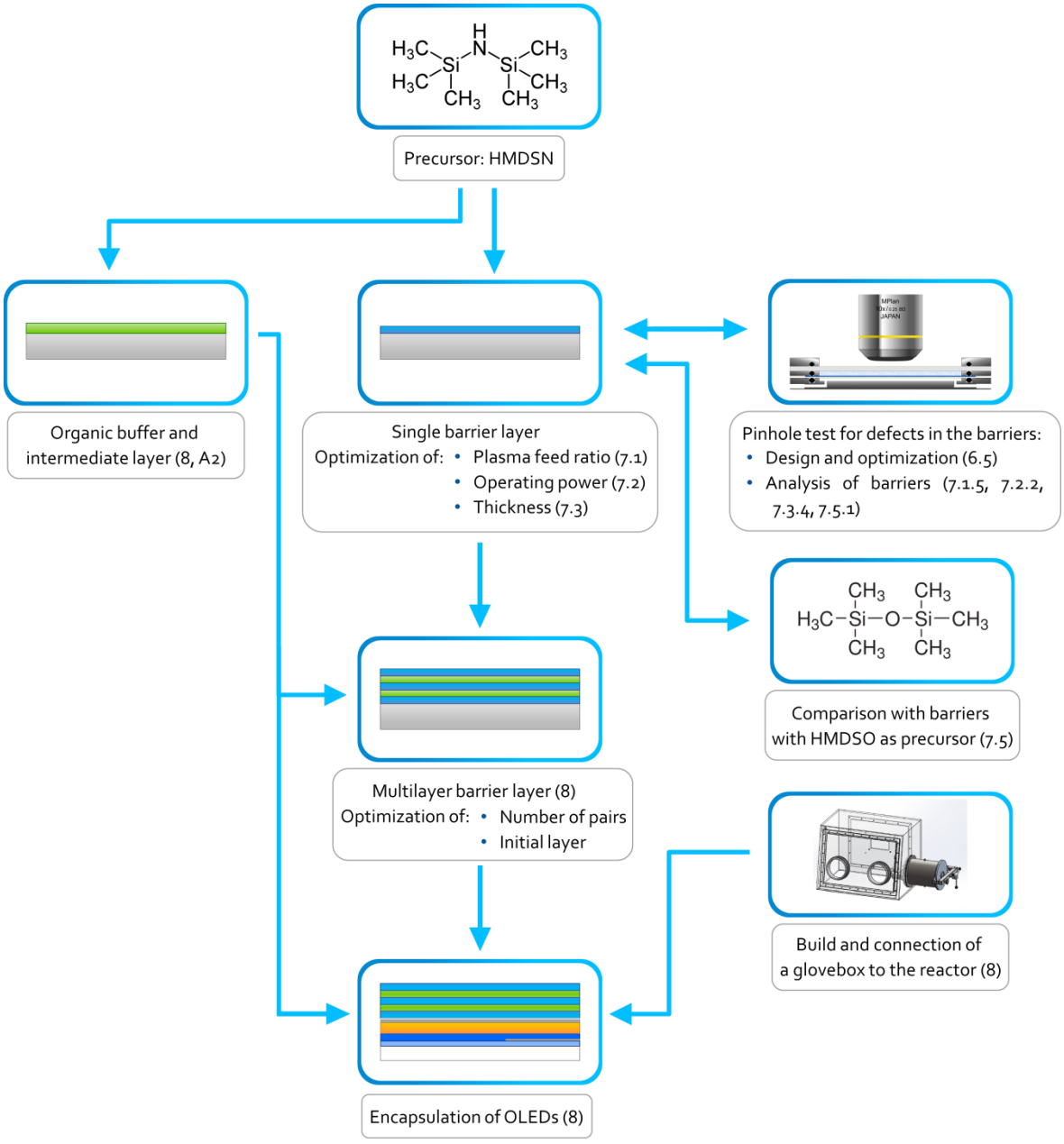

Figure 1.1: Overview of the current work. In round brackets, the chapters and sub-chapters in which the different work packages are respectively presented and discussed.

The conventional encapsulation strategies for a variety of stiff and flexible substrates are presented in Chapter 2, together with an overview of plasma-polymerized films that can act as

barrier layers. The theoretical fundamentals of the permeation processes in a solid are thoroughly presented in Chapter 4. The plasma fundamentals, together with the operating principles on which the plasma reactor employed in the current work is based, are shown in Chapter 3. An overview of the chemo-physical processes taking place inside a plasma, with a focus in particular on the plasma-enhanced deposition processes from a gaseous phase, is also included. The experimental setup for the plasma reactor and the operating conditions, the employed substrates and the monomers acting as precursors for the deposited films are detailed in Chapter 5. Chapter 6 deals with the diagnostic methods employed for the investigations on the properties of the thin barriers. The chapter also includes a thorough discussion regarding the method, developed in the current work, for the identification of defects in the film, including a short overview on the state of the art, the fundamentals and the assumptions on which the test relies on, and an evaluation on its validity and effectiveness.

Chapter 7 extensively presents and discusses the results regarding single layer barriers, including the optimization of several operating parameters related to their deposition process and the characterization of their properties, particularly those connected to their performances as barriers against oxygen. Chapter 8 on the other hand focusses on multilayer systems, their properties, and their application as barriers on OLED prototypes. The changes in the experimental setup and in the reactor preparatory to the handling of such devices are also here included. A summary of the current work and a brief outlook are finally offered in Chapter 9.

Chapter 2

State of the art of oxygen barrier layers

Some degree of protection against external gases, mostly oxygen and water vapor, is preferable, and sometimes required, for countless commercially available goods and products. Sensitive food products may extend their shelf life when sealed with appropriate barrier packaging. Liquid crystals displays and light emitting devices, if left unprotected against atmosphere, would quickly cease to function. The organic counterparts of the latter possess even stricter requirements, in order for them to be commercially viable [1-4]. Some of the lower limits in oxygen transmission rates required for a small collection of products are offered in Figure 2.1. Other times, not a complete barrier, but rather a partial one that can act as a release regulator, becomes necessary: such is the case for example for drugs and medicaments, or for organs-on-a-chip which must remain at least partially permeable and allow the human cells inside them the necessary amount of oxygen. In all such cases, a solid barrier must be applied on the product of interest or on its casing. Inorganic coatings acting as such, for example, have been commercially employed since the 1960s for the reduction of the permeation rates of polymer foils [5,6]. The physical and mechanical properties of such barriers will then determine the amount of gas per square meter per day allowed to permeate through them. In order to be commercially suitable, moreover, the production of such barriers must be quick, and inexpensive, i.e. the barriers must be as thin as possible and be deposited preferably on large areas in quick steps [7]. Last but not least, a progressive switch from glass and metal oxides packaging to lighter, cheaper and more functional systems consisting of a combination of polymer plus a barrier is also becoming increasingly supported by the current European legislation [8]. A further advantage of such almost completely organic systems, moreover, is their inherent recyclability.

In the following sections, a more in-depth overview on organic light emitting devices (Section 2.1) and their conventional encapsulation methods is presented. In Section 2.2, a

brief overview on barrier systems based on plasma-polymerized thin films will be given.

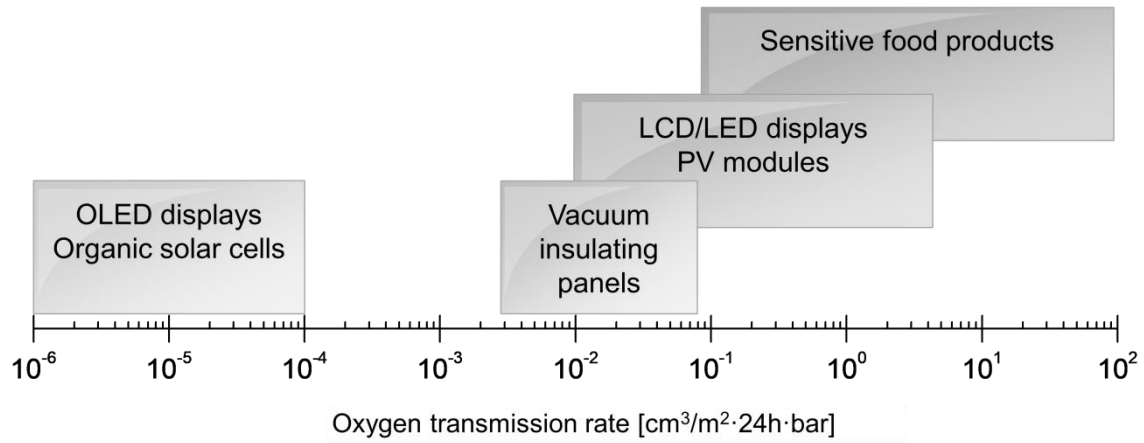

Figure 2.1: Oxygen transmission rates required for commercially available products. Data taken from [9].

2.1 Organic light emitting devices and their encapsulation

Organic Light Emitting Devices (OLEDs), as the name suggests, are optoelectronic light sources in which the injection of charge carriers (electrons and electron holes) at a material junction and their later recombination produce the emission of photons in the visible range (electroluminescence). Contrary to conventional LEDs, based on appropriately doped semiconductors, the active layer in OLEDs is organic and polymeric, often constituted by long π-conjugated hydrocarbon chains acting as chromophore, or by saturated chains with isolated lateral groups containing iridium or other rare earths complexes [10] which are responsible for the emission of light. The device is completed by means of a pair of electrodes, one of them transparent in order to ensure the transmission of the produced photons, and several intermediate layers that help maximize the charge transport and injection efficiency. Contrary to inorganic LED, they are much cheaper to produce, ensure very high efficiencies and operate at considerably lower voltages, down to few mV [11].

Since the first operative prototypes, emitting in the green spectrum range, were reported in 1987 [11, 12], OLEDs for general illumination purposes became available on the market only in 2009, distributed by Philips and Osram [13]. Nowadays, Active Matrix OLEDs (AMOLEDs) are widely employed in large scale and high resolution displays, for TVs and smartphones, among many other applications [14, 15].

Organic LEDs principally require protection against oxygen and water vapor, too. In both cases, in fact, oxygen atoms quickly react with the unsaturated sites or other high-energy bonds in the active matrix, destroying the conjugation that causes the electroluminescence or otherwise compromising the emitting layer's integrity and conductivity. The otherwise unprotected devices can operate in air for few hours at best, before catastrophic failures. By contrast, in order to be suitable for commercialization and large-scale use, a light device should possess a guaranteed lifetime of at least 10000 hours [16, 17].

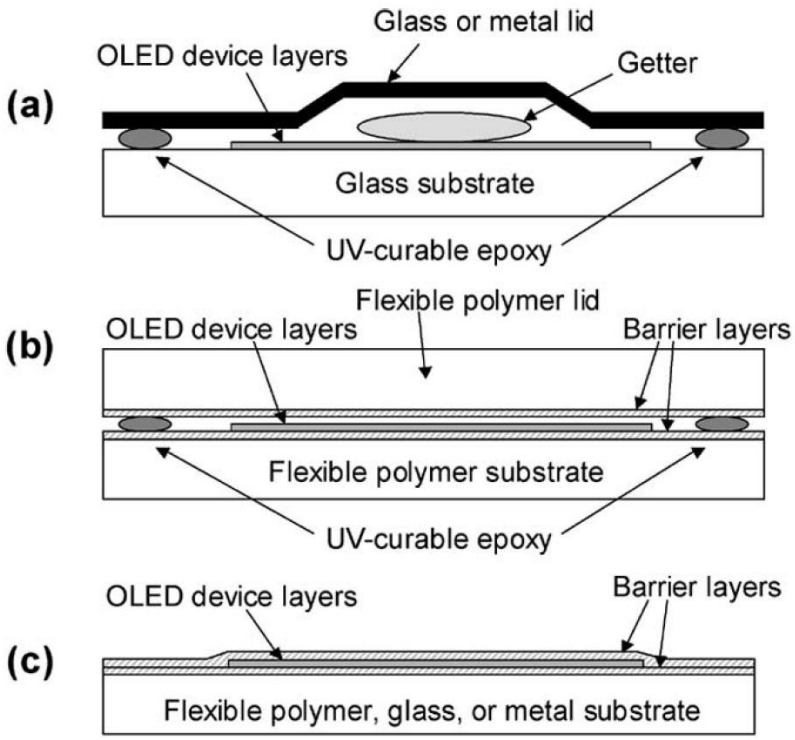

Figure 2.2: Schematic sections of OLEDs encapsulation strategies: (a) on glass substrate, (b) on polymeric substrate with a top polymeric lid, and (c) on polymeric substrate with an upper thin barrier layer. Picture from [5].

If the device is built onto some rigid substrate that also possesses suitable barrier properties against such gases, as for example glass, then only a top encapsulation is required. Vice versa, a back encapsulation becomes mandatory, too. The top encapsulation is usually carried out in inert atmosphere, like nitrogen or argon, by means of a glass or metallic lid [18]. The lid is glued to the substrate by means of beads of epoxy resin, to be later hardened in an UV-curing step – keeping in mind that UV can promptly destroy the aforementioned emitting layer –. As the resin vapors thus developed are also extremely detrimental to the OLEDs functioning, a sufficient amount of

a getter substance, usually elemental calcium and barium to be later oxidized to CaO and BaO [18, 5], must also be deposited beneath the lid. Such additional layers are usually fractions of millimeters thick [5] and tend to swell upon contact with water vapor, thus stressing the device and accelerating its eventual degradation. The encapsulation process must be carried out at low temperatures, care must be taken so that no solvent comes in direct contact with the emitting layer or cathode of the device, and finally the resin sealing requires substrates much larger than the actual dimensions of the to-be-encapsulated OLED [19, 5]. The lid must however still allow stable electric contacts to be established with the device within. The resulting structure is always several times, or even a few orders of magnitude, thicker than the proper OLED alone, as shown schematically in Figure 2.2a and 2.2b. Such end product, moreover, is extremely stiff and both the lid and the now-hardened epoxy resin are brittle and prone to fail in case of applied mechanical stresses. Therefore, the approach is not suitable for Flexible OLEDs (FOLEDs), which can be produced on polymer substrates [20-23]. A similarly polymeric lid provides flexibility and resilience, but the brittle epoxy resin is still required in order to successfully glue together the two halves. Thin barriers laying in intimate contact with the OLED, on the other hand, can reduce the overall thickness by a factor of two and ensure mechanical robustness, good adhesion and stability [5]. They would also render superfluous both the resin and the getter, and are therefore particularly suitable also for large scale production of flexible, cheap OLEDs with short-lived applications. Their thinness compared to traditional methods is exemplified in Figure 2.2c.

2.2 Plasma-polymerized barrier layers

A wide variety of materials obtained by means of Plasma Enhanced Chemical Vapor Deposition (PECVD) processes has shown good barrier properties against oxygen: a short, partial list include aluminum and thallium oxides and silicon nitrides and oxides [18]. The silicon-based films in particular also possess good dielectric properties [7], which render them microwaveable and particularly suited for the food packaging industry [24], also thanks to their atoxicity. This, together with a more retortability, flexibility and recyclability [25], and in the case of SiO_x transparency and colorlessness [26], render them perfect candidates for the encapsulation of light emitting devices, among others. Their deposition process, on the other hand, is operationally easy, tunable, cost effective [24], up-scalable [27] and can be carried out at very low temperatures [25], without being limited by the size and shape of the substrates [24]. It also often shows better results when compared to other deposition techniques such as sputtering, thermal evaporation or chemical vapor deposition [18, 28, 29]. For a more detailed overview of the polymerization processes taking place in the plasma phase and how they differ from more conventional chemical reactions, see also Chapter 4.3 and 4.4.

Single SiO_x thin layers deposited by means of radiofrequency and microwave plasmas alike have shown to possess good barrier properties [25, 30-35], with normalized values down to 10^{-1} $cm^3/m^2 \cdot day \cdot bar$ and more, when coupled with adequately poorly permeable substrates [36]. This proves more than enough for food packaging [34], but it is still several orders of magnitude too high to meet the requirements for organic devices [5], as previously shown in Fig. 2.1. Micro- and submicro-scopic defects extending for the whole length of the plasma-polymerized barriers cause their performances to be far from those of their silica counterpart, which is often assumed to be completely impervious to oxygen [7, 37]. Along such defects, the gas can permeate freely or scarcely unhindered [38]. In order to further improve the performances of such barriers, then a multilayer system consisting of alternated inorganic and organic dyads must be employed [4, 9, 19, 30, 39, 40], similar to the Barix© sputtered encapsulation multilayer developed by Vitex System [3]. The structure of such systems is illustrated in Figure 2.3. The insertion of a layer with a completely different chemistry between the barriers decouples the defects and prevents them to propagate through the whole structure. The effective, tortuous length that the permeand particles have to travel before reaching the substrate, therefore, becomes much longer than the nominal thickness of the multilayer, improving the overall barrier performances [41, 42]. The number of dyads in a system and the average defect densities and transmission rates of the barriers embedded in it become then the limiting factors that determine a multilayer's effectiveness. Thinner barriers, when possible, are favored as they retain a higher intrinsic resilience, flexibility and integrity [27, 31], and also result in shorter deposition steps suitable for large-scale applications.

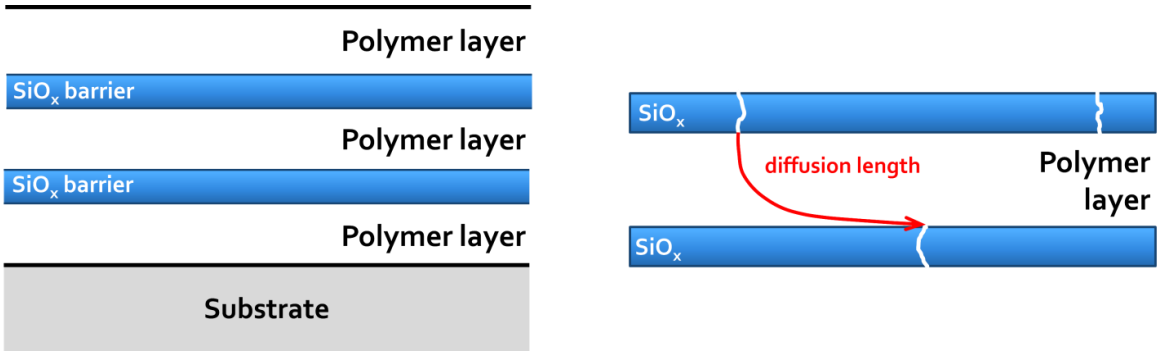

Figure 2.3: Schematic structure of a multilayer system on a substrate (left), and representation of the increase in the diffusion length caused by defects decoupling. Based on [18].

Chapter 3

Permeation theory

3.1 Permeation process

The permeation is a physico-chemical process in which a liquid or gaseous species, called *permeant*, moves through a solid medium under the effect of a spatial and temporal concentration gradient of the former. For most solids, and for organic polymers in particular, the process can be envisioned after the free volume theory [43, 44]: such theory states that the permeant atoms or molecules can move through the bulk of a solid material thanks to the small free spaces inside it caused by thermal movement of its molecules or polymeric chains. As a consequence, such process is directly dependant on the temperature, as an increase in the mobility of polymers chains induced by the temperature, for example, results in an increased density and frequency of free spaces through which the permeant can move. For a quantitative description of the dependence on temperature, also refer to Section 3.4.

The overall diffusion process in a homogeneous solid can be split schematically into three steps:

i. adsorption of the permeant gas or liquid on the surface of the solid to be permeated;
ii. dissolution of the permeant in the solid and diffusion through it;
iii. desorption of the permeant upon reaching the back interface of the solid.

The second step is often the rate-determining one in the overall process and is strongly affected by the solubility and the diffusivity of the permeant in the solid phase. Such dependence is better illustrated through the permeation coefficient *P*, defined as [45]:

$$P = D \cdot S \,, \tag{3.1}$$

where *D* is the diffusion coefficient and *S* the solubility of the permeant species.

The solubility of the permeant in the permeate depends on their mutual interactions, as

for example dipole-dipole and van der Waals forces [45]. Assuming that no chemical reaction takes place between them, that the concentration of the permeant molecules in the permeated solid is low and that the former are homogeneously distributed, then the solubility can be rewritten by means of Henry's law as [46, 47]:

$$S = \frac{c}{p_g} = const. \ , \tag{3.2}$$

where c is the concentration of the permeant in the solid and p_g is its partial pressure outside the solid.

The diffusion coefficient is a measure of the speed of the permeation process and, according to the Einstein–Smoluchowski relation, can be expressed as [48-50]:

$$D = \mu \, k_B \, T \ , \tag{3.3}$$

where μ is the mobility of the permeant molecules in the solid, k_B is the Boltzmann constant and T is the temperature. Knowing that the mobility can be written as:

$$\mu = \frac{1}{6\pi\eta r} \ , \tag{3.4}$$

then Eq. 3.3 can be rewritten as:

$$D = \frac{k_B T}{6\pi\eta r} \ ; \tag{3.5}$$

r is the radius of the permeant species and η is the viscosity of the permeated solid, which as hinted before is also dependent on the temperature. The diffusion coefficient for a fixed permeant-permeated pair will therefore increase with the temperature (see also Section 3.3). The dependence of the diffusion coefficient on the concentration gradient inside the solid has to be made explicit by means of mathematical models as the one in the following section.

3.2 Fick's laws of diffusion

The diffusion process can be treated mathematically by means of the Fick's equations, which describe the spatial and temporal variation of the permeant concentration in the solid. For the most general case the two Fick's laws can be written as [46]:

$$\vec{j} = -D \cdot \vec{\nabla} c \ ; \tag{3.6}$$

$$\frac{\partial c}{\partial t} = \vec{\nabla}\left(D \cdot \vec{\nabla} c\right); \tag{3.7}$$

j is the diffusion flux and is expressed as [mol m^{-2} s^{-1}], i.e. the amount of permeant per unit area in unit of time, and $\vec{\nabla}c$ is the concentration gradient. Here, the diffusion coefficient is a function of the concentration, the spatial coordinates in the solid, and the temperature, or:

$$D = f(\vec{x}, c, T). \tag{3.8}$$

Both Fick's laws can be reduced to a one-dimensional case, assuming the solid to be isotropic regarding diffusion (more on this in section 3.4), and D to be independent from the concentration. Eq. 3.6 and 3.7 become then:

$$\vec{j} = -D \cdot \frac{\partial c}{\partial x}; \tag{3.9}$$

$$\frac{\partial c}{\partial t} = D \cdot \frac{\partial^2 c}{\partial x^2}; \tag{3.10}$$

in order to obtain analytical solutions for both equations, a system of boundary conditions is to be provided. By considering a solid with a thickness d which separates two gaseous phases, so that the permeating gas is initially the sole component of the first and is completely absent from the second, as well as from the solid, i.e. there is an initial concentration gradient at the two interfaces of the solid, and considering how for longer times the permeant molecules will diffuse through the solid acting upon such gradient, until they reach the second gaseous phase and they are continuously removed from here, so that their concentration is zero, the following set of boundary conditions can be proposed [44]:

$$\begin{cases} c(x, t=0) & 0 \le x \le d \\ c(x=0, t) = c_0 & t > 0 \\ c(x=d, t) = 0 & t \ge 0 \end{cases} \tag{3.11}$$

By means of the Fourier method for separating variables it is then possible to obtain a solution for the temporal differential equation, and moreover to calculate, for $t \to \infty$, the steady-state concentration value c_s for the whole solid thickness:

$$c_s(x) = c_0 \cdot \left(1 - \frac{x}{d}\right); \tag{3.12}$$

the concentration inside the solid therefore decreases linearly the further away from the permeant-rich gaseous phase. A representation of such trend is reported in Figure 3.1. By substituting the solution to the second Fickian law in the first one, and by solving the differential equation with x=d, i.e. in correspondence of the second solid-gas interface, it is possi-

ble also in this case to obtain a steady-state value for the permeant flow, equal to:

$$j(x = d) = D \cdot \frac{c_0}{d} \; ; \tag{3.13}$$

The non-steady-state flow can then be expressed as an approximated function of the previous value [51]:

$$j(x = d, t) = 2\, j(x = d) \cdot \sqrt{\frac{d^2}{\pi D t}} \cdot e^{-\frac{d^2}{4Dt}} . \tag{3.14}$$

A typical time value τ, corresponding to the following conditions:

$$j(x = d, \tau) = 0.616 \cdot j(x = d), \tag{3.15}$$

can be introduced, the value of which can be expressed as [43, 46]:

$$\tau = \frac{d^2}{6D} , \tag{3.16}$$

so that:

$$D = \frac{d^2}{6\tau} . \tag{3.17}$$

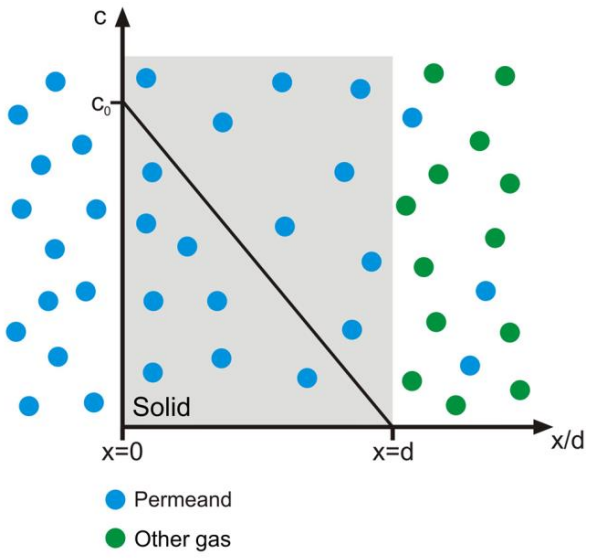

Figure 3.1: Concentration profile in the one-dimensional case for a solid with thickness d, with an initial concentration on its first interface (left) equal to c_0 that linearly decreases to zero on its second interface (right). The picture refers to the boundary conditions reported in Eq. 3.11. [52].

An instrument that allows the record of a permeant flux vs. time permeation curve, as the one displayed in Figure 3.2, will therefore enable the calculation of the diffusion coefficient of the solid film under investigation by means of the aforementioned equation. For further informations on the experimental setup and how it obeys the boundary conditions employed for the analytical solution of the Fick's laws, see also Chapter 6.4.

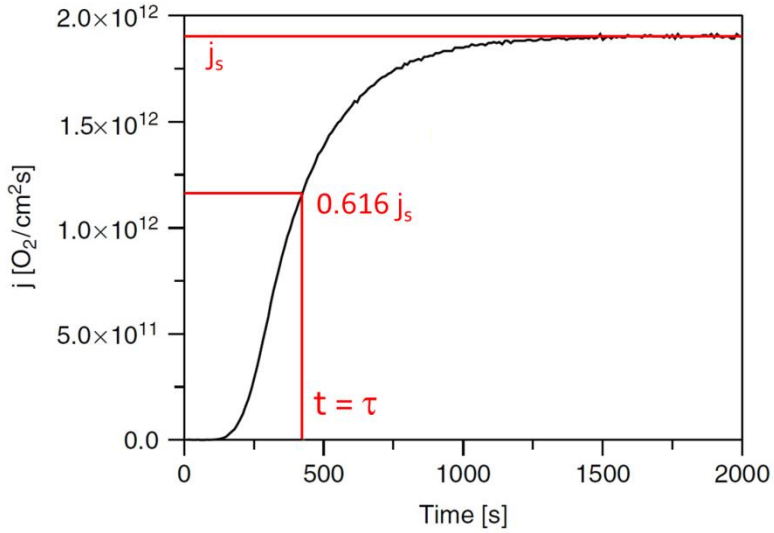

Figure 3.2: Permeation curve as a function of time, with j_s as the steady state permeand flux and τ the typical time at which $j = 0.616\ j_s$. Picture based on [53].

3.3 Fickian diffusion through multilayer systems

In case of systems consisting of several solid layers, each one of them still obeying the Fickian laws for diffusion of gases (under the assumption that the diffusion coefficient is again independent from the concentration), their overall permeability and, consequently, their diffusion coefficient, can be described by the ideal laminate theory (ILT), i.e. a series resistance type equation [30, 38, 54, 55]:

$$P_{TOT} = \left(\sum_{i=1}^{n} \frac{\Phi_i}{P_i} \right)^{-1}, \tag{3.18}$$

where P_{TOT} is the total permeability of the system, i refers to the number of layers of which the latter consists, with P_i being their respective permeabilities. Φ, the thickness fraction, is thus defined [38]:

$$\Phi_i = \frac{d_i}{d_{TOT}}\,, \tag{3.19}$$

such that:

$$d_{TOT} = \sum_{i=1}^{n} d_i\,, \tag{3.20}$$

$$\Phi_{TOT} = \sum_{i=1}^{n} \Phi_i = 1\,. \tag{3.21}$$

By substituting Eq. 3.1 in 3.13, and by then using Eq. 3.2:

$$P = j(x=d) \cdot \frac{d}{p}\,, \tag{3.22}$$

$$=> j(x=d) \propto P, \tag{3.23}$$

so that the previous equations for a multilayer can be rewritten in terms of the permeant flux at the steady-state, the physical quantity that can be experimentally measured as seen in Chapter 6.4.

It is noteworthy to stress that Eq. 3.18 shows how, in case of layers with severely different permeabilities, the composite system is overall characterized, or better limited, mainly by the layer with the smallest value of *P* [55], so that the overall flux could be reduced to:

$$j_{TOT} \cong \frac{j_k}{\Phi_k}\,, \tag{3.24}$$

where *k* is the index referring to the permeation-limiting layer.

For a bilayer system, as the majority of cases in the current work, consisting of a polymeric substrate and a thin barrier on top of it, therefore, the total permeant flux can be written as:

$$j_{bar}(x=d) = \frac{d_{bar}}{\frac{d_{TOT}}{j_{TOT}} - \frac{d_{pol}}{j_{pol}}}\,, \tag{3.25}$$

where the subscripts *bar* and *pol* refer to the barrier and the polymeric film, respectively.

Besides the assumptions made *ab initio* in order to apply a Fickian approach to the diffusion process, in this case a further assumption is made necessary: that the interfaces between the layers in the system are no low-energy conduits to transport [30] (on the subject, see also Section 3.5 and 3.6). In practice, especially in case of plasma-deposited thin films, however, the presence of an interface with unknown thickness, chemical composition and

barrier properties induced by the plasma itself [36, 56, 57], which may not necessarily fulfill the assumptions for a Fickian diffusion, introduces errors hard to precisely quantify.

Finally, recent work in literature [58, 59] provide an even more simplified relation, by not accounting for the layers thickness when splitting the single contributions, so that:

$$\frac{1}{P_{TOT}} = \sum_{i=1}^{n} \frac{1}{P_i}, \tag{3.26}$$

and for a bilayer:

$$\frac{1}{P_{TOT}} = \frac{1}{P_{pol}} + \frac{1}{P_{bar}}. \tag{3.27}$$

3.4 Dependence of the diffusion coefficient on temperature and activation energy

As already stated in Sections 3.1 and 3.2, diffusion processes modeled after the free volume theory and obeying Fick's laws are dependent on the temperature, more specifically they are thermally activated, i.e. facilitated by its increase. The permeation through polymeric materials can then be modeled after the solid diffusion model, or Arrhenius model [39, 54], and the dependence of the permeation coefficient on the temperature can be expressed through an Arrhenius-like equation [38, 54, 60] that is found to be valid both for inorganic, silicon-based [61] and organic polymeric materials [62]:

$$P(T) = P_0 \cdot exp\left[-\frac{E_p}{RT}\right], \tag{3.28}$$

where R is the ideal gas constant, P_o is the maximal permeation coefficient typical of the solid, and E_p is the apparent activation energy for the process, being related, also but not only, to the energy necessary to a permeant particle to squeeze through the empty spaces in the lattice / amidst the polymer chains [54]. Such quantity can be also written as [35]:

$$E_p = \Delta G, \tag{3.29}$$

i.e. the thermal activation energy or the variation of Gibbs energy associated with the overall process. For an isothermal process, the latter can be rewritten as:

$$\Delta G = \Delta H - T\Delta S, \tag{3.30}$$

where ΔH is the enthalpic variation for the permeation process, i.e. it includes both the effects of the dissolution of the permeant and its diffusion in the solid [35], and ΔS is the variation of entropy. The latter depends on the disorder in the lattice or more generally in the structure of the permeated solid [63]. By substituting Eq. 3.30 in Eq. 3.28:

$$P(T) = P_0 \cdot exp\left[\frac{\Delta S}{R}\right] \cdot exp\left[-\frac{\Delta H}{RT}\right], \tag{3.31}$$

the exponential growth of the permeation process is mediated by the enthalpic contribution alone, while the entropic one can be included in the pre-exponential factor.

Knowing that both S and D exhibit in turn an Arrhenius-like dependence on temperature [46, 47, 64], then:

$$S(T) = S_0 \cdot exp\left[-\frac{\Delta H_s}{RT}\right], \tag{3.32}$$

$$D(T) = D_0 \cdot exp\left[-\frac{E_a}{RT}\right], \tag{3.33}$$

where S_o and D_o are the typical pre-exponential coefficients, ΔH_s *is* the enthalpy of solution and E_a the diffusion activation energy. By substituting Eq. 3.1 in Eq. 3.28, then:

$$P(T) = S_0 \cdot exp\left[-\frac{\Delta H_s}{RT}\right] \cdot D_0 \cdot exp\left[-\frac{E_a}{RT}\right], \tag{3.34}$$

with, comparing Eq. 3.34 with Eq. 3.31:

$$\Delta H = \Delta H_s + E_a . \tag{3.35}$$

A further simplification may at this point be made: the coefficient of solubility S, on which the solubility depends [65], depends in turn linearly on the temperature, but changes less than 1 % in the 0-100 °C temperature range [54, 66], so that the solubility may therefore be assumed to be constant. The variation in enthalpy for the overall permeation process then coincides with the activation energy of the diffusion process alone, the latter becoming then the rate-limiting step [54, 59]:

$$\Delta H \cong E_a . \tag{3.36}$$

The activation energy may be experimentally obtained by taking again into account Eq. 3.23, so that in a steady-state condition:

$$j(x = d) \cong j_0 \cdot exp\left[-\frac{E_a}{RT}\right], \tag{3.37}$$

and, turning the previous equation in its logarithmic version:

$$\ln \frac{j(x=d)}{j_0} = -\frac{E_a}{RT}, \tag{3.38}$$

$$=> \ln j(x=d) = \ln j_0 - \frac{E_a}{RT}, \tag{3.39}$$

with the last equation bearing the following structure:

$$y = q + mx, \tag{3.40}$$

where the line gradient is equal to the activation energy over the gas constant and the intercept still contains an entrophy-related term inside it, as already shown in Eq. 3.31. A fitting procedure of a set of data for the same sample tested at different temperatures will then provide the activation energy of the latter [67]. The fitting procedure will remain valid provided that the investigated temperature range is reasonably small.

3.5 Limits of the Fickian approach

As already mentioned in Section 3.2, several assumptions have been made in order to obtain an analytical solution for the two Fickian laws. As a consequence, several limitations apply to solid whose permeation mechanism is to be considered Fickian. Firstly, in order to reduce the differential equation to a one-dimensional case, such solid has been considered isotropic and non-porous, while the diffusion coefficient has been assumed to be independent on the permeant concentration [55]. The latter condition is valid only for extremely diluted 'solutions' (Henry's law limit), i.e. small amounts of permeant dissolved in the solid bulk [68], and in case of non-condensable gases: this can only be for temperatures above the permeand critical values, which in most cases lie well outside the normally investigated ranges [68].

Moreover, the diffusion coefficient being independent on the concentration bars interactions, especially chemical, between the solid and the permeant particles. Such is, for example, not the case when the latter are water vapor [69], which in polymeric solids results in swelling and poorly understood permeation mechanisms, with memory and hysteresis effects [30, 68].

For polymeric materials, in particular, most of the commonly investigated temperature ranges lie below their glass transition temperature, with the possibility of resulting at best in non-Fickian diffusion and dual-mode sorption [68, 70]. In this case, a second term for the solubility appears, depending on the density of microcavities in the bulk of the polymer in the glassy state, their size and their affinity with the permeant particles that can be housed in them and remain stuck. For a more in-depth analysis of the model, see also [48, 71-73].

Even neglecting the aforementioned deviations, the biggest limitation to the Fickian

approach is the intrinsic anisotropy of the solid bulk, both for an organic polymer and an inorganic barrier. The former unavoidably, even in a glassy state, possesses a certain crystallinity degree, with the presence of randomly scattered and oriented sub-domains in its bulk. The relative diffusion coefficient can at best be simplified in some sort of 'average' value. For a much more thorough overview and description of crystallinity in commercially available polymers employed in the current work, refer to Appendix A1.

For inorganic thin films acting as barriers, on the other hand, the Fickian model completely fails to take into account the presence of macro- and micro-scopic defects in their bulk, which cause small volume fractions to present severely different permeation properties. Such defects, moreover, are often strongly oriented, further invalidating the premise of a homogeneous, isotropic solid. The following two paragraphs will deal in great detail about the type and size of defects, the permeation processes through them, their activation energy and dependence on the temperature.

3.6 Permeation through defects in barrier layers

Permeation through defects follows usually completely different pathways when compared to the passage of a permeant in a defect-free solid bulk. Moreover, such pathways depend on the lateral size of the defects selves, particularly when compared to the radius of the permeant particles [54, 74]. A classification of defects based on such mechanisms can be made by introducing the Knudsen number K_n, a dimensionless quantity that can be thus defined [75]:

$$K_n = \frac{\lambda_f}{d_p}, \tag{3.41}$$

with λ_f as the mean free path of a permeant particle in the defect between collisions against the walls, and d_p as the diameter of the defect or pore being permeated.

For $K_n < 1$, the amount of particle-walls collisions is negligible when compared to the particle-particle ones: the transport can then take place freely inside the defect, without being hindered by the latter's lateral size. This regime is called *free diffusion* and can be assumed to be dominant already for diameters of 1 nm [54], while at the same time becoming independent of the permeated solid thickness [70]. The defects fulfilling the condition of such transport mechanism are called, somewhat improperly, 'macro'-defects, as their size is several times, and often several order of magnitudes, bigger than the permeant particles. In case of thin coatings, this ranges from pinholes still invisible to optical microscopy up to macroscopic uncoated areas which leave the underlying substrate exposed, cracks, delamination

and otherwise damages to the film integrity. A diffusion coefficient pertaining such permeation mechanism can be defined as [76]:

$$D_{fd} \propto \frac{1}{p\,\sigma\,\sqrt{M}} \cdot \frac{T^{2.5}}{T + C_{su}}, \tag{3.42}$$

where p is the permeant partial pressure, σ its cross section, M its molecular weight, and C_{su}, the Sutherland constant, is typical for each gas and takes into account the effects of temperature on its cross section [55]. In a steady-state condition then, similarly to Fickian diffusion, the flux of permeant through such defects will then be proportional to $T^{2.5}/(T+C_{su})$.

When the lateral size of the defect becomes comparable or slightly smaller than the free path of the permeant, the particles collisions against the walls are not anymore negligible. In standard conditions, this happens for defects with a diameter in the 0.3 ÷ 1 nm range [54]. In this case, K_n is greater than one and the regime is called *Knudsen diffusion* [75]. The corresponding diffusion coefficient D_{Kn} can be written as [77, 78]:

$$D_{Kn} = \frac{\epsilon_p}{\mu_p} \cdot \frac{4}{3}\, d_p \cdot \sqrt{\frac{RT}{2\pi\, M}}, \tag{3.43}$$

with ε_p the effective porosity of the medium, i.e. considering only defects/pore extending fully between the two solid interfaces, and μ_p the tortuosity of the defects. In this case the diffusion coefficient loses its dependence upon the pressure but becomes related not only to the dimension of the defects, but also on their tortuosity, since at such nano- and subnanometrical ranges they cannot be equated anymore to straight channels [78]. The steady-state flow is now linearly dependent on the square root of the temperature.

Finally, for $K_n \gg 1$, the defects size become equal to the interstices in a crystalline lattice or to the small free volumes in an amorphous solid, and the diffusion coefficient becomes much more strongly dependent on the temperature, as the latter now increases not only the mobility of the permeant by avoiding its condensation in the small volumes, but has also an effect on the volume of the cavities. In this case then the whole model goes back to the solid diffusion model and Fickian diffusion described in Sections 3.1 and 3.2. The three simplified regimes here described are schematically depicted in Figure 3.3. Further possible effects as surface diffusion or capillary condensation [55, 70] have been here overlooked.

In a practical case, most if not all of these permeation pathways are to be found in a solid barrier on a substrate: as a consequence, the overall process won't exhibit one single activation energy, as assumed in Section 3.4, but more of a gradual threshold in a relatively small temperature range, with the values being mostly comprised between the upper limit corresponding to a defect-free layer in which a Fickian diffusion is the only component, and the lower limit constituted by the activation energy of the underlying substrate, which usually

possesses higher permeabilities [54].

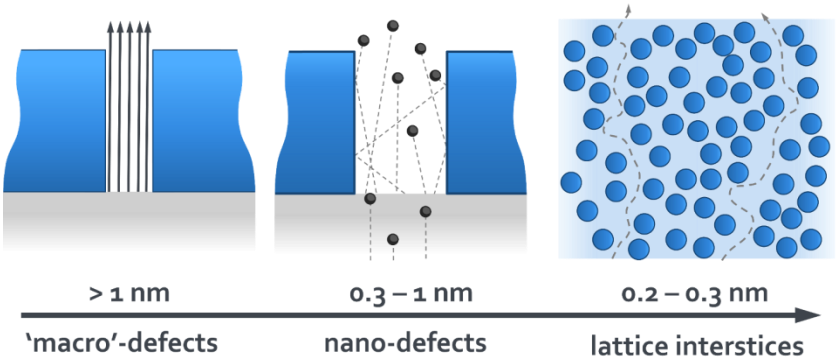

Figure 3.3: Schematic representation of three possible diffusion mechanisms of a gas inside a solid with macro-defects (left), nano-defects (center), and with only interstices in its lattice (right). Picture based on [54].

3.7 Effects of defects on barrier layers' properties

In the most general case of a barrier layer on a polymeric substrate, the permeability, P_{bar}, will depend on the contribution of the single permeation mechanisms reported in the last section, in a way that can for example be generally stated by the following equation [54], in case of multilayers with defects with a radius equal to or bigger than 1 nm:

$$P_{sys} = P_{md} + \left(1 - \frac{P_{md}}{P_{pol}}\right) P_{ILT} , \tag{3.43}$$

where P_{sys} is the overall permeability of the multilayer system, P_{md} is the contribution of defects, calculated by considering the case of an ideal barrier with a bulk permeability close to zero, P_{pol} is the permeability of the underlying substrate and P_{ILT} is the barrier permeability calculated by means of the ideal laminate theory (so that, omitting the presence of defects in the barrier, the former equation would become $P_{sys} = P_{ILT}$).

In case of nano-defects, moreover, their contribution and even the permeation through the barrier lattice, as the size of the former are comparable to the interstitial void in the latter, must be taken into account. The barrier permeability will therefore results in the sum of up to three different pathways [54]:

$$P_{sys} = C_{md} \cdot P_{pol} + \left(\frac{\phi_{pol}}{P_{pol}} + \frac{\phi_{bar}}{P_{la} + P_{nd}}\right)^{-1} , \tag{3.44}$$

where P_{la} and P_{nd} are respectively the permeabilities due to the lattice and the nano-defects contributions, both still depending on the temperature and with a different activation energy, ϕ_{pol} and ϕ_{bar} are the volume fractions of the substrate and the barrier film compared to the total, so that:

$$\phi_{pol} + \phi_{bar} = 1, \tag{3.45}$$

and C_{md} is a dimensionless constant that depends on the density and the lateral size of the defects in the film, but *not* on the temperature, nor on the permeant.

In most cases, for a given bulk permeability of the barrier, it's the presence of defects that limits and determines the film's performances [25, 79]. Their size and density in turn determine their weight in the overall permeation. Rossi *et al.*[80] found out, by resolving the case of a single defect with a cylindrical geometry in an otherwise impermeable film, that the permeant flux through defects with a lateral size R much larger than the film thickness depends on R^2, and on R alone when the latter is much smaller than the film thickness. The dependences on the defect area then hold true even when considering other geometries. This would seem to prioritize the contribution of large defects over small ones, but it was also found out that, in case of multiple defects with a high surface density, small ones compromise the barrier properties much more than fewer large defects with the same total area [80]. Such results have been confirmed by Hanika *et al.*[81] and da Silva Sobrinho *et al.* [60], among others, by means of numerical simulations. Indeed, for a very high density of minute defects it is even possible for the film to lose all its barrier properties [60]. This can be explained by introducing an effective radius of the defects that includes to some extent their surrounding volume: for sparse defects, with spacings far exceeding such radius, the defects are considered to be independent and bear no effect on each other. Otherwise, the defects act as a single, bigger defect, so that clusters of defects, grain boundaries (which are in fact considered to be macro-defects [54]) in crystalline or polycrystalline layers, and columnar structures surrounded by highly disordered, low-density regions profoundly affect the permeability of the barriers, much more than the sum of their independent contributions would have [60]. Their mutual interaction is caused by the strong concentration gradients lying in the immediate proximity of a defect [7, 79]. The permeant flux is strongly increased, not only perpendicularly to the layer surface, but also parallel to it: as a consequence, a defect acts as a funnel for the permeant particles and nearby low-energy conduits (i.e., other defects) may be quickly reached and permeated by the latter.

The dependency of the steady-state permeant flux on the defects' density can be also made explicit thus [60]:

$$j(x = d) \propto n^{\alpha}, \tag{3.46}$$

i.e. a power law where n is the defect's density and the α factor is roughly equal to 0.5 [60]. In case of a substantial density of defects, furthermore, the steady-state flux ceases to depend inversely on the layer thickness (see Eq. 3.13) and becomes constant [7, 38, 82]. The defects become then the one and only factor in determining the permeability of a thin film.

3.8 Effects of defects on activation energies

The presence of defects in at least one in a multilayer system alone invalidates the ideal laminate theory described in Section 3.3, as they provide low-energy conduits passages between solid layers. This may have in turn an effect on the overall effective activation energy [30, 38, 70]. As shown in Figure 3.4, for the simplest case of a bilayer constituted by a substrate, like an organic polymer with a purely Fickian activation energy (Fig. 3.4 a), and a thin barrier on top of it, two different outcomes may result: in case of an ideal, defect-free barrier, the activation energy of the system will result to be strongly increased, and equal to the one of the barrier alone. The permeant will in fact travel relatively unhindered through the polymer and then with much more difficulty through the bulk of the barrier. The latter is therefore the thermodynamically limiting factor (Fig. 3.4 b). In case of a barrier with defects in its volume, however, beside the Fickian diffusion through its defectless bulk's fraction, a second pathway becomes available, i.e. the unhindered passage through the discontinuous layer, in case of large uncovered areas, and through other, smaller defects which present much higher local permeabilities. The predominant contribution, which depends on statistical mechanics [30, 83], will then also become the determinant factor for the activation energy of the bilayer system. If most of the particles permeate through the barrier's defects, then the activation energy will still resemble the one for the uncoated polymer. The barrier, therefore, acts only as a partial block to the passage of the permeant [30], which has to move parallel to the barrier-polymer interface until it finds a defect through which quickly permeate. The average diffusion path and its tortuosity increase [30, 39], but it is only the kinetics of the process to be thus affected, not its thermodynamics. It is however this phenomenon that still allows multilayer to act as better barriers than single films: the presence of intermediate layers between two barriers causes the defects in them to be decoupled, i.e. they are not growing on top of each other, thus increasing the distance the permeant has to cover inside the multilayer. Such diffusion path is still limited by the average distance between neighboring defects, and it is therefore still useful for the barriers in the multilayers to possess as few defects as possible.

In this way, the transient regime of the permeation process, before a steady-state condition is reached, increases of several orders of magnitude [9, 39]: the multilayer will effectively reduce the amount of permeant on the basis of such changes in the kinetics of the process,

even though the expected final steady-state flux and the correlated activation energy show no significant improvement [39]. Of course, for a general improvement of the barrier performances, interlayers with low transmission rates, good coverage of the underlying barrier and smoothing properties (in order not to get bypassed by the permeant in the uncoated areas) are to be preferred [9]. For intermediate layers with a thickness inferior to the mean radius of the defects in the barrier layers, moreover, a severe drop in the permeant conductance has been found by means of simulations [39, 55], effectively containing the effect of the latter.

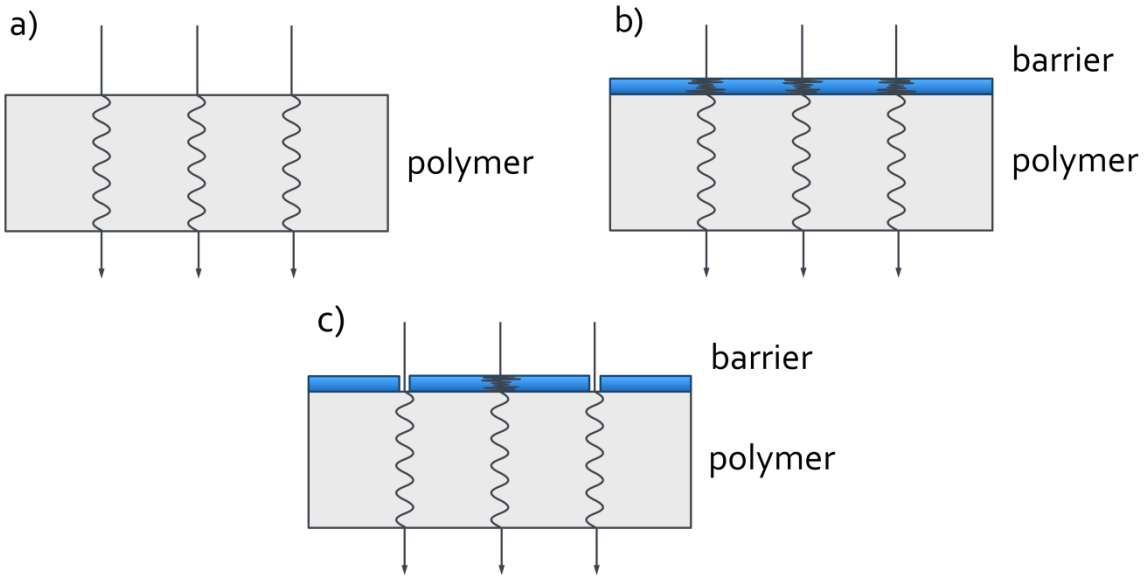

Figure 3.4: Simplified permeant transport modes for a polymer layer following a Fickian diffusion regime (a), a bilayer with a defect-free barrier on top of it (b), and a bilayer with a defective barrier as the uppermost component (c). The defects are simplified as uncoated areas offering no resistance to the permeand particles. Picture based on [30].

Chapter 4

Plasma fundamentals

The current chapter defines and describes the state of matter known as plasma, together with some of its fundamental properties. It will then focus on the interaction of the former with electromagnetic waves (Section 4.2), in particular when in electron cyclotron resonance conditions. The chapter will then present the general chemical processes taking place inside the plasma. One of them, the plasma-enhanced deposition, will be focused on in the last paragraph, as the one process most employed during the current work.

4.1 Plasma properties and classification

Plasma is a state of matter commonly defined as a partially ionized gas, i.e. in which a fraction of its total constituents is made up of free electrons and ions. Because of the presence of such free charges, plasma can be considered as an electrically conductive fluid in which the electromagnetic interactions between its particles and the outward environment extend on a much longer distance, when compared to the normally short-range forces acting in near-neighbors region inside a gas [84]. As a consequence, plasmas exhibit a collective behavior in which equally-charged particles move synchronously against external perturbation. The collisions thus arising with neutral species, in turn, cause the latter to often lie in excited states or to dissociate in highly reactive radicals. The collisions and subsequent relaxation and recombination mechanisms also cause a strong emission of photons, spanning from the infrared to the UV and occasionally up to the X-ray range, and causing the typical plasma glow.

Plasmas can be characterized by their ionization degree X, i.e. the fraction of its atomic and molecular components which has been ionized at least once, thus defined:

$$X = \frac{n_i}{n_i + n_n} \simeq \frac{n_i}{n_n}\,, \tag{4.1}$$

where n_i is the density of the ionized particles and n_n the density of the neutral species, with the latter in most cases much larger than the former. Depending on the kind of plasma, the former factor can range from 10^5 m^{-3} to 10^{30} m^{-3} [82], as it can be seen in Figure 4.1.

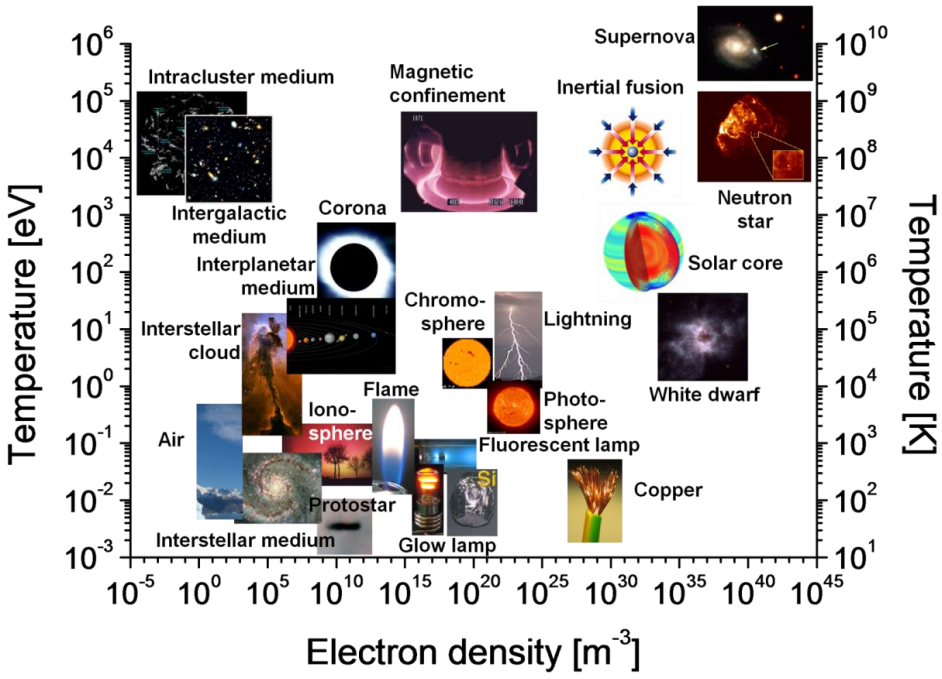

Figure 4.1: Plasmas in nature and in technology arranged as a function of their electron density and temperature [85].

As for the electrons, since in most of technical plasmas the majority of the ions are positive, and most of them are ionized only once, their density n_e can be thus approximated:

$$n_e \simeq \sum_k Z_k n_k \simeq \sum_k n_k \simeq n_i\,, \tag{4.2}$$

where Z is the charge of the k species of ions with density n_k. Plasmas are mostly considered to be quasi-neutral, i.e. the sum of their positive and negative charges should be close to zero, as the higher mobility of the electrons causes a small fraction of them to usually escape the plasma volume.

As previously mentioned, the charged particles in a plasma can interact with electromagnetic perturbations, usually so to minimize them and act as a shield. Such is the case also for charged particles inside of it, which are shielded by a tridimensional cloud of particles of opposite charge.

The length at which the electrical potential of the former drops to 1/e of its original value, based on the Debye-Hückel theory and called the Debye length λ_D, shows how such decay inside a plasma takes place faster than in vacuum [86, 87], and can be thus defined:

$$\lambda_D = \sqrt{\frac{\varepsilon_0 k_B / e^2}{n_e/T_e + \sum_{i,j} j^2 n_{ij}/T_i}} \simeq \sqrt{\frac{\varepsilon_0 k_B T_e}{n_e\, e^2}}\,, \tag{4.3}$$

where ε_o is the dielectric constant of vacuum, k_B is the Boltzmann constant, e the electric charge of an electron, T_e and T_i the temperatures of electron and ions, respectively, n_{ij} the density of the i species with a positive ion charge equal to j times e; as the ionic term is often neglected, the Debye length is usually approximated to the third term reported in the former equation. In this case, it is possible to observe how the length is not dependent on the mass of the charged particle. The aforementioned quasi-neutrality of a plasma, on a macroscopic level, can then be considered valid when the dimension of the plasma itself, L, is many times longer than the Debye-length, i.e. [86, 87]:

$$L \gg \lambda_D\,. \tag{4.4}$$

Because of the different masses of the species inside a plasma, oftentimes differing from each other for several orders of magnitude, not every species in a plasma is equally effective in following external perturbations. By considering a harmonic oscillator model, then, a typical frequency of oscillation does depend on the mass on the moving particle and can be defined, for electrons and cations respectively, as:

$$\omega_{p,e} = \sqrt{\frac{ne^2}{\varepsilon_0 m_e}}\,, \tag{4.5}$$

$$\omega_{p,i} = \sqrt{\frac{n\,Z^2 e^2}{\varepsilon_0 m_i}}\,, \tag{4.6}$$

with m being the masses of the species considered. As electrons are several orders of magnitude smaller than bulkier ions, the former can follow much higher frequencies than the latter, up to a point where the overall plasma eigenfrequency ω_p is dominated by the electron contribution alone, as:

$$\omega_p^2 = \omega_{p,i}^2 + \omega_{p,e}^2 \simeq \omega_{p,e}^2\,. \tag{4.7}$$

The plasma will therefore counteract external perturbation up to the electron frequency, which in turn depends on their density, and appear 'opaque' to such electromagnetic waves by reflecting them. Higher frequency will on the other hand penetrate freely inside it, travelling in a transpar-

ent medium that cannot timely counteract them. The cut-off electron density n_c acting as a threshold between the two behaviors can then be obtained from Eq. 4.5 as:

$$n_c = \frac{\varepsilon_0 m_e}{e^2} \cdot \omega_p \,. \tag{4.8}$$

A further property of low-pressure, non-thermal plasmas, already somewhat hinted at in the previous paragraph, is that not all their particles necessarily possess the same temperature for all their possible degrees of freedom: this arises once again because of the latter's severely different masses, so that collisions in the plasma volume between heavier particles and electrons are seldom elastic. This on one hand causes a large fraction of molecules and atoms to lie in an excited state than what otherwise observed in neutral gases – a fraction which would be obtained only by heating at several thousands degrees Kelvin –, but on the other leaves the kinetic energy of such heavy particles to remain significantly lower than the electrons' one. As a consequence, then, the kinetic energy distribution of each species in the plasma is still at an equilibrium that follows an approximated Maxwellian distribution, but each with a different corresponding temperature. Ions and neutrals in particular exhibit a thermal temperature $T_i = T_n \ll T_e$.
Ionization degree, electron density and their temperature, and partially the plasma's pressure too, can be used as parameters to characterize and classify plasmas into broad sub-categories:

- Thermal or equilibrium plasmas: the total energy of this kind of plasma is equally parted between all the degrees of freedom of its various particles (i.e., $T_i = T_n = T_e$); each equilibrium shows the same kinetic temperature, which is usually considerably high, hence also the alternate naming as 'hot plasmas'. Such condition can be favored by high pressure regimes, in which the collisions are frequent enough to effectively redistribute the kinetic energy among all species, in spite of the relatively low fraction of elastic collisions. In such plasmas the ionization degree is usually very high, in some cases even approaching unity.
- Non-thermal or non-equilibrium plasmas: in this case, different thermodynamic equilibriums are described by different kinetic temperatures, and plasma exhibits at least two kinetic temperatures, about 10^4 K for electrons and around 300 K for heavier particles (i.e., $T_i = T_n \simeq T_{room}$). Such is often the case for low pressure plasmas, in which the collisions between heavier particles and electrons are sparse enough to prevent an even distribution of their kinetic energies. As a consequence, the ionization degree too is several orders of magnitude lower than for thermal plasmas, usually in the 10^{-3} range or less.

Such broad classification leaves room for intermediate conditions in which for example the temperatures of electrons and heavier particles in excited state are the same (plasmas in partial local thermal equilibrium [88].

4.2 Electron cyclotron resonance (ECR) plasmas

As with electromagnetic waves, plasmas can interact with standing electromagnetic fields thanks to the free charged particles in their volume. The latter, considered to possess a mass *m* and a charge *q*, are subjected to a Lorentz force equal to:

$$\vec{F} = m \cdot \vec{a} = \frac{\partial \vec{v}}{\partial t} = q \cdot \left(\vec{E} + \vec{v} \times \vec{B} \right). \tag{4.9}$$

Here, $\vec{v}$ and $\vec{a}$ are respectively the velocity and acceleration of the particle, and $\vec{E}$ and $\vec{B}$ are the electric and the magnetic component of the applied field. The scalar product $q\vec{E}$ causes the particle to be accelerated along the lines of the electric field, and the vector product $q\vec{v} \times \vec{B}$ causes it to accelerate perpendicularly to the magnetic field. As a consequence, a charged particle moves in a circular motion, with a typical radius and an angular frequency that depend on the imposed magnetic field and the mass and charge of the moving particle. Called gyration or Larmor radius r_L and cyclotron frequency ω_c, they are defined as [87]:

$$r_L = \frac{m v_\perp}{|q|B}, \tag{4.10}$$

$$\omega_c = \frac{|q|B}{m}. \tag{4.11}$$

For the Larmor radius, only the velocity component perpendicular to the magnetic field is to be taken into account. The movement of an electron in such an electromagnetic field is shown in Figure 4.2. In such case however it is already possible to observe that the magnetic field lines are not straight, and as a consequence the electrons cannot move in a perfectly closed circle. While traveling in between the two magnetic poles, in particular, because of the magnetic mirror effect [89, 90], a continuous bouncing between the latter takes place, on the curved field lines, while at the same times the particle still moves in the magnets plane. Such bouncing arises from energy conservation principles, in particular because of the thicker field lines in close proximity of a magnetic pole. As a result of such increasingly complex motion, a drift velocity v_D develops in the *x* plane of the magnets array, which can be defined as follows [91]:

$$\vec{v}_{D,x} = -\mu \frac{\nabla \vec{B} \times \vec{B}}{eB^2}. \tag{4.12}$$

The resulting motion is illustrated in Figure 4.3 in the case of an open configuration. In this case, the current arising from the electron movement in the *x* direction, $\bar{J}_x$, combined with the magnetic field causes a force in the *z*, thus defined [89]:

$$\vec{F}_z = \vec{J}_x \times \vec{B} \tag{4.13}$$

that drives the electrons in the *z* direction, i.e. away from the plasma volume and to the detriment of the desired confinement. In case of a closed racetrack array of magnets, instead, an improved confinement in the *xy* plane arises [92], leading to a more homogeneous entrapment of charged particles in the magnetic field, even at its edges.

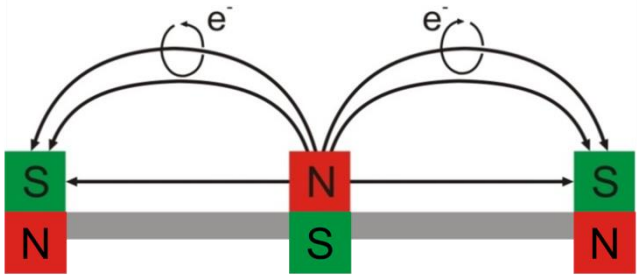

Figure 4.2: Gyration motion of an electron when immersed in a magnetic field, along the latter's lines. Picture based on [52].

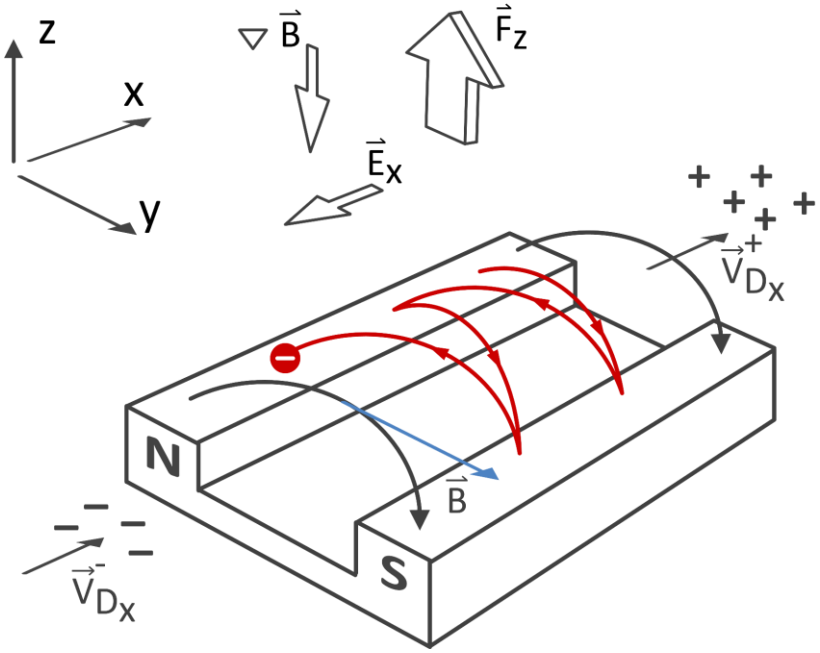

Figure 4.3: Drift motion of an electron trapped in a magnetic field with a drift velocity in the x plane v_{Dx}; here, F_z is the additional drift force directed outside the ECR region. Based on [89].

The acceleration to which the electrons are subjected can be effectively taken advantage of for the ignition of a stable plasma in low pressure regimes by means of incoming electromagnetic

waves, in what is called ECR Plasma: electromagnetic waves ranging from radiofrequencies to the microwave range (respectively in the 20 kHz to 300 MHz and in the 300 MHz to 300 GHz range, respectively) can be in fact be absorbed first by neutral atoms and molecules in order to promote their ionization, among other excitation processes, and from free electrons later, resulting in an increase of their kinetic energy. Absorption of electromagnetic waves can of course take place only if they are resonant with the considered transition, i.e. for electronic transition if they fulfill the Bohr's frequency condition:

$$\Delta E = h\nu\,, \tag{4.1}$$

where ΔE is the difference between the final and initial energy levels involved in the transition, be it more generally rotational, vibrational, electronic or kinetic in nature, h is the Planck constant and ν is the frequency of the incoming radiation. As the kinetic energy levels are densely packed, furthermore, the same radiation that causes a first small ionization of the neutral gas can then accelerate the free electrons, which in subsequent collisions with neutrals cause further ionizations and more, until a stable plasma is obtained, provided a sufficiently high and steady fluence of the electromagnetic radiation.

As for the case where a magnets array is present, then, if the frequency of the incoming radiation is equal to the gyration frequency caused by the magnet, in fact, the initial small concentration of free electrons is permanently accelerated in the magnetic field lines, causing a much higher absorption of power and a much more efficient energy transfer between electrons and neutrals. In this way, a plasma can be ignited even at very low pressures, where usually the mean free path of electrons would be too long for a stable plasma to be sustained. Such plasma would inevitably be a non-equilibrium one, as the ions are basically thermalized [89], with an energy of few meV compared to an average value of 1 eV or slightly more for the electrons [44, 89]. The resonance conditions, assuming a microwave radiation with a 2.45 GHz frequency f, are made explicit in the following equation, derived from Eq. 4.11:

$$\omega_c = 2\pi \cdot f_{\mu w} = \frac{eB}{m}\,, \tag{4.15}$$

which allows then to calculate the magnetic field necessary for such resonance condition, developed by an adequately-built magnets array:

$$B = \frac{2\pi \cdot m}{e} \cdot 2.45\ GHz = 0.0875\ T. \tag{4.16}$$

An array built so to fulfill such conditions is described in details in Chapter 5.1.

Finally, in case of a plasma on top of the magnetic array, the force to which the charged particles are subjected, from Eq. 4.9, must be updated in order to take into account a resistive component resulting from the elastic collisions, so that [93, 94]:

$$\vec{F} = q \cdot \left(\vec{E} + \vec{v} \times \vec{B} \right) - \vec{R}, \tag{4.17}$$

with $\vec{R}$ equal to:

$$\vec{R} = m \cdot f_c \cdot \vec{v}\,; \tag{4.18}$$

the frequency term here, f_c, refers to the frequency of the collisions among particles.

4.3 Plasmochemical processes for surface modifications

Artificial plasmas in low pressure ranges can be generally obtained by means of introducing gas mixtures inside sealed chambers, called reactors, in which a pumping system keeps the desired pressure. The energy necessary to the ignition and the sustainment of the plasma is then provided through electromagnetic waves or high electric potentials administered in several possible ways. Once a stable plasma is obtained, the reactive species inside it readily interact among themselves and with – but not exclusively – all surfaces exposed to the former. They can be divided into five main categories, as listed below [95]:

- **Neutrals**: as a low pressure plasma is in most cases a non-equilibrium one, the large majority of particles, be they atoms or molecules, are still not ionized. They often present however excited electronic, vibrational and rotational configurations (the latter two only in case of molecules). This causes a strong increase in their reactivity, especially when compared to normal gases at room temperatures.
- **Radicals**: this short-lived chemical species are fragments of the original molecules from which they originate and present an incomplete electronic configuration: the presence of a lone electron greatly increases their reactivity, both in complex reactions taking place in the plasma phase and with further processes at the interface of the plasma-exposed solid surfaces.
- **Positive ions**: most of the ions present in plasma phase exhibit, beside an increased chemical reactivity, a positive charge, thus being in principle subjected to the same potential that accelerates electrons too. Thanks to their much heavier mass, the transfer of collisional energy can promote bond breaking on the surfaces exposed to plasma that promotes successive chemical reactions (ion-assisted chemistry) and, for very high accelerations, even cationic implantation in their uppermost layer. The predominance of one effect over the other is usually dependent on the operating parameters of the plasma.
- **Electrons**: by means of the continuous acceleration induced by electromagnetic waves and/or standing electromagnetic fields, and the consequent elastic and anelastic colli-

sions with other heavier particles, electrons sustain the plasma and all its internal reactions. In cold plasmas a large fraction of electrons shows sufficiently high kinetic energy values to escape from plasma borders and to bombard every internal surface of the reactor, thus causing a small net positive charge of the plasma phase. Because their reduced mass, such bombardment does not damage the solids subjected to it.

- **Photons**: originating from radiative relaxation processes of the aforementioned excited neutrals, photons ranging from infrared to UV are ubiquitous in plasmas, giving them their typical glow, the color of which depending on the atoms and molecules in the plasma phase. Their interactions with surfaces, especially in case of photons in the UV range, are enough to promote bond breaking in the uppermost molecular layer, which in turn increases their reactivity and promotes the initiation of complex reactions at the solid-plasma interface. For low pressure plasmas in particular a strong vacuum ultraviolet (VUV) component, with $\lambda < 200$ nm, is also present [56].

In microwave-powered (MW) plasmas, as the one employed in the current work (for more details, refer also to Chapter 5.1), the typical frequency of 2.45 GHz is too high for heavy ions to follow, and the electrons alone are selectively accelerated and heated. As a consequence, the contribution of cations in chemical processes or in plasma sustaining is negligible, and in microwave plasmas the concentration of reactive species depends exclusively on ionization via collisions with free electrons or, on a smaller scale, on volume recombination [96]. Furthermore, considering an approximately Maxwellian distribution of kinetic energy for the free electrons, MW plasmas show a lower average value than RF plasmas [96-98]. This is however more than counterbalanced by their increased density in MW plasmas [98, 99] and, most importantly, by the higher tail in their kinetic energy distribution when compared to RF plasmas [89, 97, 98, 100, 101], provided the operating parameters being equal. Such energy-rich electrons often possess kinetic energy higher than the require a threshold for first ionizations of several elements. As the most energetic electrons are also responsible for the energy transfers necessary to promote chemical reactions among the heavier particles, then, low-pressure MW plasmas combine high reactivities with very low temperatures of radicals and molecules, thus enabling even thermally sensitive materials to be exposed to and treated with them without risk of damaging them.

One of the main advantages of employing plasmas for surface treatments is that they allow a finely tunable modification of the latter's few uppermost molecular levels while at the same time leaving the bulk properties of the material intact [102]. Plasma treatments are beside quick, reproducible, easily up-scalable [103], they can reach nanoscopic resolutions and require very small amounts of reagents, being highly efficient processes that in most cases leave little to none unwanted by-products. Because of the high concentration of reactive species in them, and their usual synergic contribution to the overall treatment, moreover, the end products often differ from what is obtained by means of traditional wet chemistry processes.

Thus, reactive species in plasma phase can create volatile products from the exposed surface, removing material from the latter (etching or ablation); in some cases, because of contemporary ion bombardment, the anisotropy of the process is strongly enhanced (Reactive Ion Etching [104]) resulting in a micro- or nano-texturing of the surface, with stochastic but evenly distributed structures on it. More generally, in case of strongly accelerated ions impinging on the surface, the ablation of material can also be obtained by sheer mechanical removal.

The somewhat opposite process is the formation of poorly volatile products in the plasma phase that travel on the exposed surfaces and form thin films on top of them, often aided in this by a previous activation of the uppermost solid layers thanks to eventual ionic bombardment or because of UV irradiation. The deposition of solid films from a gaseous phase in plasma is much more extensively detailed in the next section. Furthermore, instead of a net deposition of material on the surface, the plasma treatment can result in only an implantation of radical functional groups, which usually strongly alter the chemical properties at the interface (plasma functionalization).

Most of these processes are ubiquitous and even competitive between each other: some etching of the substrate, particularly in case of carbon-based solids, for example, is to be expected in the first steps of a deposition process, before the exposed surface is covered by the newly-formed film, when employing oxygen-containing plasmas. Similarly, a functionalization of the surface can be easily undone if the plasma conditions are too harsh and cause damages to the substrates. Such processes can be selectively chosen and tuned only by operating on the external parameters of the plasma, besides the appropriate choosing of the gaseous reagents, which in turn will influence the internal plasma parameters in a complex way, so much that for each reactor a first optimization of the intended processes is usually required. A partial list of external and internal plasma parameters is reported in Table 4.1.

Table 4.1: A partial list of internal and external parameters for plasmo-chemical processes.

External parameters	Internal parameters
Pressure	Fragmentation degree
Power density	Ionization degree
EM frequency	Density of electrons
EM pulse	Electron temperature
Duty cycle	Gas temperature
Gas composition	Debye Length
Gas flux speed	Collision frequency
Reactor geometry	Absorbed Power
Sample temperature	Plasma frequency
Treatment time	Cutoff density

4.4 Plasma-enhanced-chemical-vapor-deposition (PEVCD)

Plasma-Enhanced-Chemical-Vapor-Deposition (PECVD) is a process that allows the deposition of thin films on substrates directly exposed to or in close proximity of a plasma. The thickness of the films thus obtained, usually ranging from few nm up to several μm, depends primarily and almost linearly on the treatment time and on the gaseous precursors flow, and secondarily on other plasma parameters such as pressure and injected power. Contrary to sputter deposition, in which material is mechanically ablated from a target only to re-deposit on nearby surfaces, PECVD relies on the formation of non-volatile products through a wide array of chemical reactions taking place inside the plasma phase. Contrary to traditional Chemical Vapor Deposition (CVD), however, such process does not require strongly heated substrate [105] and, considering a low-pressure plasma to be employed, the gas temperature is practically equal to room conditions, thus allowing even sensitive substrate to be coated [106]. In the case of ECR plasmas, furthermore, the only high-speed particles, i.e. electrons, have a too small mass to cause damages to the surfaces, while on the other hand the heavier ions impinging on the latter have negligible kinetic energies. The additional presence of a magnetic field and the subsequent acceleration does not significantly increase their energies either, while at the same time still resulting in homogeneously thick films [89].

Similarly to classical radical polymerization, the precursors for the process are radicals immediately forming in the plasma volume after its ignition. While recombination processes and further fragmentations of the radicals are always a concrete possibility, compared to other reactive particles in the plasma phase radicals do possess an average lifetime long enough for them to reach the surfaces exposed to the plasma (direct deposition), or even those lying outside it (afterglow deposition). In the latter case, then, only the most stable fragment escape recombination and deposit on the substrate. Once reached the – often activated – solid surface, the radicals adsorb and wander until they form a chemical bond with the substrate, relaxing and releasing heat in the process. Because of the complex series of reactions taking place in the plasma phase, contrary to traditional wet chemistry deposition the products of PECVD exhibit no fixed stoichiometry, only an average value of it. In this sense, such process is not a strict polymerization and the end products are no polymers with a clear repeating unit: a more appropriate 'plasma-polymer' label is therefore used. Once deposited, furthermore, the thin film still in contact with the plasma can still undergo further reactions, including but not limited to partial etching and return in the gas phase and UV exposure that causes new active anchoring sites to be formed. Because of this, and since a wide array of radicals with different weights and chemical composition are produced in the gaseous phase, plasma-polymers present high degrees of branching and cross-linking, resulting in denser films than their traditional counterparts [96, 104]. As a side-effect, and because of the low operating temperatures, the final products are mostly amorphous, contrary to the crystalline films obtainable through CVD and sputter deposition methods. A sim-

plified list of the possible pathways taking simultaneously place inside the plasma volume during a PECVD process is represented in Figure 4.4. A schematic representation of the possible structure of an organosilicon-based PECVD thin film, similar to those investigated in the current work, is instead offered in Figure 4.5.

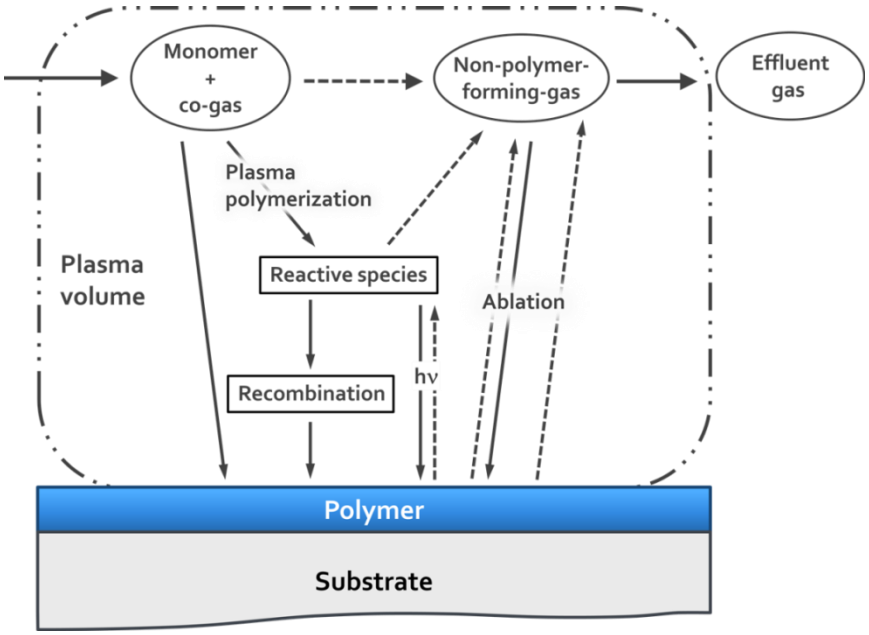

Figure 4.4: Simplified representation of the processes taking place during PECVD at low pressures. Based on [107].

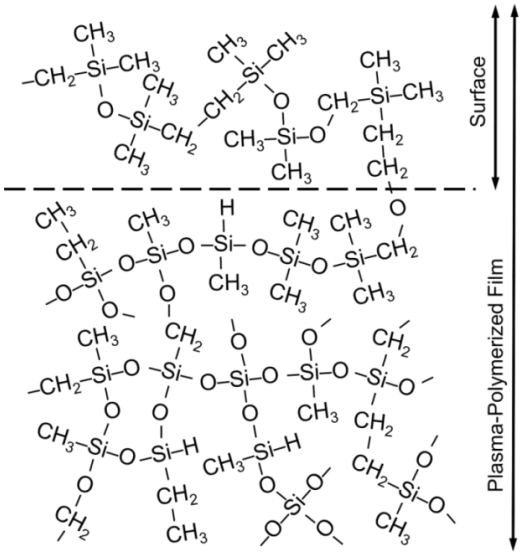

Figure 4.5: Internal structure of a PECVD silica-like film with a non-null organic component. Based on [108].

Through PECVD, then, it is possible to obtain polymers with otherwise not attainable properties, such as superhydrophobic fluorocarbon polymers ('teflon-like' films) with an average stoichiometry $–CF_x$ and with x higher than 2, which is the highest value obtainable through classical polymerization of tetrafluorethylene. Even the deposition of metallic film is made possible by employing metallorganic precursors as gaseous feed for the plasma, which often possess suitable vapor pressures [106]. The chemical and physical properties of the final films can be further tweaked by choosing an appropriate co-gas beside the proper precursor. A much more detailed breakdown of the polymerization routes which involve the precursors, also called somewhat inappropriately 'monomers', employed in the current work, is provided in the final part of Chapter 5.2 and at the end of Chapter 7.5.4, as a model arising from the experimental results presented.

A final peculiarity of the thin films deposited via plasma, is the much stronger adhesion to the substrates that they sport. Instead of an ideal substrate plus coating system, in fact, most plasma depositions result in an additional intermediate interface which usually exhibits a graded composition that smoothly and continuously varies between the chemical and physical properties of the substrate and those of the deposited film. A schematic representation of such structure is shown in Figure 4.6. The thickness of such interphase is usually difficult to determine, but it is assumed to extend at least for few tens of nanometers [36, 57]. In case of organic or polymeric materials acting as substrate, the interface is initiated via vacuum ultraviolet radiation hitting the uppermost molecular layer, which is energetic enough to cause the breakage of aromatic rings and CC and CH bonds [56]. A further cause may be the presence in the plasma phase of reactive species, such as for example atomic oxygen or fluorine, able to etch the polymeric surface. The radicals and dangling bonds originated on the surfaces act as activated sites to initiate the deposition, while the increased roughness caused by the etching causes a higher contact surface between the substrate and the deposited film. The resulting bonds are chemical in nature, which prove to be much stronger than short-range van der Waals interactions otherwise obtained [109]. As a consequence, the adhesion is significantly improved, especially in case of organic substrate with, compared to metals, show a much lower initial surface energy [56]. A further cause for an increase in the adhesion is the cleaning effect most plasmas have on surfaces exposed to them, by removing loosely bonded contamination from the uppermost layers, which is ubiquitous even in case of extensive cleaning of the substrate prior to the plasma treatment: indeed, even 0.01 cm^3/cm^2 of water with a solid residue of 10 ppm are enough to create a monolayer of contaminants [56].As for the variation in the chemical composition of the interface, it usually originates because the initial coverage of the substrate by the newly formed film could be less than optimal, and because the chemistry of the first molecular layer of the latter often differs from the one of the layer's 'bulk' [36], depending on the growth mechanisms of the layer itself. The increase in adhesion and the gradual variation of the physiochemical properties at the interface cause films obtained through PECVD to be more elastic and be able to sustain increased stresses and elongations without breaking or detaching in flakes, contrary to other deposition

techniques [27, 31, 110-112].

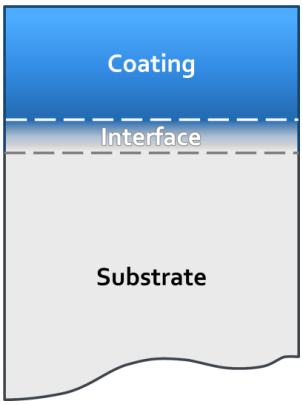

Figure 4.6: Interface between substrate and PECVD-ed thin coating, with a graded composition bridging the two extremes. Based on [24].

Chapter 5

Experimental setup

5.1 Plasma reactor and experimental conditions

All the plasmochemical processes carried out in the current work have been performed by means of the ECR reactor schematically depicted in Figure 5.1 and shown in Figure 5.2: it consists of a stainless steel cylindrical vessel with a diameter of 85 cm and a height of 50 cm, and a resulting base surface and an internal volume equal to 0.57 m^2 and 0.284 m^3, respectively. Under the bottom of the vessel, an array of magnets in a closed race track configuration with a length of 42 cm and a width of 12 cm is present: it consists of 48 permanent magnets 'Secolit 215' of a cobalt-samarium alloy, 50x10.5 mm^2 apiece [113]. Approximatively one centimeter above the array, the corresponding magnetic field is equal to 0.0875T, in order to satisfy the resonance conditions with the incoming microwave radiation (as illustrated in Chapter 4.2). The closed configuratiton is also instrumental for a more efficient confinement of the resulting plasma. The top view of the array is shown in Figure 5.3. The magnetic system is connected to an external motor that allows it to move underneath the vessel and the plasma with it, increasing the treatable surface up to $42 \cdot 33\ cm^2 = 1386\ cm^2$. A full sweep of the vessel is carried out in around 30 seconds, a round trip in about one minute. The motor can be activated or stopped at any moment by means of a switch.

The low pressure inside the vessel is produced and maintained by means of a system of a rotary vane and a turbomolecular pump from Pfeiffer Vacuum. The first one has a maximum capacity of 9.44 l/s and provides the pre-vacuum conditions, while the second one has a capacity at its maximum frequency equal to 500 l/s. The residual pressure inside the reactor is around 0.05 mbar and it is monitored by means of a pressure transducer: the latter has been first recalibrated at the beginning of the work. The venting of the reactor chamber is carried out by means of a valve: the entering air must first pass through a desiccant medium (silica beads) in order for the humidity to be removed from it. Water vapor molecules adsorbed on the inner walls of the reactor would otherwise cause much longer pumping times before reaching the steady-state low pressure conditions. The outlet for the exhaust gases towards the pumping system lies in the lower right corner of the reactor, causing a slight asymmetry whose possible consequences on

the quality and homogeneity of the deposited coatings are further investigated at the end of section 7.1.2. A valve allows the pumps to be isola ted from the vessel during the venting process, so to avoid damages to the turbomolecular pump caused by atmospheric pressure.

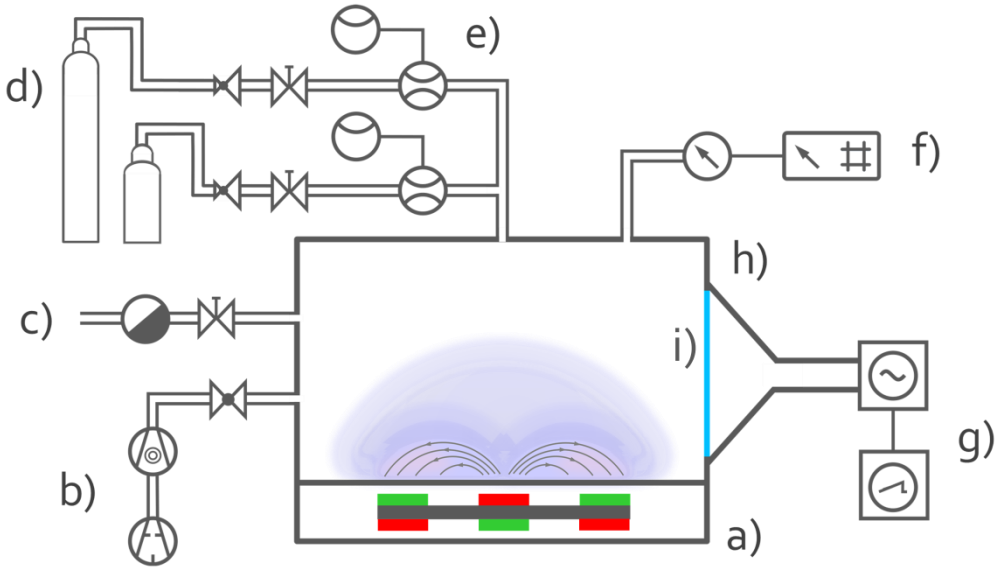

Figure 5.1: Schematic of the ECR reactor employed in the current work. It consists of a stainless steel vessel, with an underlying movable permanent magnet (a), in which a pump system (b) keeps a low pressure; the venting is provided by a valve (c), while the pressurized gases (d) are introduced into it by means of mass flow controllers (e); the working pressure is monitored through a transducer (f). The microwaves are produced in a magnetron connected to a pulse generator (g) and transferred by means of a waveguide and a horn antenna (h) in the reactor. A glass window (i) separates the latter two. The magnetic field originating from the magnet is also schematically reported, as two half-cylinders emerging from the north pole and ending at the lateral south poles.

The gases to supply the plasma are stored in compressed gas cylinders connected to the vessel, while their fluxes are regulated by means of a first pressure reduced immediately connected to the cylinders and later by thermal mass flow controllers from Tylan. The monomer gas on the other hand is regulated by a manually-controlled needle valve. The gases flow inside the reactor through a central inlet on the upper side of the vessel. The resulting average pressure, before the plasma ignition, is about 0.55 to 0.65 mbar. Because of the increased pressure, the plasma can ignite also outside the strict boundaries of the magnetic field, creating a homogeneous plasma over the magnet, as seen in Figure 5.4.

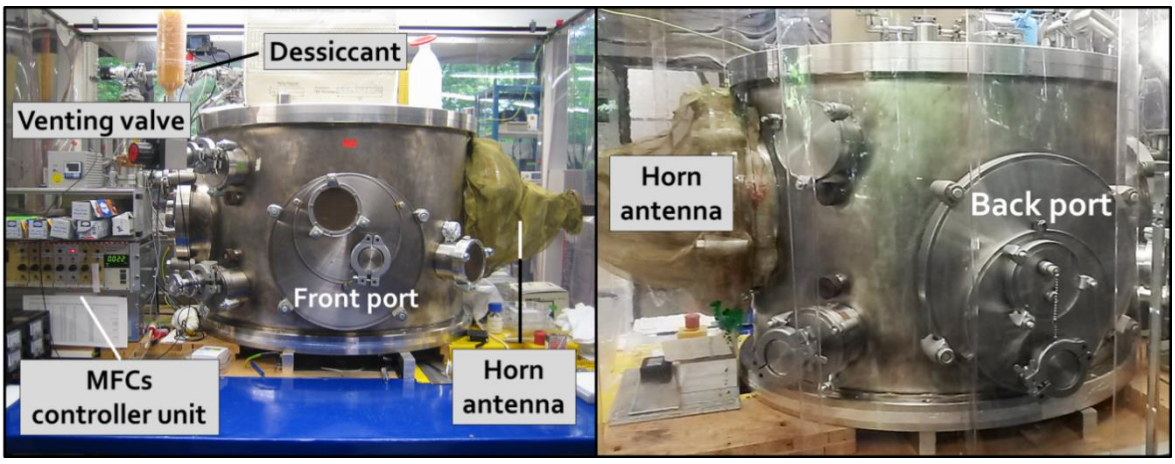

Figure 5.2: Front (left) and back (right) view of the ECR reactor employed in the current work.

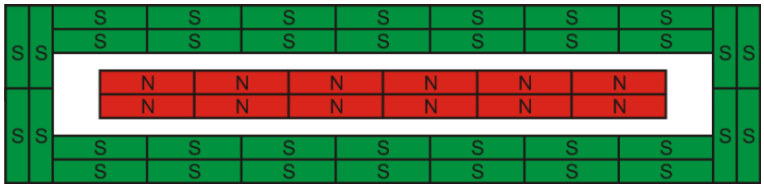

Figure 5.3: The array of 48 permanent cobalt-samarium magnets, arranged in a closed race track configuration, lying under the ECR vessel [46].

The microwaves for the plasma ignition, with a frequency of 2.45 GHz, are produced in a magnetron which can supply a maximum power of 3 kW and lead inside the reactor by means of a hollow waveguide and a horn antenna. The inlet consists of a glass window transparent to the microwaves. In order to avoid unwanted contact between the latter and the plasma, the window is covered by a removable circular Teflon shield. A water trap between the waveguide and the magnetron collects eventual reflected radiation via a circulator device and prevents damages to the microwave source. The system is operated in pulsed mode by means of a square-pulse generator connected to the magnetron. The effective power provided to the plasma must therefore be averaged for the duty cycle of the pulse.

The entire system lies under a hood with a continuous laminar flow streaming downward, in order to prevent dust particles to accumulate on the samples or on the working bench.

The samples are inserted in the vented reactor through its frontal port and are fixed on an aluminum sample holder by means of small duct tape strips, in order to prevent their misplacement during the initial stages of the pumping of the vessel. Prior to their treatment, the samples are exposed to a corona discharge for few seconds in order to remove electrostatic charges from their surfaces. For all plasma treatment, the pumping is carried out for thirty minutes, in order to

reach the minimum pressure value and remove eventual contaminants from the vessel that could otherwise alter the chemical composition of the deposited films. The depositions have been always carried out in a movable magnet configuration, with the motor being activated manually upon ignition of the plasma, and with the magnet always starting at the end of its run. The duty cycle of the microwave pulse has also been kept constant and equal to 50 %, with an overall period of 1 ms, i.e. a 500 μs/500 μs pulse/pause ratio and a pulse frequency of 1 kHz. The effective average microwave power is therefore half of the nominal value produced in the magnetron.

Figure 5.4: Plasmas seen from the side window port of the ECR vessel based on a HMDSN/oxygen (left) and a HMDSN/hydrogen (right) mixture.

5.2 Substrates

Polyethylene terephthalate (PET) is an organic thermoplastic polymer resin, whose repetitive unit is shown in Figure 5.5. A partial list of its mechanical and chemical properties is likewise listed in Table 5.1.

Thanks to its mechanical resiliency, optical transparency, chemical inertness [118] and sturdiness, in the last thirty years PET has been steadily substituting heavier and pricier materials, as metals and glass, in many industrial applications. Chief among the latter is food packaging [119], partly also in compliance of the current European legislation [8]: as of 2013, 30% of the yearly produced bottles for alimentary purposes worldwide are made by PET [118].

PET finds however countless applications also as substrate for flexible solar cells [118] or light emitting devices [20], for prosthetics [120] and medical implants, and in the textile industry [118] just to name a few, most of which require, to different degrees, barrier effects against mostly oxygen and water vapor. The intrinsic barrier properties of PET foils, however, are strongly influenced by their degree of crystallinity: the latter depends chiefly on the short- and long-

ranges forces interacting between repetition units in the polymer bulk and the resulting chain mobility when still in a viscous state (i.e., during the production process). Closely-packed crystal regions are often considered to be practically impenetrable [121], with the permeation taking place in the free spaces of the more porous amorphous fractions. Most of commercially available PETs possess a relatively low crystallinity degree (usually not above 30 %), with the crystalline micro- and nano-domains evenly scattered in the predominant amorphous matrix. Finally, thanks to the polar functional groups in the repetition unit, particularly the carboxylates, PET can provide a good starting adhesion, thus acting as a suitable substrate for the eventual deposition of thin barrier films on top of it [27, 55].

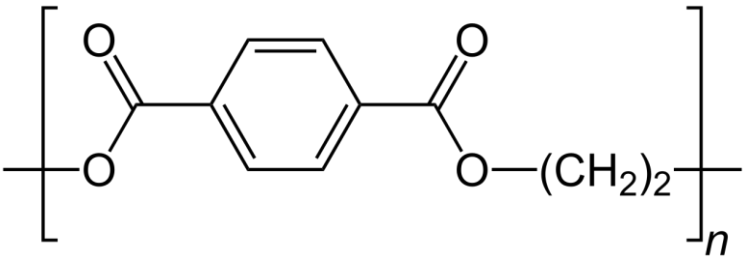

Figure 5.5: Repetitive unit of polyethylene terephthalate (PET) [122]. It consists from left to right of a carboxylate ester, a phenylene group, a second carboxylate ester and an ethylene group.

Table 5.1: Main physical properties of poly-ethylene terephthalate.

		Reference
T_g	80°C	[114]
Melting point	>250°C, 260°C	[115, 116]
Breakdown voltage	≥ 4.5 kV (thickness-dependant)	[117]
Transparency	≥ 90%	[117]
Haze	≤ 2%	[117]
OTR (25° C, 50 % r.h.)	110 $cm^3/m^2 \cdot d \cdot bar$	[117]
WVTR (25° C, 85 % r.h.)	16 $g/m^2 \cdot d$	[117]

In the current work, all plasma-polymerized thin films have been deposited on Hostaphan® RNK PET foils from Mitsubishi Polyester Film [117]. Some deposition moreover have been carried out by using Melinex® 401CW PET foils from Dupont Teijin Films [116].

Hostaphan

The PET foil from Mitsubishi (from now onwards simply 'Hostaphan') is a biaxially oriented (BoPET) extruded film with a thickness of 23 µm [117]. It possesses a laminated structure, as seen in Figure 5.6, thus presenting on both sides a 'standard' surface that ensures homogeneity. No further information upon the composition of the standard external layers or the internal core could be found in the datasheets. A better overview of the chemistry of the former is provided in Appendix A. The root mean square of its surface roughness has been found out to be equal to 0.7 nm [123].

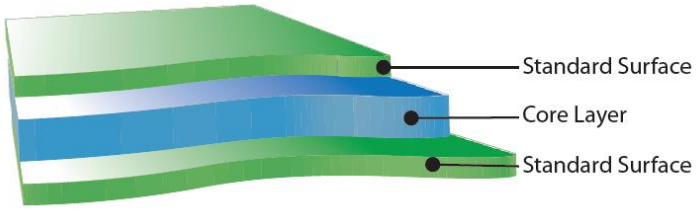

Figure 5.6: Schematic representation of a section of the Hostaphan PET foil. From [117].

The oxygen transmission rates for the uncoated Hostaphan PET have been first tested and then regularly measured on different samples throughout the whole duration of the current work, in order to have a reliable average value to be used as reference for the subsequent calculations, and in order to verify the homogeneity of the properties of the PET foil. The rates have been measured by means of both permeation systems according to the procedure described in Chapter 6.4. The normalized values, together with the calculated average, are reported in Figure 5.7. The deviation from the latter value is around 7 % maximum, but most often only a couple percent points. Such fluctuations, apart from the inherent instrumental limits related to the measuring procedure, may be caused by slight variation in the thickness of the tested samples and/or in their chemical composition, particularly their local degree of crystallinity.

Melinex 401

The PET foil by Dupont is a BoPET, plasticizers-free extruded film with a thickness of 50 µm. Such film is 'specially treated to give a slippery surface on one side,' [116] which implies an increased surface roughness on the backside: as an electrical insulator, PET can often develop strong surface electrostatic charges that causes foils to stick to each other and/or attract dust particles. An induced roughness on at least one of the sides allows for an easy stacking and a later detaching of the polymer sheets, while at the same time still offering a desirable smooth surface

on the other.

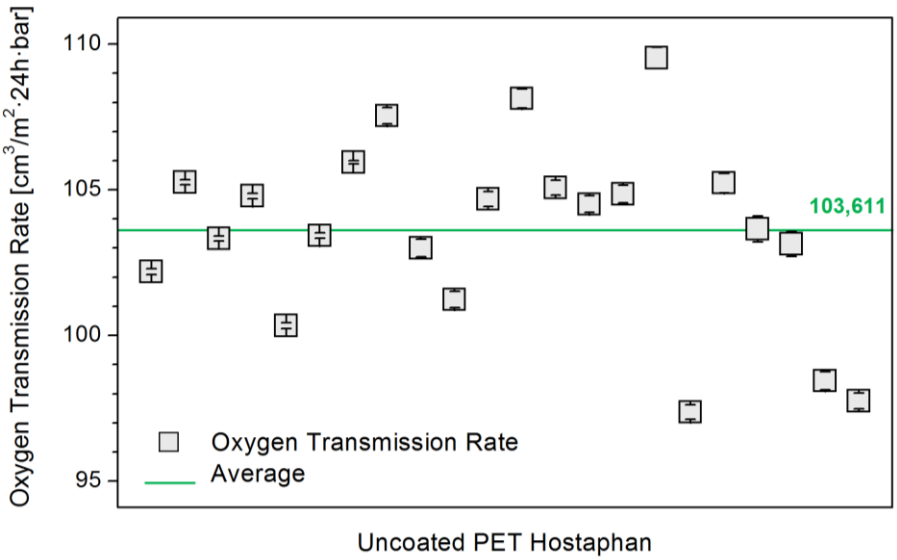

Figure 5.7: Oxygen transmission rates for uncoated Hostaphan PET foils, together with the respective average value. The measurements have been carried out by means of the permeation measurement instruments and according to the procedure described in Chapter 5.5.

The different nature of the front- and the back-side of the Melinex foils is confirmed by AFM measurements reported in Figure 5.8: while the smooth side shows an almost non-existent surface roughness, the backside exhibits a thick, although random, distribution of knobs with an average height of almost 50 nm. Such antiblock particles are shown to consist of PET cyclic olygomers and amount to 1.1 wt% of the total foil [124]. For an additional determination of the chemistry of both sides of the Melinex foil, also refer to Appendix A1.

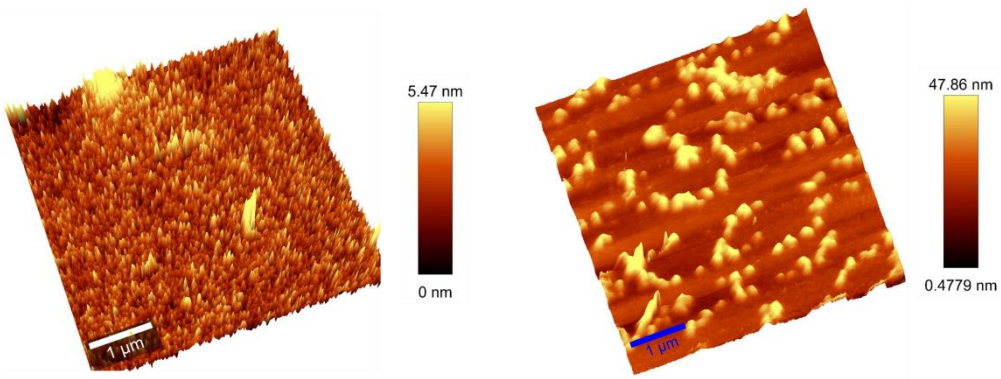

Figure 5.8: AFM scan of the smooth side (left) and the rough one (right) of the Melinex foil. Courtesy of Stanislav Dribinskiy.

For the Melinex foil, too, a few uncoated samples have been tested for their oxygen transmission rates in the permeation System I with the procedure reported in Chapter 6.4. The resulting normalized values and the average transmission rate are reported in Figure 5.9. The thicker foil (50 µm instead of 23 µm) results in a lower oxygen transmission rate, roughly 47 % lower than Hostaphan. The results are in very good accordance with the thickness ratio of the two foils, which is equal to 46 %.

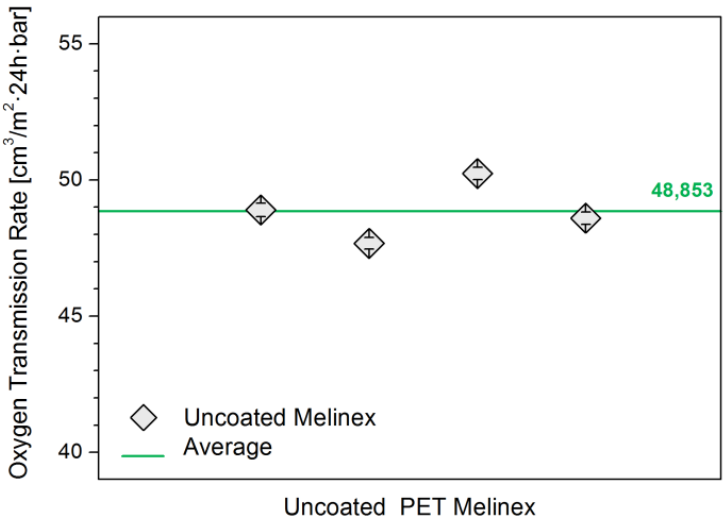

Figure 5.9: Oxygen transmission rates for uncoated Melinex PET foils and calculated average value displayed as a green line. The measurements have been carried out by means of the permeation measurement instruments by following the procedure described in Chapter 6.5.

5.3 Monomers as plasma feed gases

In contrast to more classical gaseous precursors for silicon-based thin films, like silanes or disilanes, organosilicon compounds are safe to manufacture, easy to handle, non-explosive at room temperature [125], poorly toxic and flammable [126]. Such class of compounds includes several dozen molecules, both linear and cyclic, like tetraethoxysilane (TEOS), tetramethylsilane (TMS), and octamethylcyclotetrasiloxane (OMCTS), just to name a few, most of them successfully employed for PECVD processes [96, 104, 127, 128]. The main disadvantage over classical silane compounds is the relatively more complex structure and the presence of bulky organic substituents that require a further oxidation step, thus slowing the chemical reactions and the deposition of inorganic silica-like films.

The main monomer employed in the current work is 1,1,1,6,6,6-hexamethyldisilazane

(HMDSN), whose structural formula is shown in Figure 5.10 together with its bond energies [125, 129]. The molecule consists of a main backbone of two silicon atoms bond to a secondary amino group. Each silicon atom is furthermore bond to three trimethyl groups. As most other silazanes, at standard conditions it presents itself as a transparent and colorless liquid, with a vapor pressure high enough to be suitable as gaseous precursor in plasma processes without the need of being preliminary heated. The associated absorption spectrum in the 4000 – 400 cm^{-1} range of its vapors, recorded with the instrument and the procedure reported in section 6.2.1, is shown in Figure 5.11. The latter also includes the attribution of the monomer's main peaks.

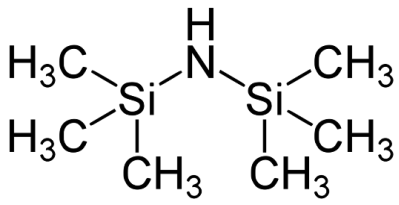

	[eV]
Si-C	3.12
Si-N	3.42
N-H	4.05
C-H	4.31

Figure 5.10: Molecular formula of hexamethyldisilazane and its respective bond energies.

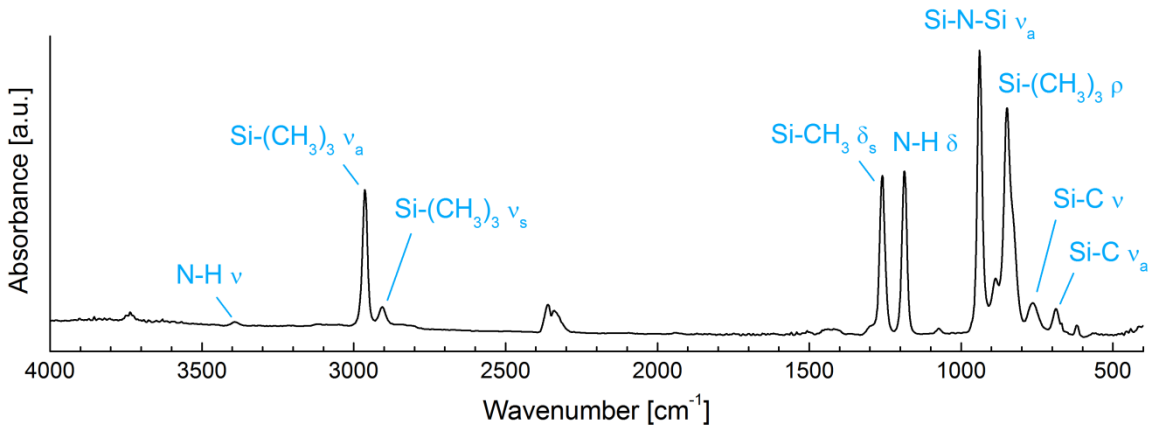

Figure 5.11: Absorption infrared spectrum in the 4000 – 400 cm^{-1} range for gaseous HMDSN. Unlabeled peaks refer to residual CO_2 and water vapor in the sample-holding cell atmosphere. ν = stretching, δ = bending, ρ = rocking, s = symmetrical, a = asymmetrical.

As a secondary monomer used for a limited series of plasma deposition processes (see also Chapter 7.5), 1,1,1,6,6,6-hexamethyldisiloxane (HMDSO) has also been employed; the molecular formula with the bond energies is reported in Figure 5.12 [125, 130, 131]: the molecule differs

from HMDSN because of the central oxygen instead of the secondary amino group. Similarly, the corresponding absorption infrared spectrum, reported with the attribution of the main peaks in Figure 5.13, lacks the typical signal associated with nitrogen-containing bonds and sports the silicon oxide peaks. An initial advantage of HMDSO over HMDSN as precursor for inorganic silicon oxide thin film is that the former already contains oxygen, with an initial O/Si ratio equal already to 0.5, to be later increased in the plasma polymerization process ideally up to 2, for a stoichiometric silicon dioxide film [126].

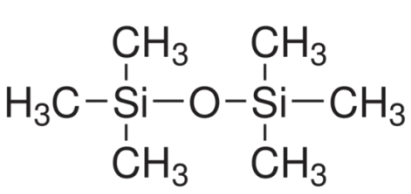

	[eV]
Si-C	3.12
Si-O	4.56
C-H	4.31

Figure 5.12: Molecular formula of hexamethyldisiloxane and its respective bond energies.

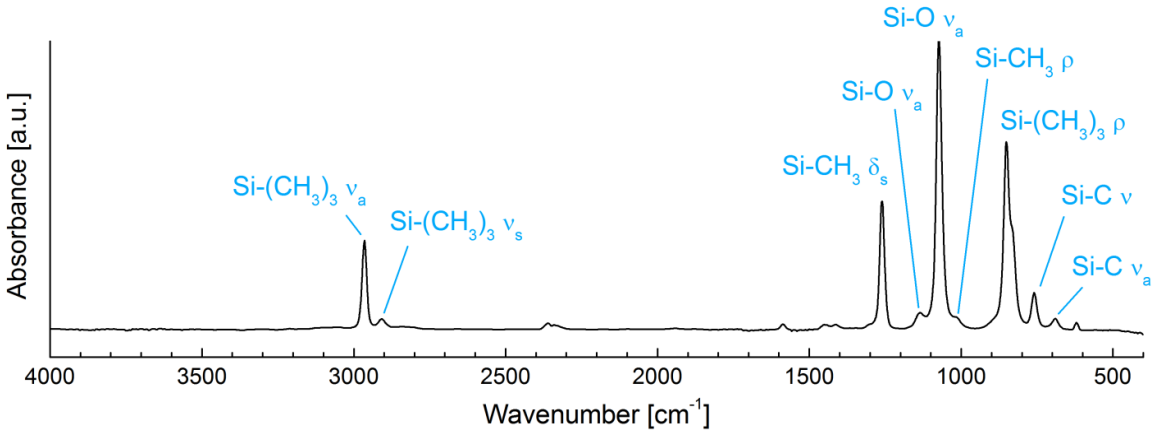

Figure 5.13: Absorption infrared spectrum in the 4000 – 400 cm^{-1} range for gaseous HMDSN. Unlabeled peaks refer to residual CO_2 and water vapor in the sample-holding cell atmosphere. ν = stretching, δ = bending, ρ = rocking, s = symmetrical, a = asymmetrical.

Some of the main physical properties of the two monomers and of the two co-gases, oxygen and hydrogen, employed in the deposition processes, are reported in Table 5.2. Oxygen has been employed in the production of inorganic, silica-like films, while hydrogen has been used in order to obtain organosilicon film as intermediate buffer in a multilayer approach. In the current work, both monomers have been provided by Merck Millipore.

Table 5.2: Physical properties of the monomer employed as precursors and the co-gases in the plasma feed for the performed PECVD processes.

	HMDSN	HMDSO	O_2	H_2
Molecular formula	$C_6H_{19}NSi_2$	$C_6H_{18}OSi_2$	O_2	H_2
State of matter	liquid	liquid	gaseous	gaseous
Molar mass	161,39 g/mol	162,38 g/mol	32 g/mol	2 g/mol
Density	0,78 g/cm^3	0,76 g/cm^3	–	–
Vapor Pressure	20 hPa	20 hPa	–	–
Fusion point	-82 °C	-68 °C	-218,8 °C	-259 °C
Boiling point	126 °C	100 °C	-183 °C	-253 °C
Purity	≥ 98,5%	≥ 98,5%	99,995%	99,995%

Film deposition

Considering a stoichiometric inorganic end product resembling silica, an extremely simplified reaction path for HMDSN and HMDSO, respectively, can be summarized as:

$$4\,Si_2NH(CH_3)_6\,(g) + 55\,O_2(g) \xrightarrow{plasma} 8\,SiO_2(s) + 38\,H_2O(g) + 24\,CO_2(g) + 4\,NO_2(g) \quad (5.1)$$

$$Si_2O(CH_3)_6\,(g) + 12\,O_2\,(g) \xrightarrow{plasma} 2\,SiO_2(s) + 9\,H_2O\,(g) + 6\,CO_2\,(g) \quad (5.2)$$

In reality, the complex nature and high number of possible reactions taking place in the plasma phase, almost all of them being furthermore reversible, causes the polymerization process to be much less straightforward. The first fragmentations of the monomers in absence of further co-gases, and the initial cross-linking processes and the formation of the polymer precursors will be qualitatively described below. When not openly stated otherwise, the following breakdown is meant to be valid for both monomers presented in the previous section. Furthermore, the plasma polymerization in the current case is assumed to follow a radical mechanism scheme [132, 133].

The first step of the process is the fragmentation of the gaseous precursor via collisions with accelerated electrons, which is generally most likely to take place at the ends of the monomer, i.e. [134]:

$$R - Si - CH_3 \xrightarrow{e^-} \begin{cases} \rightarrow R - Si\cdot + CH_3\cdot \\ \rightarrow R - Si - CH_2\cdot + H\cdot \end{cases} \tag{5.3}$$

R here is used as label for the rest of the precursor molecule and/or to indicate the presence of a longer organosilicon chain attached to the highlighted functional groups. The first pathway is slightly more favored than the second [135], as the bond energy between C and H is more than 1 eV higher than for the Si-C case. The smaller radicals produced in both cases can either recombine forming stable products as ethane and hydrogen (the bond energy of the latter being 4.52 eV [125]) or spontaneously recombine with the heavier fragments, or further react with the initial precursor, thus still advancing the overall polymerization process via formation of 'more useful' fragments, here shown via an exemplified schema [136]:

$$CH_3\cdot + Si - CH_3 \rightarrow CH_4 + SiCH_2\cdot \tag{5.4}$$

$$H\cdot + Si - CH_3 \rightarrow H_2 + SiCH_2\cdot \tag{5.5}$$

The precursor-based radicals, on the other hand, may be subjected to secondary reactions that neither advance nor terminate the polymerization process, as in the following example [136]:

$$R - Si\cdot + (CH_3)_3 - Si - R \rightarrow R - Si - CH_2\cdot + H - Si - R \tag{5.6}$$

Alternatively, the products of Eq. 5.3 may also react with themselves, forming bigger and less volatile fragments or accreting those already present in plasma phase, according to the following possibilities [134]:

$$R - Si - CH_2\cdot + \cdot Si - R \rightarrow R - Si - CH_2 - Si - R \tag{5.7}$$

$$2\,R - Si - CH_2\cdot \rightarrow R - Si - CH_2 - CH_2 - Si - R \tag{5.8}$$

$$2\,R - Si\cdot \rightarrow R - Si - Si - R \tag{5.9}$$

The second reaction is slightly less favored than the other two since [137], as previously reported, the methylene radical is energetically less likely to form than the sylil one. The cross-linked fragments thus formed, often labeled plasma-olygomers [138], are heavier than the original precursor molecules and less volatile, and thus more likely to deposit onto a surface exposed to or in close proximity of the plasma, forming a thin film that will keep on growing as long as new fragments are formed in the plasma phase. The process here reported for the formation of dangling bonds can and will happen also on the newly-deposited surface, meaning that the film accretion is a process taking place simultaneously at several activated sites. In this case, some steps can be also catalyzed via UV or VUV radiation escaping the plasma phase and impinging on the solid surface. The former reactions are then to be taken only as a partial breakdown of the overall pos-

sible process, especially since, being exemplified pathways, their ideal stoichiometry is hardly found in a real plasma. As an example, thin films may also be formed via stronger participation of cations in the overall process, along the lines of [139]:

$$R - Si - CH_3 \xrightarrow{e^-} [R - Si - CH_3]^+ + e^- \tag{5.10}$$

with the cation being then subjected to a heterolytic cleavage, so that:

$$[R - Si - CH_3]^+ \rightarrow R - Si^+ \cdot + \cdot CH_3 \tag{5.11}$$

i.e. neutral radicals that can still follow the aforementioned pathway.

Another possibility is an electron collision resulting only in an excitation of the precursor molecule, which can at a later stage decompose via a homolytic cleavage still resulting in the same products of Eq. 5.11 [139]:

$$R - Si - CH_3 \xrightarrow{e^-} [R - Si - CH_3]^* \tag{5.12}$$

$$[R - Si - CH_3]^* \rightarrow R - Si \cdot + \cdot CH_3 \tag{5.13}$$

For HMDSN in a microwave plasma, in particular, the fragmentation via breaking of the Si-N bond is also to be taken into account, contrary to most other cases [96, 125]. For HMDSO on the other hand, with the Si-O bond being the strongest in the precursor molecule, it can be assumed that most of the fragment resulting in net deposition on the surfaces still contain the original and intact Si-O-Si backbone.

In case of oxygen being added as co-gas in the plasma feed the reagents must also include molecular oxygen both in the ground state and in an excited configuration and extremely reactive atomic oxygen. In this case, the final solid products will inevitably incorporate oxygen both in their main chains and in their side branches. For HMDSN, oxygen will cause an easier rupture of the Si-N bond and the substitution of the amino-group with a single oxygen or an hydroxyl group, the latter to be expected thanks to the high abundance of hydrogen in the plasma phase. For HMDSO, on the other hand, an excess of oxygen will cause an even higher retention degree of the silicon oxide backbone of the precursors. More generally, oxygen will act as a scavenger, sequestering carbon and hydrogen atoms by forming very stable volatile products (see Eq. 5.1 and 5.2), and leaving only non-volatile silicon to form an oxidized solid with SiO_x as general formula, with a variable and possibly non-integer *x* value. Residual organic groups on the solid surface may always be ablated or substituted by oxygen in the plasma phase at a later stage than their deposition. As apparent in chapter 7.1.2, the actual reactions taking place in the plasma phase are not stoichiometric, as an inorganic film can be obtained for much higher dilution than those suggested by Eq. 5.1. The complex mechanisms in an oxygen-rich plasma leading for both monomers to a deposition of silica-like plasma-polymers are further detailed in Chapter 7.5.4.

Chapter 6

Diagnostic methods

In the current chapter, the diagnostic methods for the characterization of the PECVD films are listed and described. The methods for the measurement of the layers' thickness will be elucidated, then the analyses for the study of their chemical composition. The microscopy methods for the study of the surface morphology will be described, followed by the methods for the evaluation of the barrier properties of the films: in this case, a description of the two instruments employed and their cross-calibration will also be given. Finally, a full overview of the methods for the non-destructive localization of defects in barrier layers will be offered, starting with an introduction on the state of the art for such detection methods, the principles on which the test operates, a description of the experimental apparatus and an in-depth evaluation of its reliability and feasibility.

6.1 Profile measurements

The thickness of the plasma-deposited films has been measured by means of a profilometer, the *Perthometer C5D* from the company *Perthen*. The instrument consists in a movable head connected to a data processor. The head is equipped with a thin metallic tip that can be lowered on a solid sample until it is brought in contact with the surface; the tip moves on the surface for an adjustable scanning length, following the surface profile thanks to the flexible arm to which it is connected. The processor registers the height variations and displays them as a surface profile that can be later printed on millimeter paper. An ensuing conversion of the profile displayed in centimeters accordingly to the scale selected on the instrument gives the desired values.

For the measurement of the thickness of the PECVD films, a glass substrate is covered at its extremities with two thin strips of duct tape, with a typical width of ≤ 1 mm, and later inserted in the reactor together with the other samples to be coated. The strips act as a mask, preventing the film to deposit on the underlying glass surface. After the deposition step, the glass slide is cleaned with compressed air, in order to remove eventual dust particles, the duct tape is re-

moved and the surface profile in correspondence to the uncoated strips is recorded. The profile resembles a trench, with the height of the artificial steps corresponding to the thickness of the deposited film. The height is measured in centimeters with the help of a rule and later converted into nanometers or micrometers. For each deposited film, two profile readings have been carried out: for each of them, three values have been measured, two at the extremities of the displayed step and one in the center, in the latter case by prolonging the film surface profile over the 'trench'. The measurement process is schematically represented in Figure 6.1.

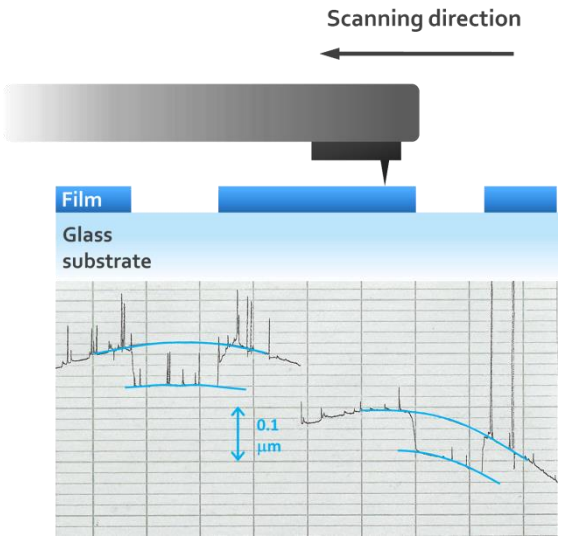

Figure 6.1: Profile measurement for the determination of the thickness of thin films (top): the tip connected to the movable arm of the profilometer slides on the sample surface, following the steps caused by the duct tape strips applied on the glass substrate before the deposition step. The stored height are displayed and printed on millimeter paper (bottom), on which the profile can be measured and converted in nanometers. In case of vertical tilting of the substrate, a curved baseline is to be observed (bottom right).

In practice, the overall film thickness is assumed to be the calculated average. The sensitivity limits of the millimeter paper are equal to 0.5 mm, which for the smaller employed scale correspond to a margin of error of 5 nm. The accuracy of the instrument itself is listed as 1 nm [140]. These values are then combined with the standard deviation associated to the average thickness in the total error affecting the measurements, according to the formula:

$$\sigma_{TOT} = \sqrt{\sigma_{st.dev.}^2 + \sigma_{scale}^2 + \sigma_{instr.}^2}\,, \tag{6.1}$$

where σ_{TOT} is the total error, $\sigma_{st.dev.}$ the standard deviation arising from the six measured values, σ_{scale} the sensitivity limits caused by the millimeter paper and $\sigma_{instr.}$ the accuracy of the profilometer. The minimal measurable step has been found out to be around 10 nm high at the smaller

scale, and it can be assumed to be the resolution limit of the employed instrument. Such value is however much smaller than the one for other techniques such as TEM or ellipsometry, that for colorless films become unreliable already for thicknesses around 50 nm [141].

6.2 Chemical analyses

The chemical composition of the deposited films has been investigated by means of Fourier Transform InfraRed absorption spectroscopy (FTIR) in Attenuated Total Reflectance (ATR) and single-reflectance mode, and with X-ray Photoelectron Spectroscopy (XPS), as described below.

6.2.1 Fourier-transform infrared (FTIR) spectroscopy

In molecular bonds, the atoms involved rotate along their bond axis and vibrate, changing the bond's angle and/or length, with typical frequencies that depend on the atoms forming the molecular bond and the latter's type (single, double, triple), similarly to an unidimensional harmonic oscillator, with the mass of the atoms representing the weights and their bond acting as the spring connecting them. Yhe characteristic frequency ν at which the system oscillates is then thus defined:

$$\nu = \frac{1}{2\pi} \cdot \sqrt{\frac{k}{\mu}}\,, \tag{6.2}$$

where k is the elastic constant of the spring and μ is the reduced mass of the system. A molecule with more than two atoms will show several vibrational modes for each of its molecular bonds, according to the following equation [142]:

$$Z = 3N - 6\,, \tag{6.3}$$

where Z is the total number of possible vibrations and N is the number of atoms in the molecule. For each vibrational mode, several connected rotational modes are possible. The combined roto-vibrational typical frequencies lie in the infrared range of the electromagnetic spectrum, i.e. into a range of wavelength between 800 nm and 1 mm. If a molecular bond possesses a permanent dipole, which is absent only in cases of homoatomic molecules, and if the vibration induces a change into the dipole moment, then it can be excited or relaxed by an incoming photon with a frequency resonant to the aforementioned one ν. Such is the principle of InfraRed (IR) spectroscopy, a diagnostic technique that allows to identify the unknown chemical composition of a

sample by exposing it to the full IR frequency range and by recording the variation in transmitted or absorbed intensity of said wavelengths. The method, as different molecular bonds possess different cross-sections and therefore different degrees of interaction with the resonant radiation, cannot be used for quantitative determinations. It can, however, not only detect the elemental composition of a sample, but also the way the different elements are bond to each other. Moreover, different substituents of the vibrating atoms, because of their different electronegativity values, cause fine shifts in the typical frequency that can be detected and properly attributed. The main physical quantities involved in IR spectrometry, wavelength λ, frequency ν and wavenumber $\bar{\nu}$ are thus related to each other:

$$\bar{\nu}\,[cm^{-1}] = \frac{\nu}{c} = \frac{1}{\lambda}\,, \tag{6.4}$$

with *c* being speed of light in vacuum.

Fourier-Transform IR spectroscopy (FTIR) allows to record spectra in a much faster way than conventional single or double-ray IR spectroscopy: instead of recording the whole analyzed range by selecting and directing on the sample one frequency at a time, in FTIR spectroscopy all the desired frequencies coming from the source *S* are sent to the sample *Sa* simultaneously, after traveling in a Michelson interferometer, schematically represented in Figure 6.2.

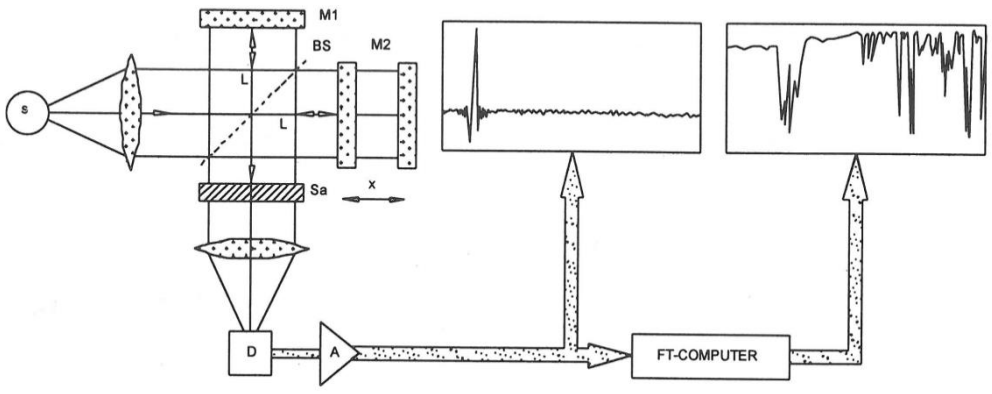

Figure 6.2: Schematic representation of the Michelson interferometer connected to the IR spectrometer (left) and how the output signal is first amplified, recorded as interferogram and finally displayed as an absorption spectrum after an inverse Fourier transform (center and far right). Picture from [143].

The incoming radiation is divided by the beam splitter *BS* and sent in two orthogonal directions. One of the mirrors *M* at the extremities of the interferometer is steadily moved during the

analysis (the span of the movement being labeled as *x*), so that the two beams are reflected and sent back to the beam splitter, where they recombine forming an interference pattern. The recombined radiation then reaches the sample, is partially depleted of the frequencies resonating with the rotovibrational modes of the sample's constituents and is finally focused on the detector *D*. The output is recorded as an interferogram in the *x* [cm] domain and the computer, via an inverse Fourier transform, display the absorption curves (defined as the ratio between a reference value recorded without sample and the later output intensity for each frequency) in the wavenumber [cm^{-1}] domain. It is thus possible to record and average several spectra of the same sample in the same time span necessary for a single scan with traditional spectroscopy, thus also increasing the signal-to-noise ratio for a better spectra quality. No information is lost, thanks to the properties of the Fourier transform function. A schematic representation of the process is given in Figure 6.2.

As in the current work the investigated films have on average a thickness of only 100 nm, single reflection modes would not be sensitive enough to analyze such thin films. An Attenuated Total Reflectance (ATR) mode has therefore been employed. In such configuration, two substrates coated with the film to be investigated are pressed against a high refractive index crystal with a trapezoidal shape. The crystal index is so chosen, that the incoming radiation from the interferometer entering in the crystal from one side is completely reflected at the crystal-sample interface, keeping traveling along its length before leaving it and being focused on the detector with a fixed mirror system. The system of mirrors before and after the sample holding cell and the details of the crystal in the latter are shown respectively in Figure 6.3 and 6.4.

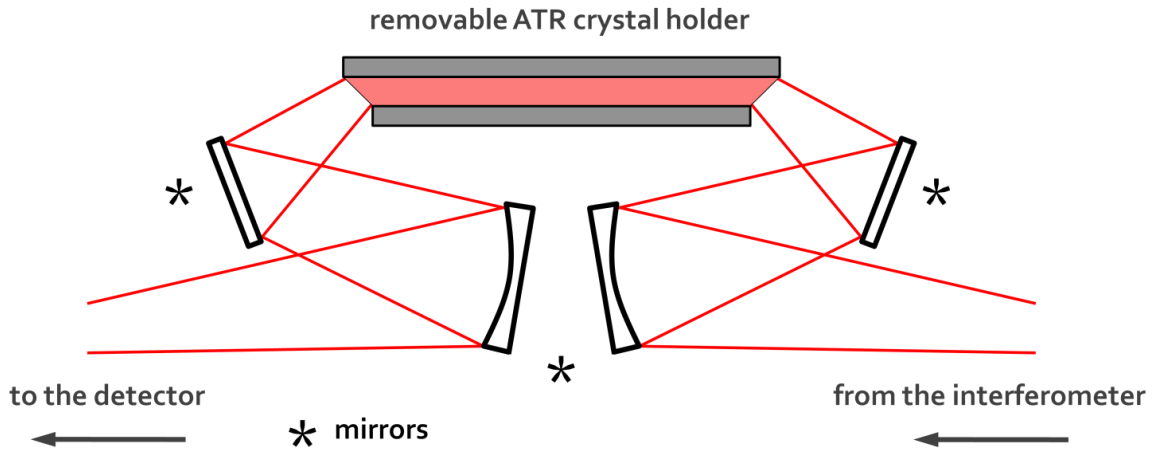

Figure 6.3: Top view of the attenuated total reflectance unit: the radiation modulated in the Michelson interferometer is focused inside a crystal where it travels along its whole length; once leaving the crystal, the infrared radiation is focused by means of a second pair of mirrors to the detector and the connected amplifier.

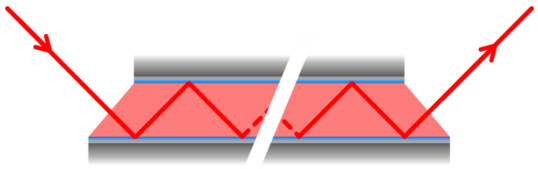

Figure 6.4: High refractive index crystal with the coated aluminum foils (thin film in blue) pressed against its faces in the sample-holding steel element. The incoming IR radiation is reflected up to 25 times in the crystal before leaving it.

At every total reflection at the interface, an evanescent wave penetrates for a very short depth (few wavelengths) in the sample: the frequencies resonant with the molecular bonds of the latter are partially absorbed, leaving only the depleted fraction to travel further in the crystal. At each reflection, the selective absorption is repeated, thus increasing the sensitivity by several times. After up to 25 total internal reflections, the infrared radiation leaves the crystal and is then focused on the detector by a pair of mirrors and is processed as in normal reflectance mode. The penetration depth of the evanescent wave d_p is however dependent on the wavelength of the radiation according to the following equation [144]:

$$d_p = \frac{\lambda}{2\pi \cdot \left(sin^2\theta - n_{s,c}^2\right)} , \tag{6.5}$$

where θ is the tilting angle of the radiation at the entrance of the crystal and $n_{s,c}$ is the ratio between the refractive index of the sample and the one of the crystal. As a consequence, longer wavelengths (i.e. shorter wavenumbers) penetrate deeper in the sample and vice versa: compared to normal reflectance configuration, then, an ATR spectrum will show an increased sensitivity in the low-wavenumbers section and damped signals in the high-wavenumbers one.

In the current work, all the absorption spectra have been recorded by means of an FTIR spectrometer Vector 22 from the company Bruker equipped with a silicon carbide rod (Globar®) as infrared source. When not stated otherwise, each spectrum is the average of 30 single recordings for the same sample, carried out with a slit opening of 4 cm^{-1}. For the ATR unit, a KRS-5 crystal made of a mixture of thallium bromide and iodide, with a refractive index equal to 2.37 [142], has been employed. The thin films to be analyzed have been deposited on strips of aluminum foils (aluminum being IR inactive). Before the recording of the proper absorption spectra, a blank aluminum sample has been analyzed in order to provide a reference and a background signal: such spectrum is later automatically subtracted by the recording software. Further processing of the acquired spectra has been carried out by means of the spectrometer software OPUS v6.5 and v7.8.

The recording of the spectra of the gaseous monomers has been carried out by removing the ATR unit from the sample-holding cell and inserting a Pyrex glass containing kitchen paper drenched in the liquid monomer, in order to slow down the latter's evaporation. After few

minutes of purging, necessary to flush away residual CO_2 and water vapor from the cell, an absorption spectrum has been recorded with the same aforementioned procedure.

6.2.2 X-ray photoelectron spectroscopy (XPS)

X-ray photoelectron spectroscopy (XPS or Electron Secondary Emission for Chemical analysis, ESCA) is an analysis technique which allows to obtain both qualitative and semi-quantitative information on the chemical elemental composition of the uppermost molecular layers of an investigated surface. It is based on the photoelectron effect, i.e. the ionization of the target and subsequent emission of electrons after an irradiation of photons with the appropriate energy (in the X-ray range, 100 eV – 100 keV). With the absorption of a photon with an energy greater than the first ionization threshold, valence and core electrons are extracted from the sample, with a residual kinetic energy E_k equal to the surplus energy given by the photon E_{ph}, according to the following equation:

$$E_k = E_{ph} - E_B + \Phi\,, \tag{6.6}$$

where E_B is the binding energy for the electron and Φ is a work function depending on the irradiated material and the instrument. Knowing the energy of the incoming X-ray produced inside the XPS spectrometer and the work function, and by measuring the kinetic energy of the photoextracted electrons, it is therefore possible to trace back to the original binding energy typical of a given atomic level in a given element. A mandatory condition for the analysis to be successful is that the extracted electrons do not collide with other particles while leaving the surface or traveling towards the detector (the latter can be avoided by operating in vacuum conditions). Stray electrons are not useful for the analysis and form the background noise, usually in the form of long tails after an emission spike. The X-rays are produced by Bremsstrahlung after extracting electrons via thermoionic effect and accelerating them against a metallic target. Some of the highest energy electrons, after a certain threshold, start to ionize the target with subsequent emission of X-rays with a narrow energy dispersion. By counting the number of electrons with distinct kinetic energies being collected in the detector, it is therefore possible to calculate the relative abundance of an element in the investigated volume (usually displayed as fraction or percent). Moreover, in spite of the extracted electrons coming from core levels largely uninvolved in the formation of molecular bonds, the different electronegativities of the atoms surrounding them still exerts an influence in their binding energy, inducing small shifts that can give also qualitative information about the chemical composition of the probed material.

As the electrons must not undergo collisions or scattering, the probed volume is reduced to the first few atomic and molecular surface layers, i.e. few tens of nanometers. The absence of contaminants on the surface becomes therefore of great import: the vacuum needed for the X-

ray not to be absorbed on their path to the target and, as mentioned above, to prevent the scattering of the extracted electrons, can also help prevent the formation of adsorbate monolayers on the surface. For solid contaminants, on the other hand, a cleaning step with argon cations can be performed: in this case, however, the original bonds on the surface are altered or destroyed and the qualitative analysis of the shifts in the main peaks cannot be anymore representative of the 'real' surface chemistry.

The ESCA analyses reported in the current work have been performed at the Fraunhofer-Institut für Grenzflächen- und Bioverfahrenstechnik (IGB) by means of a Kratos Axis Supra equipped with a clustergun and a monochromatic Al Kα X-ray source (1486.6 eV). Scans of the signals originating from the samples in the 1350-0 eV range have been recorded before and after a cleaning step of their surfaces. Elemental quantitative analyses have been performed by means of the instrument's associated ESCApe software, the atomic percentage being calculated through the internal standard factors for each peak. Correction of the eventual surface charging effects has been carried out by means of the C-C(H) bond (binding energy of 284.7 eV), used as an internal standard. Best fitting procedures for the C1s, N1s and Si2p high-resolution spectra have been carried out by means of the OPUS v7.8 software. For each peak, five to six purely Gaussian components have been employed. Their position has been kept fixed, while their full width at half maximum and intensity has been left without restraints. The position of each component is reported in Table 6.1, together with their assigned chemical bond(s) and the reference sources.

6.3 Microscopy

In the current section, the methods for surface imaging based on interaction with light and electrons will be illustrated. Optical microscopy will for the most part remain confined as supporting tool for the pinhole test described in section 6.5.

6.3.1 Optical microscopy

An optic or light microscope is a system of lens that focuses visible light on a surface and magnifies the obtained pictures, up to 2000 times, i.e. when the size of the photons becomes greater than the features to be investigated. The microscope can be coupled with a CCD camera that records and saves pictures and videos. In the current work, an OLYMPUS BX60 optical vertical microscope has been used in order to provide real-time pictures of samples subjected to the CO_2 test for the localization of defects in barrier layers (see also section 6.5). The microscope is connected to an OLYMPUS DP27 color CCD camera with a maximal resolution of 2448 x 1920 pixels

and a computer. Further processing of the acquired pictures and videos has been performed by means of the camera software OLYMPUS Stream Essentials (v19.3).

Table 6.1: Peak positions and attributed chemical bonds of the components employed for the curve fitting of high resolution C1s, N1s and Si2p signals in ESCA analysis.

Label	Peak position	Chemical bond	Reference
	eV		
C_0	284.7	C–C(H)	[145-149]
C_1	285.7	C–R–O	[148]
C_2	286.5	C–O	[148, 149]
C_3	287.8	C=O	[150]
		O–C–O	[150]
C_4	289	O–C=O	[150]
		O–C–O–O	[150]
N_0	397.2	Si–NH–Si	[151]
N_1	398	NSi_3	[151]
N_2	399	NSi_2C	[151]
N_3	400	N–R–O	[148,149]
N_4	400.5	$N–(R–O)_2$	[148,149]
Si_0	100.6	Si_3–Si–C	[149]
Si_1	101.5	Si–O	[138,152]
		Si–N	[151]
Si_2	102.1	$Si–O_2$	[138,152]
Si_3	102.8	$Si–O_3$	[138,152]
Si_4	103.4	$Si–O_4$	[138,152]

6.3.2 Scanning electron microscopy (SEM)

Scanning Electron Microscopy (SEM), similarly to light microscopy, provides pictures of a surface. In this case however electrons are used in place of photons, allowing much higher resolutions to

be reached, and features up to 1-2 nm large to be detected: the former associated thermal de Broglie wavelength is in fact several orders of magnitude smaller than those of the visible range in the electromagnetic spectrum. Because for such imaging methods electrons are employed, high vacuum conditions are necessary in the whole microscope column, in order to prevent their reabsorption and deceleration caused by collisions with neutral atoms and molecules. The electrons are generated by extracting them via thermoionic effect from a tungsten filament (the electron gun) and are accelerated by means of a high voltage against an open cathode. Magnetic coils along the main microscope column focus the electron beam in the two dimensions and determine the size of its spot, that in turn affects the overall resolution of the instrument. A second set of coils down the column allows the beam to impinge on different areas of the sample surface, i.e. the coils can control and tune a systematic scan of the latter. A schematic representation of a typical microscope column is shown in Picture 6.5. Once the electrons impinge on the surface, several signals are produced, most of which reported in Figure 6.6:

- back-scattered electrons (also called primary electrons), i.e. electrons from the beam which are reflected at various angles after multiple collisions taking place in the uppermost atomic or molecular layers of the sample;
- secondary electrons emitted from the sample because of collisions with primary electrons with sufficient kinetic energy to trigger ionization processes;
- Auger electrons as consequence of the first wave of ionizations: if an electron from a core level is extracted, the vacancy is soon replenished by another electron decaying from the upper levels of the same atom. The subsequent high energy photon emitted can cause further ionization in the sample volume and further electrons to escape the surface;
- emission electromagnetic radiation at various wavelengths, ranging from X-rays to thermal microwaves.

Because of the high voltage applied to them along the column, primary electrons remain the most energetic ones and can escape the surface even after penetrating for several nanometers inside it with an energy of some keV. By contrast, secondary electrons already possess a reduced starting kinetic energy, which is likely to further diminish following collisions in the bulk of the sample. As a consequence, the only secondary electrons to successfully escape are those coming from the uppermost molecular layers of the surface with an energy of few eV, at the same time providing the most informations about the sample's morphology. Several detectors, either built slightly off-axis in the column or at an angle in the sample chamber, collect the emitted electrons and provide a picture of the surface, assembled by moving the electron spot along lines on the desired area (hence scanning microscopy). The black and white picture's brightness is directly proportional to the number of electrons collected.

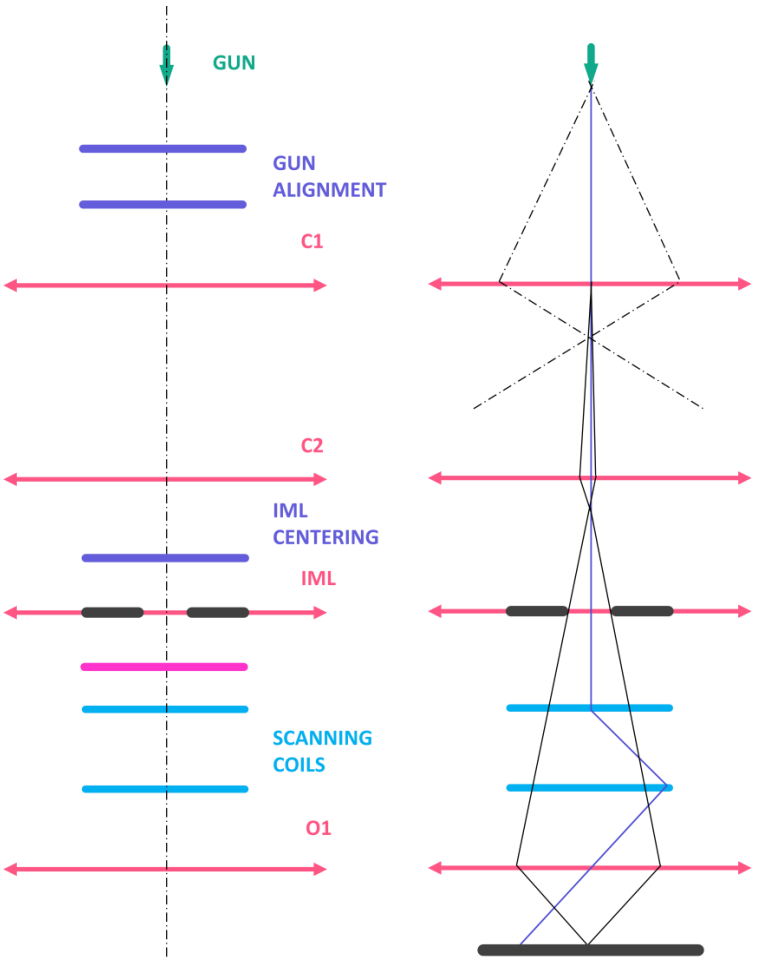

Figure 6.5: Schematic representation of the SEM column (left) and focusing of the electron beam (right). The first two coils (gun alignment) center the electron beam extracted from the source (gun) in the two dimensions. C1 and C2 are two magnetic lenses regulating the beam diameter by changing the current flowing through them; C1 tunes the source attenuation, C2 the aperture angle. An InterMediate Lens (IML) adjusts the size of the beam reaching the last lens (O1), that focuses the beam on the sample surface. Stray electrons leaving the main beam can still reach the surface but do not contribute to the imaging process. The picture is acquired by moving the electron spot on the surface by means of the scanning coils.

Because of the net electric current flowing into the sample, it is necessary, for the latter to be suited for SEM analyses, that its surface is electrically conductive; the induced charge cannot otherwise be effectively dissipated, causing a progressive charging of the surface and consequent repulsion of further incident electrons, thus compromising the scansion outcome, either by deformation of the pictures or by whiteout effects. Surface can be made conductive by applying beforehand a thin metallic (usually gold, chromium or platinum) or graphite layer by means of sputter deposition. Too thin layers can still result in poor conductivity and surface loading effects.

Thick conductive layers however should be avoided as well, since they result in surface topography alterations.

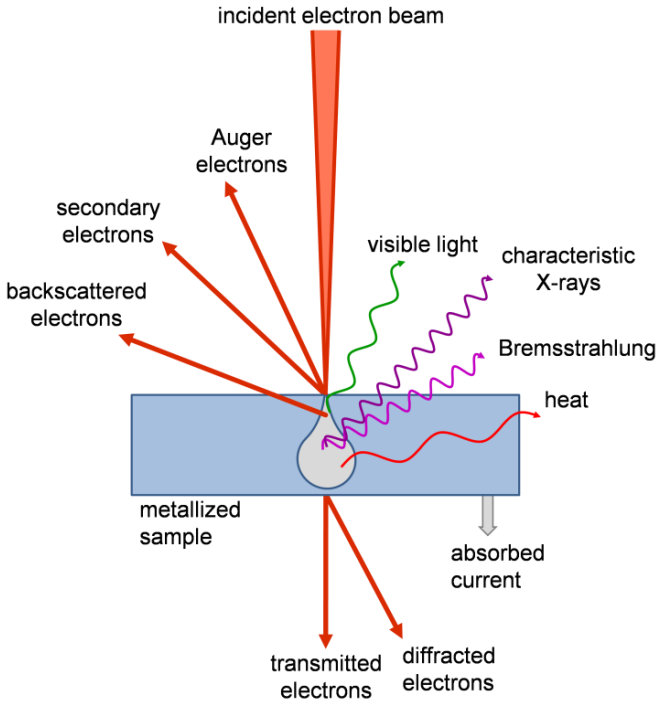

Figure 6.6: Signals produced by an accelerated electron beam impinging on a sample at the end of a SEM column. The section interacting with the incoming particles becomes wider as the beam penetrates in the sample bulk (drop-like gray area).

In the present work, the PECVD films deposited on a PET foil have been investigated by means of a VEGA Plus TS 5135 MM SEM from the company Tescan [153]. The accelerating voltage employed has not exceeded 10 keV, in order not to damage the soft polymeric substrate.

The samples have been metalized prior to the SEM analysis by means of a sputter coater from Cressington [154], the Sputter Coater 108auto, with a gold target. The operating parameters have been tuned in order to obtain a homogeneous deposition of roughly 30 nm of metal. The electric contact between the samples and the metallic stubs they are fixed on (by means of graphite-based adhesive films) has been further enhanced by bridges made up of a silver colloidal paste-like dispersion.

Further analyses have also been carried out at the Fraunhofer IGB by means of a Zeiss (Leo) 1530VP scanning electron microscope. The samples for such analyses have been prepared by sputter coating them with 1-2 nm of platinum.

6.4 Permeation measurements

In the following section, the methods for the evaluation of the barrier properties of thin films against oxygen will be illustrated. The two instruments employed in the current work will be described and, finally, the accordance of the experimental results obtained through them will be shown.

6.4.1 Experimental set-up

The determination of the oxygen transmission rates of the thin films takes place by means of the so-called carrier gas method: according to it, the polymeric substrate with the to-be-investigated thin film on top of it is placed in a sealed sample-holding cell, schematically drawn in Figure 6.7. The foil acts as a separator between the two halves of the cell, one of which is flushed with an inert gas, in this case nitrogen, while the second has a pure flux of the gas the transmission rates of which are to be investigated, in this case oxygen. The outlet of the half of the cell flushed with nitrogen is connected to an oxygen detector that provides in real time the parts per million [ppm] of oxygen in the carrier gas flux.

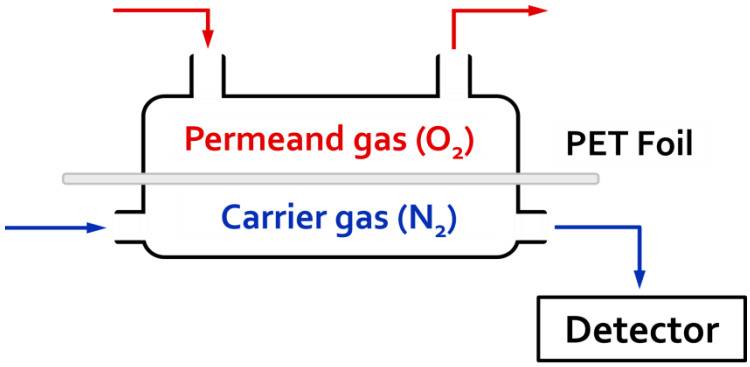

Figure 6.7: Schematic view of the sample-holding cell for the carrier gas method. The molecules of the permeand gas moving from the upper to the lower cell through the investigated foil are then flushed to the detector that measure and displays their relative abundance in real time.

In the current work, two different measuring systems based on the carrier gas method have been employed (more information in the following 6.4.2 section); they are reported in Figure 6.8. In both cases, the system consists of a sample holding cell submerged in a water bath, in order to keep the temperature constant for the whole duration of the measurement (see Chapter 3 for the dependence of permeation on temperature). The cells (shown in Figure 6.9) are equipped with two concentric O-rings, the most external one to seal the cell against the water, the second

one (with a corresponding ring in the upper lid of the cell) to block the sample and allow gas transfer only through it. The diameter of the latter determines the diameter of the investigated area. Upstream, the cell inlets are connected to gas bottles by means of mass flow controllers operated through a control unit. The outlet of the upper half of the lid ends in open air, while the second is connected to the oxygen detector. A computer connected to the latter allows for the data to be stored and displayed as a permeation curve vs. time by means of a program designed in the LabVIEW platform from National Instruments.

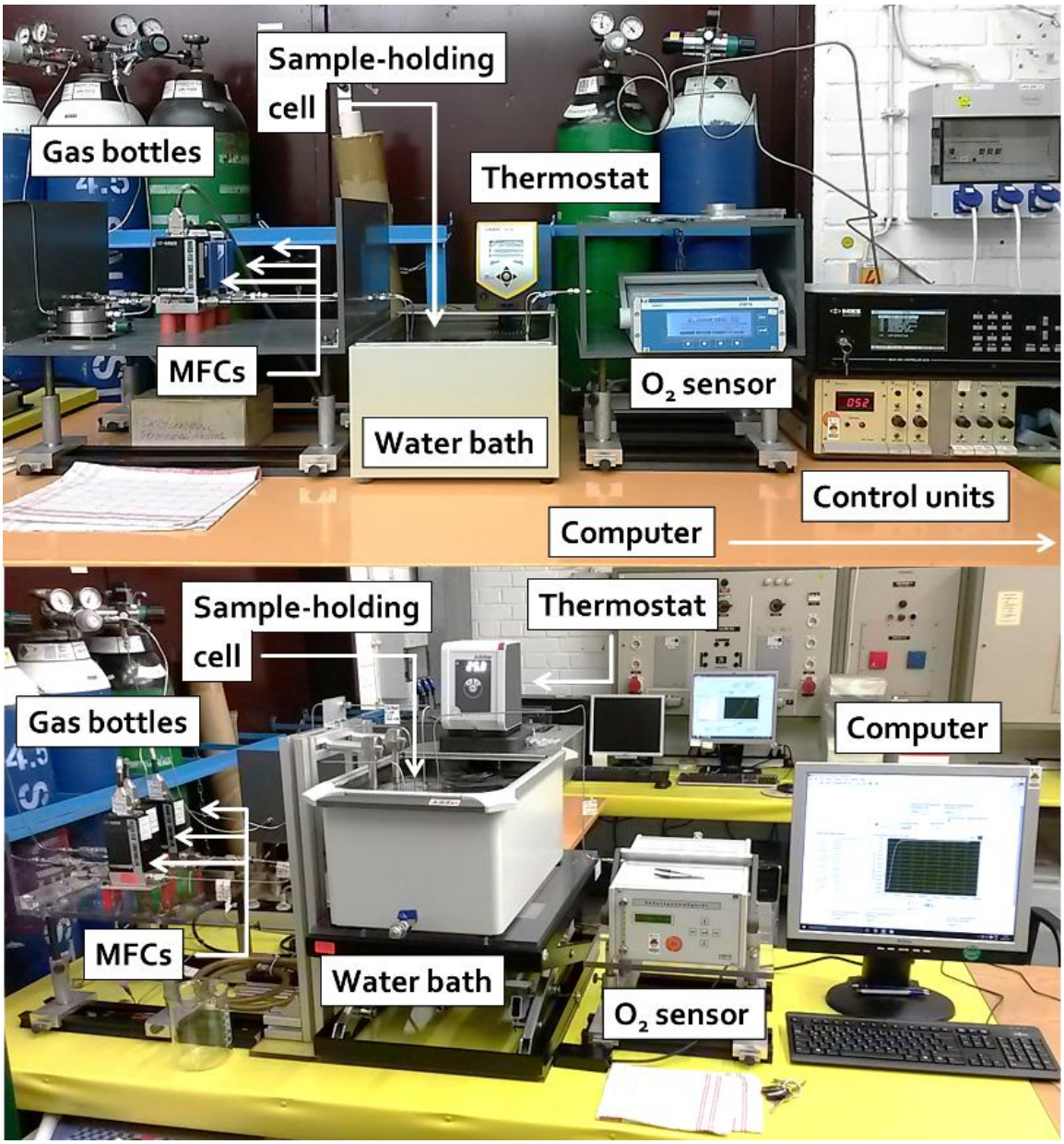

Figure 6.8: Systems for the measurements of the oxygen transmission rates of thin plasma-polymerized barrier layers.

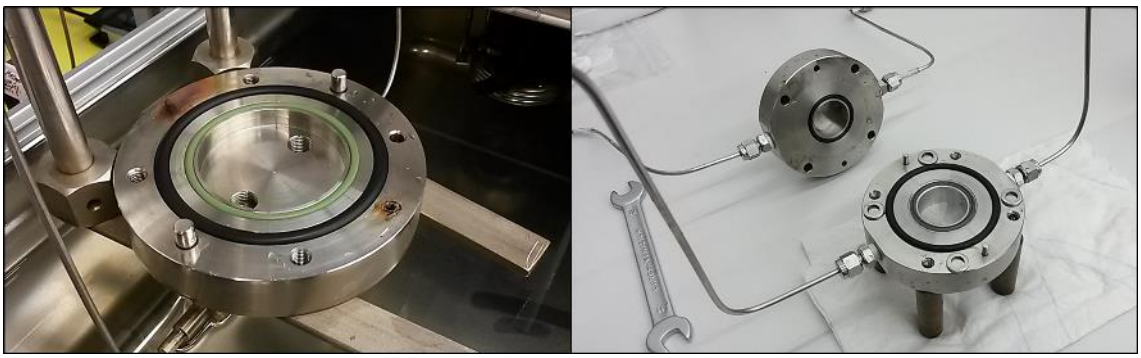

Figure 6.9: Open sample-holding cells showing the pair of O-rings in the lower half and the corresponding O-ring in the upper one, for the smaller diameter only. The outer O-ring provides a sealing against the bath water, the inner pair against gases and keeps the foil in position.

The operating principle of the oxygen sensors is based on the Nernst equation for a solid state electrolytic cell:

$$U = \frac{RT}{4F} \cdot \ln \frac{P_{O_2,Air}}{P_{O_2,Gas}}, \tag{6.7}$$

where U is the cell potential (measured in [V]), R the universal gas constant, T the temperature (measured in [K]), F the Faraday constant (expressed in [C mol^{-1}]), $P_{O2,Air}$ is the partial pressure of oxygen in dry air in correspondence of the reference electrode and $P_{O2,Gas}$ is its partial pressure in the carrier gas at the working electrode. The cell inside the sensor is shown in Figure 6.10: it consists of two platinum electrodes isolated from each other. The reference electrode is sealed in dry air inside a ceramic compartment. The working electrode lies inside a zirconia (ZrO_2) cylinder through which the to-be-measured gas flows. The difference in the oxygen partial pressure induces an electric potential between the electrodes and a consequent electric current trough the zirconia. As the latter's conductivity depends exponentially on the temperature, the cylinder is kept at a constant operating value of 750 °C by means of an electric oven. The measured values are converted in the oxygen concentration in the flowing gas φ_{O2}, displayed in vol% (in part per million) according to the following equation:

$$\varphi_{O_2} = 20.64 \cdot \exp\left[-46.42 \cdot \frac{U}{T}\right], \tag{6.8}$$

where U is the potential in mV between the two electrodes, T is the operating temperature in K and the first term corresponds to the concentration of oxygen in air with an humidity of 50%, expressed in vol% [155, 156]. In the current work, an SGMT1 and an SGM5 sensor from the ZIROX Sensoren und Elektronik Company have been employed. In both cases, the instrument error is declared to be smaller than 5 % [155, 156].

The permeation measurements are thus carried out (some steps are illustrated in Figure

6.11):

i) the sample to be investigated is cut in a circle of the appropriate radius, slightly larger than the measured area in the sample-holding cell;
ii) the cell is disconnected from the system and opened; the sample is inserted and the cell closed and reconnected again;
iii) for the permeation process to follow a Fickian behavior, it is necessary that the initial concentration of oxygen in the lower half of the cell is null. As both halves of the cell are rich in oxygen upon being exposed to air, both are flushed with a pure nitrogen flow (Fig. 6.11 a). The output signal from the Zirox sensor is recorded;
iv) when the oxygen level reaches a stable minimum, the gas in the upper half of the cell is switched to oxygen by means of the mass flow controller (MFC) central unit (Fig. 6.11 b);
v) the three steps of the permeation process described in section 3.1 take place (Fig. 6.11 c); after further time, the first oxygen molecules reach the sensor and are detected (Fig. 6.11 d); the delay depends on the barrier properties of the investigated sample and on the employed carrier gas flow;
vi) the measurement is carried out until a steady-state value in the oxygen level is reached; the necessary time is dependent on the barrier properties of the investigated sample;
vii) a new sample is prepared and the process starts again from step one.

The entire procedure is devised so that the process follows the boundary conditions, introduced in Chapter 3.2, necessary for an analytical solution of the Fick's laws. The carrier gas in particular, besides enabling the sensor to register the permeated oxygen fraction, helps keeping the system at a steady state where the concentration gradient is still at its maximum. Were this not the case, errors like back diffusion or slowing down of the permeation process would be introduced, invalidating the measurements.

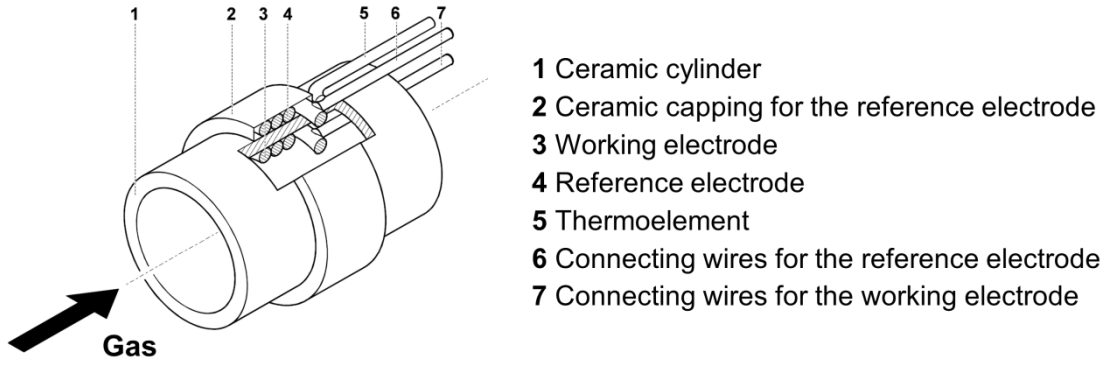

Figure 6.10: Galvanic cell for the determination of the oxygen concentration in a gaseous flux. Picture from [151].

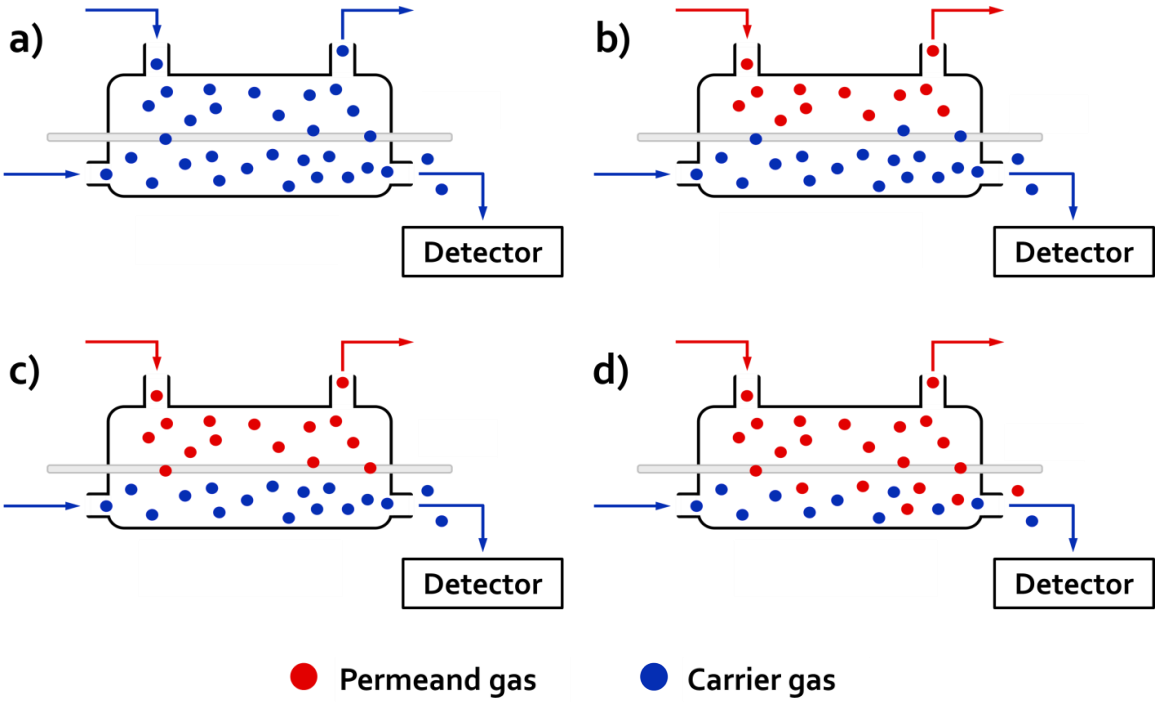

Figure 6.11: Schematic representation of the main steps in the permeation measurement routine: flushing with nitrogen (a), switching to permeand gas (oxygen) flow (b), adsorption, diffusion and detachment taking place in the sample (c), detection of the first permeated molecules brought to the detector by the carrier gas (nitrogen) (d).

The final value out of the process is obtained through an average of the oxygen concentration recorded in the steady-state value range, and comes with an associated standard deviation. The average of the residual oxygen concentration in the carrier gas before the beginning of the measurement is then subtracted from it. Such values, still displayed in [ppm], are converted in an oxygen transmission rate (OTR) normalized for gas volume, area unit, pressure and day through the following equation:

$$OTR\ [cm^3 \cdot m^{-2} \cdot d \cdot bar] = \frac{X \cdot \varphi_{carrier}}{A \cdot P} \cdot 60 \cdot 24\ , \qquad (6.9)$$

where X is the oxygen concentration displayed in ppm, φ is the carrier gas flow in sccm, A is the area of the investigated circle in squared meters, P is the ambient pressure, in bar, at which the measurement has been carried out, and $60 \cdot 24$ (minutes · hours) is a factor needed to obtain the daily OTR value. The normalization has to take into account the carrier gas flow, as it affects the measured values by artificially 'diluting' the permeated oxygen fraction. For the same sample, different carrier flows would then result in different O_2 fractions. The effects of the pressure must also be taken into account, as both outlets of the two halves of the sample-holding cell end up in the atmosphere: a relatively high pressure can 'push' against the gases during their release,

slowing them down, artificially increasing the measured oxygen concentration and decreasing the concentration gradient, and vice versa.

When not explicitly stated otherwise, the permeation measurements in the current work are to be assumed to have been carried out with a set temperature of the water bad of 35 °C, in order to have a good signal-to-noise ratio. For all the investigated samples, moreover, the carrier gas flux has been set and kept at 10 sccm for both lines. The systems have been kept constantly flushed with nitrogen even when not employed for sample testing, in order to keep oxygen residuals at a minimum, as stopping the gas flows only to restart them later causes the first purging sessions to last much longer.

6.4.2 Instruments cross-calibration

Table 6.2 reports the specifics for the two systems displayed in Figure 6.8. The Lauda E200 bath has a reported temperature stability of ± 0.2 °C, the Julabo CORIO CD.B27 one equal to ± 0.03 °C.

Table 6.2: Specifics of the two permeation measurement systems employed: radius and area of the sample-holding cell, thermostats connected to the water baths, oxygen sensors.

System I			
Cell		Bath thermostat	Sensor
radius [cm]	1.6	Lauda E200	SGMT 5
area [cm^2]	8.04		
System II			
Cell		Bath thermostat	Sensor
radius [cm]	3.7	Julabo CORIO CD-B27	SGMT 1
area [cm^2]	43.01		

The second system has been built and assembled *ex novo* at a later stage of the current work. The main difference in the two systems is the size of the cell, which determines the amount of oxygen that permeates through the samples: the bigger cell, for a given sample, and with carrier gas flows constant for both systems, results in a detected signal roughly five times higher than for the smaller cell. Such increase in sensitivity is especially useful for measurements carried out at lower temperatures, where for the smaller cell the signal becomes comparable with the noise level of the background. The length of the pipe system, both up- and downstream the sample-holding cell, is also much greater for System II. This in turn causes longer de-

lay times during a permeation measurement, i.e. the time needed for the oxygen molecules only to reach the upper half of the cells and later to reach the sensor. Such delay is not related to the proper time needed for the molecules to permeate in the samples and needs to be measured and then excluded in the subsequent calculations for the diffusion coefficient. Figure 6.12 shows the line length and the correlated delay time for both systems: the latter has been calculated by leaving the cells empty of samples and then measuring the time needed for a first increase in the measured oxygen concentration. In both systems, the same carrier gas flow (10 sccm) has been employed. The displayed values are averaged out of five measurements per system.

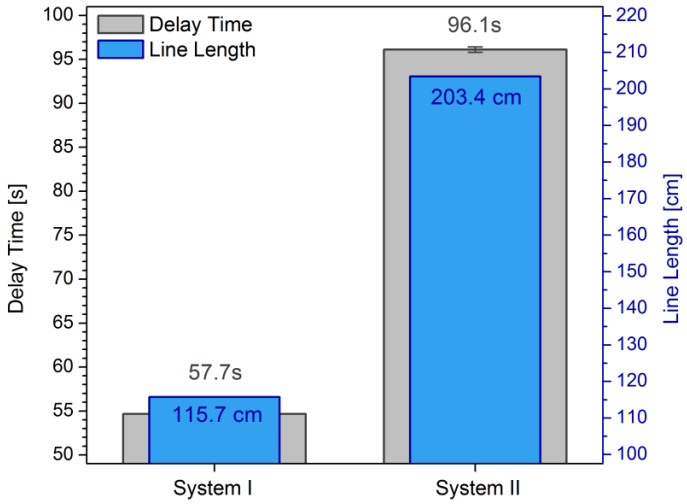

Figure 6.12: Delay time (left axis) for the first oxygen molecules to travel the entire line, from MFC to sensor, without samples in the cell, and their overall covered distance (right axis) for the two systems employed in oxygen permeation measurements.

Finally, in order to confirm the agreement of the results obtained by the two systems, one foil coated with a good barrier has been tested in System II. After the measurement, the central area of the sample has been cut out in order to be accommodated in the smaller sample-holding cell, and the measurement has been repeated with System I. The measured curves of the oxygen concentration as a function of time for both systems are reported in Figure 6.13. The curves have been normalized to their respective steady-state value, as the first measurement would result in a 'raw' curve five times higher than the second, and corrected in order to account for the different length of the pipelines. The two spikes observed for System II are systematic random errors caused by the older oxygen sensor: they bear no effect on the recorded final values, as the oxygen signal after the spike returns to its original values. The curves are in good agreement with each other, they possess similar shapes and rise times. The shoulder appearing in the initial stages of the rising signal (not an error, but caused by the properties of the tested barrier) is likewise

preserved also in the second measurement. The normalized values for such curves are displayed in Figure 6.14. It is possible to observe again a good agreement between the data, with a discrepancy of around 6 %, only slightly higher than the reproducibility limits listed for the two sensors. In light of such cross-calibration, therefore, the normalized values coming from both systems have been freely compared to each other in Chapter 7 without further corrections or limitations.

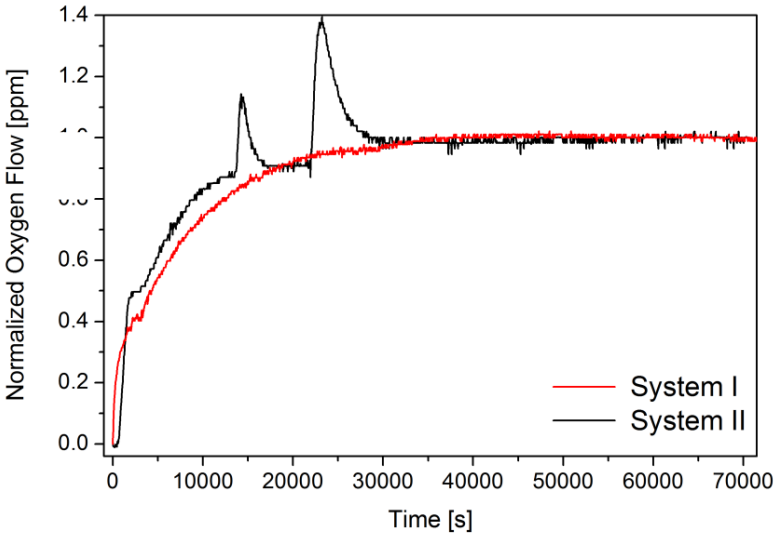

Figure 6.13: Oxygen concentration in the carrier gas, displayed as ppm, as a function of time in the two systems, for the same coated sample.

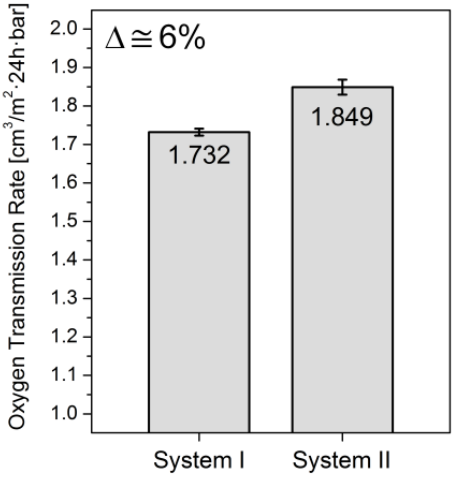

Figure 6.14: Oxygen transmission rate values for the measurements in the two systems of the sample coated foil. The associated discrepancy between the two values is reported in the top left corner.

6.5 CO_2 test for the localization of defects in barrier layers

In the current section, before presenting the new test developed in the current work, a brief review of the already existing methods for the localization and identification of defects will be given. The principles and the chemical processes on which the newly developed detection test will be subsequently presented. The experimental set-up will be described and, finally, a series of preliminary tests will be shown and commented, in order to evaluate the reliability and of the test and to ascertain if it can be successfully employed for the detection of defects in thin PECVD barrier layers.

6.5.1 State of the art for other defect detection methods

Defects in opaque thin films can be easily spotted even with the naked eye, provided they are sizeable enough, or alternative with optical microscopes in light transmission mode [76]. Colorless films, as silica-like plasma-deposited layers, on the other hand, do not provide enough contrast for such localization. Other methods must therefore be employed, usually based on enlarging the defects or otherwise selectively modifying the substrate lying underneath them. Later retrieval is however always limited by the resolutions of the employed techniques. So for optical microscopy the lower threshold is constituted by the diffraction limit of visible radiation, around 0.2 μm, and even with transmission electron microscopy it is sometimes difficult to detect features smaller than one micron on thin films [79].

Calcium test

The so-called calcium test consists of depositing the thin film, the barrier properties of which are to be investigated, on a layer of known thickness of pure elemental calcium. Calcium is degraded by reacting with water vapor and oxygen permeating through the pinholes, and turns from an opaque metal to a transparent oxide, resulting in the formation of circles underneath the defects that can be spotted with optical microscopes [157, 158]. The size of such circles, and consequently the amount of oxidized calcium, can be then accurately correlated to the permeation through the single defects. The main limitations of such test are several: the calcium layers, usually deposited by means of thermal evaporation [159] on a transparent, stiff substrate, need to be protected from exposure to air before the proper barrier deposition step; this can be achieved by spin-coating a temporary barrier on top of them. The presence of such intermediate layer can have consequences on the subsequent growth of the barrier layer, and on its defect density, which are not easily foreseeable. Moreover, a full corrosion of the calcium layer needs to take

place, for the defects location to become apparent: the amount of oxidized calcium depends on the size and permeability of the overlying defect, which can results in tests running for several hundreds of hours before an oxidized circle becomes visible. In such amount of time, on the other hand, the calcium layer underneath bigger defects will be completely oxidized, resulting in the merging of adjacent defects and in an underestimation of their density. Finally, such test does not discriminate between O_2 and water vapor [18].

A variation of the former method is to employ proper OLEDs as substrates to be coated: in this way, it is possible to localize the defects in the barrier layers by the formation of black inactive spots in the emitting layer of the device. The main limit of such method is of course the high cost of such sacrificial substrates, their time-consuming production step, and the poor reproducibility of the test itself, as most of the OLEDs are themselves prototypes.

Electrodeposition

With this method, the film to be investigated is deposited onto a metallic copper layer on top of a glass substrate: such system is later submerged in an electroplating bath, where copper may deposit on the sample only through and on top of the barrier defects. The induced surface bumps, with a radius of 10 microns or more, can later be retrieved by atomic force, scanning electron or optical microscopy [160]. While the size of the defects plays a role in the amount of deposited copper, and can therefore be at least inferred through this test, the deposited copper completely destroys the defects channel, nor does it allow to determine what caused their growth in the first place. Close defects finally result in irregular patches of copper of uncertain attribution.

Selective solvent

Similar to the above described case, this method is based on the selective absorption of a solvent by the polymeric substrate underneath the barrier film: the sample is brought in contact with the liquid, whose molecules travel through the defects and are absorbed by the polymer. The local swelling can be later retrieved by atomic force or optical microscopy [161]. The main disadvantage of such method is again its destructiveness, as the increase in the polymer volume causes the barrier to buckle, crack and possibly detach in large flakes. The resolution limit is constituted by the solvent molecular size, which is almost always much larger than for oxygen molecules. Defects with smaller radii are therefore overlooked, leading to an underestimation of their densities. Merging of the bumps of defect lying too close to each other is also to be observed.

Plasma etching

Such method, developed by da Silva Sobrinho *et al.* [32, 33 36, 60, 141] specifically for plasma-deposited thin barriers, and based on known undercutting effects on coated polyimide in aerospatial applications [162], relies on a second plasma treatment that can take place immediately after the deposition step. The sample, with the oxygen barrier on the upper side, is exposed to a

pure oxygen plasma; the oxygen molecules and atoms penetrate selectively through the pinholes and reach the polymer, etching it directly underneath the defects. The process, assumed to be isotropic, digs circular hemispheres in the substrate, with radii depending on the duration of the etching and on the size of the defect. Several ways of making them retrievable for later analyses are possible. The etching can be protracted long enough (several hours [32]) until the foil is completely etched and a punch-through on the backside is visible. Such holes can be made more apparent by applying moist corn starch on the backside on the polymer and then expose the coated side to iodine vapors [141]: the reaction with the latter causes blue spots to appear, which can be readily detected even with the naked eye. While useful for a quick test of the homogeneity of large surface areas, particularly for industrial purposes, the macroscopic size of such stains completely prevents the individuation of single defects with a microscopic spacing.

Alternatively, scanning electron microscopy can be employed for the detection. The hemispheres etched in the polymer may be made more apparent by applying beforehand a strip of duct tape on the barrier side of the sample and then stripping it away: the barrier layer 'hanging' over the etched foils will detach with the tape. In this way, of course, the barrier in proximity of the defect is completely destroyed. Another possibility is to simply observe the barrier surface: the products of the polymer etching, being trapped underneath the barrier, build locally higher pressures that do often result in pinholes being forcefully enlarged and presenting jutted, outwardly twisted rims with diameters in the micrometric range [163]. In this case, too, the barrier is destroyed.

The main advantage of such method over the previously described ones is that the size of the etched areas is linearly dependent on the radius of the defects, and therefore not only a numerical density of the latter, but also a distribution of their size can be calculated, by plotting the radii of the etched areas as a function of the etching time and then, through linear regression, by obtaining the original size of the defect [33]. Moreover, by employing oxygen as reactant, all 'active' pinholes can be detected. Such method suffers however from extremely long treatment times, and is fundamentally destructive in nature, both towards the polymer substrate and, most of the times, the overlying barrier film.

Cyclic voltammetry

With this technique, the barrier is deposited on a gold substrate than later acts as electrode in a ferricyanide/ferrocyanide reversible redox reaction. The latter can take place only on the uncovered areas of the electrode, i.e. at the bottom of the defects in the barrier film. Knowing the voltammogram for an uncoated electrode of similar size and shape, acting as a reference, it is then possible to calculate the surface coverage provided by the barrier and, therefore, the total surface fraction covered by defects [164]. The main limitation of such method is that it can only calculate the overall area of defects, but it says nothing about their average size, the distribution of the latter, or about their location on the surface. Most importantly, the redox complex employed

has a radius of 0.96 nm [165], almost one order of magnitude higher than the respective value for the oxygen molecule (0.12 nm). Defects inaccessible to the former may well still be permeated by oxygen molecules, and therefore this detection method suffers from systematic resolution limits.

The defect densities calculated by means of some of the aforementioned methods for thin films with 'good' barrier properties, not all of which deposited via plasma, are reported in Table 6.3. When available, the corresponding normalized oxygen transmission rates have been included.

Table 6.3: Tabulation of defect densities for single-layer inorganic barrier films deposited on polymeric substrates by means of different techniques, together with the corresponding oxygen transmission rates when available.

Defect density	Barrier film	Deposition method	Substrate	OTR	Reference
mm^{-2}				$cm^3/m^2 \cdot day \cdot bar$	
200	AlO_x	Magnetron sputtering	PET	1.94	[30]
600	AlO_xN_y	Magnetron sputtering	PET	1.2	[25]
80	SiO_x	PECVD	PET	0.4	[32]
25	Al (commercial)	PVD	n.a.	n.a.	[79]
130 - 400	Al	PVD	PET	1 - 2	[79]
11 - 1100	SiO_2	PECVD	PET	4 - 40	[32]
5 - 100	Si_3N_4	PECVD	PET	0.06 - 53	[32]
100 - 300	Al	evaporated	PET	n.a.	[7]
200	Al	sputtering	PET	n.a.	[166]
100 - 1000	Al	evaporated	BOPP	n.a.	[167]
3000	SiO_x	PEVCD	PET	1	[34]
40 - 170	SiO_x	PEVCD	PET	0.89 - 1.78	[163]
700	AlO_xN_y	Magnetron sputtering	PET	3	[168]

6.5.2 CO_2 pinhole test – chemical principles and processes

Calcium carbonate is a salt of carbonic acid with a poor solubility in aqueous solutions, where it usually precipitates in the form of crystalline aggregates: calcium carbonate presents three anhydrous polymorphs, calcite, aragonite and vaterite, belonging respectively to the trigonal, orthorhombic and hexagonal crystal system. At standard condition, calcite is the most stable polymorph and vaterite the least, with the latter tending to dissolute again and to recrystallize as the former (same applies, to a lesser extent, to aragonite) [169, 170]. Calcium carbonate forms spontaneously in water in which dissociated calcium cations are present, together with dissolved carbon dioxide diffusing from the atmosphere. The latter reacts weakly with water by forming carbonic acid, which can in turn dissociate first in hydrogen carbonate and then in carbonate; both carbonate species can react with calcium cations and form calcium carbonate. A list of the equilibrium reactions for the whole process is here presented [171-176]; the source for calcium is in this case presented as calcium hydroxide; all reactions are to be assumed to take place in aqueous phase:

$$H_2O \rightleftharpoons H^+ + OH^- \tag{6.10}$$

$$Ca(OH)_2 \rightarrow Ca^{2+} + 2OH^- \tag{6.11}$$

$$Ca^{2+} + OH^- \rightleftharpoons CaOH^+ \tag{6.12}$$

$$CO_2(g) \rightleftharpoons CO_2(aq) \tag{6.13}$$

$$CO_2(aq) + H_2O \rightleftharpoons H_2CO_3 \tag{6.14}$$

$$H_2CO_3 \rightleftharpoons H^+ + HCO_3^- \tag{6.15}$$

$$HCO_3^- \rightleftharpoons H^+ + CO_3^{2-} \tag{6.16}$$

$$Ca^{2+} + CO_3^{2-} \rightleftharpoons CaCO_3(\downarrow) \tag{6.17}$$

$$2HCO_3^- + Ca^{2+} \rightleftharpoons CaCO_3(\downarrow) + CO_2 + H_2O \tag{6.18}$$

The overall simplified reaction can be then written as:

$$Ca(OH)_2 + CO_2 \xrightarrow{aq} CaCO_3(\downarrow) + H_2O \tag{6.19}$$

The reaction of calcium with the hydrogen carbonate is slightly more favorable than the one with the carbonate anion for pH values in the 6 to 9 range. The rate limited step is constituted by the formation of carbonic acid and its dissociation, with the equilibrium of the reactions being strongly shifted to the left (the ratio of CO_2(aq) to H_2CO_3 being close to 400:1). On the other hand, calcium carbonate is poorly soluble (15 mg/L in pure water at 25 °C [177], so the equilibrium

for the precipitation step is strongly shifted to the right.

The formation of the crystals themselves remains far from being completely understood: it is generally accepted that without a crystallization seed already present in the solution, a high level of supersaturation is required in order to overcome the energetic barrier for the formation of a solid crystal [169, 178], but precipitation will nonetheless always take place, after a more or less long induction time [179]. The oversaturation *S* is defined as:

$$S = \frac{[Ca^{2+}][CO_3^{2-}]}{{}^{c}K_S}, \tag{6.20}$$

where $[Ca^{2+}]$ and $[CO_3^{2-}]$ are the concentrations (in [mol/L]) of calcium and carbonate ions, and ${}^{c}K_S$ is the concentration solubility product constant of calcium carbonate [180, 181]. The oversaturation value, in case of a solution with saturated concentration of calcium ions, such as for example lime water, depends essentially on the amount of carbon dioxide present in the atmosphere surrounding it, in accord with Henry's law:

$$[CO_2^*] = \frac{K_H}{p_{CO_2}}, \tag{6.21}$$

where $[CO_2^*]$ is the total concentration of the hydrated and non-hydrated forms of carbon dioxide in solution, i.e. the dissolved CO_2, carbonic acid, bicarbonate and carbonate, K_H is the constant typical for each gas and p_{CO_2} is the partial pressure of the carbon dioxide in atmosphere. Finally, the dependence of the activation energy for the crystallization, ΔG_a, on the oversaturation is equal to [179, 180]:

$$\Delta G_a \propto \frac{1}{S^2}. \tag{6.22}$$

Once a sufficient oversaturation is attained, the nucleation process follows allegedly the Ostwald step rule [181, 182], according to which the system will first quickly go through a series of metastable phases, each one lowering the surface energy of the solid being formed and with a relatively small activation energy for the conversion in the following one, before finally reaching a stable and final solid phase, i.e. one crystalline polymorph. For calcium carbonate, this means first the formation of nano-clusters during the prenucleation phase via Brownian motion collision [183], then a gelatinous phase with an inhomogeneous density that seems to coalesce into amorphous $CaCO_3$ via expulsion of water [184]. The amorphous calcium carbonate [169, 185], in turn, is partly hydrated ($CaCO_3 \cdot 1.5H_2O$) [170] and still unstable, so it will quickly transform in calcite in few minutes [169, 170]. Eventual formation of vaterite and aragonite as first crystalline polymorphs will too results in recrystallization as calcite, with the process taking hours for the former and months for the latter [169]. Calcite is therefore always the final product, and the other two polymorphs, in ambient conditions and without additives in the solution, are to be consid-

ered intermediate 'Ostwald' steps in the crystallization process.

The crystals thus obtained, especially in case of high oversaturation levels [186] and viscous systems (as in the case of the gelatinous precursor, in fact), are polycrystalline, highly branched aggregates called spherulites [187, 188]: their formation mechanism is still not fully understood [187-190], but they mostly consist of an initial crystalline core that branches with non-crystallographic angles, i.e. not dictated by its crystalline group [187] and that grows through transport of matter and heat onto its surface [191]. Alternatively, spherulites can result from multi-directional growth, similarly to dendrimers [188, 192]. In the former case, they often results in sheaf-of-wheat or dumbbell-like shapes [190, 193], that keep branching until they close on themselves, resembling spheres with equatorial lines where the lobes conjoined together [193] and two internal eyes at the side of the initial crystal (uncrystallized hollow regions) [189], as shown in Figure 6.15 [194]. Despite claims that spherulites can only originate in the presence of additives in the solution or more generic – even solid – impurities [187, 188, 193], several studies demonstrated how the latter cannot be the general cause for such aggregates [186, 191], and that indeed spherulites and dumbbells can form in pure solutions [181, 184, 190, 195,196] and in very short timespans (minutes [190] or even seconds [196]).

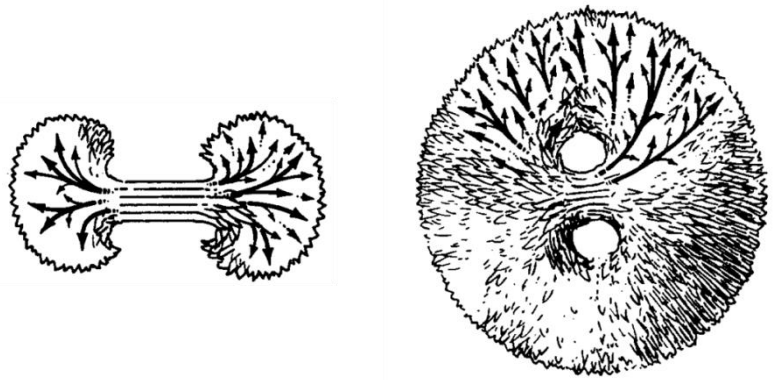

Figure 6.15: Sheaf of wheat precursor for a spherulite: the black arrows show the direction of growth from the ends of the initial crystallite; the final result is a symmetrical spherical body with two internal hollows [194].

In light of what said up to now, then, a possible, non-destructive test for the localization and identification of defects in thin barrier layers has been devised: the sample to be investigated acts as separator in a sealed cell between a pure CO_2 atmosphere and a saturated lime water solution. The first underlying assumption is that carbon dioxide will permeate preferentially and very quickly through the defects and will come in contact with the aqueous solution at their 'mouths'; such assumption is corroborated by the extremely high transmission rates of CO_2 in polymeric materials, which are five times higher than the corresponding values for O_2 [197]: such discrepancy arises because carbon dioxide, a 'fast gas', possesses a small kinetic radius (3.3 Å) and a strong

polarity, both of which ease its passage in the intramolecular voids in a bulk material. Oxygen, on the other hand, has a slightly bigger radius (3.46 Å) but no dipolar moment [74]. The permeation process will therefore be much shorter than the several hours required for oxygen permeation, as reported in section 6.4. Having reached the barrier film on top, then, CO_2 will quickly pass through the latter's micro-defects into the aqueous solution above. The permeation of carbon dioxide will act therefore as a counterpart to the injection of $CaCO_3$ precursors in more classical precipitation studies. Andreassen *et al.* [190] have demonstrated how precipitation in absence of crystallization seeds via simple CO_2 bubbling at room temperature is possible.

The second assumption for the test is that, at this point, a quick precipitation process will take place, resulting in crystals lying on top of such defects, making them retrievable for later analyses. The process *must* be quick, so that the initial nano-aggregates cannot diffuse in the solution, away from the defects, and precipitate somewhere else. This assumption is corroborated by the previously reported studies indicating that a quick crystallization is possible. Furthermore, a saturated lime water solution, with a pH of 12.4, will also have beneficial effects on the precipitation process. With increasing pH, hydrogen carbonate ions tend to convert into carbonate ions, so much that the latter become the prevalent form of hydrated CO_2 for pH ≥ 10.5, thus increasing the oversaturation S values [198]. On the other hand, in accord with Henry's law, the pure CO_2 atmosphere will maximize the oversaturation, thus favoring a concentration gradient strong enough for precipitation, but only in the immediate proximity of the defects ($p_{CO_2} = 1$).

No additives in the solution will be required, as not strictly necessary for calcium carbonate crystallization, and in order to avoid their possible effects on the precipitation process and on the shape of the thus obtained crystals [190, 193, 198-200].

Such CO_2 test will overcome the destructiveness of most of the techniques reported in section 6.5.1 while at the same time being much faster than the plasma etching method. The crystals, when equated to the defects, will allow the latter's numerical densities to be calculated, while they shape and size may provide qualitative information about the underlying defects (see also section 6.5.4). The theoretical resolution limits are moreover virtually non-existent, as the similar radii of CO_2 and O_2 allow the former to permeate only and all the defects accessible to the latter, while eventual crystallites too small for a detection by optical microscopy can be easily made visible by letting them grow with longer test times. A complete depletion of the lime water solution that could invalidate the reliability of the test has to be considered unlikely, as the expected crystallites total mass produced during a test run would still require a negligible amount of the calcium ions in the saturated solution.

6.5.3 Sample-holding cell and experimental set-up

The main piece of experimental set-up, built specifically for such purpose, is the sample-

holding cell, a schematic representation of which is illustrated in Figure 6.16: it consists of a system of stainless steel rings, sealed by means of O-rings, forming two half chambers: the lower chamber is made up by a single steel piece and presents an inlet for the pure CO_2 flux, connected through two adjustable pressure regulators to a pressured bottle, and an outlet that ends in open air. The bottom of the chamber is covered by a thin Teflon film, in order to provide a white background. A first steel ring equipped with an O-ring fixes then the to-be-tested sample in place. The inner radius of the cell is equal to 8 cm, corresponding to a sampled area of $\pi \cdot 64$ cm^2. A second ring constitutes the upper half of the cell, later to be flooded with limewater. On top of it a polycarbonate plate acts as a window for real-time observation of the sample surface. The whole system is pierced by screws fastening it to an object plate that can be mounted on the microscope movable stage. The single components of the cell and the whole system assembled and mounted under the microscope are shown in Figure 6.17. Because of the total thickness of the sample-holding cell, only the x5 and x10 magnification lenses can be successfully focused on the surface. Such is then the current resolution limit. The microscope, as reported in section 6.3.1, is equipped with a digital camera connected to a computer and a dedicated software.

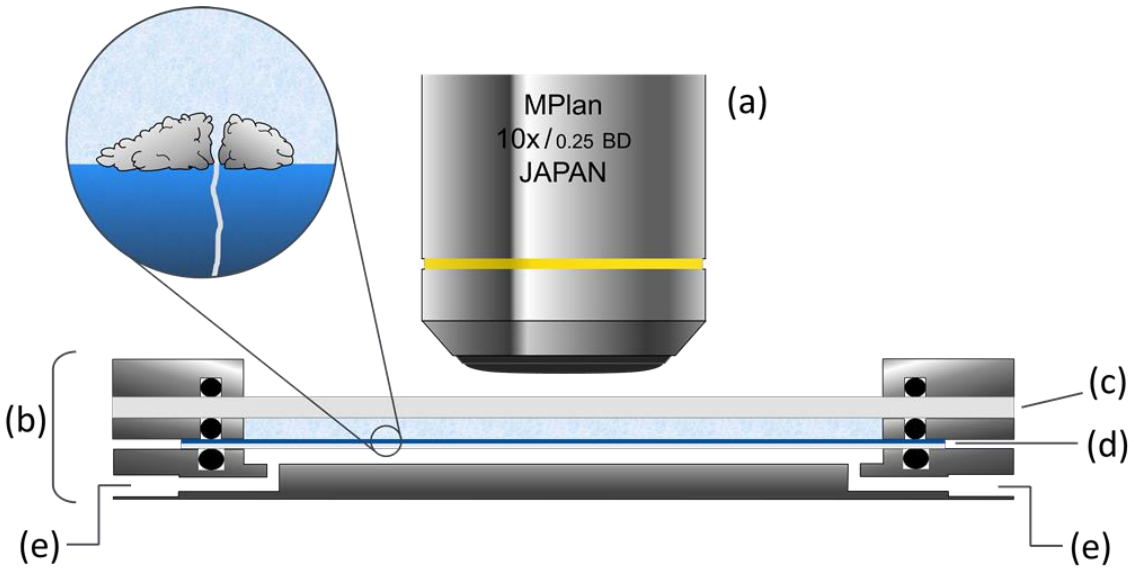

Figure 6.16: Schematic section of the sample-holding cell for the pinhole test: a) microscope objective with a x10 magnification lens; b) sample-holding cell on the microscope moveable stage; c) polycarbonate plate acting as window for the real-time observation of the reactions at the sample surface; d) polymeric substrate coated with the thin barrier film (in blue) acting as separator of the two halves of the cell, with the upper half filled with lime water; the foil is kept in tension by means of a pair of O-rings; e) inlet (left) and outlet (right) for the CO_2 flux in the lower half chamber; in the inset, schematic representation of the operating principle of the test: calcium carbonate crystallites forming in the immediate proximity of the defects in the barrier layer.

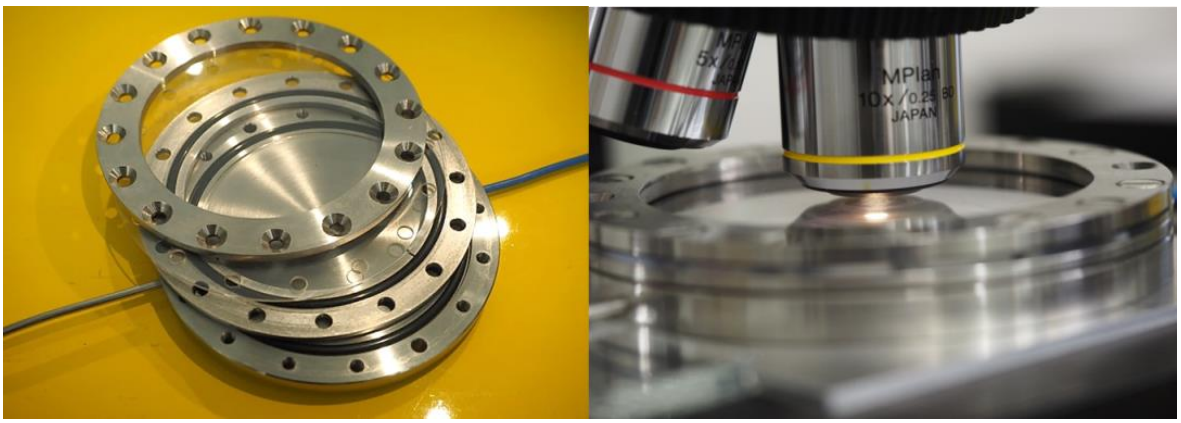

Figure 6.17: Left: sample-holding cell disassembled, with the single components slightly off-axis. Gas inlet (steel pipe) and outlet (blue rubber) are also visible. Right: the sealed cell on the microscope stage and under the lens during a test.

The preparation and the mounting of the samples for the pinhole test, and how the latter is run, can be thus listed:

i) the sample is cut with a radius slightly broader than the width of the cell and a small piece of duct tape acting as a marker is carefully placed on its central area by means of a lancet. If during such step the tip of the lancet scrapes the area surrounding the marker, the sample is discarded. The coated foil is then placed on the O-ring sealing the lower half of the sample-holding cell;

ii) the first ring is aligned on top of the lower half chamber and fastened to it by means of four screws. The O-ring pair blocks the sample and keeps it taut;

iii) a saturated lime water solution is poured on the sample with the help of a pipette, until the whole sample surface is covered (for the preparation of the solution, see further down). The timer is started when the lime water first comes in contact with the sample;

iv) the second steel ring and the screwed-in polycarbonate window are aligned on top of the cell and closed shut by means of four screws, extending all the way down and fixing the whole sample cell to the underlying aluminum plate;

v) the plate, with the cell fixed on it, is lifted horizontally and placed on the microscope stage, where it is blocked by means of two screws;

vi) the CO_2 flux in the lower chamber is opened. Excessive flows must be avoided, lest the sample foil be bent and pushed upwards;

vii) the sample is quickly brought in focus with a x10 magnification, the marker is retrieved and one of its corner is kept in the picture, to act as a reference;

viii) a first picture of the still pristine surface is taken;

ix) the sample is observed in real time, with pictures taken at regular intervals: during the

nucleation stage pictures are usually taken every minute, while later in the test, as no more crystals appear, every five minutes;

x) the test is left running until completion; if involuntary movements of the stage occur, the inspected area is retrieved with the help of the marker;

xi) the CO_2 flux is closed, and the sample surface is scanned in order to acquire more pictures;

xii) the cell and the plate are removed from the microscope stage; the cell is opened, and the sample removed;

xiii) the sample is then quickly placed in a demineralized water bath, with the coated side facing down, in order to wash away eventual dust particles or the carbonate crust forming on the liquid surface (more on this later);

xiv) the sample-holding cell is cleaned and dried;

xv) after about 10 minutes, the sample is removed from the bath and left to dry in air, with the coated side upwards, under but not in contact with a polycarbonate lid, in order to prevent dust from depositing on its surface;

xvi) the sample may be inspected again at the microscope for further images and at bigger magnification, once removed from the sample-holding cell. It is later stored in a closed sample holder for eventual SEM analysis at a later stage.

The saturated lime water solution is prepared as 80 mL aliquots per time by adding 130 mg of $Ca(OH)_2$ to demineralized (but not degassed) water in a Pyrex bottle of the same volume. The small excess of calcium hydroxide is to account for losses caused by reaction with the residual air in the sealed bottle. The solution is spun with the help of a magnetic stirrer and left to decant for at least one day prior to its use. Smaller volumes (5 to 10 mL) are then collected by means of a three-way propipette to be employed in the pinhole test. The liquid is collected from the mid-section of the bottle, in order to avoid eventual dregs on its bottom and the carbonate crust that forms on the liquid surface because of the repeated opening/closing of the bottle. The solution is discarded when less than 20 mL in the bottle remain or after five days since its preparation, in order to assume a constantly saturated concentration.

When not explicitly stated otherwise, each test after the first one for the evaluation of the method has run for one hour, with an ambient temperature between 22 and 28 °C and a pressure between 940 and 965 mbar. For each tested sample, a series of pictures of the same area at one of the marker's corners has been taken at different times, in order to build a number of crystals vs. time curve. At the end of the test, a minimum of four other pictures has been taken at different places of the sample surface, in order to faithfully represent the latter and its eventual inhomogeneities in crystal distribution. With a x10 magnification, each frame has an area of approximately 0.53 cm^2, calculated by means of the scale provided by the camera software. The numerical densities of the crystal have been calculated as average of such pictures.

Samples investigated by means of scanning electron microscopy have been further treated: first, pictures of their dried surface are to be taken, in order to act later as reference for the corresponding SEM pictures; the area of interest is then cut out in a $1 \cdot 1$ cm^2 square and fixed on a sample holder by means of a conductive graphite adhesive layer. In case of investigation on the surface lying underneath the crystals, the latter have been gently removed from the dried sample surface by means of a soft brush. Pictures of the to-be-investigated areas are taken before and after the brushing: residual crystals still on the surface will act as further reference to triangulate the position of the defects at the scanning electron microscope with a higher precision.

6.5.4 Evaluation of the pinhole test

First and foremost, the general feasibility of the test needed to be ascertained, i.e. if the design of the sample-holding cell allowed for a direct observation of the sample surface under the microscope, and if it was possible to observe real-time changes in the latter. The frames reported in Figure 6.18 come from a video recorded during one of the first test runs, carried out with samples coated with 'poor' barrier layers. In the areas highlighted by white circles it is possible to observe, as the time progresses, a small cloud-like shape first appearing, and then quickly coalescing into a fairly circular dot, which later has been found out, upon optical inspection, to be indeed a crystal. The whole crystal formation process takes place in few seconds: this is paramount, as it implicitly confirms one of the fundamental assumptions made for this test to localize pinholes, i.e. the precipitation step is fast and the crystal formation takes place in the immediate proximity of the defect.

The small cloud can then be assumed to originate almost as soon as the CO_2 molecules reach the solution after the permeation step and it is even possible for it to be the gelatinous, partly hydrated precursor of the final crystal: in this case, its rapid collapse would correspond to the rapid expulsion of water discussed in section 6.5.2. More importantly, the crystals seen in real-time are shown to form directly on the surface and not in suspension in the solution, only to fall on the sample at a later stage. The nucleation phase is found to take place some minutes after the beginning of the test, and once slowed down to a finish, no new crystallization step occurs: the crystals already present on the surface slowly and slightly grow bigger over time, as CO_2 keeps permeating in the solution and forming the nanoscopic building blocks for the $CaCO_3$ crystals [188], but the oversaturation, even locally in the surrounding of the defects (assuming at this point that the crystals do indeed form on them), never reaches again a value high enough to trigger a second nucleation phase. A possible explanation for such apparently counterintuitive phenomenon is provided in section 7.1.6. Also important is to notice how no Ostwald ripening processes have been observed, for all tested samples. Crystals which precipitate can grow only bigger and never dissolve back in the aqueous solution: as the net growth of a crystal can only occur

when the flux of molecules attaching on the surface is bigger than the one of particles leaving it [179], then, for such crystallites to be stable, a steady and continuous source of $CaCO_3$ must be available, more than enough to counteract their possible coalescence. This hints again at the crystals being located in close proximity to the 'source' of CO_2 in the solution, i.e. the defects. An example of crystals formed on uncoated PET foils, retrieved later at the SEM, is reported in Figure 6.19, in order to provide a visual reference and a comparison. A more detailed discussion on such crystals can be found in chapter 7.1.6.

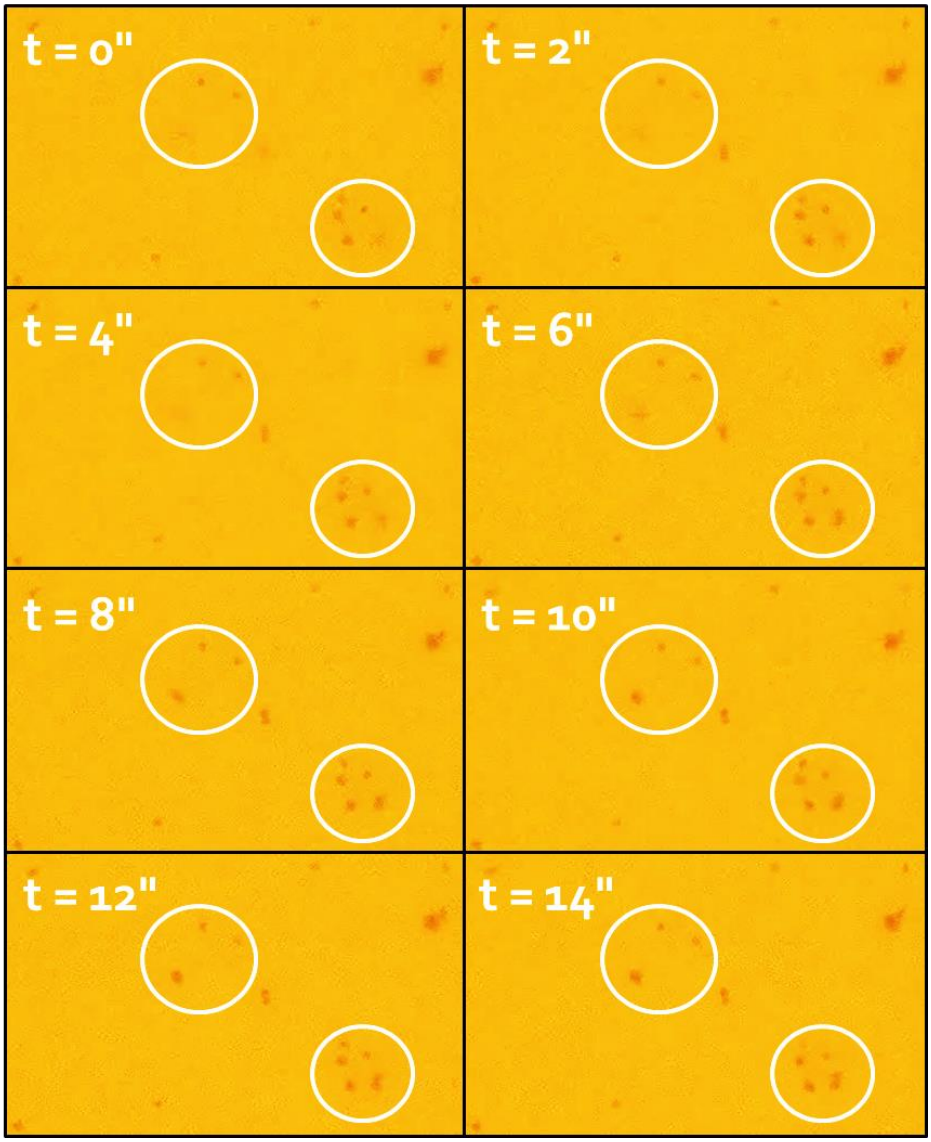

Figure 6.18: Details of an optical microscope frame at different times of a pinhole test: in the white circles, two crystals precipitating in the span of few seconds, preceded by a short-lived grayish cloud of smaller particles that coalesces in the proper crystal. Time has been arbitrarily assumed to be zero in correspondence of the first frame. All frames have been acquired with a x10 magnification.

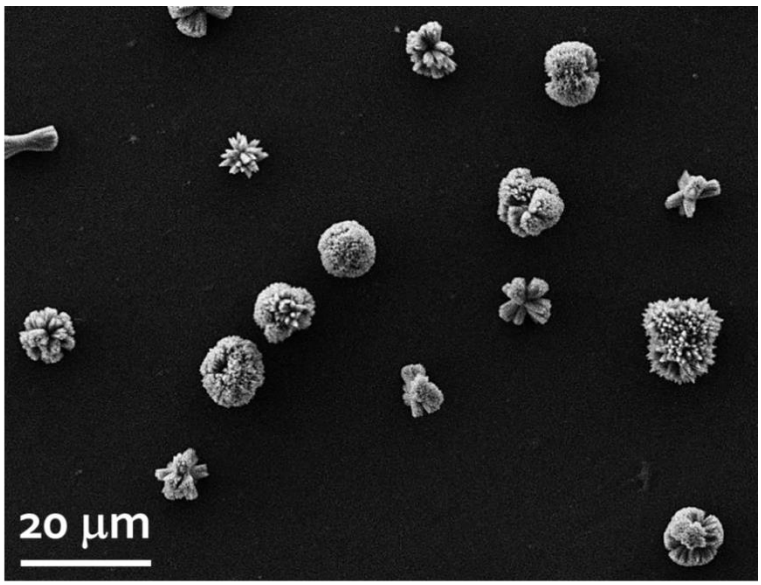

Figure 6.19: SEM picture (x2k magnification) of an uncoated PET foil after the pinhole test and the spherulite-like crystal lying on its surface.

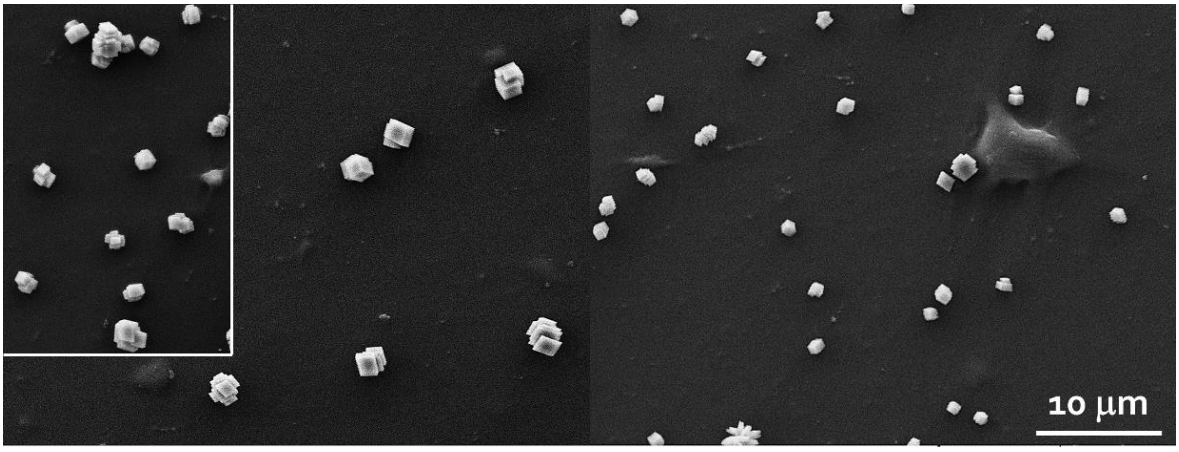

Figure 6.20: SEM pictures of uncoated PET tested with an underlying aluminum foil in the sample-holding cell. The small polycrystalline aggregates are mostly rhombohedrons or stacked sheet-like rhombi.

Secondly, it is necessary to exclude the presence of external sources of CO_2 apart from the pinholes, like leakages through the cell sealings and permeation through the polycarbonate window (PC having a CO_2 transmission rate of 25000 $cm^3/m^2 \cdot day \cdot bar$ [197]), that can cause side crystallization processes. To this purpose, an aluminum foil has been placed under an uncoated PET foil acting as a sample, thereby isolating the upper half of the cell from the underlying CO_2 flux. The test has then been carried out as described in section 6.5.3. At the end of it, the surface has been investigated at the SEM: the small crystals shown in Figure 6.20 were not visible through

the optical microscope and are at least one order of magnitude smaller than those observed during the normal testing of uncoated PET foils. They consist of small interpenetrating cubes and rhombohedrons, or square platelet stacked on each other, thin enough to be partially transparent to the incoming electron beam and most likely calcite re-crystallized from the possibly amorphous initial precipitates. Such crystals, starkly different from the spherulites observed in the other cases, can originate from residual CO_2 in the water solution or in the residual atmosphere in the upper half of the sample-holding cell, but not through the same reaction process causing the crystals allegedly on top of the defects to precipitate. Even their reduced size hints at very small quantities of CO_2 taking part in their formation. It has been then concluded that leakages in the sample-holding cell are minimal and can be neglected when discussing the formation of the spherulites on the samples surface. Moreover, CO_2 molecules coming from outside the liquid film/droplet are prevented from reaching the sample surface, as they are much more likely to react with the overlaying volume of lime water before they can diffuse to the bottom of the half cell: as a consequence, for very long testing times it is possible to observe the formation of a thin calcium carbonate crust at the interface that can sometimes partially blur the pictures. Such phenomenon takes place however only for poor barriers or uncoated foils, i.e. only when great quantities of carbon dioxide permeate in the cell. The concentration gradient of CO_2 necessary for the crystallization process, therefore, not only is strongest on the samples surface, but it also decreases steeply, so much that formation of calcium carbonate at the liquid/gas interface can take place only when poor barriers are tested.

That the main effect on the shape and size of crystals is determined and limited by the reagents availability, in particular of carbon dioxide (assuming a constant concentration of calcium ions in the solution), instead of the surface morphology and/or chemistry and the presence of eventual contaminants, is confirmed when depositing only a drop of lime water on the central area of the sample, instead of coating the latter with a continuous aqueous layer: in this case, the CO_2 permeating through the 'dry' surface accumulates in the sample-holding cell atmosphere; as a consequence, at the edges of the drop the local oversaturation value is much higher than the one attained in the drop's core, with the CO_2 coming through the sample being orders of magnitude more than the traces coming from the external atmosphere through the cell lid, as schematically shown in Figure 6.21.

The resulting crystals forming at the edges of the droplet, retrieved at the SEM, show completely different morphologies, dimensions, and even 'patterns' than the crystals obtained by the continuous layer method, or even those precipitated in the core of the same drop, as reported in Figure 6.22: instead of showing a typical spherulite-like appearance (Fig. 6.22 c), the polycrystals at the edge are constituted by dense, 'solid' interpenetrating rhombohedrons (particularly evident in Fig. 6.22 d) which clearly originate from larger reactant quantities. Moreover, in most cases the polycrystals are surrounded by large circles of smaller, discoidal or polylobate crystallites (detail in Figure 6.23), growing smaller as they lie nearer to the bigger central crystals.

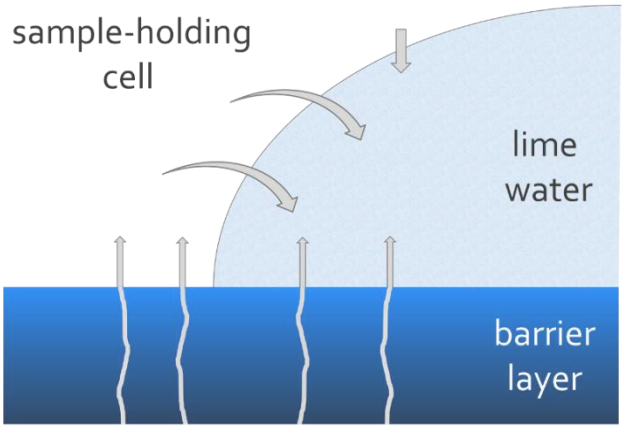

Figure 6.21: Schematic representation of the increased CO_2 concentration in the lime water solution when a drop instead of a continuous film lies on top of the coated sample in the testing cell. The grey arrows represent the CO2 fluxes through surface defects, its dissolution in the liquid from the sample-holding cell atmosphere and the smaller contribution permeating through the polycarbonate window of the cell.

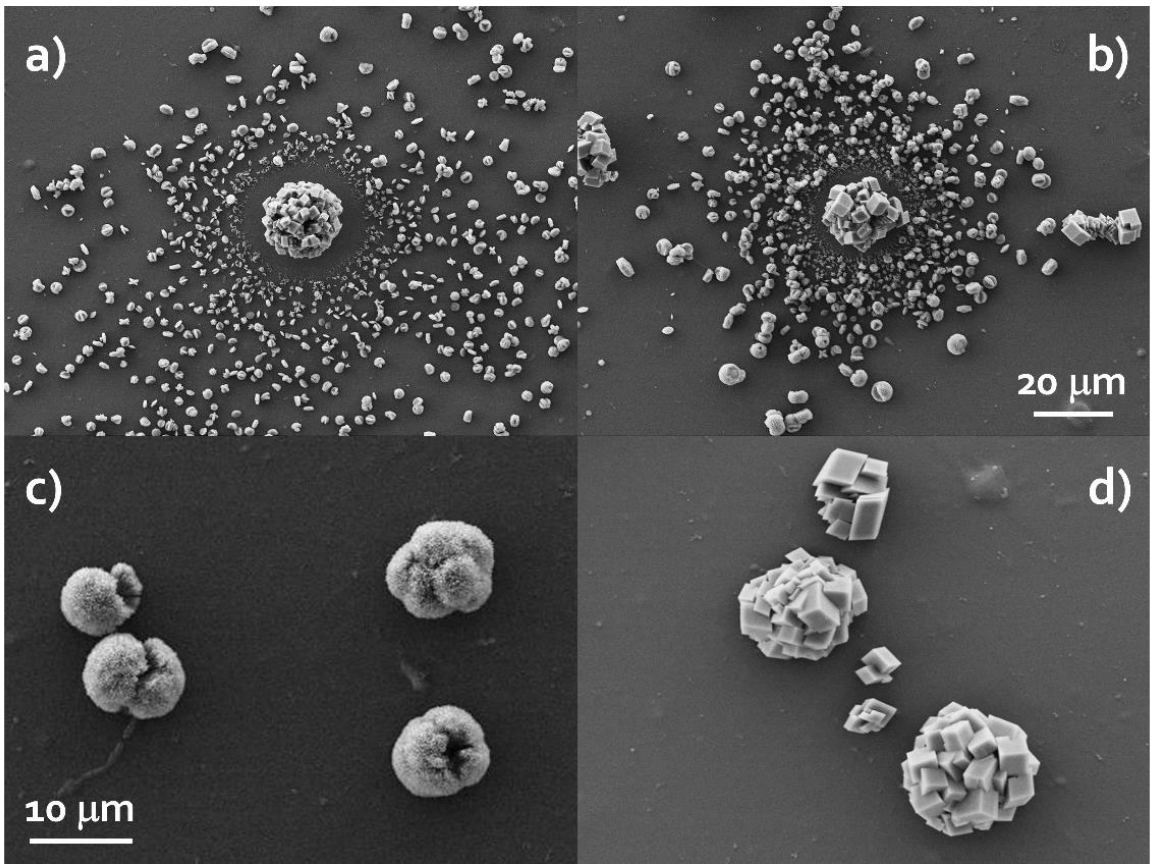

Figure 6.22: SEM pictures of crystals on top of a coated sample (medium barrier properties) at the edges of the lime water drop (a, b, d), and at its center (c). Fig. a) and b), and Fig. c) and d) refer respectively to the same scale.

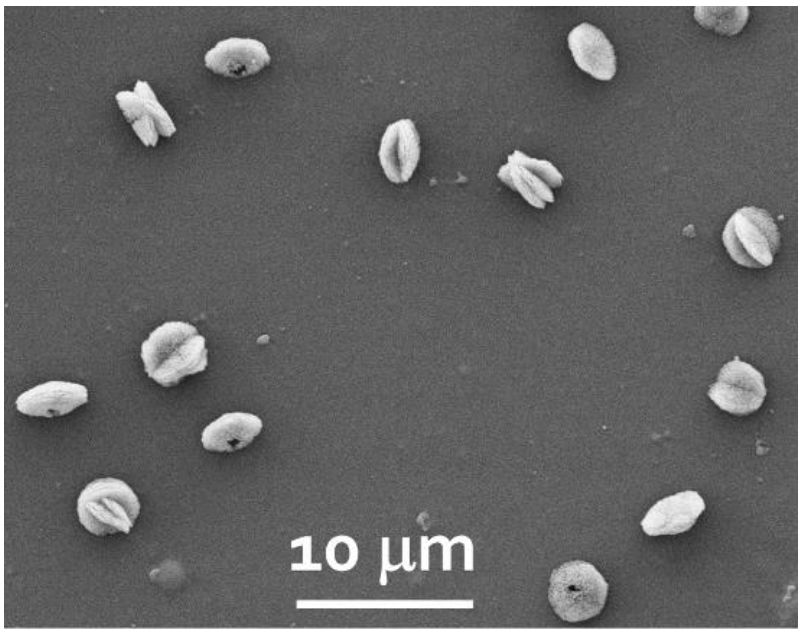

Figure 6.23: Detail of the smaller crystallites surrounding the larger crystals at the edge of a lime water drop on a coated sample.

The crystals appearance closely resembles the crystals obtained by Ogino et al. through precipitation of supersaturated solutions [169] that resulted first in amorphous and vaterite crystals and later in their spontaneous transformation in the more stable calcite polymorph (with the strongest resemblance to intermediates still in the process of converting to calcite). As vaterite is the most unstable and most kinetically favorable of the three calcium carbonate polymorph [193], the precipitation processes at the edge of the droplets must take place very quickly and with extremely high oversaturation values, consistent with the increased CO_2 availability: the latter is enough to also cause prolonged precipitation steps resulting in numerous nucleation sites. The partly dissolved crystallites around the bigger rhombohedra aggregates moreover suggest Ostwald ripening processes, confirming that, at least in such unusual conditions, a relevant fraction of the dissolved CO_2 must come from other sources outside the alleged defect under the biggest central crystal. While perhaps the central crystals in such formations lie on top of defects, the smaller crystals surrounding them most certainly don't, and the results obtained at the edges of the droplets are not reliable enough to be taken into account.

The following step in the evaluation of the pinhole test has been to ascertain whether the crystals do actually form on top of the defects: for a better discussion on the topic, see also section 7.1.5. Some provisional conclusions can however be already inferred through the preliminary tests. Figure 6.24 shows the surface of an organic layer (see also Appendix A.2): the roughly circular patch showing weak iridescent effects is likely to be an uncoated area of the surface, probably masked by a dust particle or other solid particles during the PECVD process. The iridescence

is caused by diffraction at the edges of the deposited colorless layer. The foreign particle, regardless of its origin, has rolled away from the sample surface during the preparatory steps for the pinhole test, and as such could not be positively identified. As shown in the picture, as the running time of the test increases, apart from crystallites forming on the surrounding coated area, it is possible to observe the uncoated PET area being quickly covered by a continuous, thick calcium carbonate layer, as locally the barrier properties are worse. Furthermore, the uncoated area is also the first one to be completely permeated by the CO_2 molecules, since without the deposited film it is around 100 nm thinner. As explained in Section 3.7, such kind of defect will act as a funnel, collecting CO_2 from a large volume of the surrounding polymer bulk, thus hastening the formation of a greater amount of calcium carbonate on top of it. Such is already a confirmation that through this analysis method it is possible to localize defects, albeit in this case relatively large (approximatively $25 \cdot 35\ \mu m^2$, assuming that the calcium carbonate layer covers the entirety of the defect).

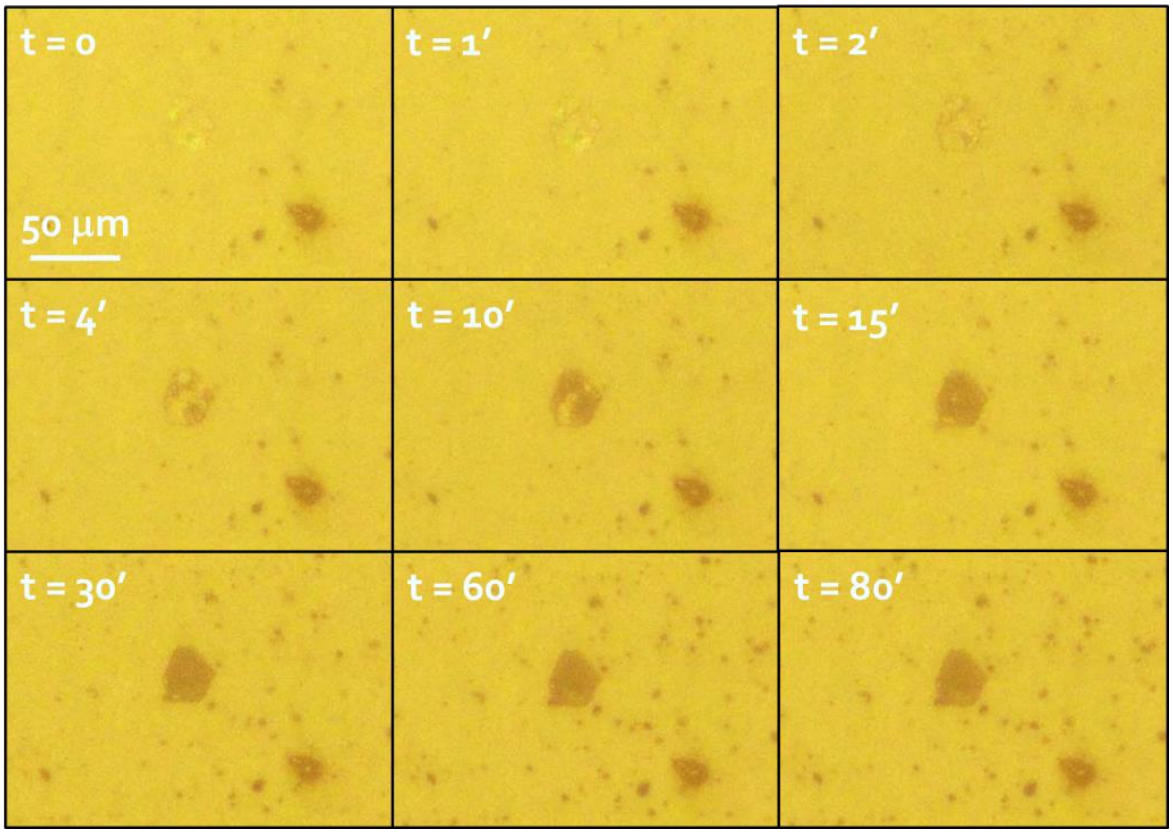

Figure 6.24: Detail of an uncoated patch of polymer substrate at the optical microscope during a pinhole test (magnification x10): the uncoated PET is preferentially covered by calcium carbonate that allows the macrodefect to be spotted despite the PECVD thin film being colorless. The film itself, being a mediocre barrier, is also covered by further crystallites.

The same applies for superficial scratches of the barrier layer, as seen in Figure 6.25. In this case, while applying the marker on the sample surface, the lancet blade has inadvertently scraped against the barrier, damaging it. No sign of it was visible at the naked eye, but during the test the crystallites formed preferentially along thin lines that formed a recognizable scratching pattern. The effect cannot be caused by bizarrely scattered dust particles or other impurities on the surface, as the rest of the surface remains crystal-free even at the end of the test. Curiously, the same result has been achieved by purposefully scratching an uncoated PET foil and then running the test, as shown in Figure 6.26. As in this case a remarkable pressure was applied to the blade, it is possible that the scratched parts suffered from indentations or material removal that made them artificially thinner than the surrounding polymer; as a consequence, it is in this areas that the first permeand CO_2 molecules reached the lime water solution, creating a concentration gradient sufficient to trigger a strong nucleation process, but only locally. The possible explanation for this phenomenon is therefore akin to the one provided previously for the accidental uncoated patch shown in Figure 6.24.

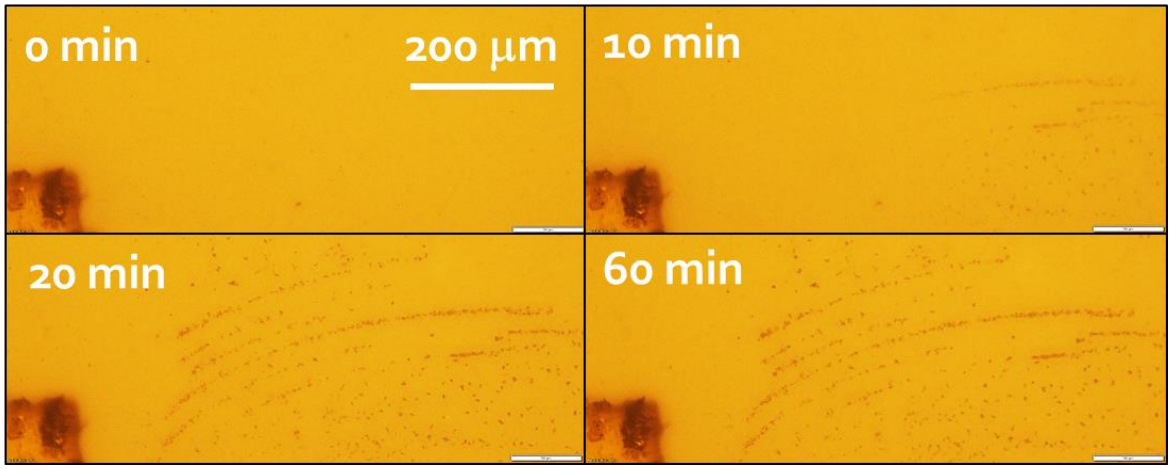

Figure 6.25: PET foil coated with a good barrier layer that has been damaged during its handling by a lancet blade: the calcium carbonate crystals precipitate preferentially along the scratches where the barrier offers no protection against permeation.

Another case of detection of macro-defects is finally shown in Figure 6.27: the thin stripes covered in calcium carbonate that propagates radially from the vicinity of the marker are probably caused by a punch-through effect caused by an involuntary folding of the foil during its preparation for the test. The elevated local stress caused the thin film to fracture, like glass, leaving thin cracks through which no opposition to the permeation is offered. In this case the barrier possessed poor qualities, so even the undamaged surface which surrounds the scratches has gotten covered by crystals. No corresponding sample for an uncoated PET foil is in this case available.

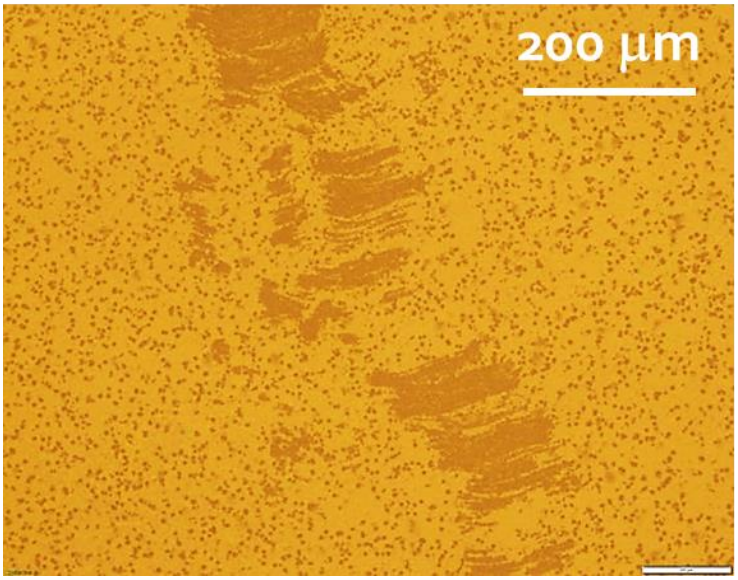

Figure 6.26: Uncoated PET foil purposefully scratched before the pinhole test by means of a lancet, and subsequent scratch marks revealed by the calcium carbonate deposits Picture with a x5 magnification.

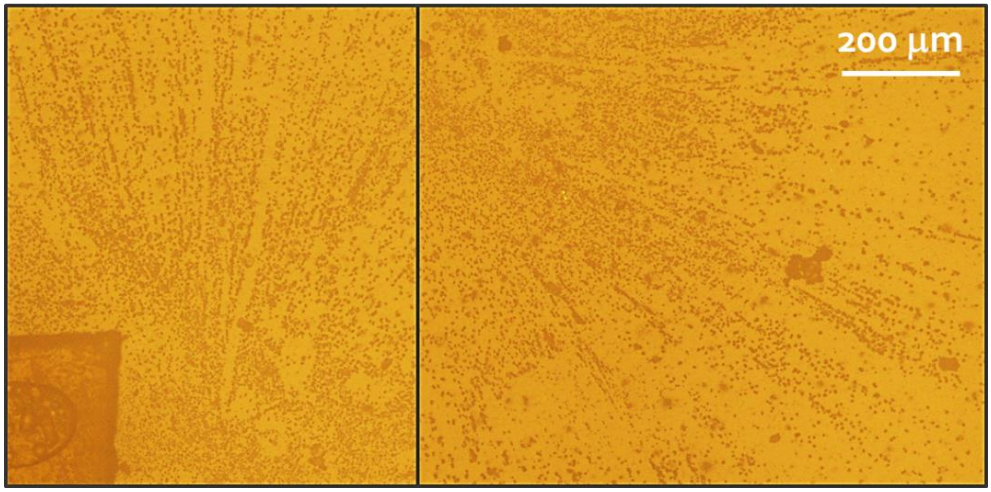

Figure 6.27: Damages on the barrier layer caused by involuntarily folding of the substrate foil revealed by the pinhole test (x5 magnification). Both pictures refer to the same sample.

Finally, for an accurate analysis by means of SEM of the crystals and eventually of their underlying areas, it had to be possible to retrieve the exact same frame observed through the optical microscope during the pinhole test run. Figure 6.28 shows how this has been achieved by means of the markers. In the highlighted white frame in the SEM picture it is possible to recognize the same crystals left undisturbed by the washing, drying, cutting and coating steps taking place between the proper pinhole test and the later observation at the scanning microscope.

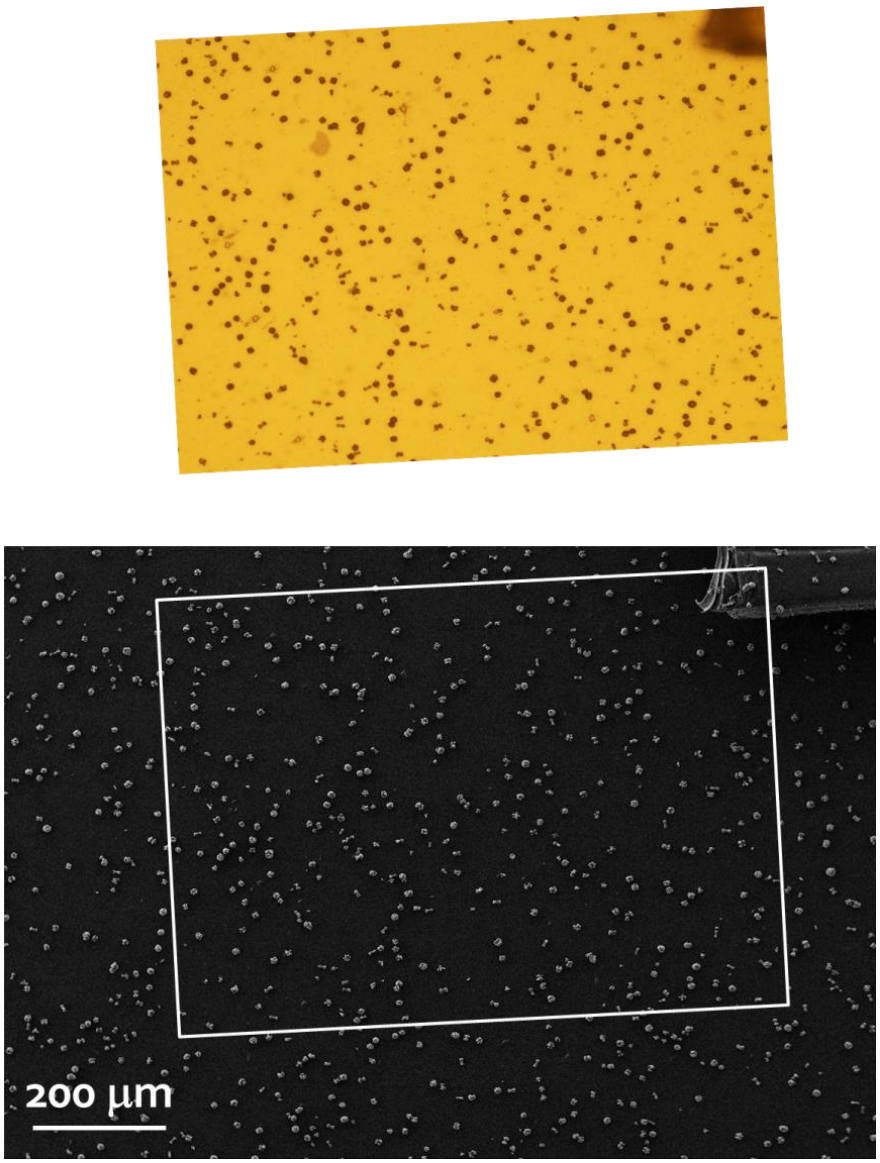

Figure 6.28: Optical microscope picture with a x5 magnification factor (top) of the area surrounding the marker applied on the sample and same are (white frame) later retrieved at the scanning electron microscope (bottom).

In conclusion, through the examples here shown and discussed it is possible to assume that:

i) the formation of crystallites and their precipitation is an extremely quick process even at room temperature, that can be assumed to take place immediately on top of the defects through which carbon dioxide permeates; the diffusion time of the latter in the solution must therefore be minimal. Similarly, the rate-limiting step in the overall process must be the permeation through the foil and the eventual deposited thin film;
ii) the test is able to localize macroscopic defects like uncoated areas or scratches in the

barrier films and correctly identify them even when the coating is colorless;

iii) the handling of the samples after the test do not affects the position of the crystals on the surface which can be later easily retrieved by other microscopy techniques;

iv) the test in itself does not in any way damage the underlying surface of the tested sample; eventual damages are caused by mishandling of the samples or their incorrect preparation.

In summary, the test is quick, reproducible, reliable, non-destructive, and must provide useful and consistent data to be paired with other methods for the study of the barrier properties of thin films. Further details are given in the discussion of the experimental results presented in section 7.1.5.

Chapter 7

Single barrier films – Results and discussion

The current chapter presents the results regarding the investigations on the plasma-deposited thin films and how the operating parameters of their deposition processes can affect and tune their chemical and physical properties, chiefly among them the barrier performances with oxygen as permeand gas. The aim has been to find suitable operating conditions that could allow the deposition of films with the best barrier properties achievable in the current experimental set-up.

Good mechanical stability that ensures the retention of the aforementioned barrier properties is also extremely valued, together with a good adhesion to the underlying substrate. Short deposition times, where possible, are also favored, as they allow for faster multi-step encapsulation processes and reduce the risks, among others, of thermal and/or UV-induced damages of the substrates. Thinner films, provided the barrier properties are constant, allow furthermore quicker deposition steps and prevent multilayer systems based on them to develop excessive internal stresses that could compromise or even completely destroy their structural integrity.

7.1 Study of the variation of the O_2/HMDSN feed ratio

The first step for the investigation of PECVD thin films for barrier applications has been the study of the dependence of their properties on the composition of the gaseous feed in which they are produced, in particular on the ratio between the chosen co-gas (oxygen) and monomer (HMDSN). As illustrated in Chapter 4 and Section 5.2, such ratio has an extreme effect on the composition and the properties of the films thus produced. The study is performed by keeping other variables, like operating power and film thickness, fixed at a constant value. They will in turn be later investigated in next sections.

The current section presents a short study on the deposition rates as a function of the aforementioned feed ratio, followed by extensive IR analyses in order to determine the films composition. Their surface morphology and resulting barrier properties will also be discussed.

Extensive investigations on the defects, including their contribution to the calculated diffusion coefficients and their density and type, determined by means of the pinhole test detailed in Chapter 6.5, will be presented and commented. Finally, a study on the dependence of the barrier properties of the films as a function of the temperature at which the permeation analyses are carried out will allow a discussion on the overall transport mechanisms taking place in the bulk of the thin barrier and to what extent each one of their different contributions influence the performances of the thin films.

7.1.1 Deposition rates

A first determination of the deposition rates for all the investigated oxygen-to-monomer ratios has been performed for a constant power of 555 W. The gas feed ratios have been obtained by fixing the oxygen flux at a constant value of 100 sccm, and by varying the HMDSN flux ratio accordingly, between 10 and 1.2 sccm. For smaller ratios, a coincident variation of both HMDSN and oxygen flux has been necessary, and the relative results have thus not been included in the current discussion. The ulterior variation of the oxygen flux is due to the equilibrium vapor pressure of HMDSN at room temperature, which causes the highest achievable monomer flux to be around 23 sccm. Higher fluxes, for lower ratios, would require a heating of the bottle and the line to the reactor too, in order to avoid condensation inside the pipes.

The results of these first investigations have been later employed to deposit 100 nm thick films for all the subsequent analysis. The measured thicknesses as function of deposition times for different ratios are reported in Figure 7.1. The error for the thickness values, represented in the figure by the vertical bars, has been assumed to correspond to the standard deviation associated to the profile readings (see also Chapter 6.1). For very low thicknesses, the error is greatly amplified by the detection limits of the millimeter paper, which amount to a variation of ± 5 nm for the smallest scale. Even for the longest deposition times, which exceeded 26 minutes, no thermal damaging like hazing, glossy appearance or crumpling of the polymer substrate has been visible to the naked eye. For all feed composition the increase of thickness with longer deposition times is linear. The different, progressively smaller slopes are caused in the first place by the different HMDSN fluxes employed for the deposition processes, as for higher oxygen-to-monomer ratios the precursors of the thin films are far fewer and the deposition process is limited by their availability in the plasma phase. In order to account for this, the film thicknesses shown in figure have thus been normalized by dividing them for the amount of HMDSN employed in each respective deposition process. They are displayed as [µm/sccm] in Figure 7.2.

The error bars are unevenly affected by such normalization step, so that their absolute variation is greater for lower HMDSN fluxes, i.e. higher oxygen-to-monomer ratios. It is possible to observe that the trends can still be assumed to be linear, but they also still retain different slopes,

with progressively and evenly smaller deposition rates for higher ratios and one last, steeper decline for the 80/1 value.

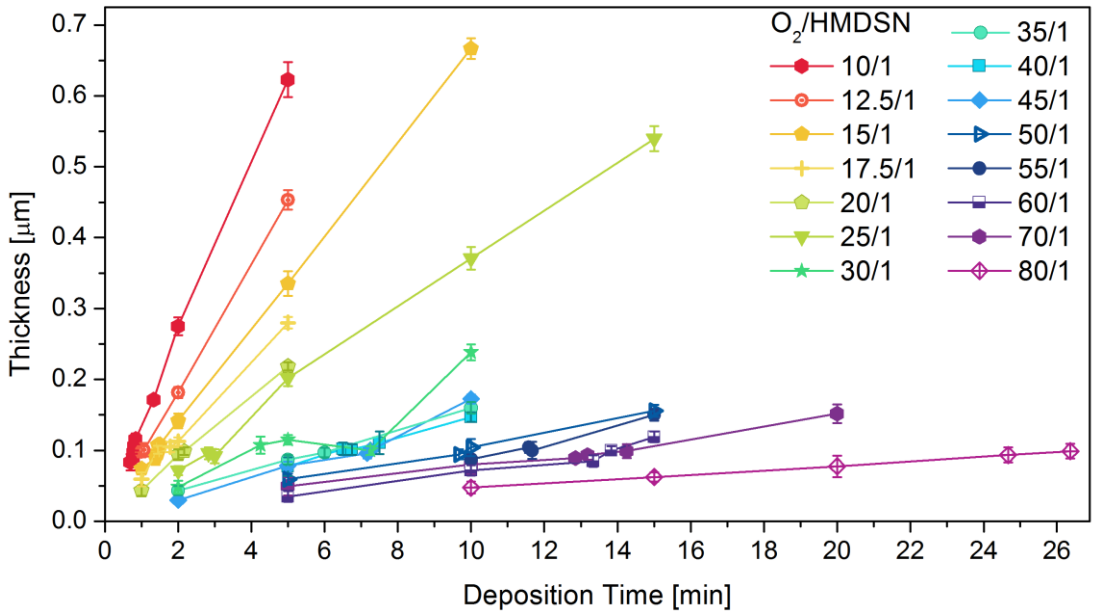

Figure 7.1: Dependence of the thickness of HMDSN-based films with different gas feed composition on the duration of the deposition time.

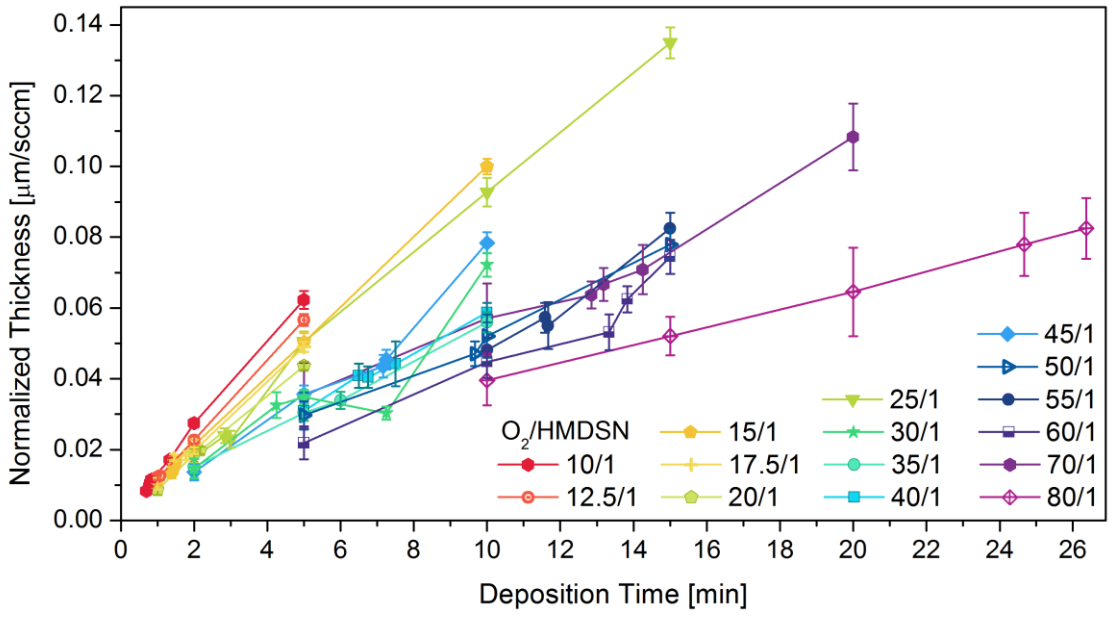

Figure 7.2: Thickness of thin films (here normalized by being divided by the amount of HMDSN employed) as a function of deposition time for different oxygen-to-monomer ratios.

The efficiency of the chemical reactions taking place in the plasma depends in the first place on the availability of suitable reagents, i.e. excited, ionized or dissociated species, chiefly in the current case oxygen radicals. Power has in turn a major effect on their concentrations. As the total amount of reagents moles in the reactor's total volume ranges from 110 mmol/min (100 mmol O_2 + 10 mmol HMDSN) to 101.2 mmol/min (100 mmol O_2 + 1.2 mmol HMDSN), with a maximum variation of 8 %, it is possible to assume that the average energy per mole remains fairly constant for all the investigated conditions. The different thicknesses are therefore to be ascribed solely on the different reaction pathways taking place in the plasma phase. With increasing fractions of oxygen, the equilibrium of the simplified reactions detailed in Chapter 5.2 is shifted towards more oxidized products, most of which are gaseous. By contrast, the less volatile fragments, which constitute the precursors of the solid film, become smaller and result for a given time in thinner layers.

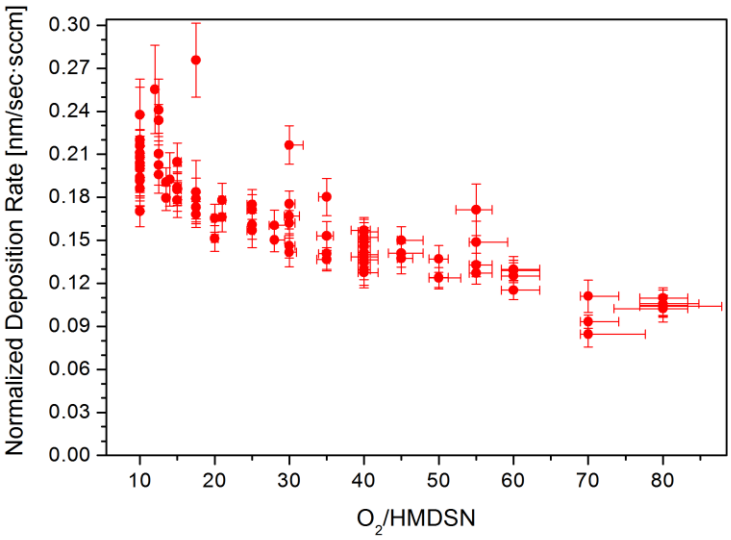

Figure 7.3: Normalized deposition rates for different oxygen-to-monomer ratios. All data refer to films with a final thickness of 100 ± 5 nm.

The normalized deposition rates as a function of the oxygen-to-monomer ratio, for films with a thickness of 100 ±5 nm, are reported in Figure 7.3. The deposition rate decreases fairly linearly for 20/1 ratios onwards, with a R^2 value of 0.79 (fit not shown). For smaller ratios, it is unclear if the trend is still linear, albeit with a steeper negative slope, or if it follows an exponential- or hyperbolic-like decay. In either case it is possible to observe the high variance for the 10/1 and the 12.5/1 ratios, caused both by a much shorter deposition time for 100 nm and by an inherently less reproducible deposition process, as the incomplete oxidation of the HMDSN molecules at low ratios leads to bigger fragments depositing quickly on the substrate. The two trends suggest

at least two different deposition kinetics, and will be related to the infrared analysis in the following sub-chapter (7.1.2).

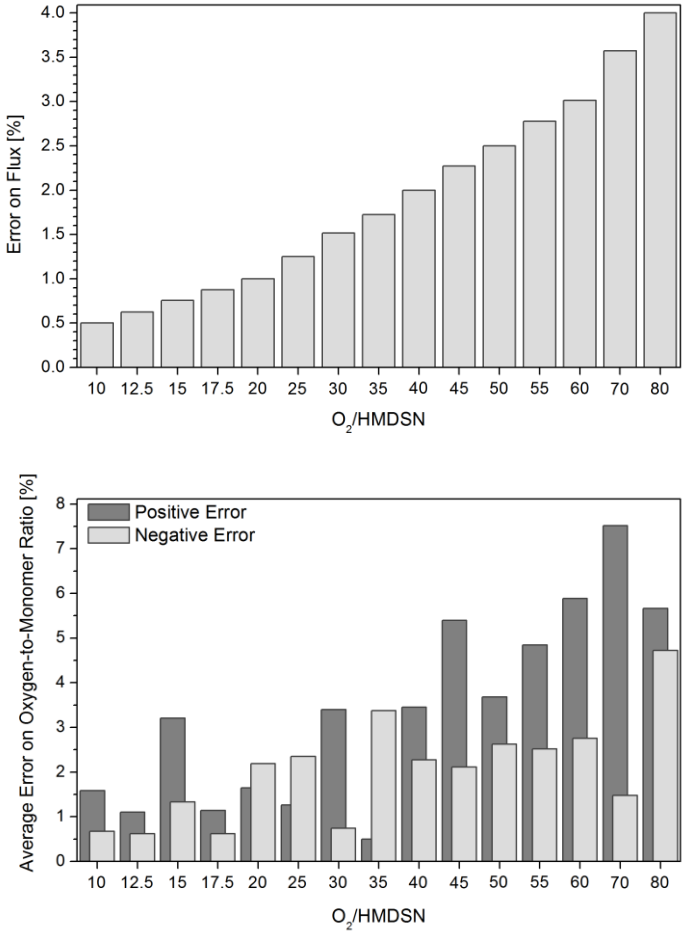

Figure 7.4, Top: percent error on HMDSN flux caused by sensitivity limits of the mass flow controller. Bottom: sensitivity error combined with HMDSN flux fluctuations displayed as average value for each oxygen-to-monomer ratio.

The vertical error bars displayed correspond to the standard deviation associated to the profile readings, while the horizontal ones arise from the combined effect of the sensitivity limits of the mass flow controllers and the observed fluctuations of the HMDSN flux. The first one, as shown in Figure 7.4 (top), is inversely proportional to the nominal HMDSN flux, growing for 0.5 to 4% in the investigated range. The second one is largely independent on the flux values, but together with the former can cause errors up to more than 7% in the actual oxygen-to-monomer ratios. Their combined averaged effects are displayed as % errors in Figure 7.4 (bottom). The asymmetry increases as the flux variations become proportionally bigger, especially those causing positive errors, as their value is yet again inversely proportional to the set HMDSN flux.

7.1.2 IR analyses of the barrier films

The 100 nm samples prepared for later permeation measurements (see Chapter 7.1.3) have been also analyzed by means of ATR FTIR spectroscopy. When not stated otherwise, the operating conditions and parameters described in Chapter 6.2.1 for the spectrometer are to be assumed. Figure 7.5 reports the spectra for each investigated oxygen-to-monomer ratio in the 4000-400 cm^{-1} range for a constant power of 555 W, together with the spectrum of the gaseous precursor (shown in Chapter 5.2) and some additional spectra for even smaller ratios, 5/1, 2/1, 1/1 and finally a pure HMDSN film. The thickness of the latter layers has also been set to 100 nm, in order to avoid possible dependences of the chemical composition on the thickness. A longer waiting time for the evacuation of the plasma reactor prior to the deposition step has been made necessary for the pure HMDSN films, in order to avoid drastic contaminations caused by even small quantities of residual oxygen in the vessel. For a better overview of the reproducibility limits of such films see also the end of this section. For a more extended discussion on the low-ratio film composition, see also Chapter 7.5.2. All spectra displayed have been normalized by their most intense signal. A full list of the position and attribution of the spectral features, a selection of which is already reported in figure, is listed in Table 7.1.

The pure HMDSN film retains most of the original functional groups, like the three methyls bond to a silicon atom, to which it is possible to attribute the three narrows bands at 2960, 2900 and 1260 cm^{-1} and the poorly resolved peak at 847 cm^{-1}. The Si-NH-related peaks at 935 and 1187 cm^{-1} are also still present, although with a noticeably wider full width at half maximum. Moreover, new bands also arise: the small band centered around 2110 cm^{-1} corresponds to the superimposition of the single peaks for SiH_x (with $x \in \{1,2,3\}$) and the main peak around 1030 cm^{-1} can be tentatively attributed to a $Si\text{-}CH_2$ bond in an organosilicon chain (more on this in Appendix A2). Both bonds are caused by the dissociation in plasma phase of the $Si\text{-}(CH_3)_3$ group and the partial oxidation of its fragments, that leaves hydrogen atoms to react with silicon radicals. The silyl groups, at least, disappear however for ratios higher than 5. The natural broadening of the bands in a solid sample, when compared to the finer structure encountered in gaseous phase, is here furthered by the inherently disordered structure of a plasma polymer, as described in Chapter 4.4, which causes a wide range of different chemical milieus and therefore different chemical shifts, resulting in a slight alteration of the natural vibration frequency of each bond. With increasing oxygen feed fractions the bands associated with the precursor quickly decrease in intensity and then disappear completely. The nitrogen-related bands are all but indistinguishable for ratios higher than 5, while the methyl peak at 1260 cm^{-1} is no more visible after a 20/1 ratio (the ostensible earlier disappearance of the two peaks at at2960 and 2900 cm^{-1} is caused by the lesser sensitivity of ATR spectroscopy at longer wavenumbers and is therefore only an analysis artifact).

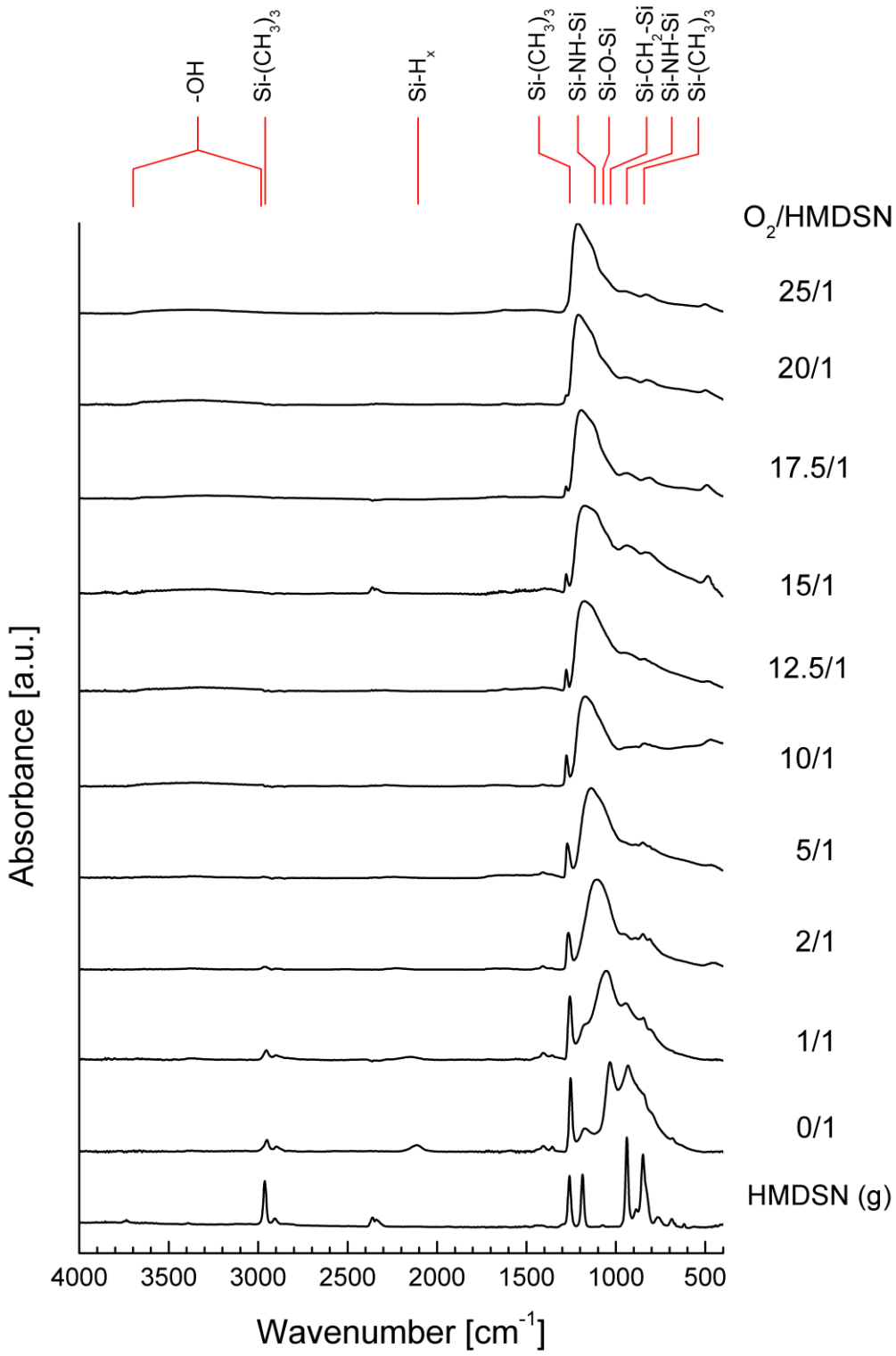

Figure 7.5: ATR FTIR spectra in the 4000-400 cm^{-1} range for 100 nm thick films deposited via different O_2/HMDSN plasma feed, plus spectrum of gaseous precursor HMDSN as comparison.

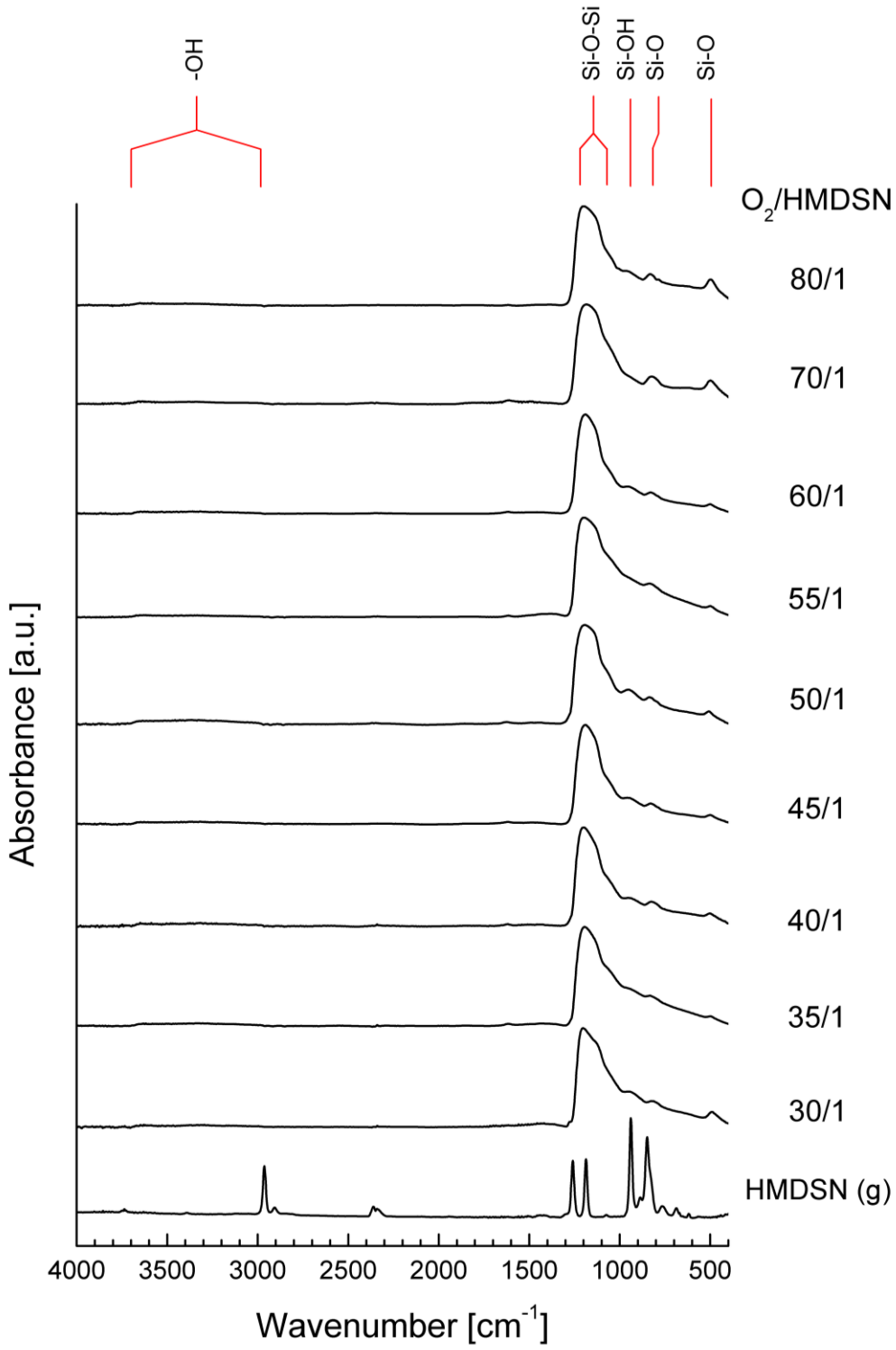

Figure 7.5 (continued): ATR FTIR spectra in the 4000-400 cm^{-1} range for 100 nm thick films deposited via different O_2/HMDSN plasma feed, plus spectrum of gaseous precursor HMDSN as comparison.

Table 7.1: Peak positions and vibrational mode assignments for the main absorption bands in the infrared spectra displayed in Figure 7.5.

Wavenumber cm^{-1}	Assigned group	Vibrational mode	Reference
3700-2950	OH	ν	[201]
3480	NH	ν	[202]
3380	NH_2	ν	[202]
2960	CH_x	ν_a	[151]
2900	CH_x	ν_s	[151]
2180	SiH	ν	[202]
	Si-C≡N	ν	[202]
1410	CH_x	δ_a	[151]
1260	$(CH_3)_x$	δ_s	[201], [202]
1160	Si-NH-Si	δ	[202]
	Si-N-C	ν	[202]
1100	[Si-O]-C		[201]
1090-1020	Si-CH_2-Si	δ, γ	[125], [202]
1080-1020	Si-O-Si	band	[203]
990	Si-CH_3	ρ	[121]
930-920	Si-OH	ν	[203]
925-850	SiN	ν_a	[202]
900-810	[Si-O]H		[201]
860	SiH	ν	[125], [201]
840	CH_3	ρ	[151], [201]
	SiC in $Si(CH_3)_x$	ν	[202]
800	SiO	δ	[204]
465	SiO	ρ	[204]

Conversely, new signals of oxidized groups appear at already low ratios and, around 25/1 and onwards, quickly becoming the only signals in the spectra: the Si-O-Si band appearing first at 1055 cm^{-1} and then shifting to higher wavenumbers, and the associated peaks at 955, 836 and 495 cm^{-1}. The strong fluctuations in the latter's intensity are caused by slightly different contacts between the samples and the crystal that mostly alter the curve shape at lower wavenumbers, where the sensitivity is greatest, and are therefore not significant. For most ratios finally a broad

but weak band attributed to –OH groups is visible in the 3700-2950 cm^{-1} range. No further variations in the spectra are visible after the 25/1 ratio.

It is clear that oxygen has a stark effect on the chemical composition of the final films, as it reacts effectively with all the organic groups of the precursor molecule, stripping them away and forming volatile products (chiefly CO_2 and H_2O), leaving only a silica-like or SiO_x final layer made up by long inorganic chains. A quantification of such oxidizing effect has been proposed by Roualdes *et al.* [74] as the ratio between the intensities of the methyl band at 1260 cm^{-1} and the newly formed Si-O-Si main band. Such relative peak intensity is plotted as function of oxygen-to-monomer ratios in Figure 7.6.

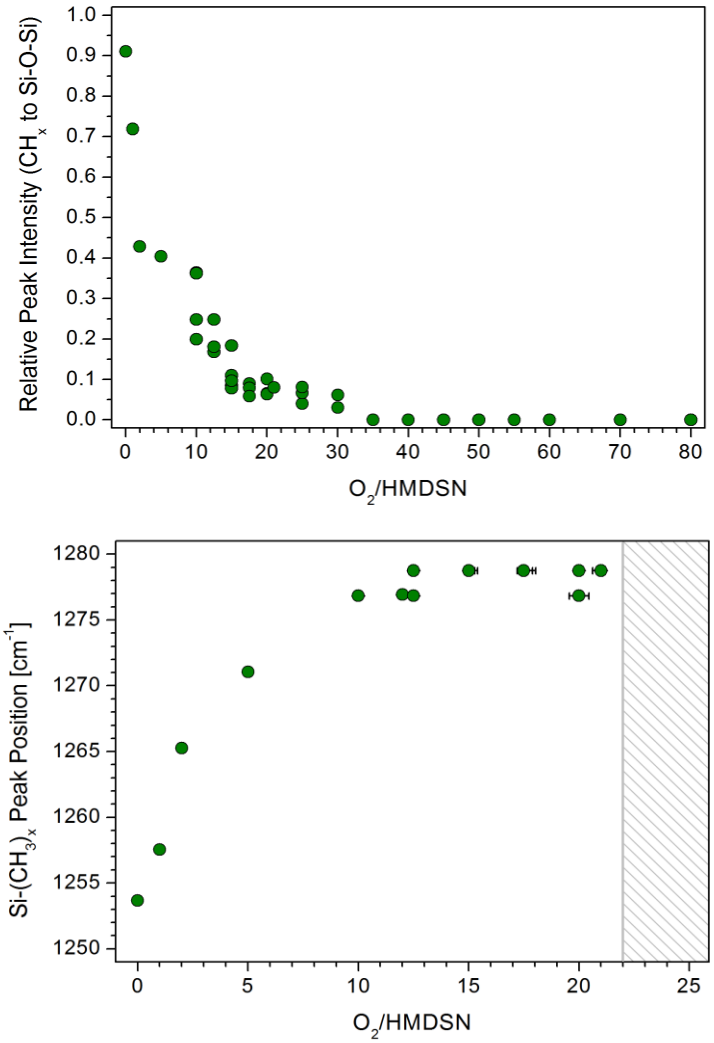

Figure 7.6: Relative peak intensity of the methyl band at 1260 cm^{-1} compared to the main SiO-band 1100 cm^{-1} (top), and peak position of the former (bottom) as a function of different oxygen-to-monomer ratios.

The initial intensity of the methyl band is almost equal to the Si-O-Si band's one, but their ratio quickly decreases to less than 0.5 already for an oxygen-to-monomer ratio of 2. Around 20/1, the intensity of the methyl band is almost zero and the deposited films seem to possess a completely inorganic composition: the residual values around the 20/1 threshold are artifacts caused by the partial superimposition of the slope of the Si-O-Si band moving to higher wavenumbers. A more rigorous approach would require the ratio between the integrated areas of the bands to be calculated, but nevertheless the peak intensities alone provide a reliable estimation of the organic content of the films. The reduction of the methyl signal is accompanied by a simultaneous shift towards higher wavenumbers, as also shown in Figure 7.6. The main band at 1260 cm^{-1} can in fact be split into three sub-peaks, corresponding to the trymethyl (1250 cm^{-1}), dimethyl (1260 cm^{-1}) and monomethyl (1270 cm^{-1}) groups bound to the same silicon atom [201, 205]. The position of the overall band gives then insight about the relative abundance of the former species. It is possible to observe that pure HMDSN films, with a band position coincident with the trimethyl peak, retain mostly the original monomer composition and result therefore in a poorly branched and porous film, as steric hindrance caused by the numerous methyl groups leaves empty spaces in the solid structure. Here too the effect of the oxygen in the plasma feed causes a strong and quick shift from the original values. The final measurable values, before the organic peak disappears, show how its prevalent components are monomethyl groups. The increasing oxygen content in the plasma phase, combining the evidences from Figure 7.6, then, causes the trimethyl groups to turn to dimethyl ones, either by oxidation of the carbon atom still bond to the silicon one or by complete ablation of the CH_3 group, the dimethyl to turn to monomethyl and the latter to be finally completely removed from the film. A similar process can be presumed to take place with the SiH_x groups, whose band disappears for even lower oxygen-to-monomer ratios.

Pictures of water droplets sitting on the surface (reported in Figure 7.7) confirm the shift from hydrophobic, carbon-based chemistries towards hydrophobic, glass-like surfaces. The water contact angle for a 40/1 oxygen-to monomer ratio is comparable to the uncoated glass slide and only slightly higher, as plasma-deposited films' first molecular layer is always richer in organic groups when compared to the bulk [108]. Such eventual residual of methyl groups is however low enough to escape infrared detection.

The main band between 1200 and 900 cm^{-1}, attributed to Si-O-Si bonds, is in fact constituted by several components, some of which are listed in Table 7.2. Contrary to the Si-O rocking and bending located at lower wavenumbers, however, the stretching peak exhibits a pronounced red shift for increasing oxygen fractions in the plasma feed, as shown in Figure 7.8 (top).

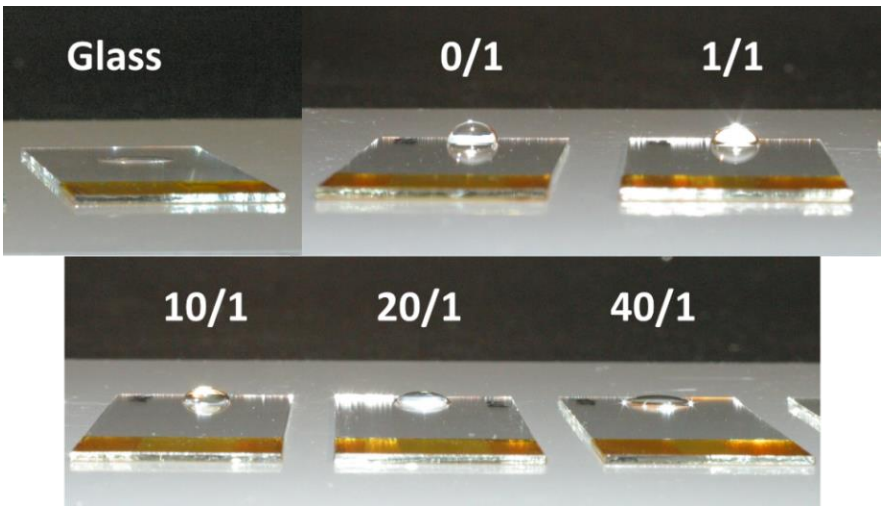

Figure 7.7: Deionized water droplets sitting on glass substrate and several slides coated with O2/HMDSN-based films with different gas feed ratios.

Table 7.2: [Si-O]-related vibration modes in the 1150-970 cm^{-1} range for thin silicon oxide films [105].

Wavenumber cm^{-1}	Assigned group	Vibrational mode
1150	[Si-O]-Si	ν, out of phase oxygen motion
1100	[Si-O]-C	n.a.
1073	O_3-[Si-O]-SiO_3	ν, in phase oxygen motion
1038	Si_2-[Si-O]-SiO_3	ν, in phase oxygen motion
1004	Si_2-[Si-O]-SiO_3	ν, in phase oxygen motion
970	Si_3-[Si-O]-SiO_3	ν, in phase oxygen motion

The stretching band shifts almost 200 cm^{-1} to higher values and then stabilizes around 1200 cm^{-1} for oxygen-to-monomer ratios of approximatively 20/1. Such value, noticeably, corresponds to the threshold after which it is no more possible to detect organic signals in the spectra. The shift is attributed to a wide range of possible reasons, including changes in the refraction index of the films, their density [206], the presence of substoichiometric domains in their bulk [207, 208], internal stresses, porosity [209, 210], but is also caused by the environment surrounding the Si-O bond: in an amorphous plasma polymer, in contrast with crystalline silica, it is possible for silicon to be bonded with other Si atoms, instead of being surrounded exclusively by four oxygen atoms.

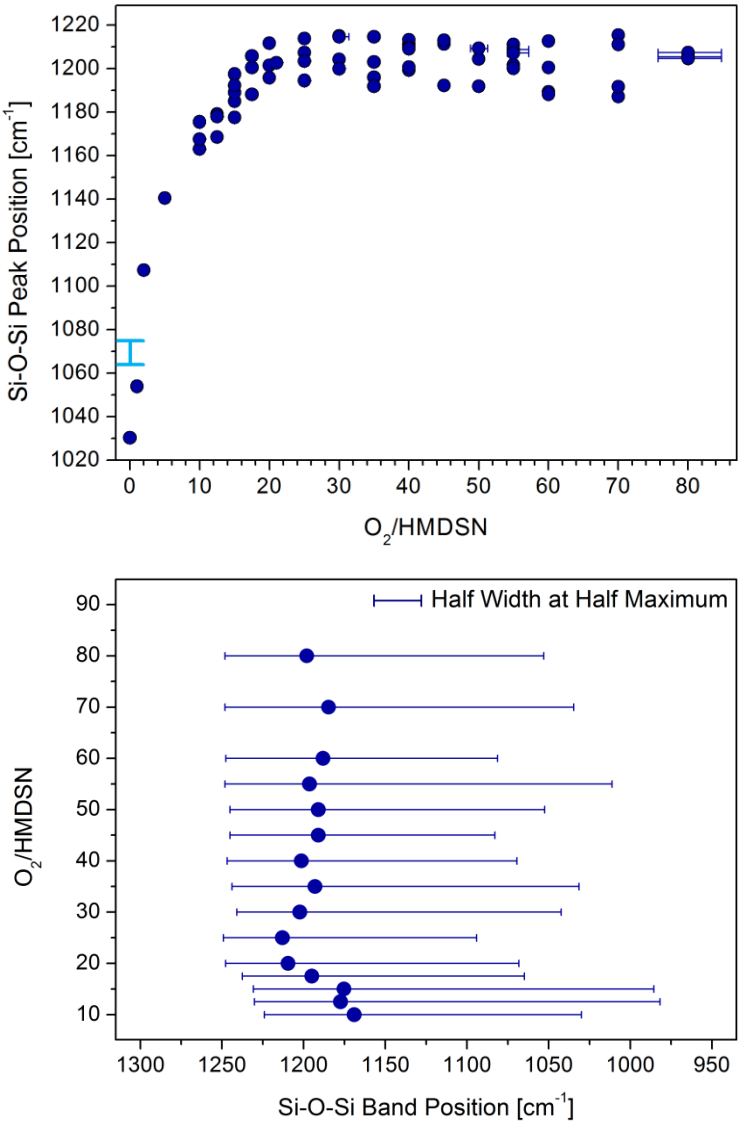

Figure 7.8: Top: Si-O-Si main band position as function of the oxygen-to-monomer ratios. The blue bar in the lower left corner shows the band position (1065-1075 cm^{-1}) for crystalline, stoichiometric silica.
Bottom: Si-O-Si main band position together with the corresponding half widths at half maximum for different oxygen-to-monomer ratios. The displayed values refer only to the peaks already shown in Figure 7.5.

The aforementioned possibility is especially true for low oxygen-to-monomer ratios, as in this case a major amount of oxygen is first consumed to react with carbon and hydrogen atoms, and often without oxidizing them completely. The lower electronegativity

of vicinal Si atoms causes a small shift of the typical vibration frequencies, to lower values [105, 211]. By contrast, films with high oxygen content will show band positions closer to those of silica.

The assumption that amorphous thin films and their spectra can be treated with the same criteria developed for crystalline SiO_2 spectrometry is valid, as rotovibrations and their shift are dominated by short-range interactions and, thus, the remarkable differences in long-range order for amorphous and crystalline structures can be neglected [210]. As plasma processes are inherently stochastic in nature, however, the local stoichiometry (i.e. the aforementioned substoichiometric domains, where $SiO_{x<2}$) causes another further broadening of the bands and their asymmetry at higher wavenumbers [206], so much that their full width at half maximum is largely assumed to be a measure of the "disorder" of a film [151].

The blue bar in Figure 7.8 refers to the usual Si-O stretching in crystalline SiO_2 [212]: no shift or further unlisted Si-O vibration mode can account for values more than 150 cm^{-1} higher. The predominant components at such wavenumbers arise from a splitting of the classical Si-O vibration modes caused by strong interactions between the partially polarized incident radiation and the surface plasmons in the thin films, the so called Berreman effect [213]. For a more detailed illustration of the effect, see also Chapter 7.3.2. Despite the presence of such spurious peaks, however, the variation in the maximum of the whole Si-O-Si band is still indicative of a change in the film structure rather than due to optical artifacts [208, 214]. Moreover, the Berreman effect depends strongly on the film thickness: being the latter almost constant for all investigated samples, it is safe to assume that the overall contribution of the Berreman effect, although unknown without performing a curve fitting of the whole band, remains constant. Such assumption is further reinforced when observing the half width at half maximum, calculated for the peaks already displayed in Figure 7.5, in Figure 7.8 on the bottom: for all inorganic films, the left half width, the one more influenced by eventual longitudinal modes, remains practically constant. The right one follows the same trend, although, because of the curvature of the background signal being the steepest for shorter wavenumbers, its fluctuations result to be wider, still affected by residual errors persisting even after the baseline correction procedure. It is therefore still possible to conclude that, for oxygen-to-monomer ratios above 20 or 25, the films show the same inorganic, silica-like chemical composition. By observing the trend for lower ratios, moreover, it is also possible to conclude that such inorganic films possess high densities and crosslinking degrees [128, 151, 215, 216].

The only absorption peaks not directly related to the vibrational modes of the Si-O-Si group that constitutes the backbone of these plasma polymerized films are the broad band in the 3700-2950 cm^{-1} range and the narrower peak at 930 cm^{-1}, although the latter is in most cases poorly resolved, as it lies in the tail of the main Si-O-Si band. The OH bands in the 3800-2800 cm^{-1} range for the spectra already shown in Figure 7.5 are reported in Figure 7.9. It is also possible to observe,

for the pure HMDSN film and the two lowest oxygen-to-monomer ratios the asymmetric and symmetric stretching peaks of CH_x centered around 2925 cm^{-1}, and for the pure HMDSN film and the 1/1 ratio also the very weak NH stretching between 3400 and 3300 cm^{-1}. The OH-related band itself starts to become visible around the 2 and 5 ratios, it grows quickly to maximum values in the 10/1 to 20/1 range and then decreases and remains almost unchanged afterwards. The change in intensity is accompanied by a variation of its shape, in particular a relative increase of signal around 3650 cm^{-1}. The whole band can in fact be divided into at least three different sub-intervals, depending on the chemical environment surrounding the vibrating -OH bond. The ranges are highlighted in Figure 7.10, which reports the OH band for an oxygen-to-monomer ratio of 70 as an example. The first sub-band, ending around 3600 cm^{-1}, is caused by 'free' hydroxils, i.e. weakly bonded or isolated Si-OH groups [217, 218]. The second sub-band, in the 3600-3200 cm^{-1} range, is mostly caused by moderately strongly hydrogen-bonded SiOH groups [217] and occasionally water vapor molecules adsorbed on the surface [218]. The latter, despite the infrared analysis being performed in dry air atmosphere, cannot be *a priori* ruled out, as water vapor readily forms a monomolecular film especially on polar surfaces. Finally, the third sub-band, stretching to 2900 cm^{-1}, refers to SiOH vibrations severely perturbed by hydrogen bridges, i.e. vicinal SiOH groups interacting with each other: in this case, the formation of further bridges shifts the stretching mode to even lower wavenumbers [218].

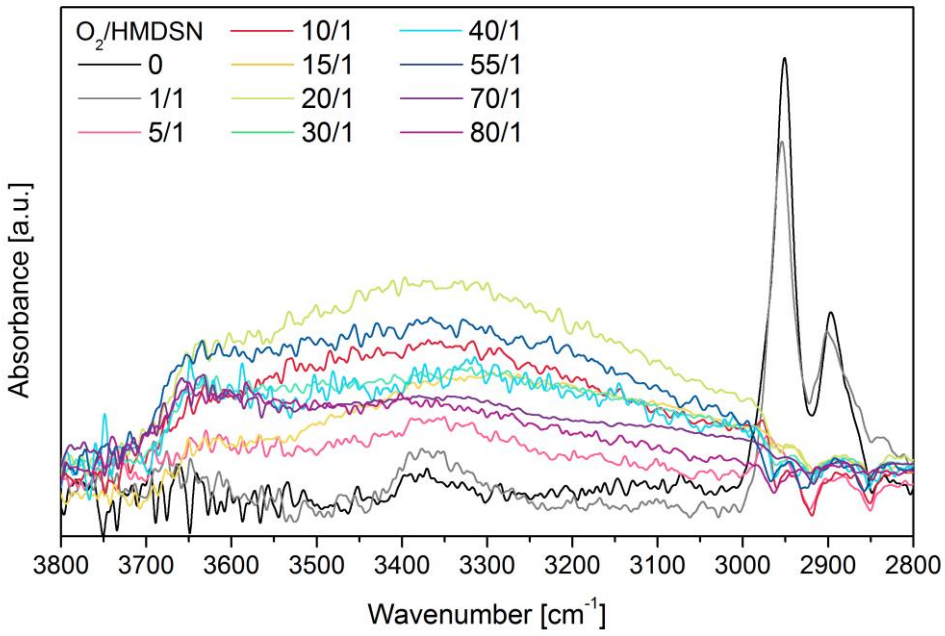

Figure 7.9: Detail of the 3800-2800 cm^{-1} range for a selection of the spectra displayed in Figure 7.5.

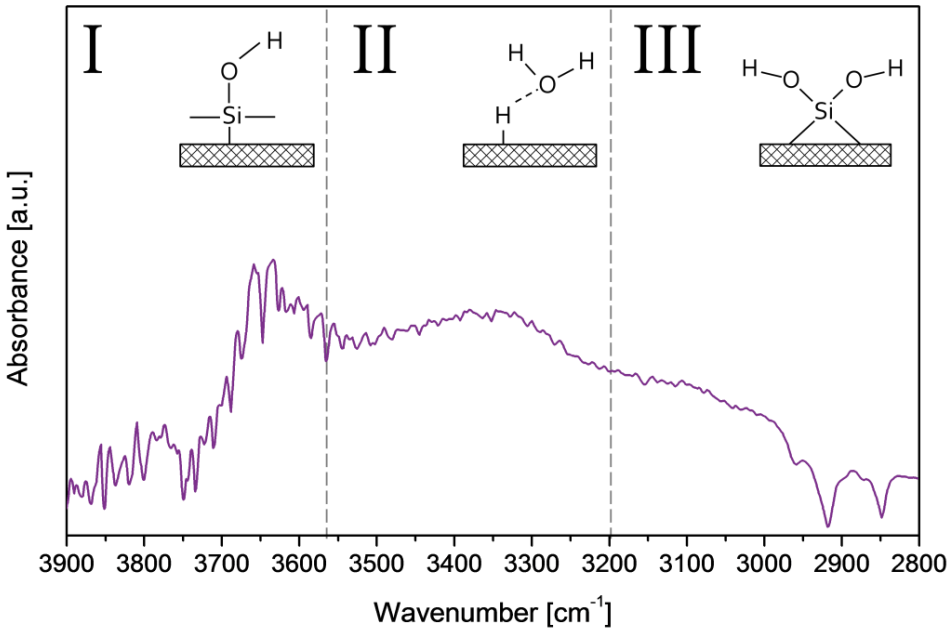

Figure 7.10: -OH stretching sub-bands for an O_2/HMDSN=70 sample. The schematics of surface OH-containing groups show isolated SiOH (I), a water molecule adsorbed on the surface (II), and multiple hydroxils bound to a single Si atom (III).

It is clear how the eventual presence and the type of –OH bonds is strongly dependent on the amount of oxygen in the plasma phase and on the kinetic of the deposition process self: for very low gas feed ratios, the oxygen atoms can only partly scavenge and oxidized the organic fraction of the fragmented precursor, leaving little to no oxygen in the film self. Thanks to its high reactivity, however, it is already possible to see a weak OH stretching signal for an oxygen-to-monomer ratio of 5 and, at only around 15/1 and onwards, the shoulder for the isolated hydroxyls starts to become visible. It is possible to conclude then that, for 'moderate' oxygen fraction in the feed, the deposited films incorporate large quantities of –OH groups, which lie close enough to interfere with their stretching frequencies. Chain-ending groups like $Si(OH)_3$ then limit the length of the silicon oxide polymer-like chains (as confirmed by the simultaneous trend for the Si-O-Si main band), while $Si(OH)_2$ prevent ramifications in the chains that would lead to a dense, cross-linked solid. The intensity of the band reaches its maximum when the last organic components are being etched away by the oxygen. After that, the excess of atomic and excited oxygen species in the plasma can only further oxidize the remaining silicon atoms and, in case of vicinal –OH groups on the surface, can cause their condensation with further release of gaseous H_2O, as shown in Figure 7.11. This explains the subsequent decrease in intensity of the band for even higher oxygen-to-monomer ratios. Finally, excluding the first surface layers which are always rel-

atively richer in end groups than the bulk [104], a relevant fraction of the residual -OH groups are isolated enough to not interfere with each other. The resulting films are therefore highly cross-linked (again in good accordance with the previous discussion about the Si-O-Si band shift) where the occasionally hydroxyl group lies only as side group in a chain. Semi-quantitative estimations of their fraction based on the ATR spectra alone will always result to be underestimated, as extremely isolated hydroxyl groups exhibit very low infrared activities [218].

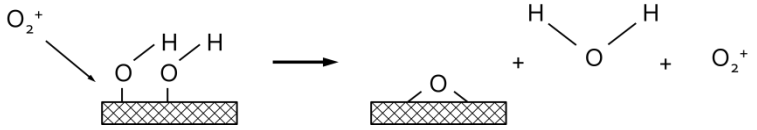

Figure 7.11: Schematic of the condensation process of vicinal hydroxils groups on a surface exposed to oxygen radicals. The surface loses two moles of hydrogens for every mole of molecular oxygen reacting. Picture based on [5].

The still present signal from the second sub-band, however, also shows at least local clusters of hydroxyls groups. These, as explained in Chapter 7.1.3, are an indirect evidence of the presence of defects in the polymerized films, whose inner walls are usually rich in –OH groups. No increase in the oxygen content of the plasma feed can cause their further abatement. Isolated -OH groups on the other hand have been shown to fill eventual nanopores in plasma-polymerized thin films [219], increasing their density and mitigating diffusion processes not defects-related (see also Chapter 3), so an evaluation of the barrier properties of the investigated films and their eventual defect density is not possible based on observations of the shape and intensity of the –OH stretching band alone. For further details on the –OH band, analyzed instead with single-reflection FTIR spectroscopy, and a further discussion about the oxidation processes in the plasma phase, see also Chapter 7.5.2.

Finally, ATR FTIR spectroscopy has been employed in order to check the reproducibility of the deposition processes and their homogeneity on the whole surface covered by the movable plasma. Figure 7.12 shows the spectra for films deposited months apart from each other. Their oxygen-to-monomer ratio, 15/1, corresponds to films about to turn completely inorganic and should therefore majorly suffer from poor reproducibility. As it is possible to observe, all spectra show very good consistency, including the position of the main Si-O-Si band and the intensity of the $Si(CH_3)_x$ bending.

Figure 7.13 finally shows the spectra for an oxygen-rich film (O_2/HMDSN = 50) and an organic one (pure HMDSN film) from samples lying at the opposite extremes of the movable magnet run, i.e. the extremes reached by the plasma in the ECR vessel. All films are again 100 ±5 nm thick

and each pair has been deposited in the same plasma discharge. It is possible to observe how in both cases the pairs of spectra are in very good accordance to each other, despite the inherent asymmetry in the reactor caused by the gas outlet (see on the subject Chapter 5.1). The small discrepancy in the peak position for the 50/1 ratio still lies in the dispersion range reported in Figure 7.8. In the ECR reactor with the current configuration is therefore possible to treat large area surfaces and deposit homogeneous films with identical chemical composition.

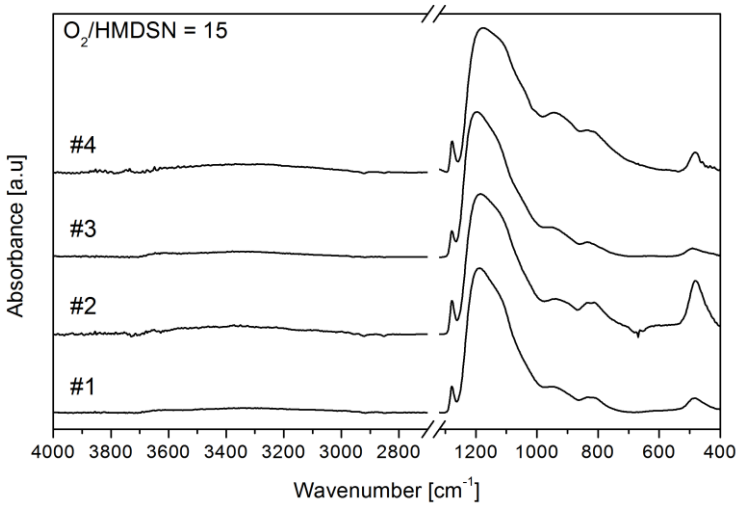

Figure 7.12: Spectra of repeated depositions (#1-4) of 100 nm thick films with an oxygen-to-monomer ratio of 15. 2700-1250 cm^{-1} range omitted for lack of film-related signals.

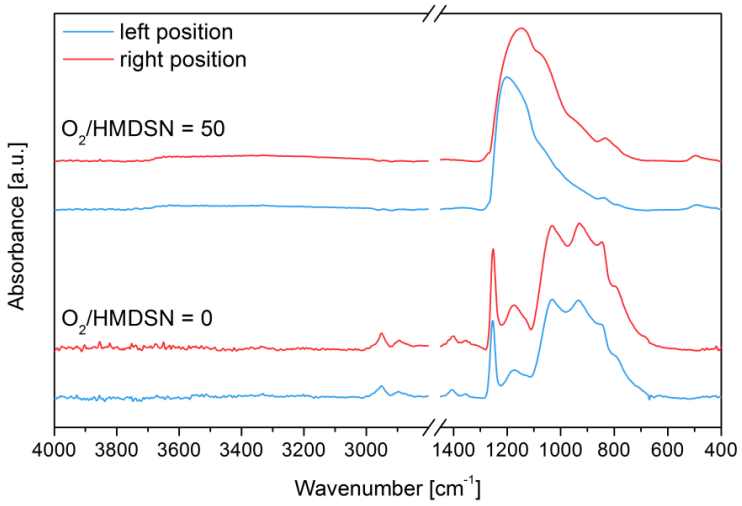

Figure 7.13: Infrared spectra of 100 nm films deposited at the left (blue) and right (red) extremities of the area covered by the ECR magnet movement. Films have been deposited with an oxygen-to-monomer ratio of 50 (top pair) and with a pure HMDSN plasma (bottom pair).

7.1.3 Morphology of the barrier films

The morphology of the films has been investigated by means of electron microscopy for three chosen oxygen-to-monomer ratios: 10/1, as it provides a fairly organic film, and 40/1 and 80/1, which by means of the results presented in the previous section can both assumed to correspond to completely inorganic films with virtually the same chemical composition. The films have been deposited on PET substrates, which have later been cut in squares of approximately 1 x 1 cm^2 and prepared for the SEM inspection (on the subject, also refer to Chapter 6.3.2). The cutting procedure inevitably causes cracking at the edges of the samples, thus allowing the observation of said cracks, their shape, size and edges, which in turn can provide useful informations about the internal morphology of the film. The resulting pictures are displayed in Figure 7.14. In all three cases the film appears to cover completely and uniformly the underlying surface. No particular inhomogeneities are to be seen in the resolution range of the scans, apart from the dust particles beneath the films which have been encapsulated during the deposition step (particularly noticeable on the 10/1 sample). The three samples all exhibit mostly curved fracture lines propagating from the rim.

The edges are very smooth in the first two cases, but for the 80/1 sample it is possible to notice a small increase in the number of minor cracks propagating perpendicularly to each other (in a further effort to release the internal stresses the film has been subjected when cut [27, 31]), together with a more jagged appearance of their edges. This contributes to give the film a more brittle look, similar to fractured glass. Such, albeit minor, difference, especially when compared to the 40/1 sample, cannot be attributed to differences in the chemical compositions, as nothing similar has been detected via IR spectroscopy. A correlation between such changes in the film morphology and the resulting barrier properties of it is presented in the following section. On the whole, however, the films along the full oxygen-to-monomer range show surface morphologies compatible with a resilient, flexible structure that can well adapt to bendable substrates without suffering major damages (more on this in Chapter 7.4.1).

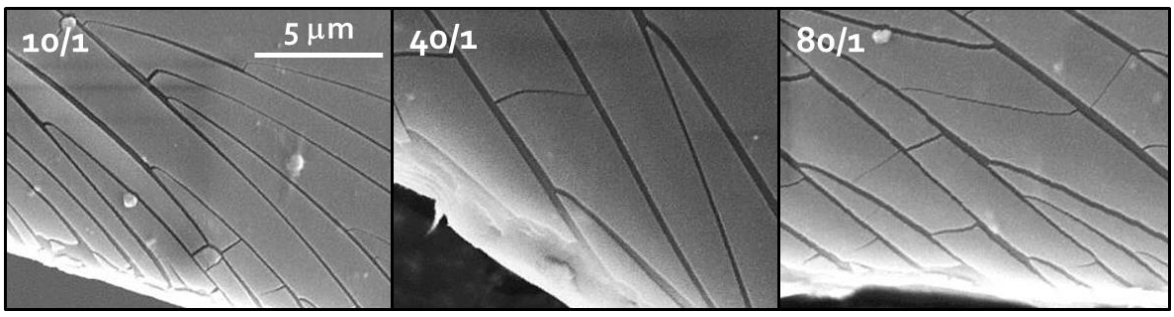

Figure 7.14: Scanning electron microscope pictures at a fixed magnification (10k) for HMDSN-based films at three different plasma feed dilutions.

7.1.4 Permeation curves of the barrier films

The oxygen transmission rates (from here onwards OTR) calculated from the permeation measurements for all the investigated oxygen-to-monomer ratios, for films produced at 555 W of operating power with a 100 ± 5 nm thickness are displayed in Figure 7.15. In the inset, the results for the 25/1 to 80/1 ratios on a reduced y-axis are shown again for better clarity. For each oxygen-to-monomer ratio, except the 0/1 corresponding to a pure HMDSN film, a minimum of three measurements have been performed, with samples produced in different plasma deposition processes. The green line is the upper limit, corresponding to the uncoated PET foil average reference. All values displayed have been normalized for unit of area and amount transmitted per day, and have further been corrected in order to take into account the effect of the outer pressure.

The initial values for low oxygen contents in the plasma feed lie in close proximity to the uncoated substrate, indicating little to none barrier properties for the thin films. Around an oxygen-to-monomer ratio of 12 the OTR starts to decrease almost vertically, stabilizing between 25/1 and 30/1 to a much lower value. The OTRs remain then constant over increasing oxygen-to-monomer ratios, save for a small increase starting at 60/1. The minimum for such curve is reached between 35/1 and 40/1. The dispersion of the OTRs for the same gas feed ratio follows a similar trend, being widest in correspondence of the vertical dip, smallest around 40/1 and then increasing again. The lowest measured value here displayed, i.e. the best barrier film, corresponds to a Barrier Improvement Factor of around 50 and to an oxygen-to-monomer ratio of 40/1. The best ratio, barrier-wise, has been assumed then to be 40/1, as it possesses both the lowest measured values, together with the 35/1, and the highest reproducibility, together with the 45/1.

By combining such results with the chemical composition of the films presented and discussed in section 7.1.2, it is possible at this point to identify three ranges in the oxygen-to-monomer ratio axis:

- from 0/1 to 25/1: in this range the films are still organic, especially for low oxygen content in the plasma feed; the copious end groups (trisilyl and trimethyl, but also hydroxyl substituents) severely limit the length of the polymeric chains in the film bulk and their cross-linking. Moreover, the methyl groups thoroughly investigated in section 7.1.2 and their steric hindrance leave a high fraction of void space in the film. The result is a porous, poorly dense film that initially offers little to no resistance to the permeating molecules, i.e. a bad barrier layer. The sudden drop in OTRs value corresponds perfectly to the strong reduction in methyl signals observed in infrared spectra, as can be observed in Figure 7.16, starting at a 12.5/1 ratio and ending when the films turn inorganic. In a similar fashion, the threshold between organic and inorganic chemistry of the films, located around 25/1, can be easily overlapped on the threshold between poor and good

barriers;

- from 25/1 to 55/1: in this range the films are inorganic, and consist of long interconnected polymeric chains closely packed against each other. The film chemistry closely resemble amorphous silica, and consequently the barrier properties resemble the latter's, too. The barrier performances in this range are stable, reproducible, and largely independent on the oxygen-to-monomer ratio employed for the film deposition;
- from 60/1: the performances of the films get worse and less reproducible. As the chemistry of the films remains unaltered and undistinguishable from the one of the previous range, however, the cause is not chemical, but perhaps morphological: as shown in section 7.1.3, high-ratio films possess a slightly more brittle appearance. The intrinsic barrier properties of the film, therefore, are not changed, but their mere handling and bending may result in micrometric damages like cracks, through which oxygen can permeate freely. The contribution from the undamaged fractions of the film to the overall oxygen permeation should on the other hand be minimal. The random chance of inadvertently damaging the samples can also explain the lesser reproducibility of their OTRs and their higher dispersion around the average value.

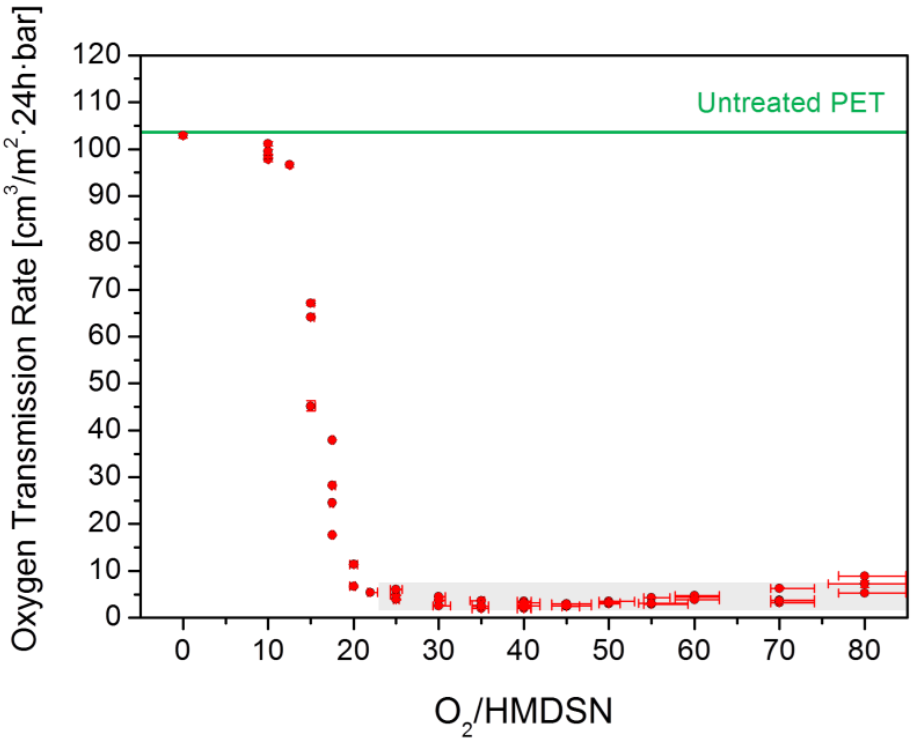

Figure 7.15: Oxygen transmission rates for 100 ± 5 nm thick films as a function of the oxygen-to-monomer ratios employed for their deposition. The vertical errors are the standard deviations associated with the single permeation measurement; the horizontal errors are caused by fluctuations in the HMDSN flow during the deposition process.

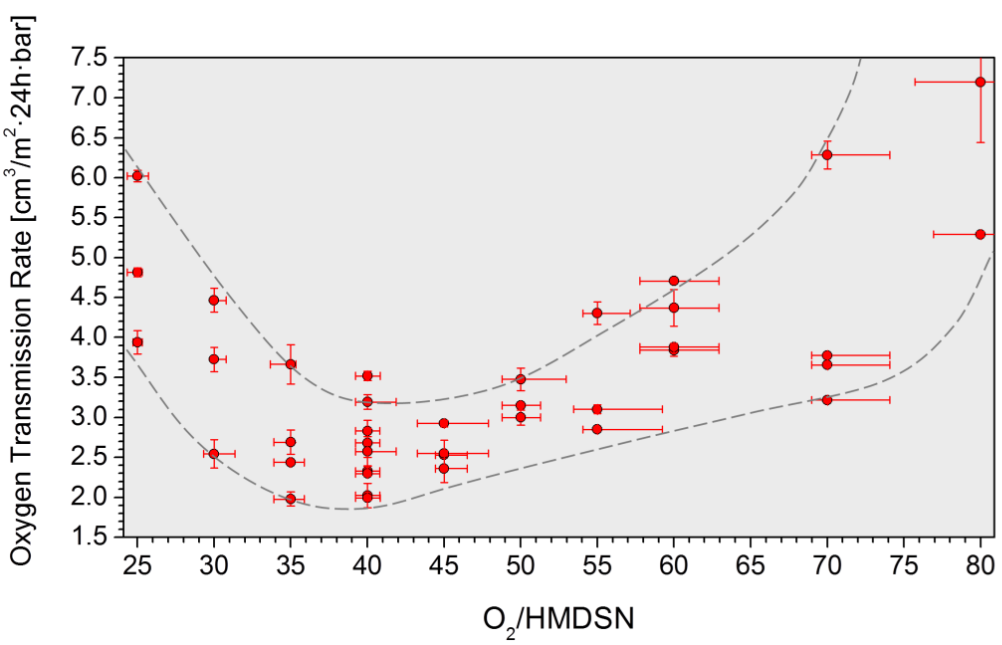

Figure 7.15 (continued): Oxygen transmission rates for 100 ± 5 nm thick films as a function of the oxygen-to-monomer ratios employed for their deposition: details of the area shaded in gray in the graph on the previous page.

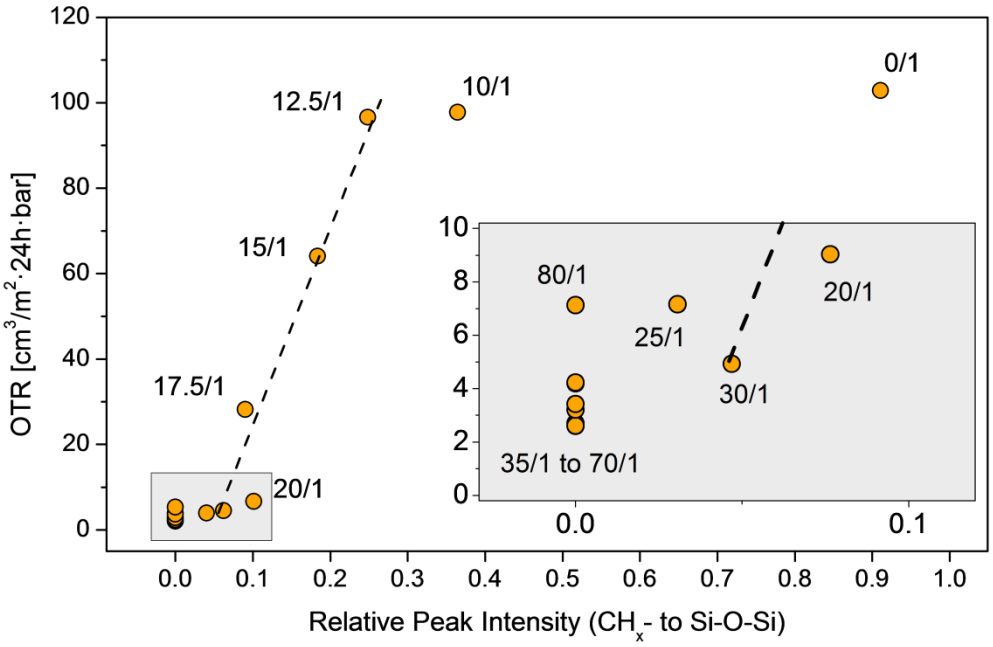

Figure 7.16: OTRs displayed as a function of the intensity of the methyl signal obtained by the IR spectra. The values for each oxygen-to-monomer ratio have been averaged over the single measurements previously displayed in Figure 7.6 and 7.15. In the inset, details for the inorganic films.

The remarks thus far expressed are graphically displayed in the aforementioned Figure 7.16: here, it must be stressed how the trend line displayed for the intermediate oxygen-to-monomer ratios does not result from a linear best fit, but has to be considered only as a visual aid to better highlight the range in which a direct correlation between the reduction in OTRs and IR methyl signals can be observed.

The variation in the barrier properties of the films is shown also by the changes in the permeation curves, as reported in Figure 7.17 for a few significant samples and an uncoated foil: the steady-statue value lowers and it is reached for longer times after the start of the measurement, which for this picture alone has been assumed to coincide with the switching to the oxygen flow.

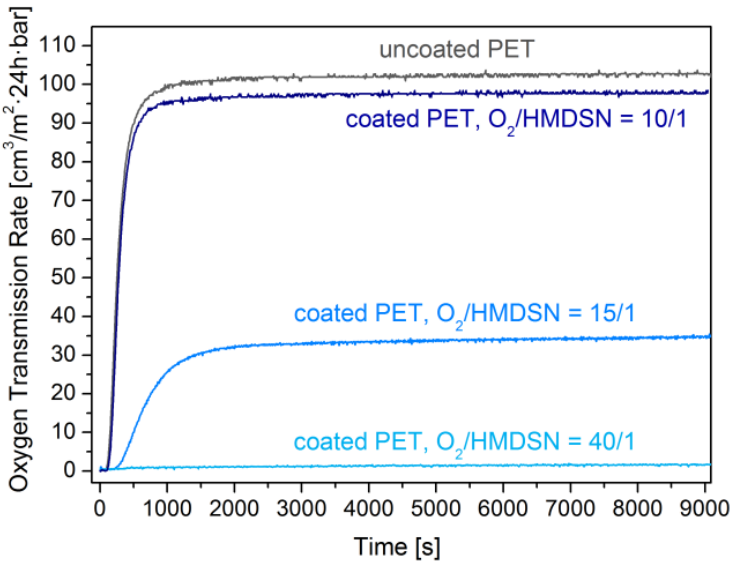

Figure 7.17: Normalized OTRs as a function of time for an uncoated reference foil and an organic film, a transition film and an inorganic film. The curves have been shifted so to assume a null oxygen concentration at the beginning of the measurement.

For a calculation of the diffusion coefficients based on such recorded curves, the assumption to be made is that the permeation process follows a purely Fickian mechanism (see also Chapter 3.2 and 3.5).First, an overall diffusion coefficient – also labelled as D_{TOT} – for the whole system of substrate plus barrier has been calculated: in order to do so, the time values have been corrected by subtracting the known delays caused by the experimental set-up, the latter being described in section 6.4.2. The rise time τ has then been calculated graphically through the method exemplified in Fig. 3.2. Knowing the thicknesses of the deposited barriers and the PET foil, then, the diffusion coefficient has been calculated by means of Eq. 3.17 and 3.27, with D in place of P. The thus calculated diffusion coefficients are displayed, together with the previously shown measured OTRs acting as a reference, in Figure 7.18. The trend for the diffusion coefficient loosely follows

the one previously observed for the OTRs, although with a general increase in the dispersion of its values, especially for very high oxygen fractions in the plasma feed. For the pure HMDSN film and oxygen-to-monomer ratios up to around 17.5/1, the two curves are in good accordance with each other, i.e.in the films in this range, which already showed poor barrier properties, the oxygen permeation chiefly takes place in the homogeneous and porous bulk, following therefore a pure Fickian process. At higher oxygen-to-monomer ratios, the calculated diffusion coefficient presents systematically higher values than the corresponding OTRs, safe for two samples deposited respectively with a 35/1 and a 55/1 plasma feed ratio. Such overestimation shows that the predominant process in the overall permeation for these samples is not Fickian anymore and that, in particular, the rise in the oxygen level is faster than expected.

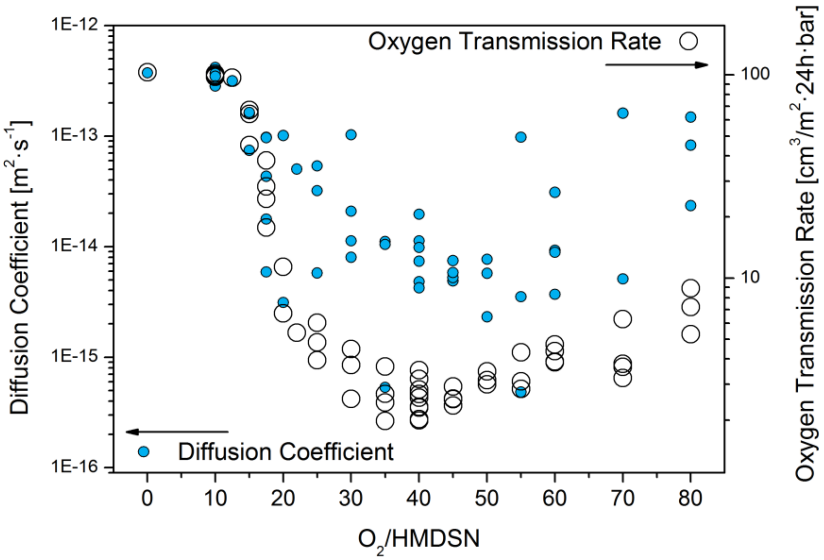

Figure 7.18: Diffusion coefficient of the substrate plus barrier system D_{TOT}, calculated from the recorded permeation curves as a function of the gas feed composition for the thin layer deposition. Left y-axis values displayed as log10. On the right axis, normalized OTRs previously displayed in Figure 7.15 as comparison.

The shape of the concentration curves confirms such assumption, as shown in Figure 7.19. A 10/1 sample shows a clear sigmoidal rising curve, as the system still closely follows a Fickian permeation process. For progressively more inorganic samples with better OTRs, however, the curves show severe asymmetries, with a strong initial rise in the signal followed by a much longer and less steep tail. The transmission curves for these samples can be therefore divided in at least two domains: the first one is ruled by fast-permeating molecules which encounter little resistance to their passage, while in the second one the permeation follows again the Fickian equations, albeit with a much longer rise time thanks to the superior barrier properties of the bulk of

these samples. The first domain may either be due to fractions in the volume of the barrier film with a higher diffusion rate whose permeation however still follows a Fickian regime, or, most likely, to sub-micrometrical defects and pinholes, through which oxygen can permeate almost unhindered. In this case, the initial sudden rise in oxygen concentration is constituted by the overlapping of the single contributions of groups of defects with different average radii. In some case, as for example in some of the curves shown in Fig. 7.19, the lag times of the different contributions are spaced enough for shoulders in the curve to become at least partly visible. The contribution of the defects to the overall permeation seems to become even more preponderant for very high oxygen-to-monomer ratios, as their alleged increased brittleness could cause microcracks to develop in their bulk, in addition to the intrinsic defects already present. As for the samples in the narrow 25/1 – 30/1 ratio interval, where infrared spectra showed small residual presence of organic groups, the discrepancy between OTRs and diffusion coefficient is also caused by the presence of organic domains still obeying Fickian diffusion but with significantly worse barrier performances.

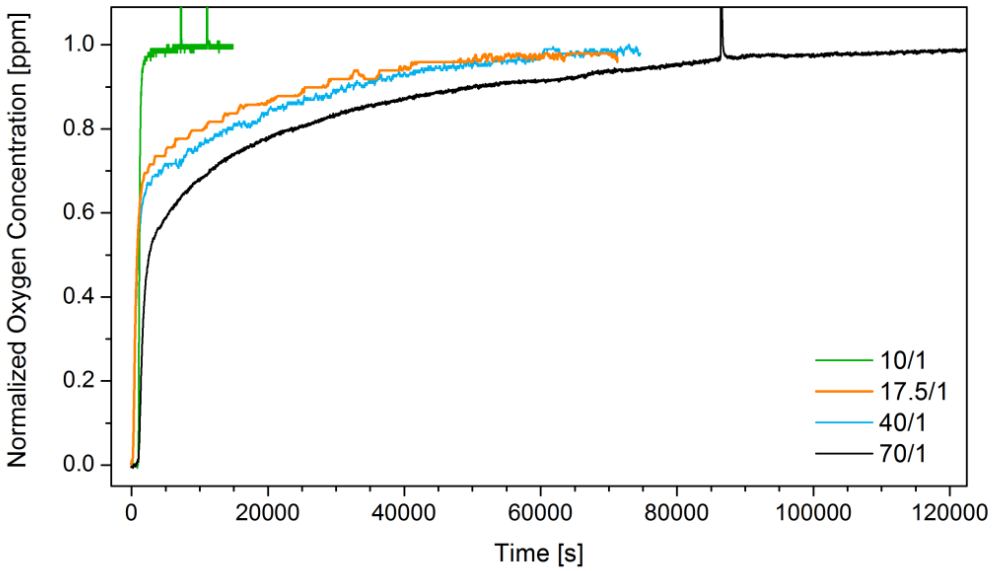

Figure 7.19: Curves of oxygen permeation fluxes versus time for a selection of four coated samples. All curves have been normalized to their final steady-state value. Occasional sudden spikes in the concentration values are caused by the oxygen sensor and bear no lasting effect on the recorded signals.

The thin layers acting as barrier are in almost all cases the limiting factor to the overall permeation in the bilayer, as confirmed by Figure 7.20: in it, the contribution of the barrier films alone (calculated from Equation 3.25, knowing with a good reliability the average diffusion coefficient for uncoated PET) are shown along with the overall diffusion coefficient. As it is possible to

observe, the two sets of values are in good accordance with each other save for the 10/1 samples. As implied in the ideal laminate theory (see also Chapter 3), in fact, when one component in a bilayer possesses much better barrier properties than the other, it becomes the determinant factor in the overall performances of the system: the worse barrier bears no effect on the final transmission rates. As a consequence, the overall diffusion coefficient should correspond to the one calculated for the barrier alone, as it is in this case. Such limiting factor, as shown by Figure 7.18, is in turn controlled by the defects in the barrier.

The discrepancy for the 10/1 oxygen-to-monomer ratio and, to a lesser extent, for all the 'organic' ratios, can be explained so: the calculation for the isolated barrier employ an average reference value for the uncoated PET; as shown however in section 5.2, polymer samples can present fluctuations in their measured OTRs values up to 10%; at the same time, the foil contribution to the overall permeation is *not* negligible when compared to such organic layers. As a consequence, high errors, both negative and positive, may be introduced by the calculations. The uncertainty then progressively abates as the films turn inorganic. The same slight overestimation of the isolated contribution of the barriers returns for the highest oxygen fractions in the plasma feed. In this case, the barriers are less a limiting factor for the overall permeation thanks to their slightly higher OTRs, which are induced by defects at least partly caused by the increased brittleness of such films.

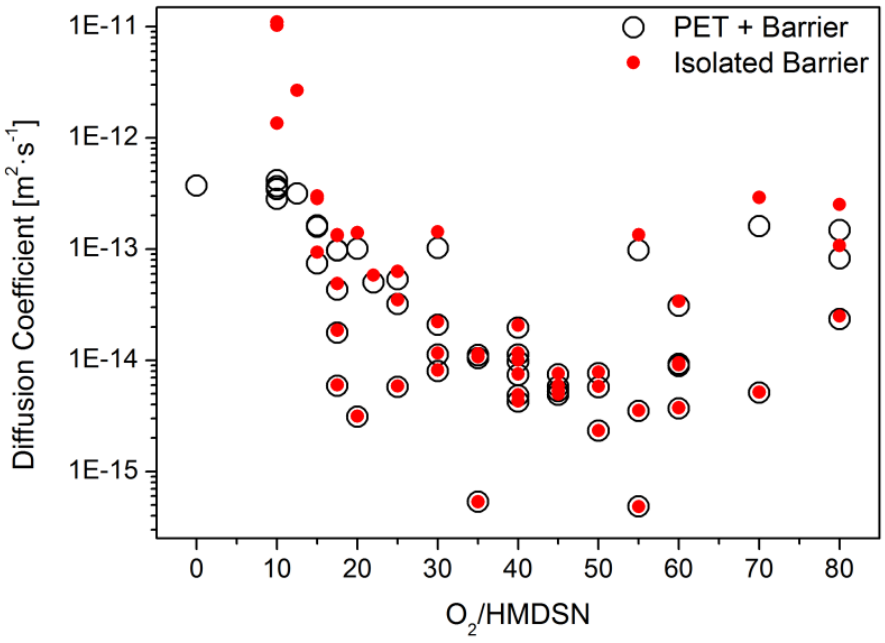

Figure 7.20: Diffusion coefficient as a function of the oxygen-to-monomer ratio in the plasma phase for the bilayer substrate+barrier and for the 100 nm barriers alone. The latter values are calculated by means of the ideal laminate model.

7.1.5 Pinhole test for the barrier films

In a further attempt at investigating their barrier properties, the thin films have then been analyzed by means of the test and the relative procedure illustrated in section 6.5. For each oxygen-to-monomer ratio previously investigated (starting from 10/1), a minimum of three samples, obtained via different discharges, have been thus analyzed. All samples have a thickness of 100 nm. Uncoated PET foils have also been tested in order to act as a reference, provided the test will demonstrate to be valid even for substrates whose permeation is prevalently Fickian. In Figure 7.21, the optical microscope pictures for the uncoated reference and three chosen barriers (with a low, medium and high monomer dilution in plasma phase, respectively) are reported, at the beginning of the test and at its end. The dark spots already visible at the beginning are embedded in the polymeric bulk and are therefore not to be mistaken with the crystals appearing onto the surfaces at a later stage: the height of the latter causes the background to be out of focus, easing their discrimination. For the uncoated polymer and the organic poor barrier it is possible to observe the appearance of numerous crystals evenly scattered on the surfaces, with some of them on the uncoated polymer showing a noticeably 'puffy' appearance. For the best barrier layer, on the other hand, even after one hour of CO_2 permeation very few small, seed-like crystals become visible. For the high dilution sample, finally, an inhomogeneous distribution of crystals is to be observed, with almost crystal-free areas flanking regions with a sudden increase in their crystal density. In the latter case, moreover, such crystals show a remarkable increase in their size, when compared to those for the 40/1 mixture ratio. A selection of investigated samples has been then observed by means of scanning electron microscopy, particularly in the same areas monitored in real time during the pinhole test. Examples of the observed crystals are provided in Figure 7.22, and an overview of the different shapes and sizes for the uncoated PET and the three aforementioned oxygen-to-monomer ratios in Figures 7.23, 7.24, 7.25 and 7.26, respectively.

The uncoated foil presents a thick coverage of crystals with radii between 5 and 10 microns. Most of them show the typical appearance of spherulites, but star- and cross-like shapes are also present, together with polycrystalline bundles resembling spherulite precursors (similar to those shown in Fig. 6.15. The spherulite-like crystallites, in particular, show thick lamellae growing from an initial bulky core and closely resemble calcite aggregates of similar size reported in literature [192, 220].

For an organic film with poor barrier performances, as the 10/1, the same kind of crystals are still to be observed: bulky spiked structures, sometimes perhaps twinned, showing the macroscopic habit of calcite, together with spherical aggregates which, in this case, exhibit fine acicular structures rather than lamellae. The anomalous appearance of the crystal in the lower right corner of Figure 7.24 is probably due to the crystal breaking off at the center of the initial seed, likely during the sample handling and preparation, leaving only its lower segment facing upward.

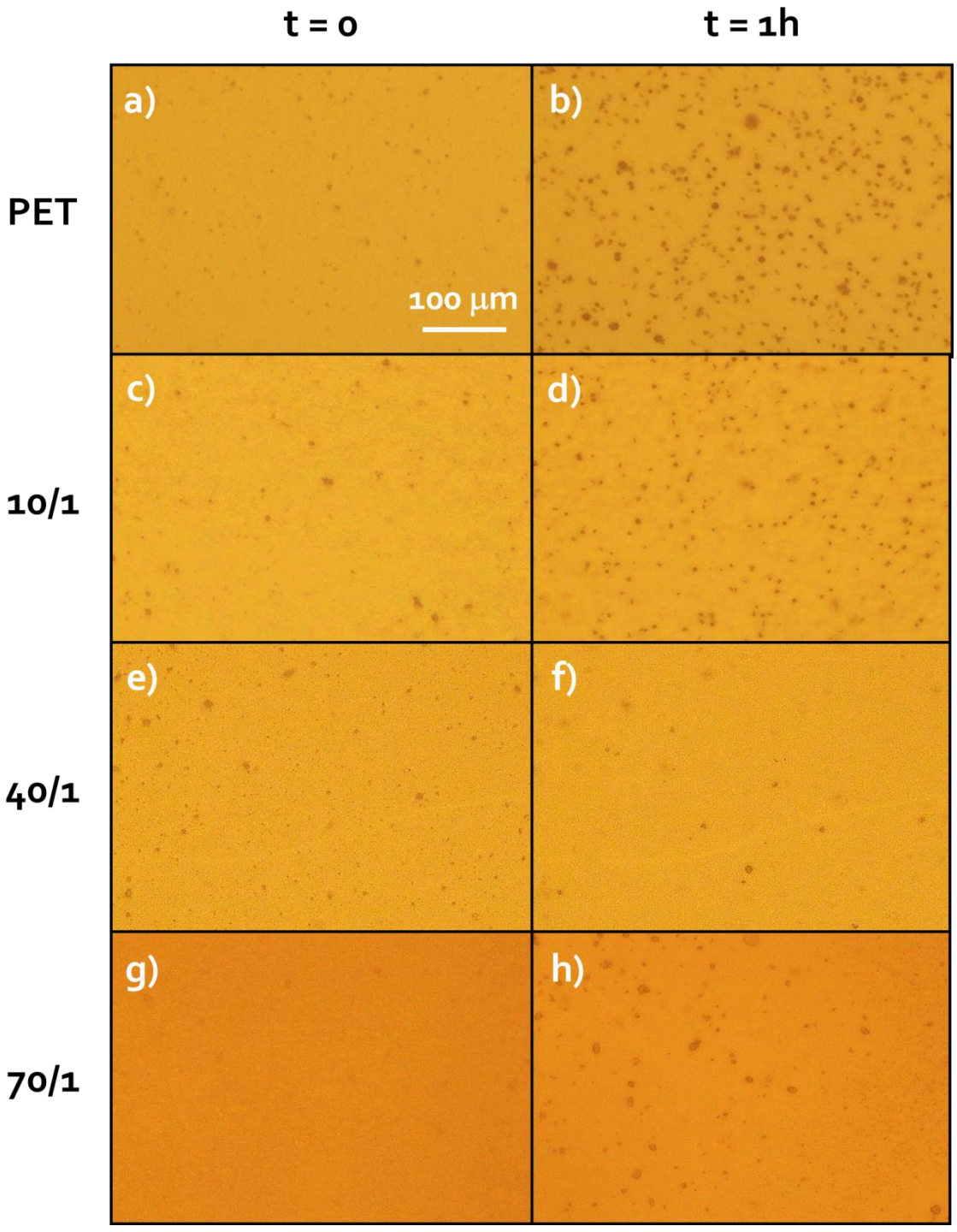

Figure 7.21: Details of optical microscope pictures with a x10 magnification of the surfaces of uncoated PET (a and b), an organic 10/1 film (c and d), and two inorganic films, 40/1 (e and f) and 70/1 (g and h), at the beginning of the test (a, c, e and g) and after one hour (b, d, f and h).

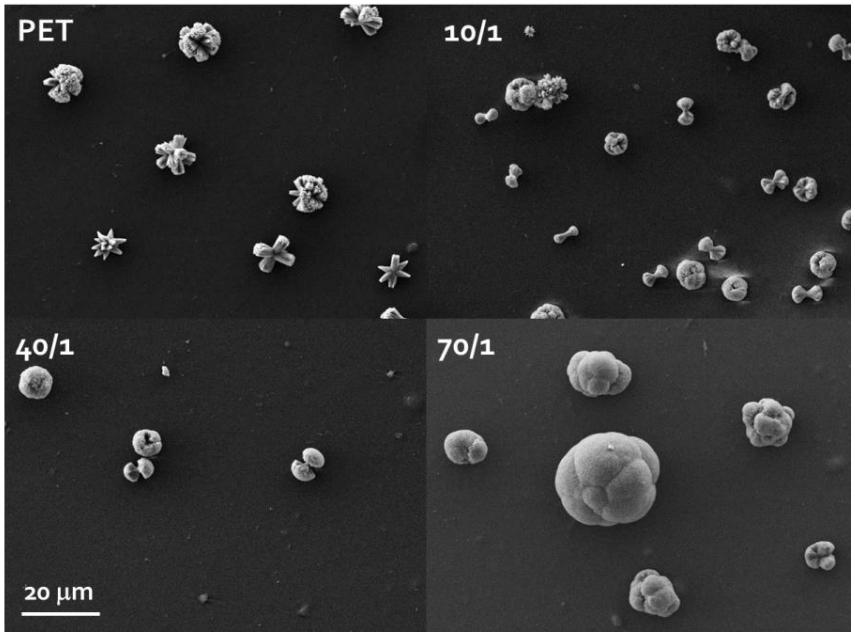

Figure 7.22: SEM pictures of the calcium carbonate crystals formed on the surface of the uncoated polymer reference and for three 100 nm thick barriers with different oxygen-to-monomer ratios.

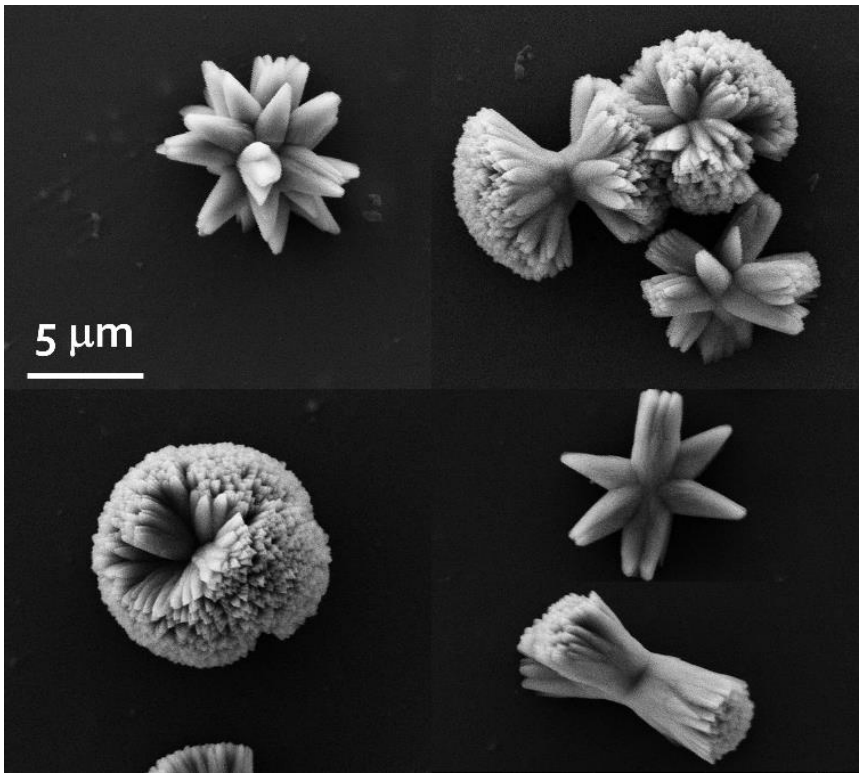

Figure 7.23: Overview of $CaCO_3$ crystals after one hour of test found on the surface of uncoated PET foil.

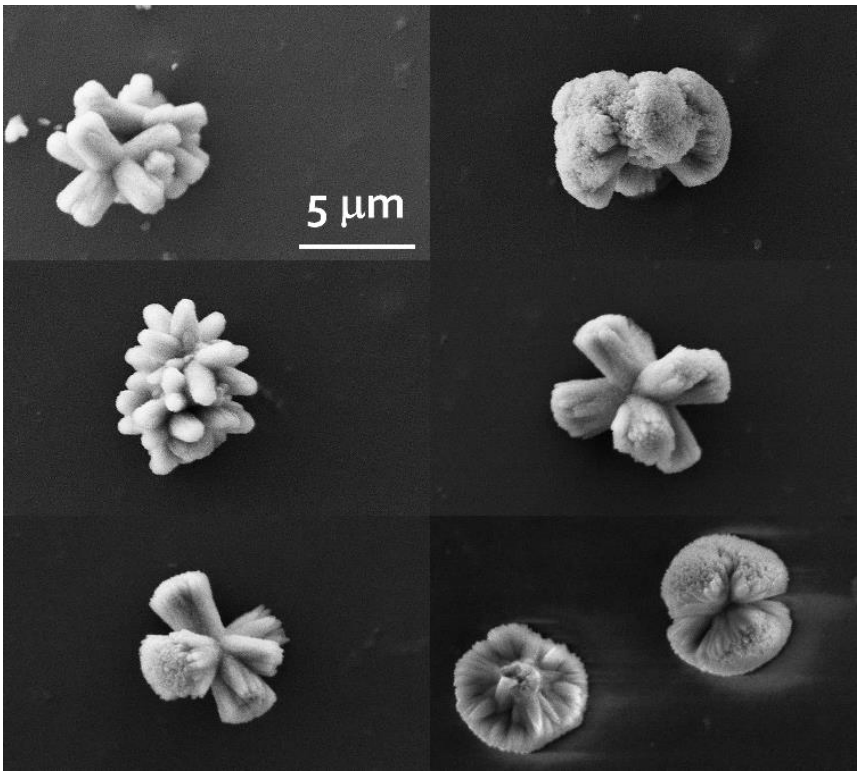

Figure 7.24: Overview of $CaCO_3$ crystals after one hour of test found on the surface of a thin film deposited with a 10/1 oxygen-to-monomer ratio (organic composition, poor barrier properties).

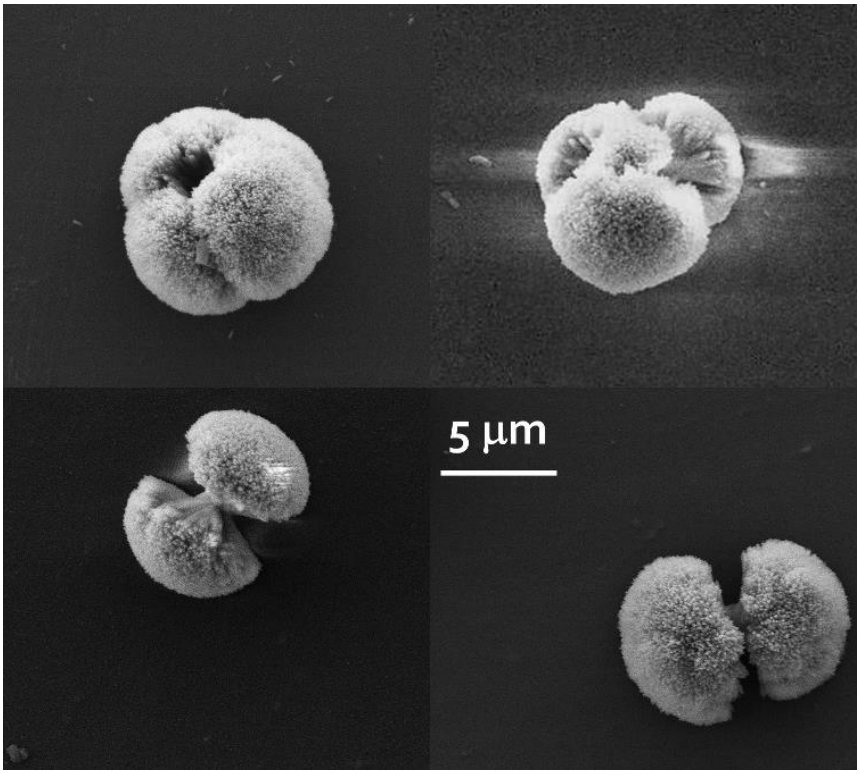

Figure 7.25: Overview of $CaCO_3$ crystals found on the surface of a thin film 100 nm thick and deposited with a 40/1 oxygen-to-monomer ratio (inorganic composition, good barrier properties).

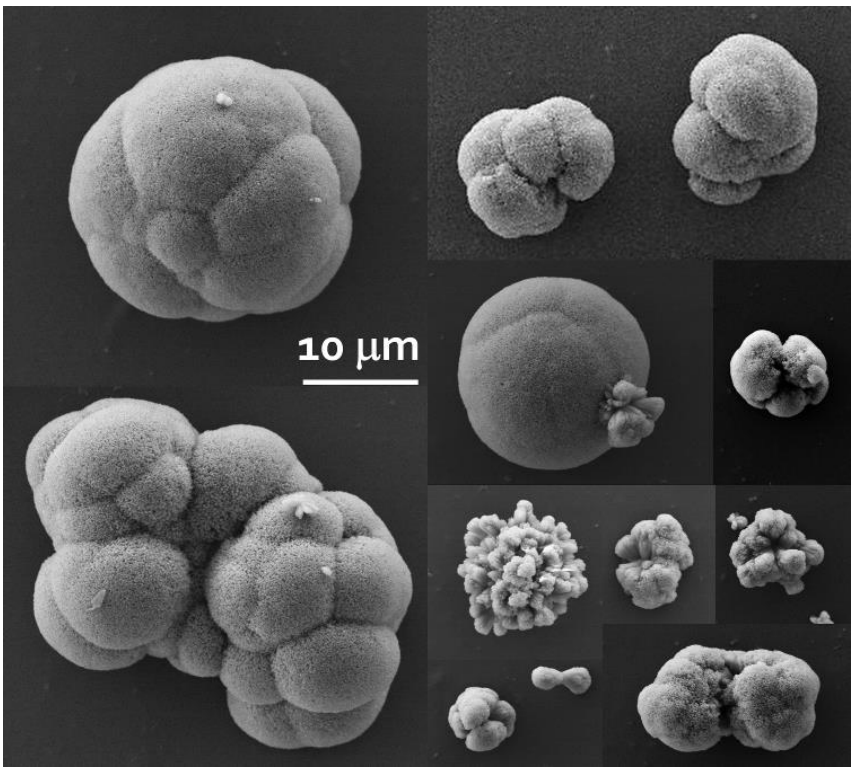

Figure 7.26: Overview of $CaCO_3$ crystals after one hour of test found on the surface of a thin film with a thickness of 100 nm and deposited with a 70/1 oxygen-to-monomer ratio (inorganic composition, good barrier properties).

As the film turns inorganic with higher oxygen content in the plasma phase, only sparse spherulites and dumbbells are to be found on the surface (Fig. 7.25), some still showing clearly the two lobes, others almost completely closed. The size of these crystals is not significantly smaller than those observed on uncoated PET, but their needles are now so thin to be easily broken even during the careful handling of the samples. In the top left corner of Fig. 7.25, in particular, it is possible to observe some of the broken fragments lying scattered on the area surrounding the main crystal. It can be therefore assumed that such crystals originate from smaller quantities of reagents (i.e., smaller quantities of carbon dioxide, as the lime water solutions have always been prepared with a saturation concentration) than those on poor barriers. The assumption that the dimensions of the crystals depend solely on their nucleation time, or on the properties of the alleged underlying defects, however, is not so straightforward (see also further in the current section).

For the highest monomer dilution, finally, inhomogeneities are not only present in the crystals distribution, but also in their shape and size, as shown in Figure 7.26: crystals with radii comparable to those observed for the previous samples are accompanied by others almost an order of magnitude larger; deformed and irregular spherulites are still present, but crystals are mostly

irregularly shaped lumps or completely closed spheres with faint radial and equatorial lines. In at least one case, such spheres present an outer burst of matter from one of their sides. As already noticed in real time through the optical observation, the biggest crystals are moreover surrounded by circles of smaller lumpy aggregates. While it is difficult to discern what the original shape of such irregular crystals may have been, it is safe to assume that the biggest crystals are the end phase of the growth process of sheaf-of-wheat aggregates, with the equatorial lines indicating where their lobes conjoined. Such bigger aggregates are to be found only in the relatively 'crystal-rich' areas of the surface, although their distribution remains completely random. A possible explanation for such increase in crystal size may be that the bulk of such highly inorganic barriers is practically impenetrable to the O_2 and CO_2 molecules: these therefore, after permeating quickly through the polymer substrate, are blocked at the interface with the barrier and start to diffuse along it. They can finally reach the solution only when they encounter a pinhole extending along the whole barrier thickness; in this case, therefore, the defects act as funnel, collecting the permeated particles from a large fraction of the defect-free bulk surrounding them. In the case of the pinhole test, then, a much higher supersaturation is achieved, resulting in bigger reaction products. More generally, the size of the precipitated crystals cannot be correlated with the size of the underlying defects. It has actually been observed at the optical microscope how crystals forming at later stages are also bigger, on average. This can be explained not only through the aforementioned funnel effect, but also by taking into consideration how, for longer times, the reagents concentration in the aqueous solution slowly increases, either by small CO_2 amounts diffusing through the bulk of the barrier or by continued diffusion through the defects, thus producing bigger crystals when a precipitation process starts locally on the defect. Such progressive increase in the reagents concentration, self-evidently, never reaches values able to trigger a nucleation step at random spots on the sample surface, however.

During the SEM inspections, by comparing the scanned frames to the optical microscope pictures referring to the same areas, it has been possible sometimes to notice small displacements of the crystals, which otherwise often remain firmly stuck on the surface. Closer observations allowed to find upturned or broken crystals and to observe their bottom side, as shown in Figure 7.27: on the left, a crystal broke off near its base, rolled on the metallized surface, scratching it in the process (the white haze on darker background) and lied upturned. Here, the acicular spherulite seems to grow out of a non-descript, squat, denser $CaCO_3$ base. The lower stump shows a fine radial structure growing out of a thin, black, possibly hollow slit: the same drop-shaped duct can be observed on the crystal upper segment. It can therefore be speculated that such channel lies directly on top of the defect in the barrier layer, and because of the small but steady CO_2 flow bubbling through it, it remains open while the crystal grows around it. Such assumption would not only confirm that the crystals do indeed grow on top of defects, but could also explain the morphologies of other almost closed spherulites, like for example the one in the lower left corner of Fig. 7.23 and the one in the upper left corner of Fig. 7.25, presenting opening

in their surfaces. The latter would then be the outlets of the CO_2 that keeps permeating through the defects.

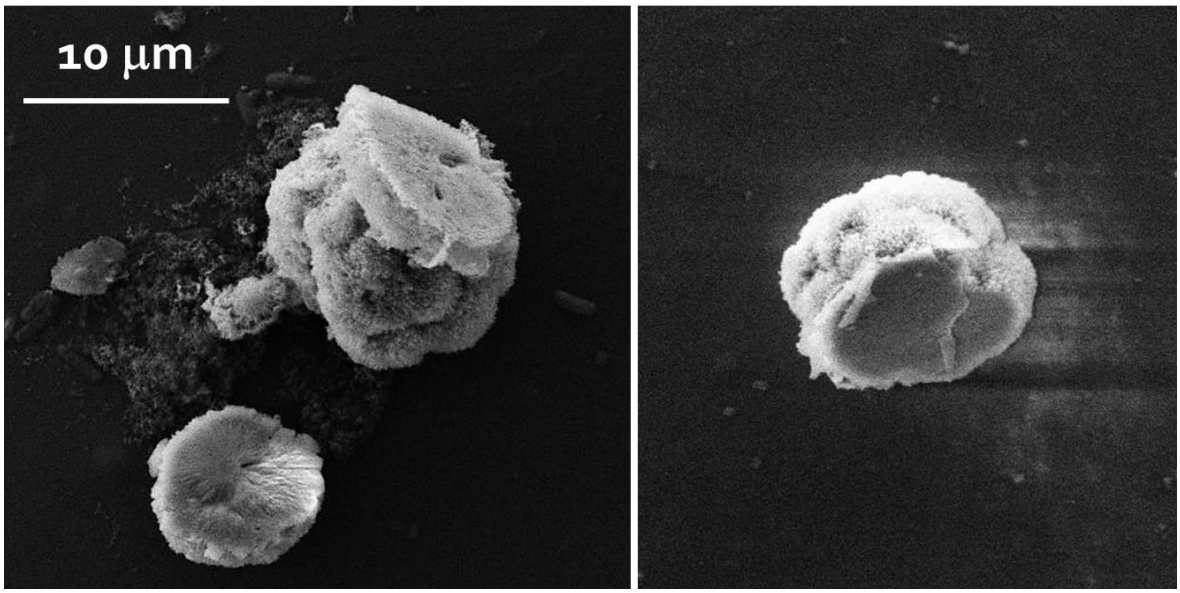

Figure 7.27: Details at the scanning electron microscope of crystals upturned or displaced during the sample handling after the pinhole test (for the left crystal, most likely after the metallization step, too).

The crystal on the right in Fig. 7.27, instead, presents a perfectly flat bottom: observation of its surrounding area could not find a 'base', nor scratches or other surface damages that would hint at the crystal being truncated. It has therefore been assumed that such crystal remained intact during its detaching from the surface: as a consequence, its bottom side lied directly in contact with the barrier surface. The lack of dents, hollows or embedded particles shows how this particular crystal did not grow around dust particles or other nucleation seeds. Moreover, a flat cleft is visible, probably the junction where the two halves of the crystal merged together. Such cleft can be assumed to have been lying on a defect and to have served as vent for the permeated carbon dioxide molecules.

Such scarce, non-systematic evidence cannot however be enough to unquestionably conclude that such crystals grow exclusively on defects. In order to do so, the following procedure has been carried out for 40/1 and 70/1 oxygen-to-monomer ratio samples:

i) the thin films have been deposited via PECVD;
ii) their barrier properties have been tested a first time in the System II permeation setup;
iii) the pinhole test has been carried out;
iv) the samples have been cleaned in the same way illustrated in section 6.5.3, leaving the

crystals on their surfaces;

v) the barrier properties have been tested again in the same permeation setup.

By assuming that the crystals grow on defects, a more or less pronounced reduction in the samples' oxygen transmission rates has to be expected, as for good barrier layers permeation takes place predominantly or almost exclusively through the latter. The results confirming it are reported in Figure 7.28.

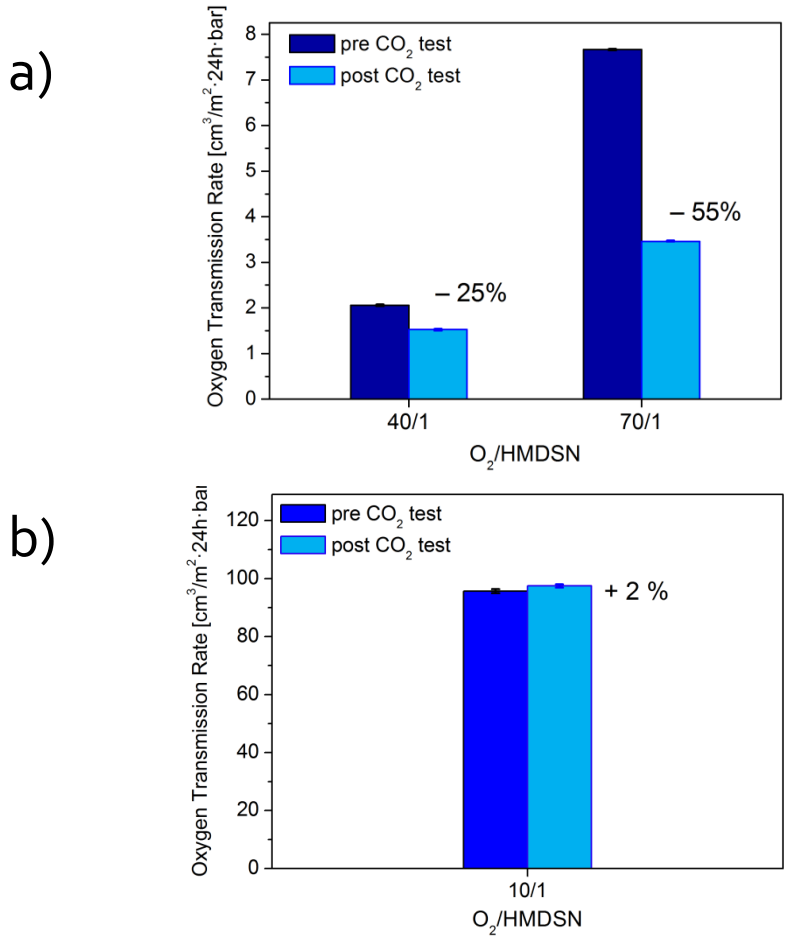

Figure 7.28: OTRs before and after the pinhole test for 100 nm thick films acting as inorganic barriers (a), and for a film of the same thickness but with an organic chemistry and poor barrier properties (b).

It must be noted, however, that the percent reductions here shown cannot be taken as a direct quantification of the contribution of the pinholes to the overall oxygen transmission rates; the analysis can only be qualitative, for the following reasons:

- it cannot be assumed that all crystals effectively and/or completely clog the underlying

defects;
- the repeated handling of the samples may cause some of them to detach or break, as already observed at the SEM, nullifying their clogging effect;
- the protracted handling can also induce surface damaging on the barrier, like scratching or microscopic cracks, that artificially increase the OTRs of the second round of measurements.

Such results can nonetheless not only confirm the growth of crystals on defects, but also elucidate some puzzling aspect of the observed precipitation process, like the presence of a single, relatively short-lived nucleation step and the very slow growth of the already existing crystals even after several hours: in most laboratory precipitation studies, in fact, the crystal growth for saturated solutions is linear [187] and can last for weeks [192], provided the liquid matrix is stable enough, with multiple and much longer nucleation phases [220]. In the current case, given the peculiarity of the experimental conditions, a comparison with previous studies is not immediately straightforward. With the crystals forming on top of the defects – i.e. the source of CO_2 in the aqueous solution –, the former act effectively as a clog, reducing the latter's permeation. As a consequence, the local oversaturation never reaches values high enough to trigger a second nucleation phase again, and severely limits the growth of the already existing crystals. The scarcity of carbonate species in the remaining volume of the solution, on the other hand, completely prevents further formation of aggregates on random, defect-free areas on the surface. These assumptions however only hold true if the main contribution to the permeation comes through the pinholes, i.e. when the Fickian permeation is negligible. Such cannot be the case for the uncoated substrate and for the organic poor barrier, as shown previously and in particular by the permeation curves in Section 7.1.4. In this case, more complex precipitation mechanisms must take place, and the precipitation of crystals on top of defects cannot be a given. The attempts of the previous analysis on the 10/1 oxygen-to-monomer ratio samples resulted not only in no reduction of their OTRs, but even in higher final values, as shown in Figure 7.28 b. The latter effect is probably caused by mishandling of the coated foils, and therefore undermines the validity of such results. Nevertheless, they act as a partial confirmation of what previously discussed about the diffusion mechanisms in poor organic barriers.

Further informations about the limits of applicability of the pinhole test are provided by the crystal number vs. time curves: the number of crystal refers to a fixed area ($5.59 \cdot 10^{-3}$ cm^2) on the investigated surface, with one real-time analysis possible for each sample. The results, for a selection of samples deposited with different oxygen-to-monomer ratios, are reported in Figure 7.29: the shape of the curves resembles those obtained for the real-time permeation of oxygen, with the delay time before the onset shifted to much lower values thanks to the higher permeability of CO_2. It is safe to assume that the first crystals to appear are those lying on the biggest or most permeable defects, as locally the CO_2 flux is at its maximum. A very high number of crystals

precipitate for lower oxygen-to-monomer ratios, with a wide dispersion for repeated tests. The progressive oxidation of the deposited films with higher dilution in the plasma feed causes a strong decrease in their number, with the latter stabilizing already around 25/1 gas feed ratios.

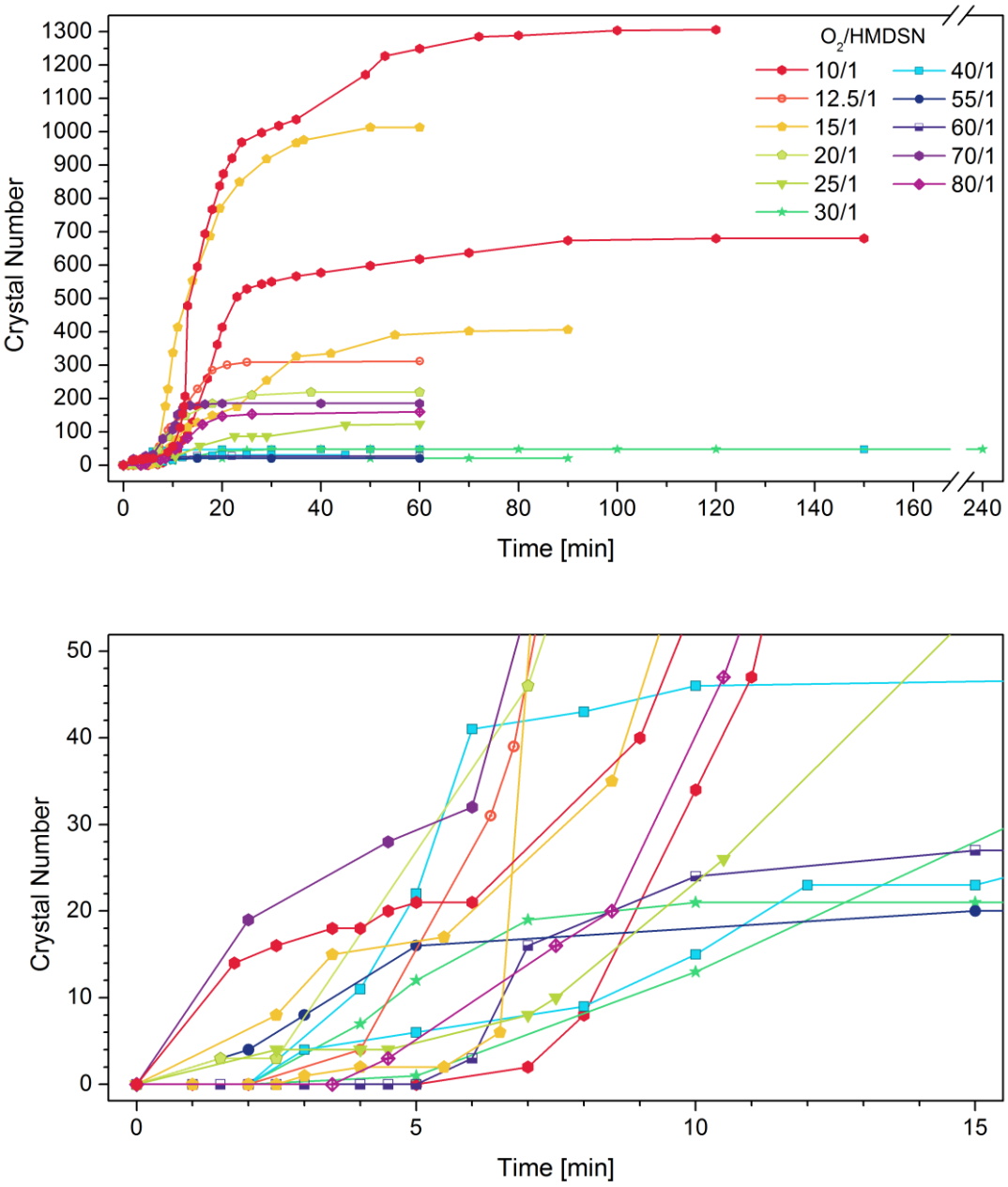

Figure 7.29: $CaCO_3$ crystals number in a fixed frame of the investigated barrier surface as a function of time. t = 0 is set for the beginning of the pinhole test as described in section 6.5.3 (top). Bottom: detail of the first minutes of the test run.

In some cases, the tests have been prolonged well beyond the standard 60 minutes, in order to investigate the possibility of a second, very late nucleation phase: such is not the case for good barriers, with their number of defects remaining stable even after 4 hours of ongoing test. For such samples, after 15 minutes the precipitation process is already over and no further variations, apart from a very weak growth of the crystals, take place. For the organic layers with poor barrier properties, on the other hand, several further steps are noticeable along the curve at later times. For the 10/1 samples in particular it is possible to observe the precipitation of new crystals well after the 90 minutes mark. This can be explained as follows: as the Fickian permeation through the bulk of the thin film is non-negligible, over time a high concentration of nano-scaled precursor of the calcium carbonate crystals can be reached in the lime water solution, suitable to trigger a nucleation phase which would not be limited to the immediate proximity of the barrier defects. The number of crystals in this case is still dependent on the amount of $[CO_2^*]$ in solution and more generally on the barrier properties of the films, but their location loses meaningfulness.

The final defects densities (assuming that each crystal corresponds to a defect), calculated as described in section 6.5.3, versus the oxygen-to-monomer ratio are reported in Figure 7.30.

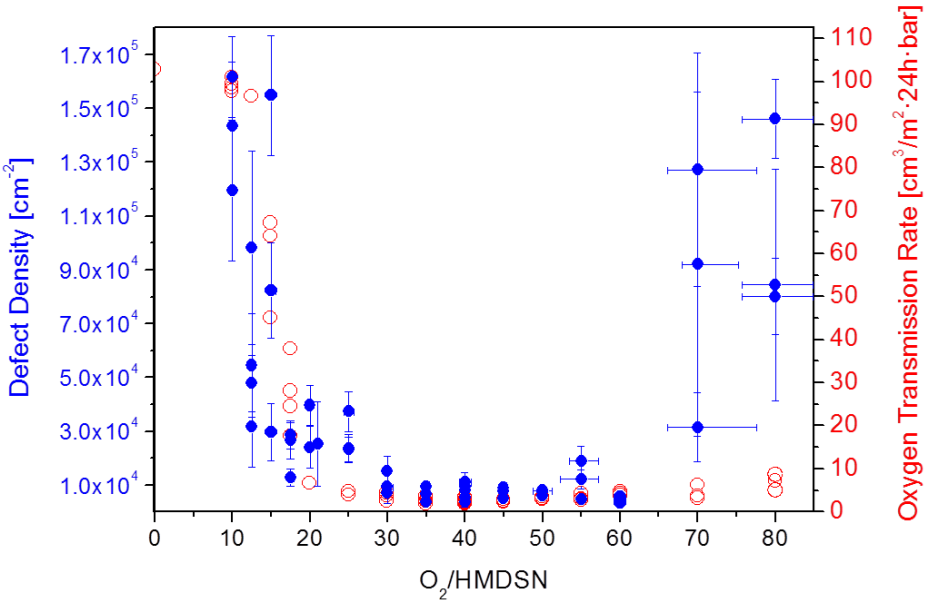

Figure 7.30: Numerical defect density for 100 nm barrier layers as a function of the oxygen-to-monomer ratio in the plasma feed (left), and OTRs for the same ratios, from Fig. 7.13 (right), for comparison.

The vertical error bars are the standard deviations associated to the average densities for each tested sample. The OTRs have been already presented and discussed in section 7.1.4 and are here reported for comparison. The curves are in good accordance with the sharp decrease

roughly coincident with the 15/1 ratio. The defect density then stabilizes to a minimum until 60/1 (coincident with the range where the best barriers are obtained), then increases sharply and with much wider associated standard deviations. The standard deviations for the organic layers, while high in absolute values, are not however proportionally much higher than those associated to the 30/1 to 60/1 range, as the crystal distribution for both types of films remains fairly homogeneous throughout the whole investigated area. The lowest defect densities are in good accord with the values found in literature and calculated by means of other tests, in particular with the results obtained by da Silva Sobrinho *et al.* reported in Table 6.2: in this case in fact even the corresponding OTRs fall in the same range. While, as mentioned before, the current pinhole test may not be strictly applicable to Fickian barriers, it is however still worth mentioning that the ratio between the highest (for 10/1) and lowest (for 40/1) defect densities, equal to about 43, is in very good accord with their corresponding BiFs, which show a ratio equal to almost 45.

As for very high oxygen-to-monomer ratios, however, as shown in Figure 7.30, high fluctuations in their distribution are to be observed, probably because of structural differences on different zones of the barriers. The rise in the average densities for such ratios is much higher than the relatively small increase observed in OTRs. Such phenomenon highlight a disadvantage of such test, when compared to other methods, in particular with the oxygen plasma etching described in Section 6.5.1. The current test provides only the numerical densities of defects, but says nothing on their size or on the amount of gas permeating through them. As discussed before, the size of the crystals gives no further indication on the subject, and the time of their precipitation only qualitative information. As a consequence, it is possible for a barrier film to possess numerous albeit very small defects, and for the total gas volume permeating through them to remain low. For such oxygen-to-monomer ratios, the test only allows to strengthen the assumption that, despite the identical chemical composition, morphological differences exist when compared to the 40/1 samples, mostly ascribable to an increased brittleness of the films.

Whatever causes the crystal aggregation on certain spot on the surface of uncoated PET, as for example local roughness or external particles acting as crystallization seed, they do not seem to be the main cause for the formation of defects in the subsequently deposited barrier layer. This has been ascertained by subjecting uncoated samples to the pinhole test, washing them and removing the crystals with a soft brush afterwards, coating them with 100 nm of the best barrier layer and finally repeating the test. The pictures taken during the first and second run have then been compared, in order to verify the superimposition of the new crystals over the old ones. One example of such test is shown in Figure 7.31: in this case, while pouring lime water from the pipette, a calcium carbonate flake ended up on the surface, hence the dark large spot visible in the second picture. In the white circles the superimposable crystals, which constitute only a small fraction of the total. It is also worthy to notice that, as detailed before, large crystals on uncoated PET do not equate to eventual large underlying defects: were it the case, the subsequent barrier films would exhibits defects on the same location or in the immediate surrounding area.

It must be stressed that such kind of repeated testing of the same surface introduces several errors, as the prolonged handling of the sample and the mechanical removal of the crystals may either increase the number of third bodies on the surface or damage the latter. This happens to be the case, as the crystal densities for barrier films deposited on such samples have always been found to be slightly higher than usual. For further considerations about the surface morphology of the substrate acting as source of defects in the barrier layers, see also section 7.4.2.

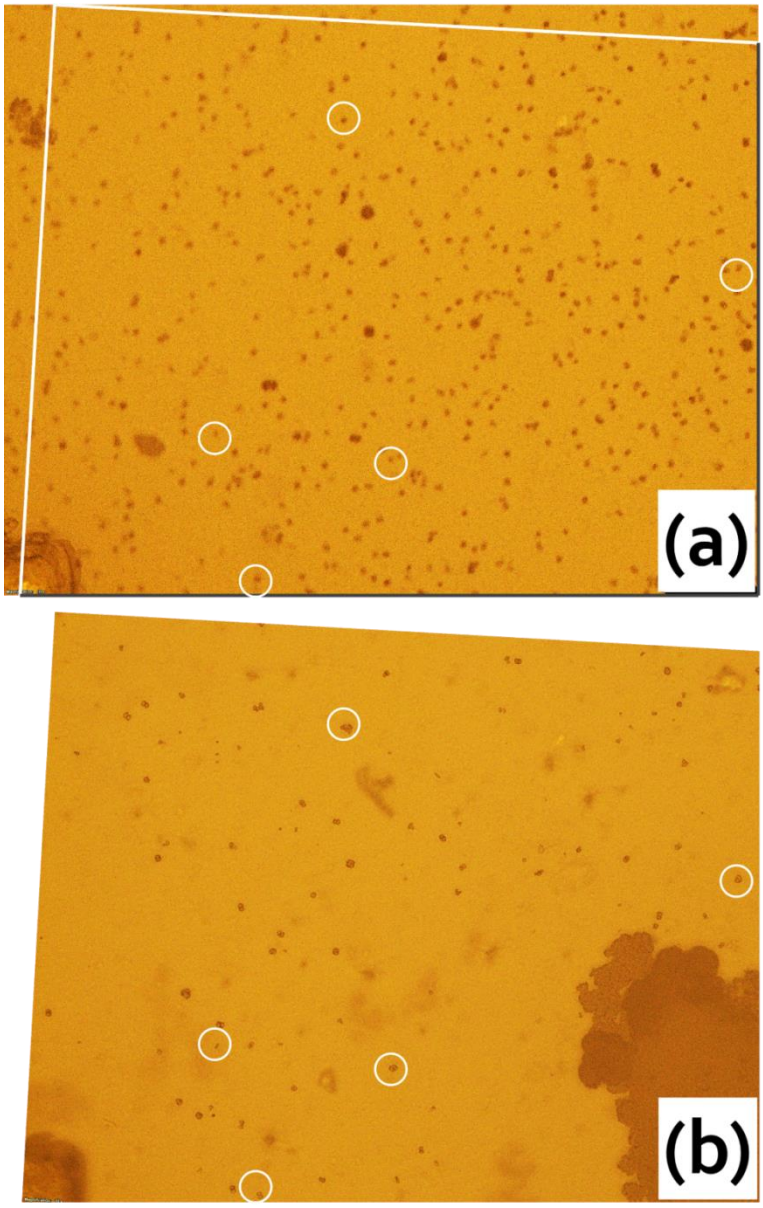

Figure 7.31: Uncoated PET sample after 1 h of pinhole test (a), and the same PET sample after being coated with 100 nm of a 40/1 barrier film and subjected to a second run of the test (b). The quadrilateral in (a) corresponds to the area shown in (b). In the white circles, superimposable crystals.

7.1.6 Effect of temperature on permeation curves and diffusion coefficients

The effect of temperature on the barrier properties of the thin films, as a way to decouple or at least clarify the contribution of their defects to their overall transmission rates, has been investigated by subjecting the same sample to permeation measurements, following the same protocol reported in Section 6.4.1, performed at different temperatures in the room temperature to 60 °C range. The upper limit is still sufficiently far away from the glass transition temperature for PET, equal to 80 °C [114], to avoid a completely different permeation process in the now viscous substrate [25]. Only a selection of samples has been investigated: an uncoated foil, to act as a reference, a poor organic barrier (10/1 oxygen-to-monomer ratio) and two inorganic films with different morphologies and similar barrier performances (40/1 and 70/1, respectively). The Arrhenius-like plots obtained from the experimental data will provide a calculation of the activation energy of the process, according to what detailed in Section 3.4. The steady-state flux corresponds in this case to the experimentally obtained oxygen transmission rate.

As polymeric materials and amorphous silica-like films possess different thermal expansion coefficients, the differential expansion may develop stress-relief cracking [27, 31] midway during the analysis, thus invalidating it. In order to exclude such eventuality, after the first run of tests on a substrate plus barrier system, during which the highest temperatures had been reached, the sample was tested again at the standard value of 35 °C. The consequent normalized OTR, reported in Figure 7.32, shows only a minor discrepancy with the first measurement at the same conditions, around 3 %, compatible with the analysis intrinsic reproducibility limits.

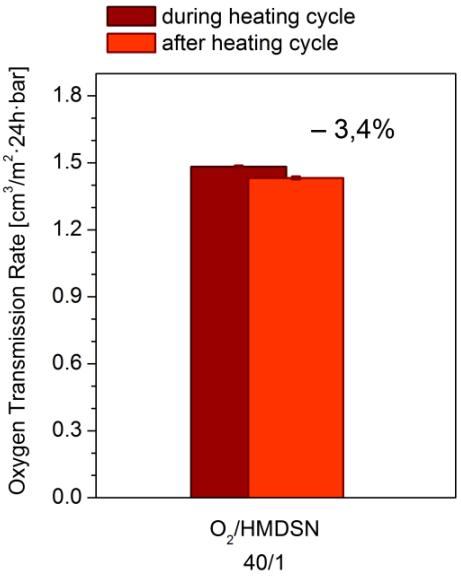

Figure 7.32: OTRs measured at 35 °C for a 100 nm thick barrier with an oxygen-to-monomer ratio of 40/1, with the second value being recorded after the sample has been heated up to 60 °C.

The oxygen transmission rates as a function of the temperature thus calculated are reported in Figure 7.33 for all the investigated samples: such data will be the foundation on which all subsequent analyses will be based. The greater horizontal errors associated with lower temperatures are caused by the stability limits of the thermostats. Eventual analyses at even lower temperatures would therefore require the use of water coolers or chillers. As foreseeable, the increase in the transmission rates is much smaller for the two good barriers, while the organic film closely follows the uncoated foil trend, with its OTR rising almost four times in the investigated range.

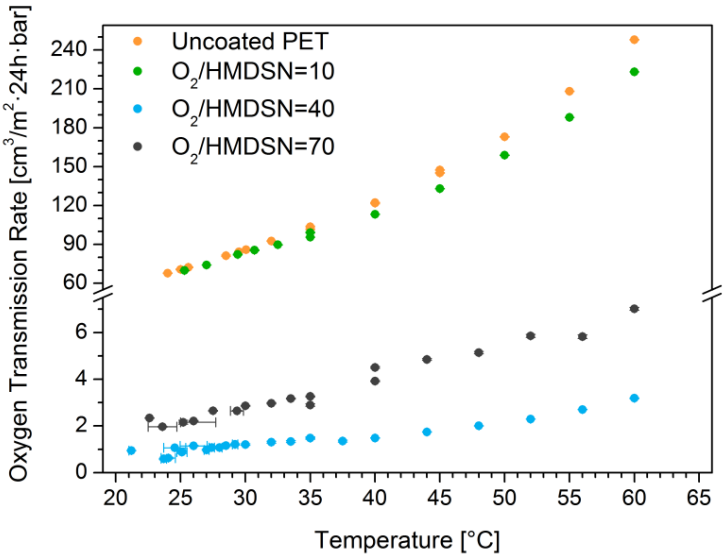

Figure 7.33: OTRs as a function of the temperature for 100 nm thick coatings with different chemical compositions and barrier properties and for the uncoated substrate for reference.

As the uncoated reference value have not been measured for all the investigated temperatures, particularly in the case of the runs for the two inorganic barriers, a fitting of the uncoated PET data alone has been necessary, before calculating the correlated BIFs. The fitting has been performed by means of an Arrhenius-like equation with an eventual non-null intercept to account for experimental errors. Such equation and the related fit are reported in Figure 7.34. It is possible to observe through the good R^2 value how well the permeation through the PET foil fits a purely Arrhenius behavior, despite its mixed amorphous/crystalline nature. The fitting equation allows then to retrieve the missing reference values for the substrate through interpolation. The thus calculated barrier improvement factors are reported in Figure 7.35.

The organic 10/1 film shows almost constant BIFs never higher than 1.1. The 40/1 barrier shows the best BiFs but, contrary to the 70/1 case, the values of which remain fairly constant throughout the investigated range, a sharp increase is registered starting around 35 °C. For lower temperatures, the apparent BIFs are around one third lower and with a much higher dispersion,

even for repeated measurements. This can be caused in the first place by the errors becoming bigger when compared to the measured signal, which in the low temperature range decreases significantly, even when employing the bigger sample-holding cell. A further, more likely explanation for such stark change will be given at a later stage in the current section.

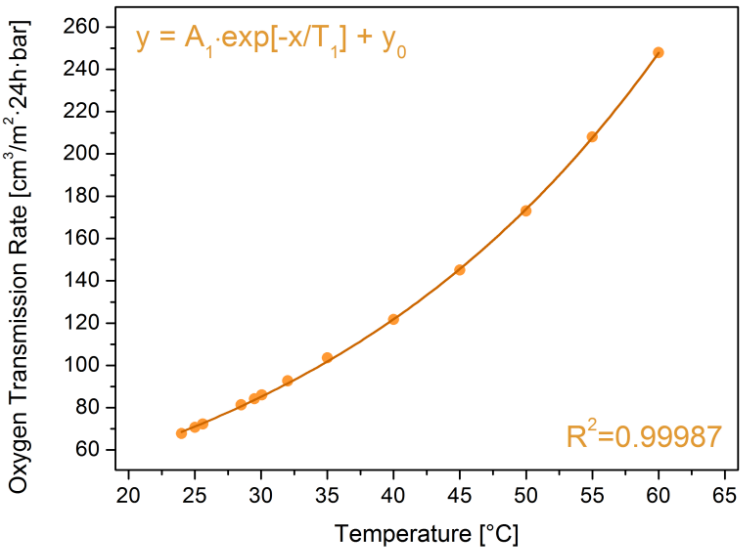

Figure 7.34: Fit of the uncoated PET data with an Arrhenius-like equation (shown in the upper left corner). The corresponding coefficient of determination is also reported.

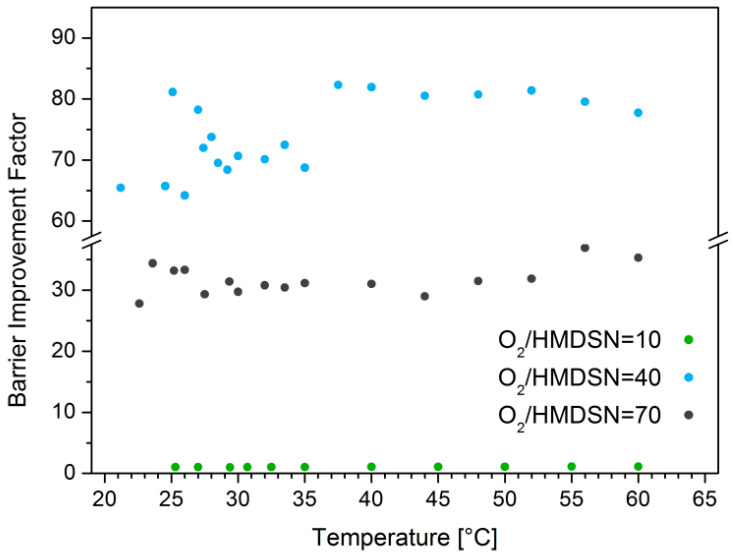

Figure 7.35: Barrier improvement factors as a function of the temperature for the three investigated thin films.

The isolated contributions of the barriers have been subsequently calculated, by means of Eq. 3.25 reported first in Section 3.3, i.e. assuming homogeneous laminated structures, which has been already proven not to be the current case. The calculated values are in good agreement with the simplified Eq.3.24 for layers with different permeabilities in the case of the 40/1 and 70/1 oxygen-to-monomer ratio, as it would have been expected, but severely differ in the case of the 10/1 sample. In the first case, the error never exceeded 1.5 % for the 40/1 sample and 3.5 % for the 70/1. The further reduced Eq. 3.26 and 3.27 version of the ideal laminate theory have also been tried, in order to calculate the isolated barrier contributions first, and then the respective activation energies, but, in addition to the high errors associated, the values obtained bore no meaningfulness and have thus been not taken into account in the further discussion.

The results for the isolated contributions of the thin films are reported in Figure 7.36 and their associated relative variations are shown in Figure 7.37. The latter values have been thus calculated:

$$Relative\ variation = \frac{OTR_{TOT} - OTR_{single\ barrier}}{OTR_{TOT}}. \tag{7.1}$$

The latter graph also includes a legend to elucidate how to interpret a box-and-whisker chart.

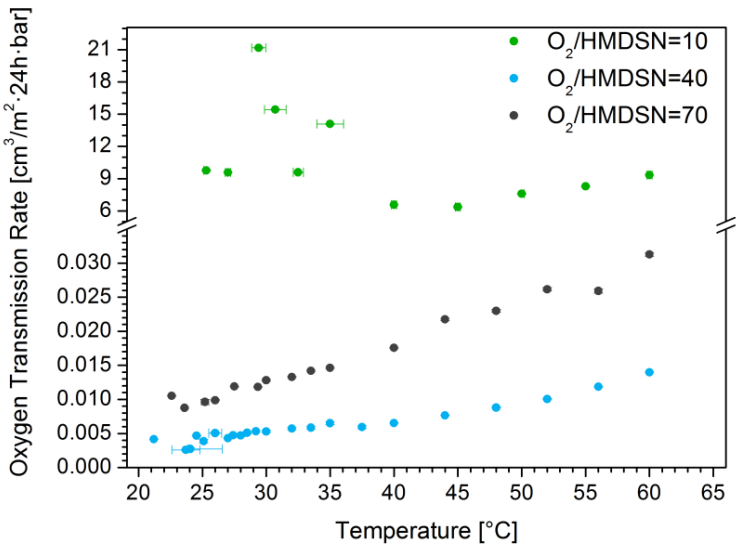

Figure 7.36: Oxygen transmission rates of the isolated barrier films, calculated by means of the ideal laminate theory, as a function of the temperature.

Fig. 7.36 shows, for the inorganic films, the same trends observed in Fig. 7.33 and still very low transmission rates, so much that the values are negligible when compared to the overall substrate plus barrier system. For the 10/1 film, on the other hand, the isolated values are several or-

ders of magnitude higher and show a strong dispersion at low temperatures, again highlighting the poor barrier properties of such porous, although homogeneous, films. The fluctuations are particularly stressed at low temperatures, for the same reasons that introduced high errors in the calculation of the diffusion coefficients for the organic barriers alone in section 7.1.4, i.e. the dispersion of the uncoated PET transmission rates. In other words, the discrepancy between the reference value for the Hostaphan PET and the foil actually serving as substrate for the organic layer induces the apparent 'underperforming' of the latter at relatively low temperatures, when the raw data are being elaborated, and causes the isolated OTRs of the thin film to artificially increase. By looking at the associated relative variations, moreover, it is possible to suppose the presence of two distinct populations in the whole data set, separated around 40 °C. The average variation for each one of such set has then been calculated and is reported separately in Figure 7.38. While the 40 to 60 °C range still presents a residual dispersion around the mean value, the data are distributed in a narrow Gaussian, contrary to the low temperature range. As a consequence, the latter set of data has been deemed too inaccurate for the subsequent analyses and thus been discarded: this in itself should not undermine the validity of the successive results, as whatever variation in the transmission rates associated with the temperature is more recognizable in the latter's higher range. For the 10/1 sample, therefore, only data recorded at 40°C or higher temperature will be from now onwards presented and discussed.

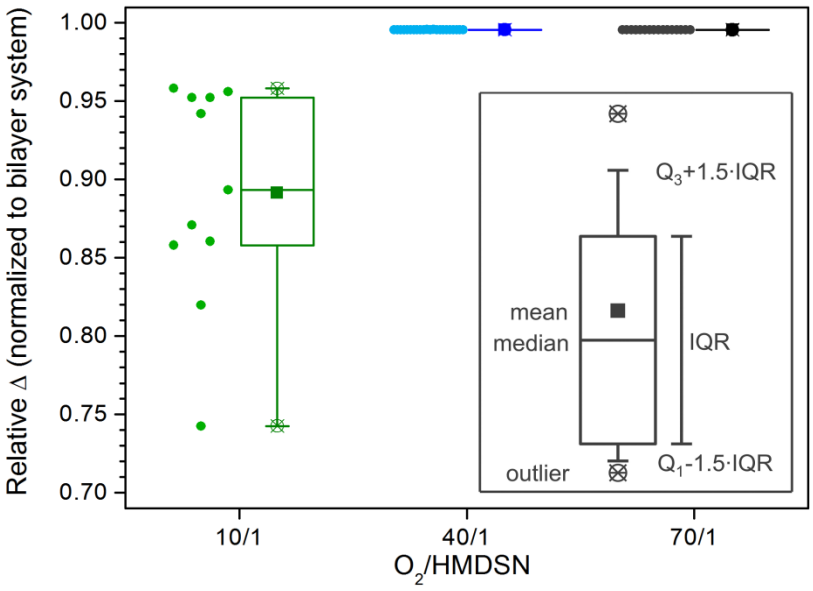

Figure 7.37: Relative variations in the OTRs for the isolated barriers alone with respect to the measured values pertinent to the substrate plus barrier system. In the legend, IQR is the interquartile range, i.e. the difference between the third quartile Q_3 and the first one Q_1, assuming a Gaussian distribution of the chosen set of data. Outlier values are assumed to be affected by anomalous errors and are therefore discarded from subsequent analyses and processing.

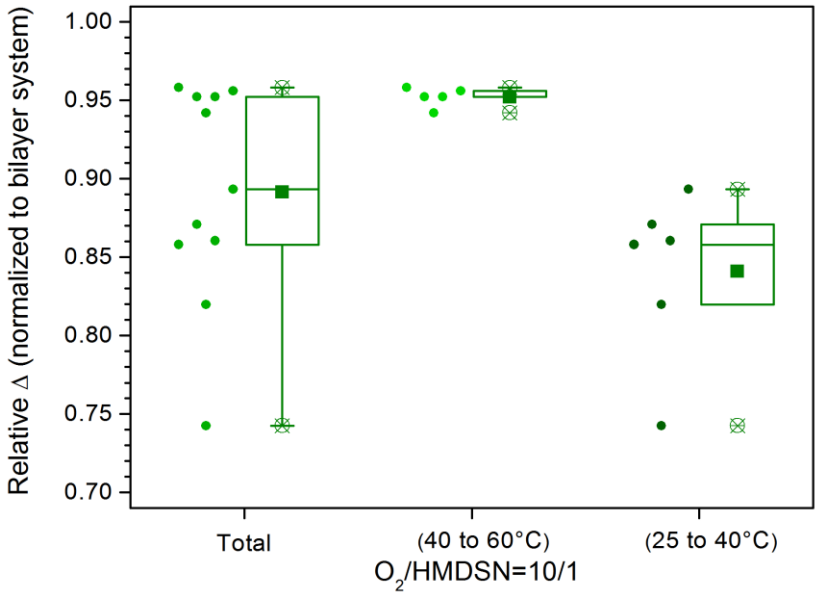

Figure 7.38: Box-and-whisker chart for the whole 10/1 sample measurements, and them after being split in two subset with a threshold at 40°C. The legend from Fig. 7.37 applies also in this case.

With the logarithmic values of the OTRs, both for the whole system and for the aforementioned isolated barrier contributions, it is then possible by means of Eq. 3.39 and 3.40 to linearly fit the experimental data and obtain, from the slopes, the activation energy for the diffusion process. The value of the ideal gas constant, necessary for the calculations, has been obtained out of an average of the values listed in [221]. The linear fits and the activation energies are reported in Figure 7.39. The latter are also reported, together with the R^2 values of the fits, in Figure 7.40.

A separation of the barrier contribution, although enabled by the faulty assumption that the film is defect-free, is nonetheless necessary. Any analysis on the 'as measured' values referring to the overall system would in fact be dominated by the contribution of the substrate which, as already seen in Figure 7.34, seems to present only a solid body diffusion pathway. Any deviation from the latter taking place in the barrier would likely be drowned by the PET contribution, both in absolute values and as kind of dependence on the temperature. Still, as the isolated contributions are affected by an unquantifiable but sure error, presenting and comparing both results has been deemed to be preferable.

For the uncoated PET foil acting as a reference, it is possible to observe again, as in Fig.7.34 and as confirmed by the R^2 value, the very good agreement with an Arrhenius-like drive diffusion process, with the obtained activation energy coincident with the values reported in literature, some of which are listed in Table 7.3.

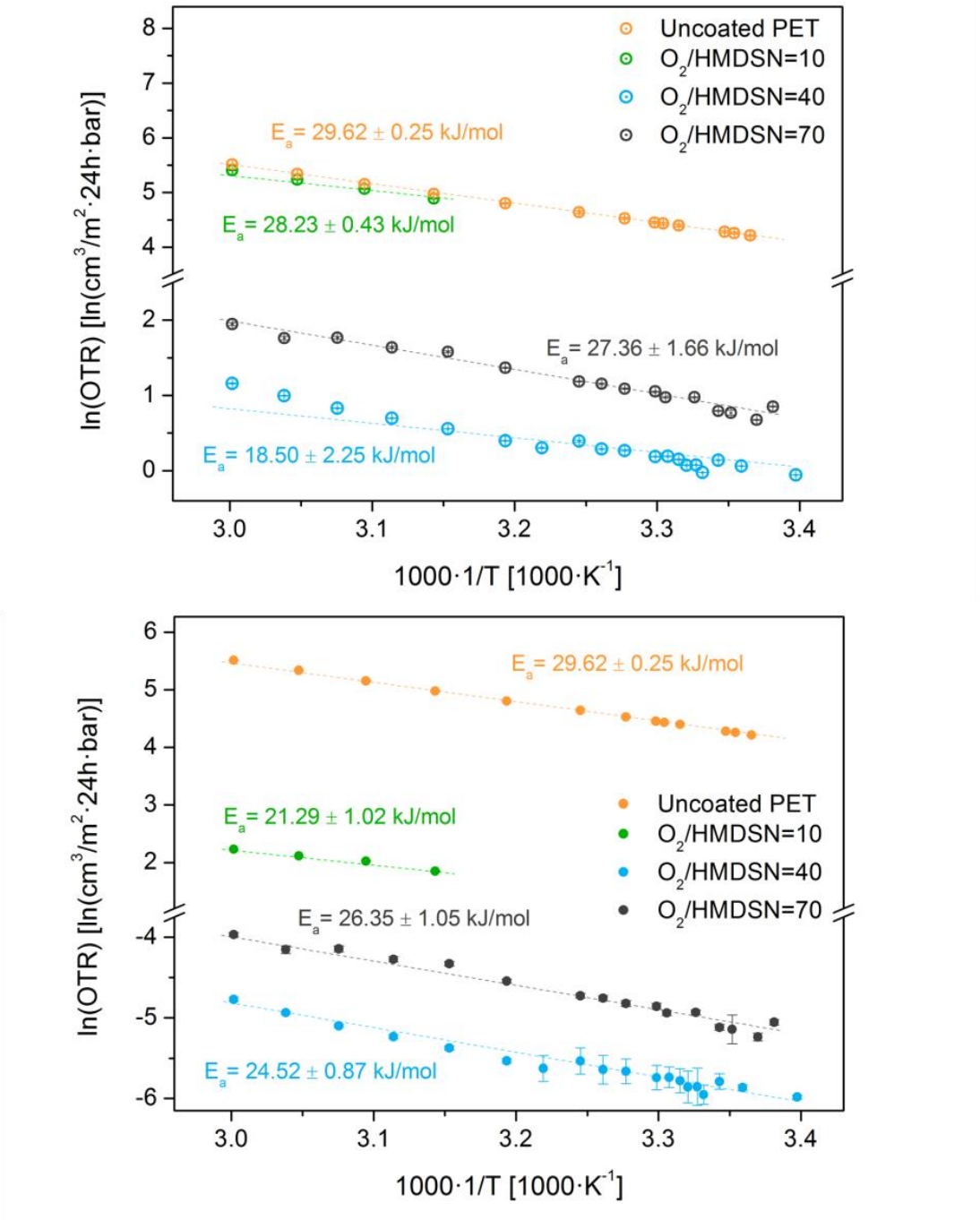

Figure 7.39: Logarithmic Arrhenius-like plots for the overall system (top) and the isolated barrier contributions (down) for the three investigated plasma-feed compositions. The calculated activation energies for the diffusion process and the associated error are also reported. The uncoated PET plot is repeated in the second graph for comparison purposes only.

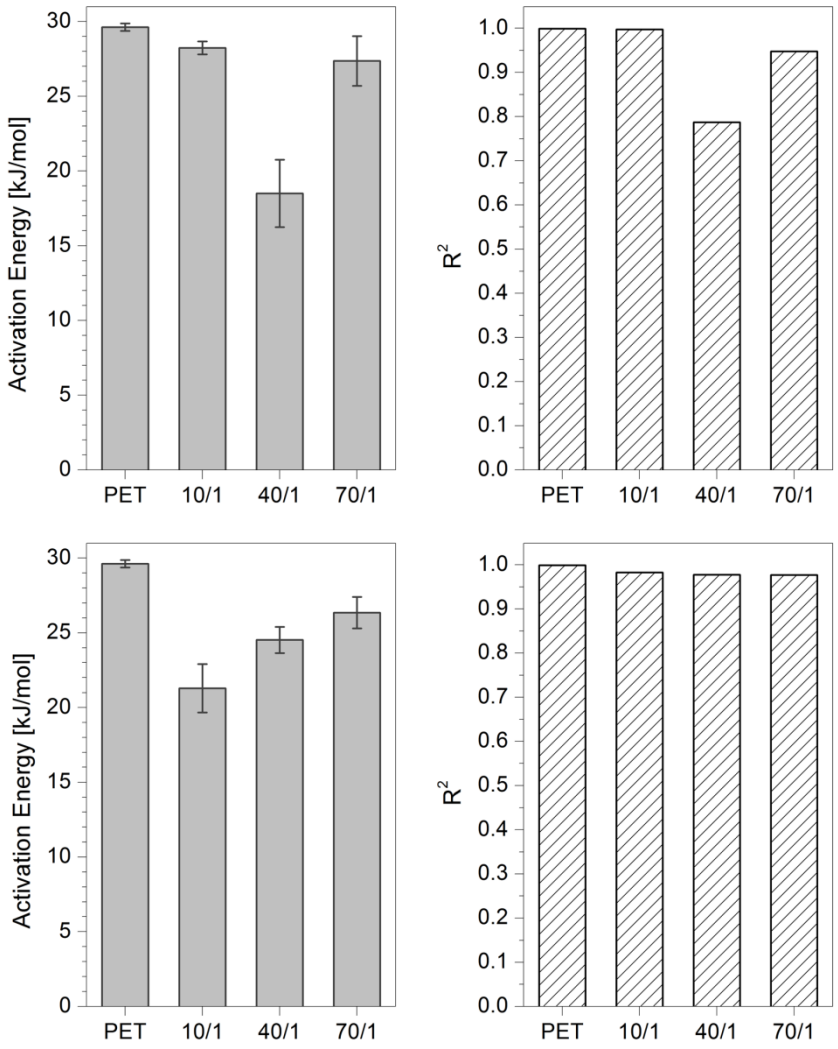

Figure 7.40: Activation energies calculated by means of the Arrhenius plots reported in Fig. 7.36 (left) and the associated coefficient of determination R^2 (right), for the substrate plus barrier system (top) and the isolated barrier contributions alone (bottom). The errors in the E_a values have been provided by the software at the end of the fitting procedure.

Table 7.3: Activation energies for uncoated PET foils calculated by means of an Arrhenius-like plot available in literature.

E_a	Reference	E_a	Reference
$kJ \cdot mol^{-1}$		$kJ \cdot mol^{-1}$	
29.3	[32]	29 ± 2	[222]
31.4	[34]	29 ± 3	[24]
29.2	[223]	29.7 ± 2.9	[30]

The 10/1 film, both in the total and in the isolated contribution, shows a higher intercept value than the two inorganic barriers, maybe because of its intrinsic higher disorder degree caused in no small part by its organic fraction. As the entropic component contributing to the intercept depends also on the defects in the layers [25, 30], then, Fig. 7.39 seems to imply that the 70/1 sample possesses a high number of defects or, more precisely, a higher fraction of its volume is affected by them, than the other inorganic barrier with a 40/1 feed ratio. This is certainly in good accord with the numerical densities calculated by the pinhole test and reported in section 7.1.5. As for the activation energies, as expected, the system with the 10/1 sample shows no difference compared to the uncoated foil. Neither the 40/1 nor the 70/1 barrier, however, result in an increase of E_a, despite the strong reduction in their OTRs and increase in the BiFs. For the 40/1 sample, in particular, the obtained value is significantly lower, and the R^2 of the fit too is the lowest among the four, when considering the results for the whole systems. The same remains generally true for the isolated contributions, although in this case the activation values of the films are even lower. It is interesting to notice however how a steady increase in the activation energies takes place from the 10/1 up to the 70/1 sample and that, at the same time, in this case the R^2 shows much better values. The errors introduced by the application of the ideal laminate theory may account for the apparent reduction in E_a but, assuming them to affect equally the three samples, it is still possible to conclude that the soft organic layer possesses the lowest activation energy out of the three, with the bulk of the 70/1 sample, possibly, being even superior to the 40/1 one, despite their measured OTRs values. The lack of an apparent increase in the activation energy compared to the uncoated substrate shows how the rate-limiting step in the permeation is still the diffusion through the polymeric substrate [30], at least in steady-state conditions. This entails that the barrier films are defective, i.e. the configuration is the one reported in Figure 3.4c and detailed in Section 3.8. In the contrary case, for a perfect barrier, the calculated activation energies should have been, at least for the inorganic barrier, closer to those of silica. At room temperature silica is practically impenetrable to oxygen [224]. Measurements can be of course carried out at much higher temperatures, yielding in this case activation energies in the range of 80 to 100 kJ/mol or even more [225, 226]. The extrapolation may not however be justifiable, according to Roberts *et al*. [54]. Indeed, in case of hydrogen, the activation energies of silica have been found out to be strongly dependent on the investigated temperature ranges, resulting in values even 2.5 times higher/lower [224]. It is important to stress, moreover, how thin films do not necessarily show the same properties of the reference bulk, and that anyway PECVD films often lack a reference material to start with [7], thanks to their unique properties and stoichiometries [104]. In this case, then, silica activation energies are to be seen more as an upper limit than a real reference to strive for. For the sake of simplicity, a 100 kJ/mol reference value has been assumed in this case for the inorganic silica-like barriers [25].

The presence of macro- and nano-defects, moreover, causes an 'overperforming' of the permeability especially at room temperatures, when compared to a purely solid body diffusion

mechanism, with values being much higher than those that could be extrapolated from data in a high temperature range (this affects even the aforementioned bulk glass, as demonstrated by the dependence of its activation energy on the investigated temperature range). The measured flux at steady-state conditions would then qualitatively be equal to a solid body contribution following an exponential increase with the temperature on top of a much more stable 'background' constituted by the contributions of the defects in the barrier, which are bound to dominate at 'low' temperatures. Such is the case observed for the 40/1 sample, as shown in Figure 7.41: here, it is possible to observe a noticeable knee in the curve which is not predicted in any single permeation model, but can only results from a multi-pathway process when one component becomes or ceases to be predominant. The knee has been first noticed in the 'as measured' plot, but it is still recognizable even after isolating the contribution of the barrier. The fitting procedure has then been repeated for the two segments, the separation of which lies around 37.5 °C: the threshold has been chosen only by observing the position of the knee. No such feature was however visible for the 70/1 sample. Interestingly, for the 40/1 sample such knee also corresponds to the sharp jump in BiFs observed in Figure 7.35.

As before, the activation energies have been calculated through the slope of the fit and are displayed with their determination coefficients in Figure 7.42, for the 'as measured' values and for the isolated film. In both cases, it is possible to observe how in the upper temperature range the apparent activation energy is higher than the uncoated reference, equal respectively to 31.8 and 32.5 kJ/mol. The associated R^2 is also closer to unity. The fit for the lower temperature range on the other hand is not only much less satisfactory, as shown by the lower R^2 values, but also provides a much lower activation energy, equal to only 11.6 kJ/mol for the overall system and to 20.5 kJ/mol for the isolated barrier. Such low values in turn caused the activation energy previously calculated through a single fit to be much lower than the uncoated PET. The linear fit for the substrate plus barrier system, in particular, is significantly poor. It can be concluded then that, at least in the lower temperature range, this activation test is completely rendered invalid by the presence of defects. It remains however still useful, not because it provides a reliable E_a estimation, but because its inaccuracy demonstrates once again the presence of defects in the barrier. The results for the higher temperature range on the other hand seem to imply that at least some part of the total flux of permeant diffuses through a solid body pathway, so that applying such barrier on top of the polymer does not equate only to an increase in the overall tortuosity, but to a real growth of the activation energy of the process which is then in part thermally activated (see also Section 3.8). Nonetheless, the activation energies are still only one third of those of 'real' glass. By comparing them to known values found in literature for porous glasses or other inorganic bulk materials, even if taking into account all the previously mentioned *caveats* about straightforwardly comparing plasma-deposited thin films to some appointed 'reference', it is interesting however to check for eventual correspondences. Thus, the activation energy for the 40/1 sample calculated in the low temperature range (i.e., as already said, where it would be most

affected by the presence of defects) for the whole system and equal to 11.6 ± 3.7 kJ/mol is in good accord with microporous glass, which lists an activation energy of around 12 kJ/mol [227]. Similarly, the E_a obtained in the high temperature range, 20.5 ± 1.9 kJ/mol, lies in proximity of the values listed for K-mordenite, an aluminosilicate zeolite, equal to 18.4 kJ/mol [54].

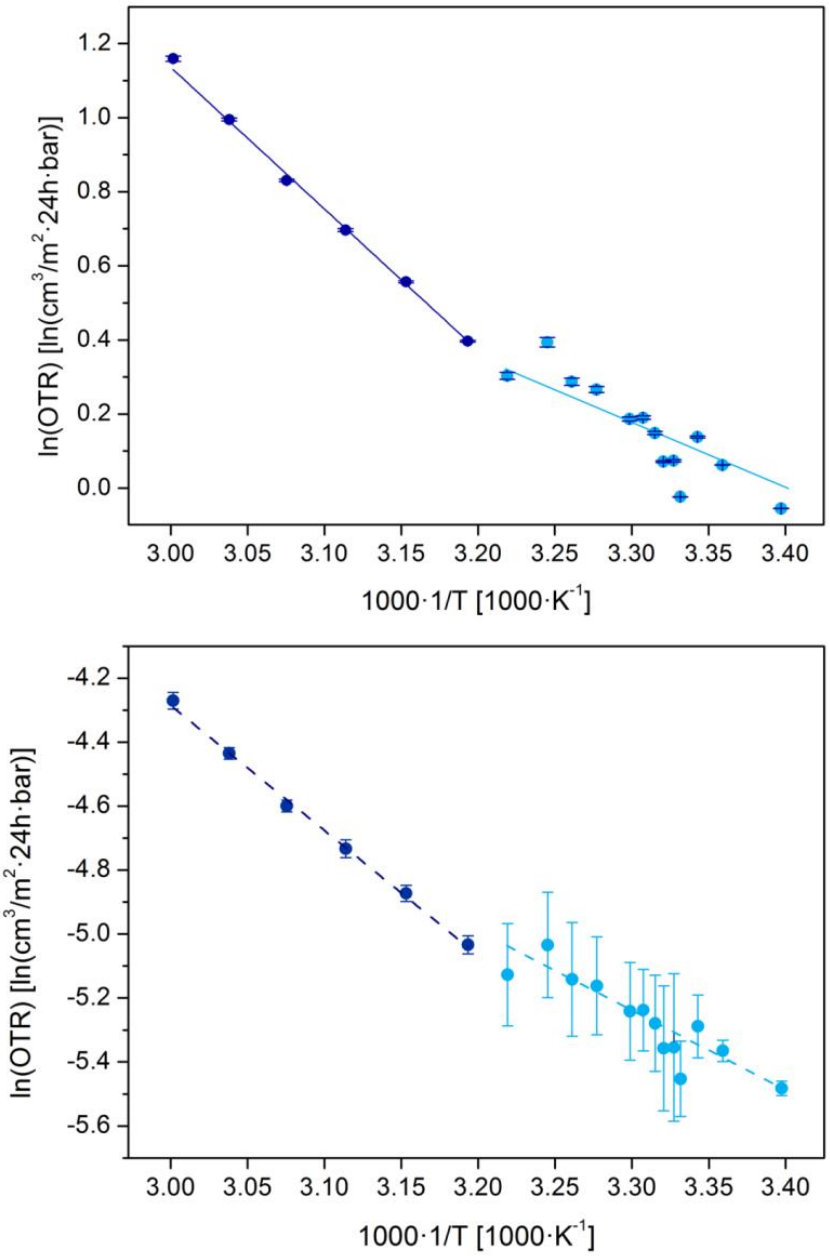

Figure 7.41: Arrhenius plots for the 40/1 sample 'as measured' (top) and isolated (bottom), showing a knee at a temperature of around 37.5 °C. The two separate fittings have been highlighted via different colors.

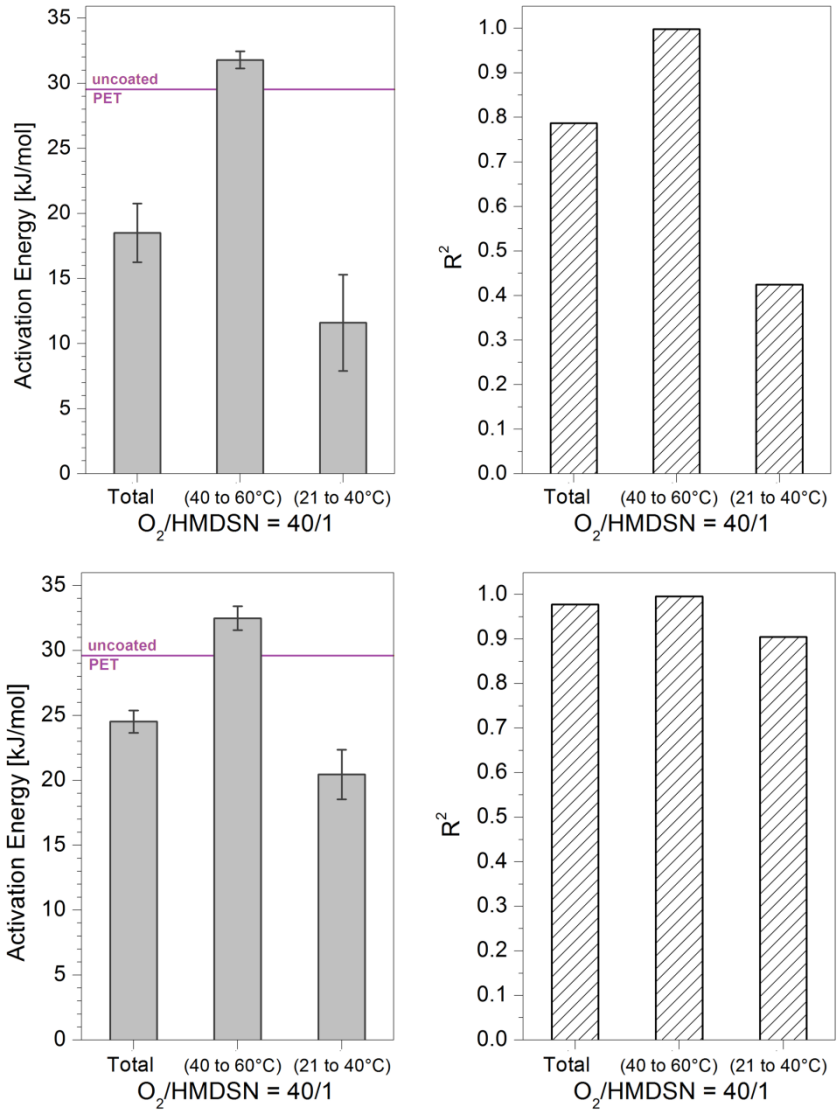

Figure 7.42: Activation energies for the 40/1 samples set of data, split in two segments, calculated by means of the Arrhenius plots reported in Fig. 7.39 (left) and the associated coefficient of determination R^2 (right), for the substrate plus barrier system (top) and the isolated barrier contributions alone (bottom). The errors in the E_a values have been provided by the software at the end of the fitting procedure.

It remains to determine whether the defects are macro- or nano-scopic, according to the definition of Roberts *et al.* [54]. This can be qualitatively assessed by noticing how, if the contribution of lattice and nano-defects in Eq. 3.44 is negligible, the whole equation is reduced to:

$$P_{sys} \simeq C_{md} \cdot P_{pol} \, ; \tag{7.1}$$

as the geometric factor is constant, then, the ratio between the permeability of the system and

the one of the polymer alone, too, should remain constant, even at different temperatures. As for Eq. 3.23, permeability and transmission rate are directly proportional, and the former ratio becomes nothing else than the inverse of the definition of the barrier improvement factor, when equating the permeability with the transmission rate. Such BiF, as previously shown in Fig. 7.35, has already been demonstrated to remain substantially unaltered for the 70/1 barrier, and for the 40/1 only in the higher temperature range. In the lower range, on the other hand, apart from the bigger dispersion, it could still be envisioned a more or less constant, albeit lower, value. Assuming then, as it would be reasonable to expect, that the defects in the layer, even when belonging to the same sub-set among those presented in Section 3.6, are still divided into different populations with different lateral sizes and different activation energies, the narrow temperature range between 37.5 and 40 °C seems to correspond to an activation threshold, above which a whole population of defects becomes active, or the contribution of which becomes much more prevalent.

Table 7.4: Average size of a monodisperse population of square defects and the area fractions covered by them, together with the factors necessary for their calculation according to Eq. 7.2, for the two temperature ranges for the 40/1 sample.

40/1 sample	C_{md}	d	L	2w=2h	χ_{def}
		µm	µm		
(40 to 60°C)	1.25×10^{-2}	23.1	153.59	6.73	1.92×10^{-3}
(21 to 40°C)	1.41×10^{-2}			7.62	2.46×10^{-3}

Because of the uncertainties connected to the data in the lower range, both inverse BiFs have then been used for the evaluation of the size of the macrodefects for the 40/1 sample. This can be carried out through the definition of C_{md} calculated by Yanaka *et al.* [31] for a monodisperse population of rectangular defects homogeneously arranged with a spacing equal to *L*:

$$C_{md} \simeq 2\pi \cdot \frac{\sqrt{wh}\, d}{L^2} \cdot \left(H\left(\frac{h}{w}\right) - \frac{\sqrt{wh}}{d} \cdot ln2 \right)^{-1}, \tag{7.2}$$

with *w* and *h* being the half lateral sizes of the defects along the x and y axis, respectively, *d* the aforementioned total thickness of the multilayer and *H(h/w)* the function thus defined:

$$H(s) = s^{-1/2} \cdot \ln\left(\sqrt{1+s^2} + s\right) - s^{1/2} \cdot \ln\left(\sqrt{1+s^{-2}} - s^{-1}\right), \tag{7.3}$$

where *s* = *h/w* is a measure of the shape and elongation of the defects. The previous two equa-

tions are valid provided that $w, h \ll d \ll L$. In the current case, following Roberts *et al.* example, it has been assumed for the sake of simplicity a perfectly square shape, so that:

$$w = h, \qquad \frac{h}{w} = 1. \tag{7.4}$$

The spacing has been equated to the average distance between crystals in the pictures obtained by means of the pinhole test, and for the 40/1 samples has been calculated as an average out of 200 measured distances. It must be noted how such value respects the assumptions for the validity of the aforementioned equations. The 70/1 oxygen-to-monomer ratio, because of the presence of areas with defects densities orders of magnitude different, has been excluded by the following analysis, as it would require first an extensive analysis of multiple samples surfaces in order to obtain a weighted L. Knowing also the average BiF and consequently the expected C_{md}, then, it has been possible to obtain the w values that, in Eq. 7.2, best approximate the latter factor. The recap data are displayed in Table 7.4, together with the resulting area fraction, χ_{def}, supposedly covered by such defects, defined as follows:

$$\chi_{def} = \frac{4w^2}{L^2}\,. \tag{7.4}$$

Even taking into account the simplifications made, it is safe to assume that the resulting defects size are being overestimated: with an average of around 7 μm, considering both temperature ranges, the defects would have been surely visible at the SEM pictures reported in Section 7.1.5, and probably even at the optical microscope in real time during the pinhole test, as their lateral size would be comparable with at least a good fraction of the calcium carbonate crystals. Furthermore, relatively large uncoated areas of similar size could have been recognized even prior to the start of the test by the interference-induced iridescence at their edges, as already demonstrated in Fig. 6.23. The assumptions made for assessing the defects size are therefore faulty, the one considering almost no permeant flux through other diffusion pathways in particular: the contribution of solid body diffusion has already been reasonably demonstrated, although it remains unclear to what extent, and the presence of nano-sized defects is more than likely, considering the certain presence of their macro-sized counterparts. It is however significant to notice how little coverage of the total surface the defects need in order to severely limit the barrier performances of the film (in this case, around 0.2%). Considering again the microporous glass and the mordenite in good accord with the activation energies for the 40/1 sample, then, the average size of the pores in their bulk is listed respectively as 0.6 [227] and ≃ 0.4 nm [54], i.e. four orders of magnitude smaller than the calculated values. In the investigated temperature range, such small pores would still be available for oxygen to be permeated through, as bigger than the molecule radius [35]. Nano-scaled defects would therefore most likely play a significant role in the overall diffusion also for the current silica-like barriers.

Unfortunately, further informations on the kind of defects and the permeation mechanism through them, particularly the contribution of nano-sized pinholes, cannot be conclusively drawn from the current set of data. The method devised by Kirchheim *et al.* [58, 59], although based on Roberts *et al.*, is overly simplistic. It proposes a fit of the isolated barrier contributions as a function of the inverse of the temperature in a classic Arrhenius plot, and then for the free and the Knudsen diffusion (see Eq. 3.42 and 3.43, respectively, with the diffusion coefficients substituted by the transmission rates), and the fit with the best determination coefficient should be assumed to be the dominant one. In the first place, the temperature-dependent term in Eq. 3.42 for the free diffusion can be reduced to:

$$\frac{T^{2.5}}{T + C_{su}} \simeq \frac{T^{2.5}}{T} = T^{1.5}, \tag{7.5}$$

i.e. a power law, like the case for Knudsen diffusion (albeit with a different order). The experimental errors alone may render difficult to discriminate between the two defect-driven diffusion mechanisms. Secondly, such approach already implies that, assuming that a major permeation pathway is present, it must be so preponderant to drown out the other two contributions and shape the transmission rate curves after itself alone.

Indeed, the current set of data (i.e. the isolated barrier contributions, with the 40/1 data split in the previous two different sub-sets), fitted for the free and the Knudsen diffusion equations, displayed respectively in Figure 7.43 and 7.44, still show very good determination coefficients, in most cases comparable to those obtained out of the respective Arrhenius plots. This is true even for the uncoated polymer, which is known *a priori* for its solid body diffusion. Such deceptive result is however easily debatable once observing the shape of the experimental curves: in all cases save one, the curves show through their concave shape a dependence on the temperature of a higher order than a power law, i.e. an exponential one. A partial exception is the 70/1 sample, whose data seem to be truly disposed in a linear fashion. The low temperature range of the 40/1 barrier too seems to show a linear correlation with the *x* variable, but in this case the associated errors cause this data to be unreliable.

In light of such results, for all the barriers here investigated the following general statement is possible: the overall permeation through such barriers cannot be reduced to a single process, either perfectly Fickian or following a tortuous path model, but on the contrary, the diffusion is regulated by more than one activated process. Thus, if a fitting of the transmission rates (as the dependent variable *y*) as a function of the temperature (the independent variable *x*) has to be made, it has to be modelled after the following equation:

$$y = A + B \cdot exp\left[-\frac{E_a}{Rx}\right] + C \cdot \sqrt{x} + D \cdot \frac{x^{2.5}}{x + C_{su}}, \tag{7.6}$$

where *B*, *C* and *D* are constant factors based respectively on Eq. 3.37, 3.42 and 3.43, and *A* is an additional constant necessary for taking into account eventual experimental errors. The second term in the sum then corresponds to a solid body mechanism, the third to the free diffusion and the fourth to the Knudsen diffusion contribution.

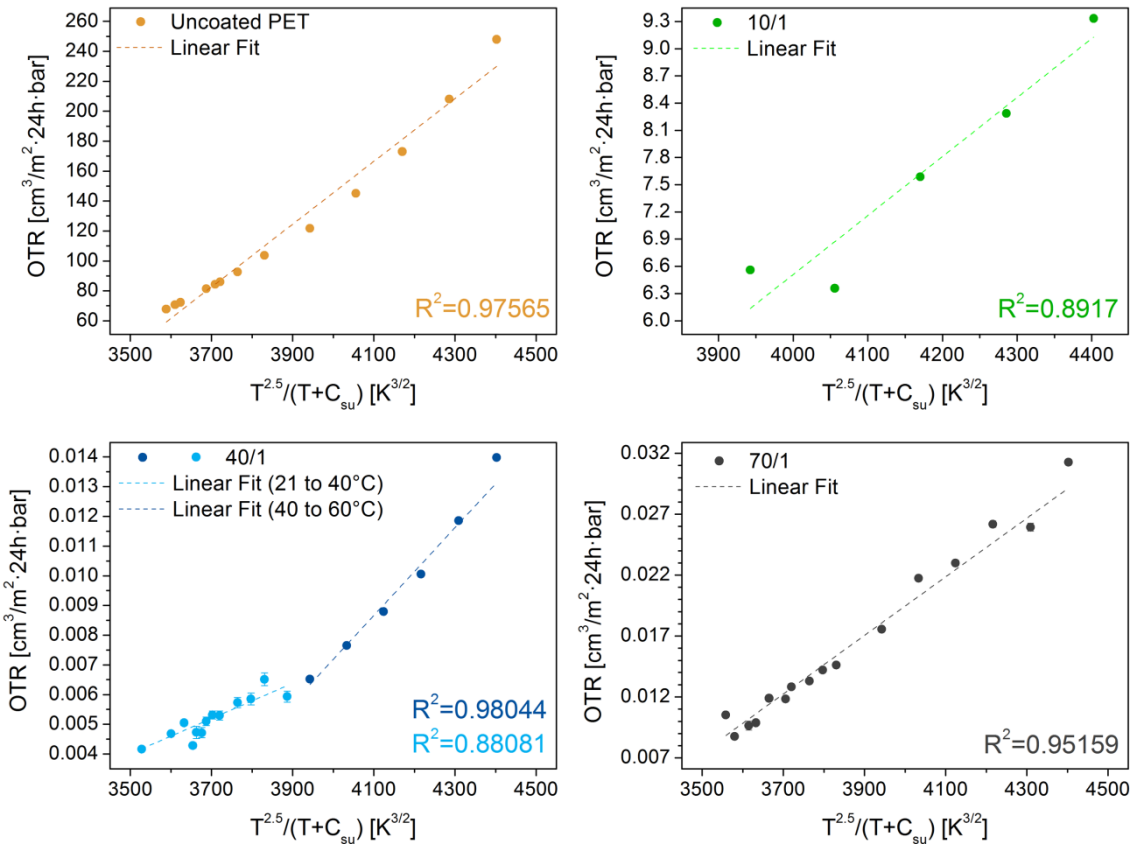

Figure 7.43: Oxygen transmission rates as a function of the temperature according to the free diffusion model, together with the determination coefficient of the relative fit, for uncoated PET (top left), 10/1 (top right), 40/1 in two segments (bottom left) and 70/1 sample (bottom right). The latter three are relative to the isolated contribution barrier alone.

In order to do this and obtain reliable results, however, a much larger data set would need to be rendered available first, both by means of repeated measurements of the same coated sample, and by testing several samples for each investigated oxygen-to-mixture ratio. The first step is necessary in order to minimize the experimental errors, which are particularly severe in the low temperature range: the latter range is however also the most interesting in order to better detect diffusion mechanisms through defects, as for such values the solid body diffusion is less pronounced. The second step on the other hand is required in order to obtain an average representative of their barrier properties and diffusion mechanisms. Especially for the good barriers,

the defects densities calculated by means of the pinhole test reported in 7.1.5 can in fact even show a 100 % variation among them. The 70/1 samples have furthermore the disadvantage of a highly inhomogeneous defect density that further limits the analyses reproducibility.

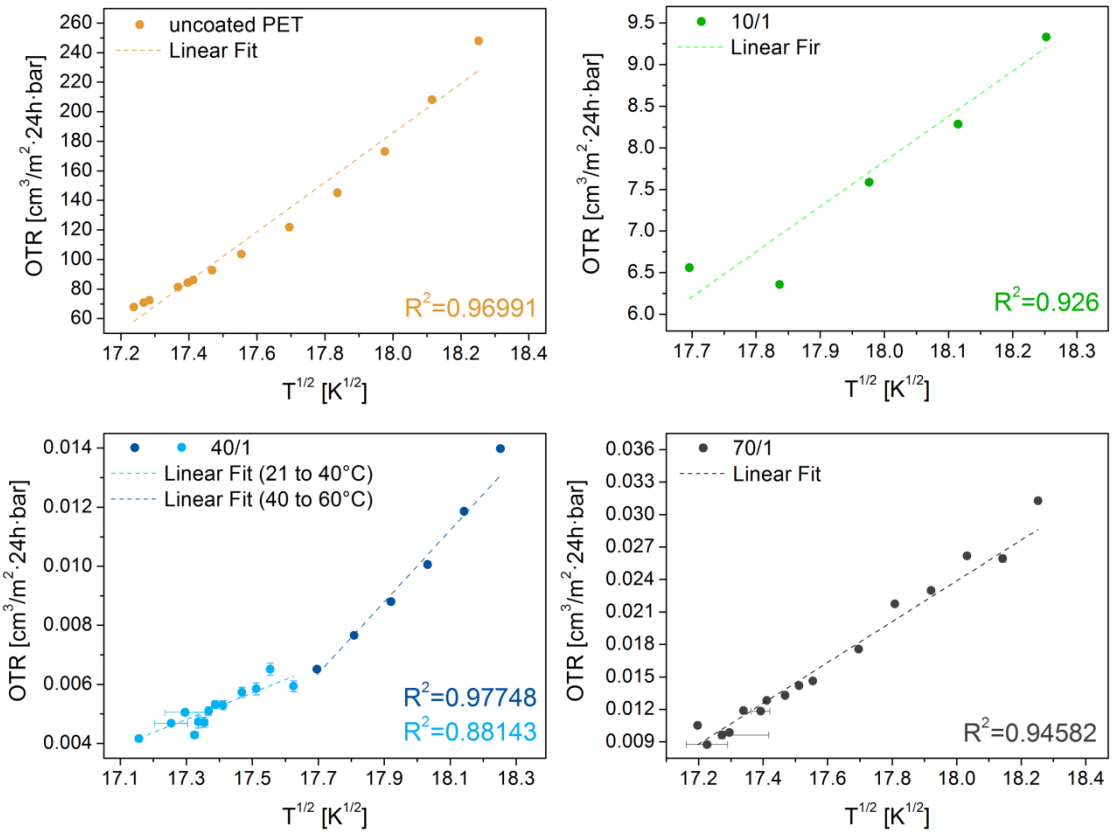

Figure 7.44: Oxygen transmission rates as a function of the temperature according to the Knudsen diffusion model, together with the determination coefficient of the relative fit, for uncoated PET (top left), 10/1 (top right), 40/1 in two segments (bottom left) and 70/1 sample (bottom right). The latter three are relative to the isolated contribution barrier alone.

In conclusion, for each investigated sample the following general, albeit non-conclusive, statements can be done, based also on Figure 7.45, which shows the activation energies as a function of the transmission rates obtained at 35 °C:

- for the uncoated foil, diffusion takes place mostly through a solid body mechanism, as largely expected [30, 37, 68, 227]; the activation energy is in good accord with values found in literature for similar PET;
- the 10/1 substrate plus barrier system shows a high transmission rate and an activation energy still comparable to the reference value. The main permeation mechanism is in this case still limited by permeation through PET although, because of the intrinsically

porous structure of the thin film, it is also possible a non-zero permeation through defect;

- the substrate with the 40/1 sample system shows a complex permeation process in which most likely all three speculated pathways play a role; the behavior at high temperatures is regulated through an Arrhenius-like dependence on temperature, while at low temperatures the contribution of macro- and nano-defects becomes more preponderant. In the first case the permeation process is at least partially thermally activated, resulting in an increase of the apparent activation energy. Not so in the second one, which on the contrary results in a much lower E_a value even if the transmission rates remain still very low;
- the system with a 70/1 sample, yet again, shows no increase in the activation energy when compared to the uncoated PET, and alone among the investigated samples seems to be mainly influenced by permeation through defects, i.e. free and Knudsen diffusion regimes, with a reduced or even almost absent permeation through the barrier's bulk. Thanks to an increase in defect's density and in the intrinsic brittleness of the barrier (see also Section 7.1.3), the resulting transmission rates are however still worse than those for a 40/1 sample.

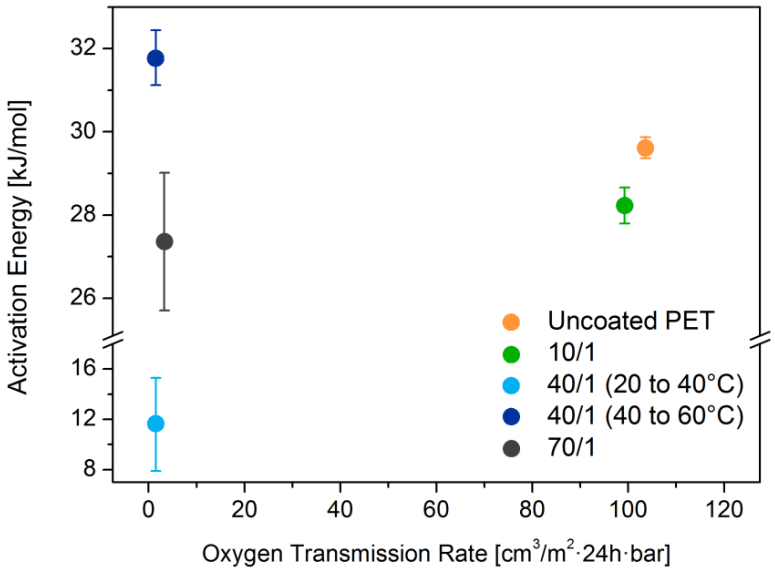

Figure 7.45: Calculated activation energies for the investigated substrate plus barrier systems (40/1 split in two sub-sets) and uncoated PET as a function of their normalized oxygen transmission rates at 35 °C.

7.2 Study on the operating power

After having studied the effect of the gas feed composition on the deposited thin films, a study on the possible equivalent effects of the operating power has been performed, in order to find better conditions that would result in films with improved barrier properties. Power has a strong influence on the chemistry and properties of the solid products, mainly by influencing the fragmentation degree of the precursor molecules and, at the same time, by regulating the chemical reactions taking place in the plasma phase, both effects at least in principle comparable to those produced by the gaseous feed composition. Instead of investigating the whole oxygen-to-monomer range covered in the previous section (see Chapter 7.1), only three ratios have been chosen: the 40/1, as for 555 W the highest BiFs have been obtained through this plasma feed composition, an extremely oxygen-rich feed, 70/1, which still resulted in completely inorganic films, and an oxygen-poor ratio that resulted in mostly organic films with poor barrier properties. The 13/1 has been chosen over the 10/1, which has been previously used as the 'organic reference', because for 555 W the former lies at the very beginning of the steep reduction in OTRs (see Figure 7.15). The different operating powers should therefore in this case provoke the most intense variations in the properties of such film. As in previous cases, the thickness has been kept constant at a value of 100 nm.

The investigated power range extends both above and underneath the previously employed 555 W. The lower limit is reached around 215 W, when the plasma ignition becomes difficult to achieve and the fluctuations of the standing plasma, when present, cannot ensure homogeneous or reproducible depositions. The upper limit of around 750 W has been chosen as for such high energies the possibility of thermal damages to the substrates becomes extremely high.

In the following sections the deposition rates as function of the operating power, and the films' FTIR spectra and OTRs for the three investigated ratios will be presented and discussed, together with some qualitative consideration on the pinhole tests performed for a small selection of films.

7.2.1 Effects on the chemical composition

The deposition rates for the three investigated oxygen-to-monomer ratios as a function of the average operating power, normalized for the monomer flux in the plasma feed, are reported in Figure 7.46. In all three cases, a clear trend is shown, with the deposition rates decreasing inversely with the power in an almost linear fashion. Such decrease is similar to the one reported in Figure 7.3 for constant power and increasing oxygen-to-monomer ratios. The only partial exception is constituted by the lower power range for the 40/1 ratio, up to around 400 W, as the deposi-

tion rate remains practically constant. Such behavior will be better explained in section 7.2.3. For the 40/1 ratio, moreover, powers higher than the upper limit of the chosen range have been investigated too. Despite the calculated value being in good agreement with the perceived trend for lower powers, however, the glossier appearance of the coated substrates suggested at least a minimal thermal damaging and, therefore, no subsequent oxygen transmission rate measurements for such barriers have been performed.

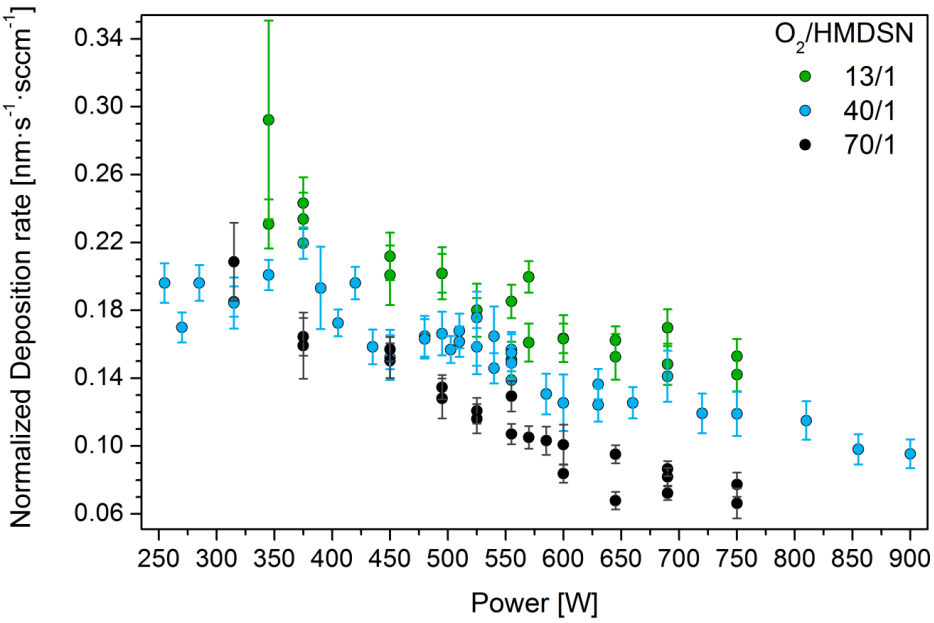

Figure 7.46: Deposition rates vs. operating power for an oxygen-to-monomer ratio of 13/1 (green), 40/1 (blue) and 70/1 (black). The values are calculated from 100 ± 10 nm thick films and have been normalized by the employed precursor flux (in [sccm]).

The ATR absorption spectra for the three ratios and different operating power, in the 1600-500 cm^{-1} in order to better display the main band, are reported in Figure 7.47. The following discussion will focus in particular on the methyl band signal as indicator of the organic fraction of the films, where present. All spectra refer to the samples that have been later tested for their barrier properties. Here again, for low oxygen contents in the plasma feed (10/1), the monomer cannot be fully oxidized and stripped of its organic groups, resulting in a thicker and still organic solid film. An increase in power values, however, does at least reduce this sort of 'starvation' regime, oxygen-wise. It is in fact possible to observe how the intensity of methyl-related band around 1260 cm^{-1} is inversely proportional to the average power. For such ratio, anyway, power alone is not enough to turn the films into completely inorganic silicon oxides.

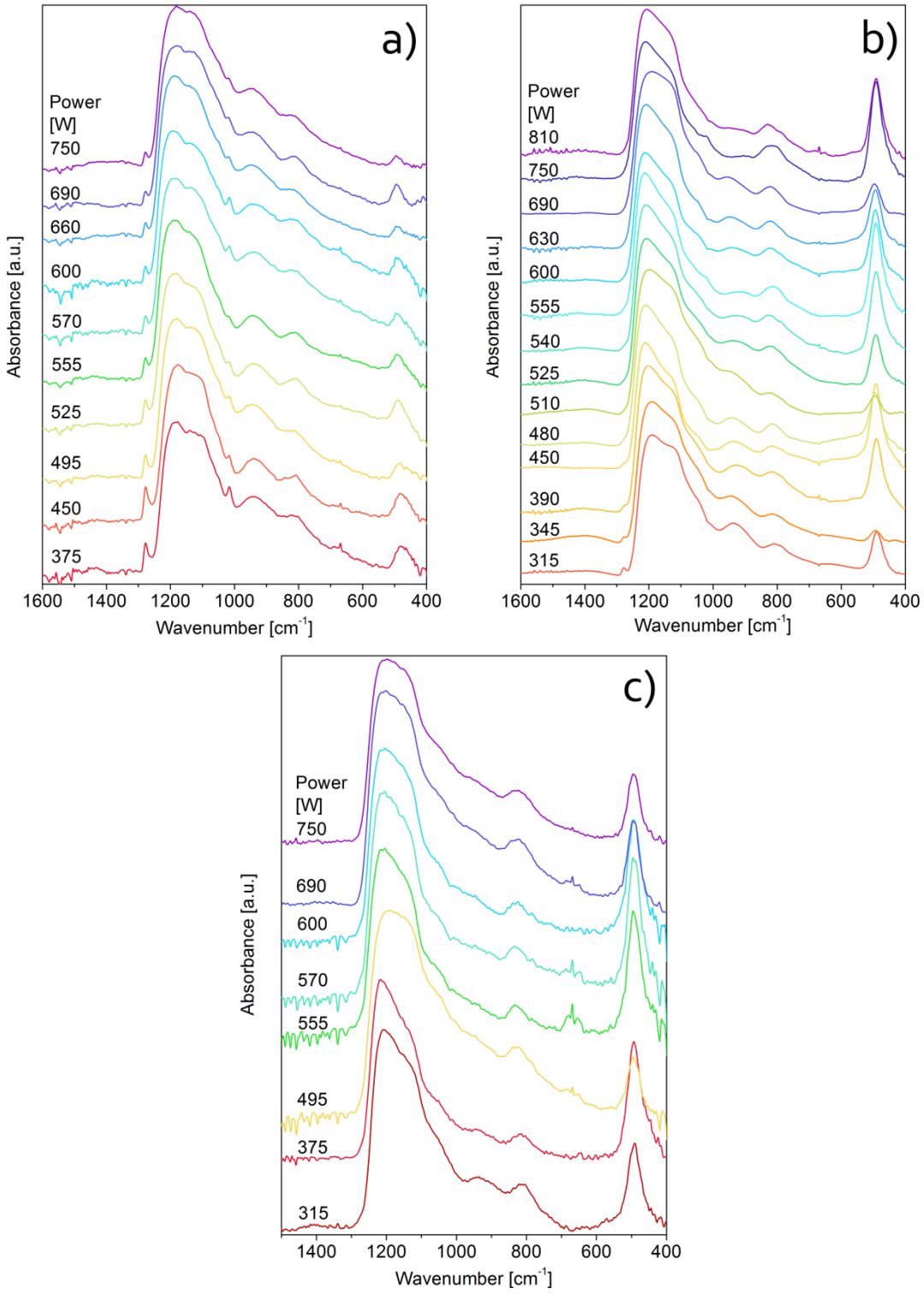

Figure 7.47: ATR FTIR absorption spectra in the 1600-500 cm^{-1} range for different operating powers and different oxygen-to-monomer ratios: 13/1 (a), 40/1 (b), and 70/1 (c). The colors of the single spectra do not necessarily correspond to the same operating power. The bands have been assigned based on the references already reported in Table 7.1 and Table 7.2.

With higher oxygen content, instead, the deposited film can turn gradually and continuously from organic to inorganic ones, as it is the case for the 40/1 oxygen-to-monomer ratio. A small methyl band is still visible up to powers of around 450 W, before completely disappearing and leaving only SiO_x-related peaks. The main Si-O-Si band itself does not show remarkable changes in shape throughout the entire investigated range. As for the 70/1 ratio, in this case the chemical composition of the film is determined mainly by the composition of the feed, rather than by the power. All displayed spectra in this case show no methyl band and a rather unaltered Si-O-Si main band, even for the lowest powers.

The Si-O-Si main band wavenumbers, together with the relative intensity of the methyl band for all the investigated conditions, are reported in Figure 7.48: the first series of data shows, for the lowest and highest oxygen-to-monomer ratios, that the main band position remains fairly constant throughout the whole power range; only the 40/1 ratio exhibits a remarkable shift to higher wavenumbers before reaching a plateau, which corresponds to the operating power (between 450 and 500 W) at which the organic signals disappear from the spectra, as inferred also by Fig. 7.47. The 13/1 samples, on the other hand, despite the progressive reduction of the methyl band intensity, even at highest power show an organic fraction still bigger than the 40/1 films at lowest power.

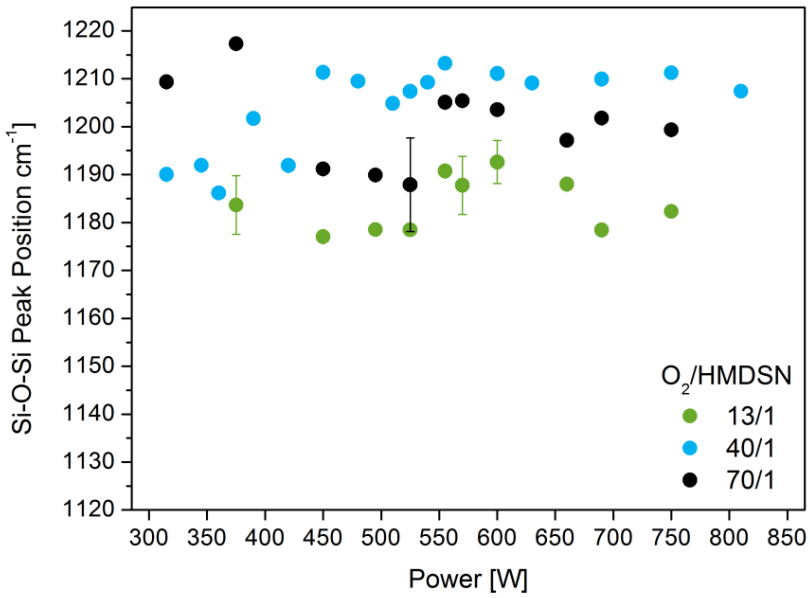

Figure 7.48: Si-O-Si main band position for the three investigated oxygen-to-monomer ratios as a a function of the operating power.

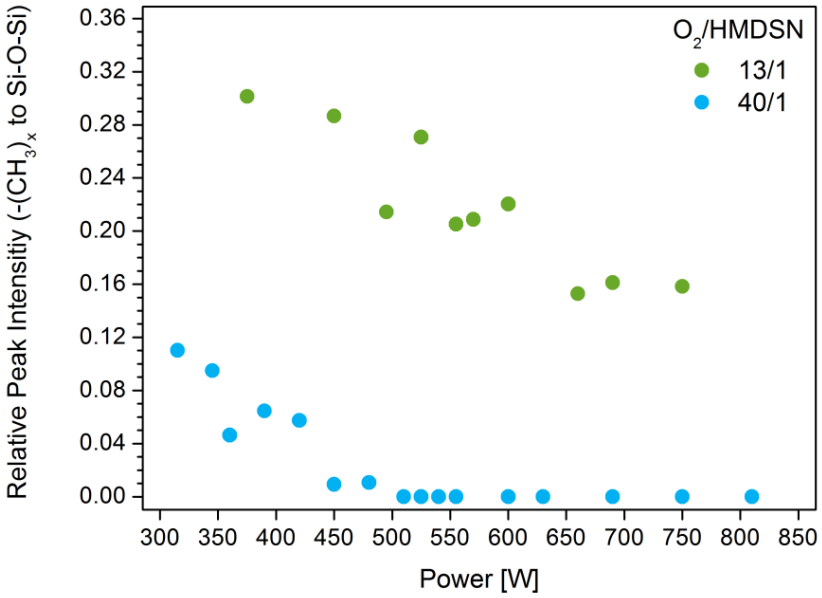

Figure 7.48 (continued): Ratio between the intensities of the methyl band at 1260 cm^{-1} and main band (bottom) for the 13/1 and 40/1 oxygen-to-monomer ratios at different powers. No 70/1 data have been reported as the films are fully inorganic for all the investigated operating powers.

7.2.2 Effects on films transmission rates

Figure 7.49 reports the oxygen transmission rates for all the investigated operating power and the three oxygen-to-monomer ratios. All tested films have a thickness of 100 ± 5 nm. For the lowest ratio, as its organic fraction remains fairly high even at elevated operating power, the OTRs show little to no decrease when compared to the uncoated reference (OTR_{PET} = 103 $cm^3 \cdot m^{-2} \cdot 24h^{-1} \cdot bar^{-1}$), with a maximum BiF of 2.8 reached for the highest operating power. For the 40/1 ratio, a steady decrease, then a range where a minimum is attained, and finally an increase of the OTRs are to be observed. The first part of the curve is in excellent agreement with the relative methyl intensity reduction in the corresponding infrared spectra shown in Figure 7.48: with decreasing free spaces in the films, caused mainly by steric hindrance of the methyl groups, the barrier properties increase. Here once again the 'threshold' between organic and inorganic films is perfectly coincident with the OTR values reducing and then stabilizing at a minimum. Interestingly, in the small 500-525 W range the OTRs show again a sudden increase and higher dispersion of their values, before stabilizing again up to 620 W, circa; after that, an almost linear increase in the OTRs, to values even higher than those for still organic layers is to be observed. In this case, the worsening of the barrier performances cannot be ascribed to the chemical composition of the completely inorganic films.

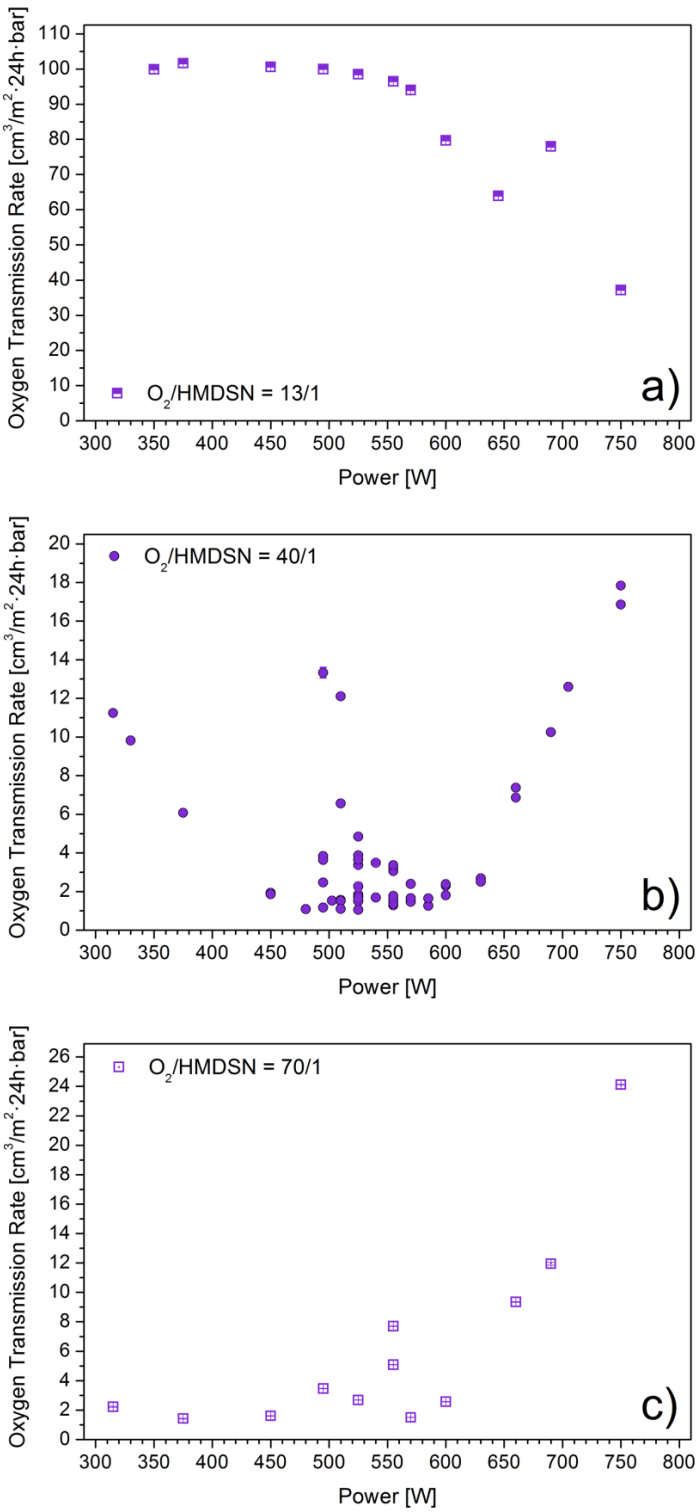

Figure 7.49: Oxygen transmission rates as function of the operating power for a 13/1 (a), 40/1 (b), and 70/1 (c) oxygen-to-monomer ratio in the plasma feed.

The fluctuations observed in the rates around 510 W are confirmed by a few CO_2 tests performed on samples produced in the same discharges as those employed for the OTRs measurements. Pictures taken at the end of the pinhole test for operating powers of 520, 580, and 660 W, respectively, are reported in Figure 7.50, but no average defect density for such samples has been calculated. The 520 W sample shows a considerably higher density of crystals, compared to the almost defect-free surface for the 580 W samples. Moreover, the size and shape of crystals in the first case closely resemble those observed on organic films shown in section 7.1.5. At 660 W, finally, the defect density increases again, and the resulting crystals, small and point-like, resemble in turn those observed on high oxygen-to-monomer ratio samples at 555 W.

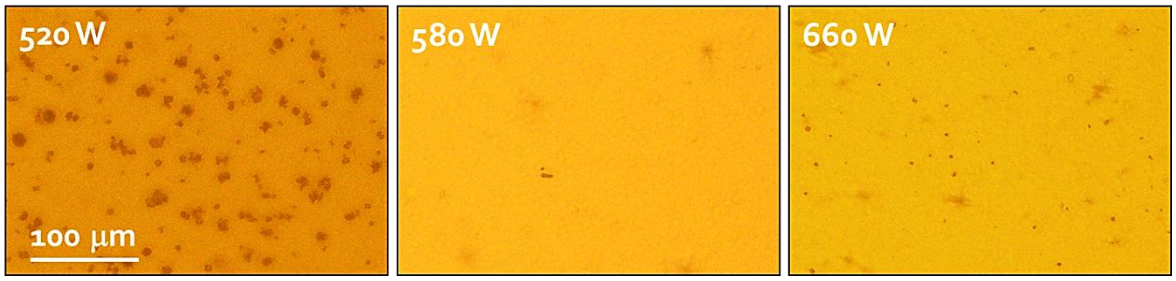

Figure 7.50: Optical microscope pictures taken at the end of the pinhole test for films deposited with an average operating power of 520 W (left), 580 W (center) and 660 W (right). The scale in the bottom left corner applies to all pictures.

The highest BiF in this case is almost twice the best one obtained for the same oxygen-to-monomer ratio in the first studies at 555 W reported in section 7.1.4, and it is equal to around 100. Such value has been obtained for a sample produced with an operating power of 525 W, i.e. on the fringe of the narrow spike in the OTRs. With such low transmission rates, however, even a small fluctuation in the defect density, still well within the normal reproducibility limits for the same operating conditions, can result in dramatic variations in the calculated BiF. It is therefore better to consider ranges, rather than single sets of operating conditions, as suitable for the production of thin films with good barrier properties.

Finally, for an oxygen-to-monomer ratio of 70, an overall similar trend in the OTR values can be observed, although shifted towards lower operating power. In this case, moreover, the range where good barrier properties are obtained stretches in a range of 300 W, instead of roughly 100 as in the 40/1 case. In such interval, the best sample produced resulted in a BiF of around 70. For comparison, the best one reached with 555 W as operating power has been equal to less than 32. Between 600 and 650 W, finally, the oxygen transmission rate of the still inorganic films starts to rise again, linearly. The threshold for such increase, being the same for the 40/1 ratio, suggests that it could be caused by thermal damaging of the substrate induced by the longer deposition times. For the 13/1 ratio, the deposition rates at high powers are significantly higher, thus result-

ing in shorter plasma treatments and a reduced heating of the substrates. The samples produced with 650 W or at higher powers do not show visible signs of damaging; it is however noteworthy to remind that, for powers exceeding 800 W, the PET substrate for a 40/1 gas feed ratio did start to exhibit a glossy appearance, caused by temperature above the glass transition values for polyethylene terephthalate. The threshold at which such thermal damages begin remains however unclear.

7.2.3 Ranges of operationality

In light of the experimental results shown in the previous two sections, it is possible to draw some conclusions about the effect of operating power on the deposition process. Power seems to have a similar effect to the fraction of oxygen in the plasma feed. An inorganic film with good barrier properties can be produced, as shown in section 7.1.4, by keeping a fixed power and increasing the oxygen-to-monomer ratio. The excess of reactive oxygen (whether dissociated or excited) will move the equilibrium of the reactions taking place inside the plasma towards their products, i.e. volatile oxidized organic compounds and a silica-like inorganic solid film. The variation in the aseous feed ratio, obtained by changing accordingly the precursor flow, leaves the average power per mole largely unaltered (as reported in section 7.1.1) and has therefore no effect on it. At the same time, for a fixed oxygen-to-monomer ratio, an increase in the operating power results in higher dissociation and excitation for both oxygen and HMDSN, that will cause the overall oxidation process in the plasma phase to be more effective. Such shift towards inorganic solid products remains however limited by the reactants' ratios: this is the case for the 13/1 ratio, where even the highest applied power cannot fully overcome the lack of enough oxygen for a complete stripping of the carbon content from the final film (what has been previously labelled as 'starvation regime'). This could be also the case for the lowest power range for the 40/1 ratios, where an increase in applied power did not immediately result in a reduction of the deposition rates, i.e. in a reduction of the average size of the radicals depositing on the substrate (from organic methyl groups to much smaller SiO_x fragments). Alternatively, in this case at very low powers most of the monomer remains in an undissociated state and takes no part in the deposition process. The increase in power causes then a significant higher fragmentation of the precursor in the plasma phase, which at least initially counterbalances the reduction in size of said fragments following the oxidation process. The onset for films with good barrier properties, a condition, as shown previously, strongly connected to the lack of organic fractions in the films, cannot therefore be shifted indefinitely to lower oxygen-to-monomer ratios. A mixture ratio of 13/1, or even 10/1, seems to represent the lower limit in the current experimental set-up. Higher oxygen-to-monomer ratios on the other hand offer large ranges of conditions that result in the best obtainable barrier layers, as most of them are mostly limited by the presence of defects rather than by

an unsatisfying chemical composition. The upper limit in this case is due to side-effects like the aforementioned thermal damaging of the substrates, rather than failures of the thin film selves. Since however, apart from the risks of thermal damages, further increases of power, past the threshold for depositing fully-oxidized films for a given oxygen-to-monomer ratio, only causes an increase in the kinetic energy of the species in the plasma, that in turn allows the latter to remain for longer times in the gaseous state and the deposition rates to decrease, the most efficient approach seems to be to operate in the middle region, both power- and feed-wise.

The presented initial investigations on the operating power have been later further expanded [229]. The combined results are reported in Figure 7.51 as the ratio between the overall absorption band for the methyl groups and the main Si-O-Si peak, and as oxygen transmission rates displayed in the form of barrier improvement factors, for powers between 315 and 825 W and oxygen-to monomer ratios between 0 and 80. The color scale intervals have been chosen so to remain consistent for both graphs: as an example, the limit of the first interval for the methyl relative intensity, 0.008, corresponds to 2% of the highest measured methyl intensity, just like the first interval for the BiF has 50 as its lower limit, which corresponds to an oxygen transmission rate of 2% of the reference for an uncoated PET (i.e. the maximal measured value), and so on. In this way, any linear correlation between the two quantities should be made readily appreciable.

The displayed values show indeed a very good agreement with each other. If a strict correlation between the methyl band's intensity and the overall organic degree of the film is to be assumed, like the infrared spectra in Section 7.1.2 and the permeation analyses in Section 7.1.3 clearly showed, then, it is possible to remark how the barrier properties of the films are mainly and in the first place influenced by the presence of organic groups. These can therefore act as a good indicator for the expected qualities of a barrier film, and can even roughly predict the resulting barrier improvement factors.

The apparent discrepancy for high power and oxygen-to-monomer ratios, where the barrier properties of the film degrade fast, have been confirmed [229] to be caused by thermal damaging of the substrate. For the 80/1, 750 W coordinates, two pieces of PET have been stacked together on the sample holder, with both one undergoing the thermal load of the deposition step but only the uppermost being coated with a film. The underlying piece, once tested again for its OTR, showed a remarkable deterioration of its properties.

In conclusion, the barrier properties of the deposited films are limited either by low powers or low oxygen-to-monomer ratios, both parameters preventing a full oxidation of the precursor and, therefore, the production of silica-like inorganic films. Once this condition is attained, a large range of operability is possible, limited not by the intrinsic properties of the films, but by the failure of the substrate to sustain the thermal loads which increase at high power, or with the longer deposition times associated with higher oxygen-to-monomer ratios. The range is highlighted in Figure 7.52, where the two best BiFs are also reported: these are roughly equivalent and correspond to a pair of 100 ± 5 nm films with OTRs smaller than 1 $cm^3 \cdot m^{-2} \cdot 24h^{-1} \cdot bar^{-1}$.

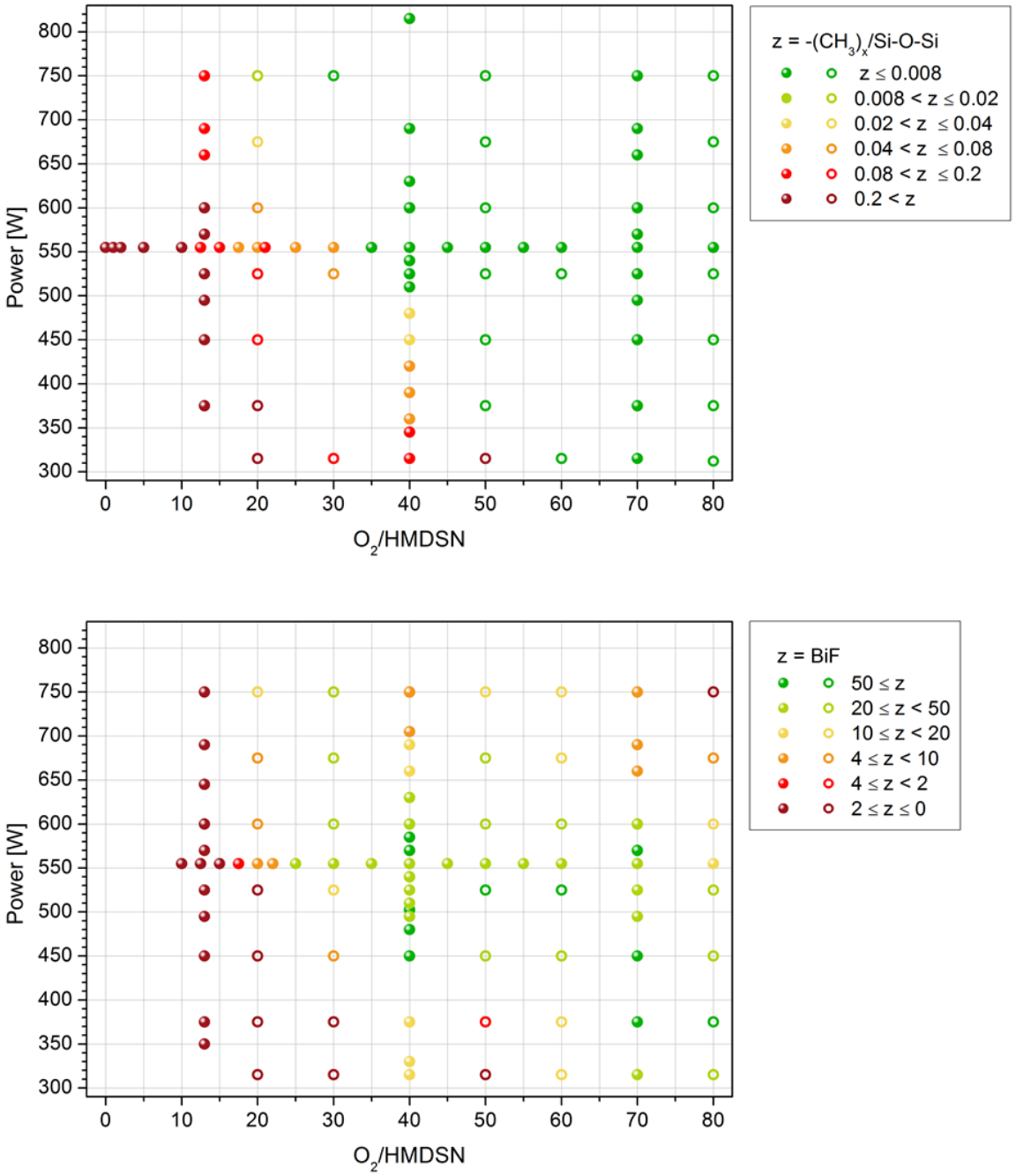

Figure 7.51: Plotted as function of different gas feed ratios and operating power, the methyl-to-Si-O-Si bands intensity ratio (top), and the OTRs displayed as BiFs of the PET substrate (bottom) with their respective legends. In case of multiple measurements for the same pair of parameters, average values have been displayed. Hollowed circles: data from [223].

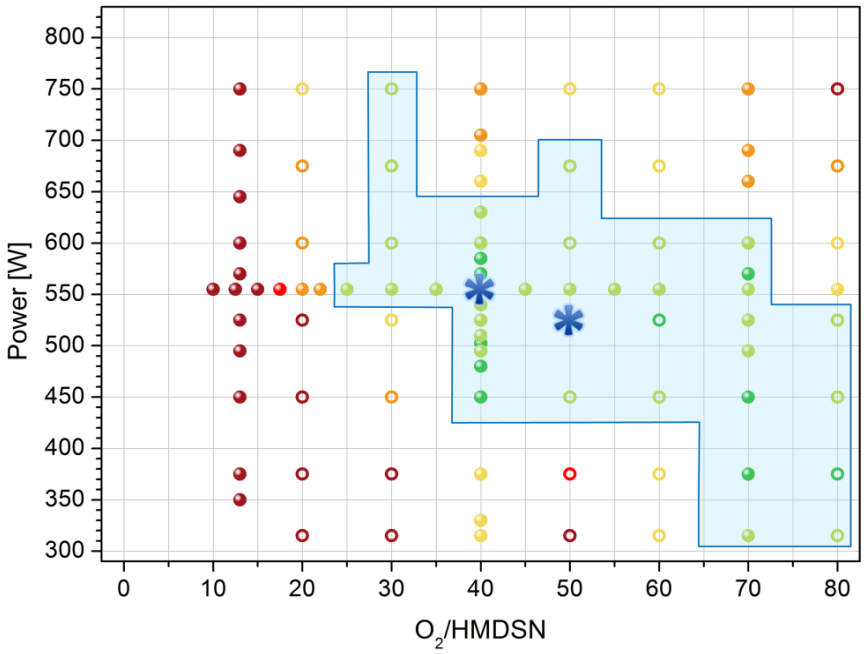

Figure 7.52: In the highlighted area, the range in which thin films with barrier improvement factors equal to or higher than 20 are attained. The blue stars indicate the pairs of parameters for the best BiFs, equal to 98 (40/1, 555W) and 97.85 (50/1, 525 W) [223] respectively.

7.3 Study on barrier thickness

After having found a pair of power and gas feed composition coordinates (555 W, O_2/HMDSN = 40/1) considered the most suitable in the investigated range, the next step has been to study the dependence of the chemical and physical properties of the thin films as a function of their thickness. The aim is to optimize the latter in order to produce reliable films with good barrier properties in the shortest deposition step possible, for a better efficiency and smaller risks of thermal damages to the substrates or other risks arising from prolonged exposure to a reactive, oxygen-rich environment.

This section presents the deposition rates and the chemical composition dependences on the layer thickness. The barrier properties and diffusion coefficients of these films have been investigated, together with the density of their defects and the influence the latter may have in determining the optimal thickness. Finally, a discussion on the morphology of the films with growing thickness and the possible growth mechanisms transpired from the presented results, and their role in the overall performance of the barrier, will be provided.

7.3.1 Deposition rates of barrier films with different thicknesses

The deposition rates, calculated as [nm/sec], for all films that have been, at a later stage, investigated by means of FTIR spectroscopy and tested as barriers against oxygen, are reported in Figure 7.53. As the HMDSN fluxes have been kept constant at 2.5 sccm for all the deposition processes, no further normalization has been required in order to compare them. The plotted numerical values therefore cannot be straightforwardly equated to those displayed in Figure 7.3. Similarly to the former plot, however, the x-axis errors correspond to the standard deviation arising from the profile measurements, and y-axis ones are too dependent on them, as the deposition rates are calculated as the ratio between the measured thickness and the duration of the deposition process.

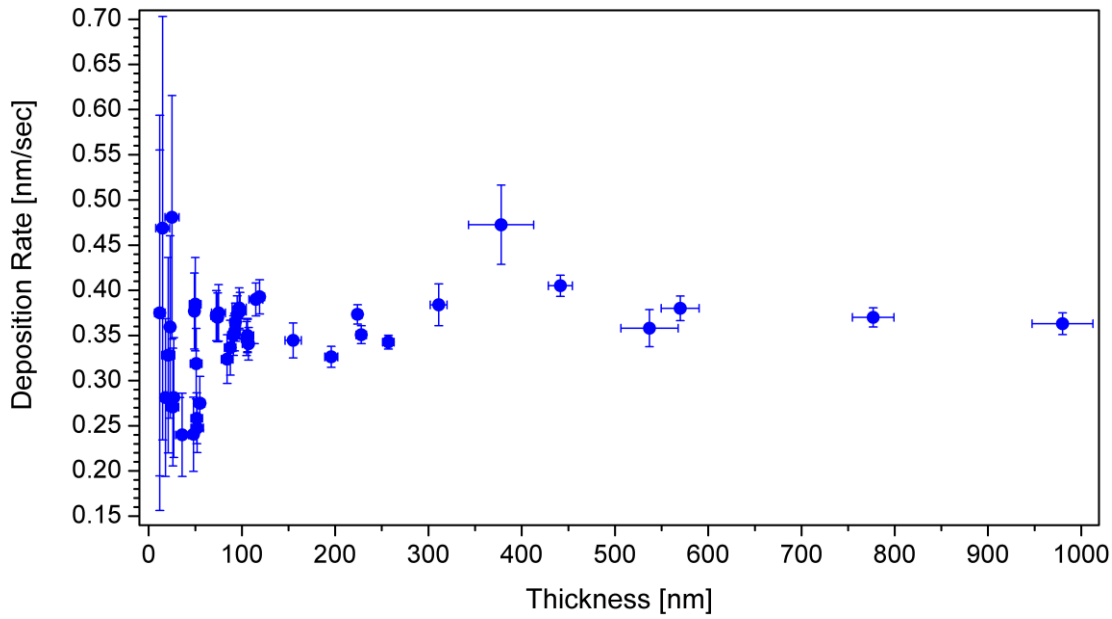

Figure 7.53: Rates for films deposited with an oxygen-to-monomer ratio of 40/1 and a thickness ranging from 10 nm to almost 1 µm.

The calculated values, for thickness from around 75 nm onwards, are shown to remain practically constant over the almost two orders of magnitude investigated and seem to point that, whatever the kinetics and the mechanisms of formation and growth of the layer, they remain unchanged as the film itself grows. This in turn hints to a very stable chemical composition, which has been later investigated by means of IR spectroscopy, the results of which are displayed and discussed in the following paragraph. For thinner films a much greater dispersion of the cal-

culated values and their associated standard deviations is to be observed. For very thin layers, this is also due to detection limits, as the maximal resolution for the perthometer is indeed 10 nm. Profiles of thinner films are likely not to be observed or equated *a priori* to 10 nm. The very short deposition times associated with such thin films, moreover, require the magnet in the reactor to sweep only once, thus potentially creating thicker films around its initial position and thinner ones at the end of its run. As a consequence, the measured values show a much more pronounced dispersion. Finally and most importantly, the deposition rates calculated for such thin films are greatly affected by side-processes taking place in the first moments after the plasma ignition, before the proper deposition process can start. In this case, on the unetchable glass substrates employed for the thickness determination, the first oxygen radicals and reactive species produced at the plasma ignition can also react with the still exposed substrate surface, apart from the dissociated HMDSN fragments in the plasma phase, and clean it from outer contaminants, including monolayers of adsorbed water vapor [56]. Only after this step will the silica-like polymerized film start to form. As a consequence, such thin films are less reproducible, at least with the current HMDSN fluxes. Moreover, because of the different interactions of an oxygen-rich plasma with organic surfaces, like the PET foils employed as substrates for the oxygen transmission rate measurements, it is possible that at least for the thinnest films (≤ 50 nm) the thickness on the glass substrates is not perfectly coincident with the actual one on PET (probably overestimated, as better explained in Chapter 7.3.3).

All the deposited films, including the thicker ones, still retain their transparency and lack of color even though, for the latter, it is possible at grazing angles to observe iridescent halos caused by Fresnel inner interference in the films. The effect starts to become observable for samples thicker than half a micrometer, i.e. with a thickness comparable with the visible light wavelengths. No further investigation has been carried out in order to obtain even thicker films, for two main reasons: first, for the thickest films the deposition times exceed 30 minutes, and even longer deposition processes could thermally damage the underlying PET foil. Secondly, both the 800 nm and 1 μm thick films already showed strong internal compressive stress that caused the coated foils, once removed from the sample holder, to curl up (with the silica-like film on the outer side); not so much for the coated aluminum foils. Such samples have been extremely difficult to handle and cut for the oxygen transmission rates measurements and CO_2 test without risking scratching or otherwise damaging them, thus invalidating subsequent analyses.

7.3.2 IR analyses of barrier films with different thicknesses

The 40/1 oxygen-to-monomer films at different thicknesses have been investigated by means of ATR FTIR spectroscopy, and the corresponding spectra are reported in Figure 7.54, with the spectrum of gaseous HMDSN as reference. For each thickness only one spectrum was displayed.

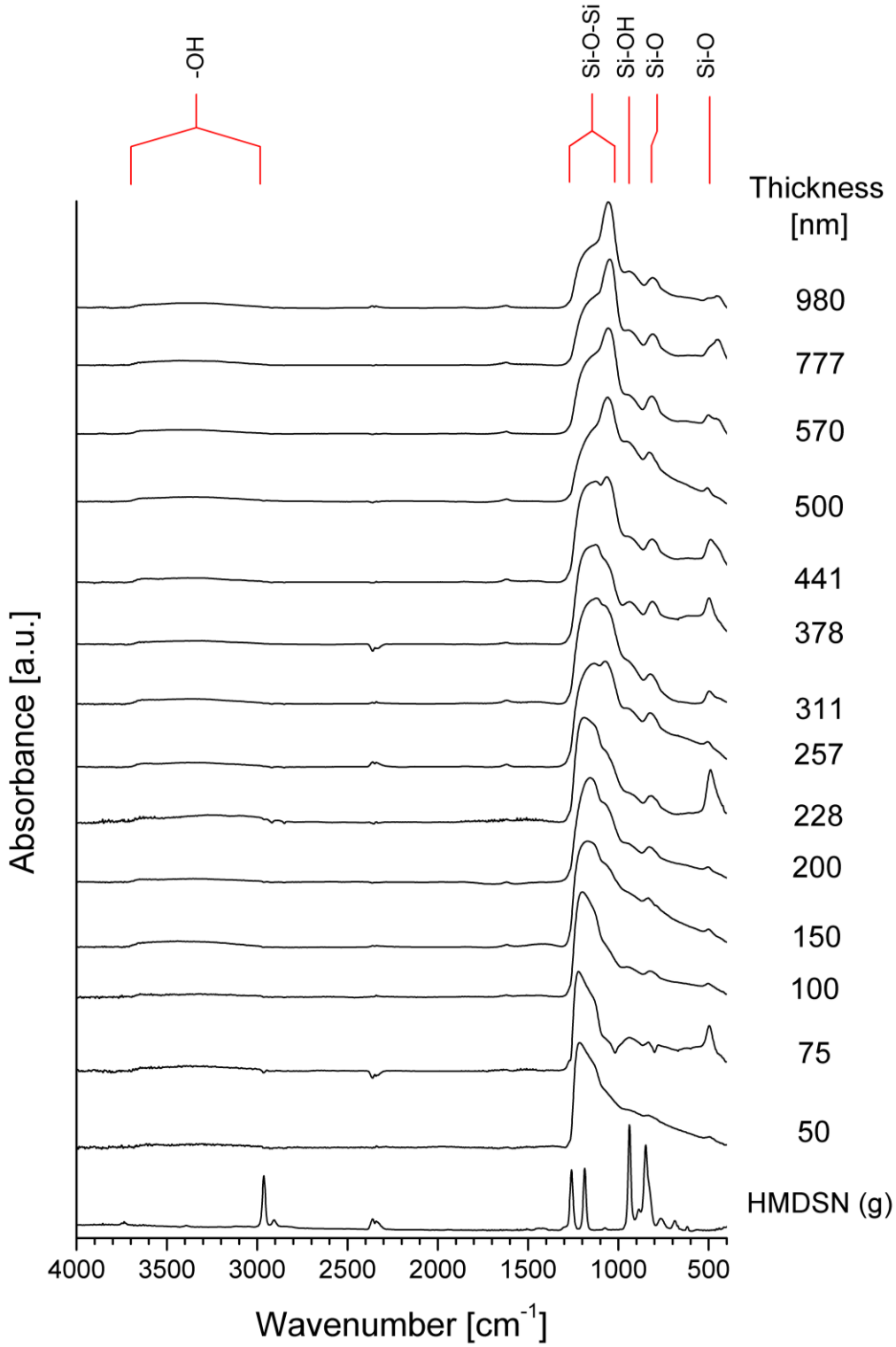

Figure 7.54: Infrared spectra in the 4000-400 cm^{-1} range for film of different thicknesses produced by means of a plasma feed with a constant oxygen-to-monomer ratio of 40/1, and for the gaseous precursor as reference (bottom). Spectra normalized for their main Si-O-Si band.

The spectra of films with thickness lower than 50 nm, albeit recorded, have not been displayed, as interference effects caused artificial deformations of the bands and the inversion of some of the peaks in the low-wavenumbers region (a partial example of such effect is already present for the 75 nm sample). Normalization for all the spectra with respect to their main Si-O-Si band has been made necessary, as the thicker films produced comparatively much stronger signals that would have rendered the analysis of the finer features of the thinner samples impossible. A complete list of the observable bands is reported in Table 7.5.

Table 7.5: Peak positions and vibrational mode assignments for the absorption bands in the infrared spectra displayed in Figure 7.54.

Wavenumber cm^{-1}	Assigned group	Vibrational mode	Reference
3700-2950	OH	ν	[201]
1250-1020	Si-O-Si	band	[150]
1090-1020	$Si-CH_2-Si$	δ, γ	[159], [202]
930-920	Si-OH	ν	[150]
900-810	[Si-O]H	n.a.	[201]
800	SiO	δ	[204]
465	SiO	ρ	[204]

For all spectra, the only visible signals are those correlated to inorganic Si-O bonds: the low – OH stretching band at high wavenumbers, the main Si-O-Si peak in the 1020-1250 cm^{-1} region, and the associated bending and rocking modes at 800 and 400 cm^{-1}, respectively. As the lowest wavenumbers also show the highest dependence on the quality of the crystal-sample contact, the latter signal shows dramatic shifts in its intensity which however can be surmised to not be related to eventual changes in the samples chemical composition. All films can be concluded to be inorganic, with silicon and oxygen as their main components and residual traces of hydrogen predominantly bond with oxygen. As already hinted by the calculated deposition rates, therefore, the film chemistry is not dependent on the duration of the plasma process and, consequently, by the film thickness itself. This may not however be true for very thin films, i.e. few tens of nanometer or less, especially when deposited onto an organic substrate.

As already mentioned in Section 7.1.2, the main Si-O-Si band is constituted by several components, mostly related to the stoichiometry of the corresponding sample, so much that the band position and eventual shift can give further information on the chemical composition of the

film. In case of extremely thin films, however, a second factor becomes preponderant in the determination of the shape and position of the band. For very thin films, much thinner than the incoming radiation's wavelength [230], in case of non-zero angles of incidence [231] and unpolarized radiation, the transverse (TO) and longitudinal (LO) modes interact differently with the solid surface. The transverse component in particular, despite classical electro-magnetic selection rules allowing only LO modes to interact with the solid surface [232], causes a displacement of electric charges, with the positive ions and the free electrons being accelerated in opposite directions, i.e. it induces a plasmon oscillation and a net electric field localized on the surface [233]. The latter in turn causes weak shifts and deformations in the absorption bands of weakly polarized bonds, like SiH and Si-CH-Si, but a full splitting of the vibration modes for polar ones, like for example Si-O.

The amount of such effect, firstly explained by Berreman in order to account for the twinning of infrared absorption bands at low angles of incidence [213], has a bell-like trend versus the film thickness: after increasing up to a maximum with the latter, so much that the LO-related signal is more intense than the 'real' TO-related one [234], it start decreasing, as the area/volume ratio of the film decreases inversely with the thickness and, therefore, the LO contribution becomes overall less preponderant [233]. Such effect has been thoroughly observed in thermally grown, crystalline SiO_2 films with thicknesses ≤ 500 nm, but also in disordered materials like a-SiO_2 [210, 235, 236]. In the current case, considering the stretching Si-O-Si band in the 1250-1020 cm^{-1} range, the four different sub-bands that have been cautiously proposed in Table 7.2 for different stoichiometries would then twin in other four peaks, similarly to what proposed by Lisovski *et al.* for thermally annealed thin SiO_2 films [237] (values reported in Table 7.6, left).

Table 7.6: Position of sub-bands induced by the Berreman effect from [237] (left), and TO and proposed (*) LO modes for the currently investigated bands (right).

Wavenumber	Assigned mode	Ref.	Wavenumber	Assigned mode	Ref.
cm^{-1}			cm^{-1}		
1300	LO	[237]	1225	LO (*)	
1252	LO	[237]	1190	LO (*)	
1200	LO	[237]	1156	LO (*)	
1147	TO	[237]	1122	LO (*)	
1091	TO	[237]	1073	TO	[105]
1056	TO	[237]	1038	TO	[105]
–	–	–	1004	TO	[105]
–	–	–	970	TO	[105]

The average shift between one LO and the corresponding TO mode, in Lisovski's case, is 152 nm. By adopting such value is therefore possible to calculate where the respective LO modes of the four Si-O-Si sub-bands should lie. This is graphically reported in Figure 7.55, for the 980 nm thick film as reference. The left low shoulder is in excellent accordance with the proposed LO modes. Still, a full fitting of the band with at least eight components should be necessary, in order to obtain exact informations on the stoichiometry of such films. A qualitative discussion of their spectra is however yet possible.

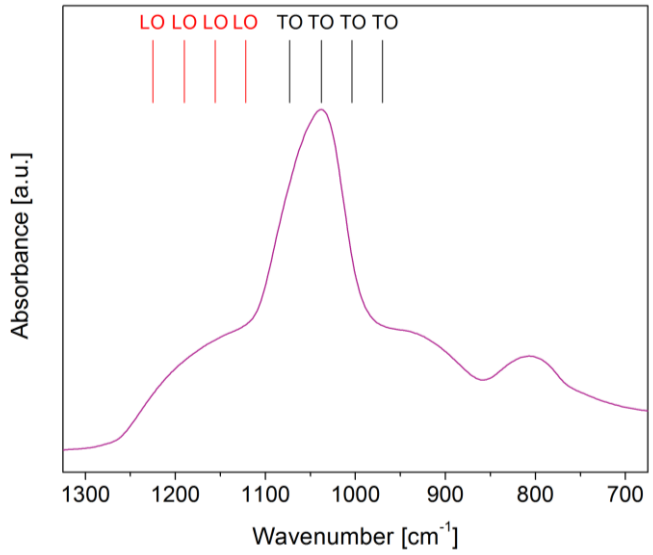

Figure 7.55: Proposed LO mode peaks arising from the splitting of the four TO components proposed for the main Si-O-Si band, for the 980 nm thick film already reported in Figure 7.54.

The interpretation of the shifts in the whole band, even taking into account the split peaks, is not straightforward, as the LO modes are shown to exhibit a blue shift, not always linear, with increasing thickness [233]. This becomes more evident when considering the half widths at half maximum of the spectra from Figure 7.54, which are in turn reported in Figure 7.56. The 'left' branch of the band, at higher wavenumbers and mostly affected by the presence of split LO modes, increases in fact with the thickness before sharply narrowing for the $\simeq$ 1 µm sample, as in this case the overall contribution of the TO peaks become preponderant. As a consequence, the peak position of the band shifts progressively towards shorter wavenumbers, as further shown in Figure 7.57. As previously mentioned in Chapter 7.1.2, the position of the main peak can provide informations about the stoichiometry of the SiO_x films, as changes in electronegativity of the surrounding environment of the Si-O bond, i.e. different vicinal atoms configurations, can lead to a blue or red shift of the typical Si-O stretching frequency. In amorphous structures like those obtained through plasma processes most configurations are theoretically possible, but with dif-

ferent probabilities, leading only to an average value to be observed by means of FTIR spectroscopy. By linear regression of the Si-O-Si band position for films with known stoichiometry, the relation of the former and the latter can be calculated by means of the following equation [105, 238]:

$$\bar{\nu}_{band} = 68.06 \cdot x + 936.4\ [cm^{-1}]\,, \tag{7.7}$$

where x is the average oxygen fraction in the silicon oxide bonds. In the current case, by considering the total band position alone, such calculation can be done only for thicker samples, when the LO modes contribution becomes lesser. As such, they yield an average value of around 1.7, showing that the investigated samples present a mostly inorganic composition along their whole thickness, save perhaps some carbon residuals lowering the fraction of oxygen bond directly to silicon, and yet too few to be detected directly by FTIR spectroscopy alone.

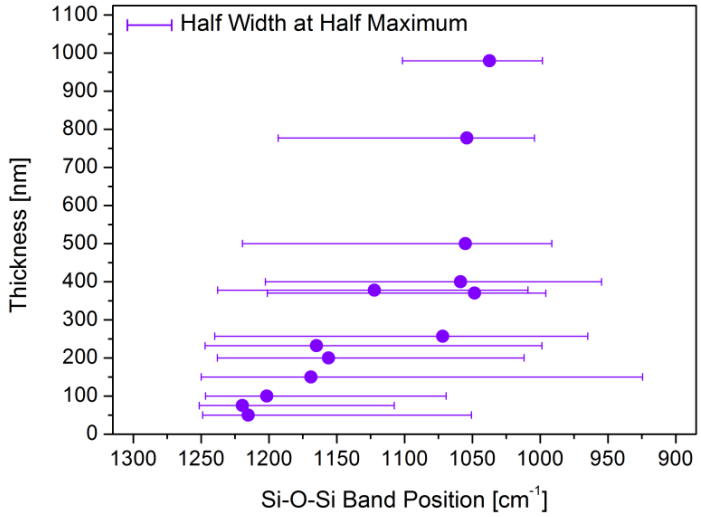

Figure 7.56: Half width at half maximum for different film thicknesses (full spectra reported in Figure 7.54).

As for the broad –OH stretching band at higher wavenumbers, some of the absorption spectra in the 3800-2800 cm^{-1} range are reported in Figure 7.58: in this case, too, the normalized intensities have been preferred to the 'as recorded' values. The selected bands present almost the same shape, with noticeable contributions from the isolated hydroxyl groups and from adsorbed water or weakly interacting –OH groups in the bulk. The 30 nm thick film, which has been previously excluded from the general 4000-400 cm^{-1} overview because of strong deformation of the bands in the low wavenumber region, is here reported. The considerably higher –OH band shows how, with such reduced thicknesses, the morphology and, probably, the chemical composition of the film is not yet stable, leading to less compact films with higher abundances of terminal

groups, like possibly $(OH)_3$. It is also noteworthy that for the other samples the relative intensities of the band are fairly independent on the final thickness, hinting again at a deposition process that remains stable and unaltered throughout the whole films growth.

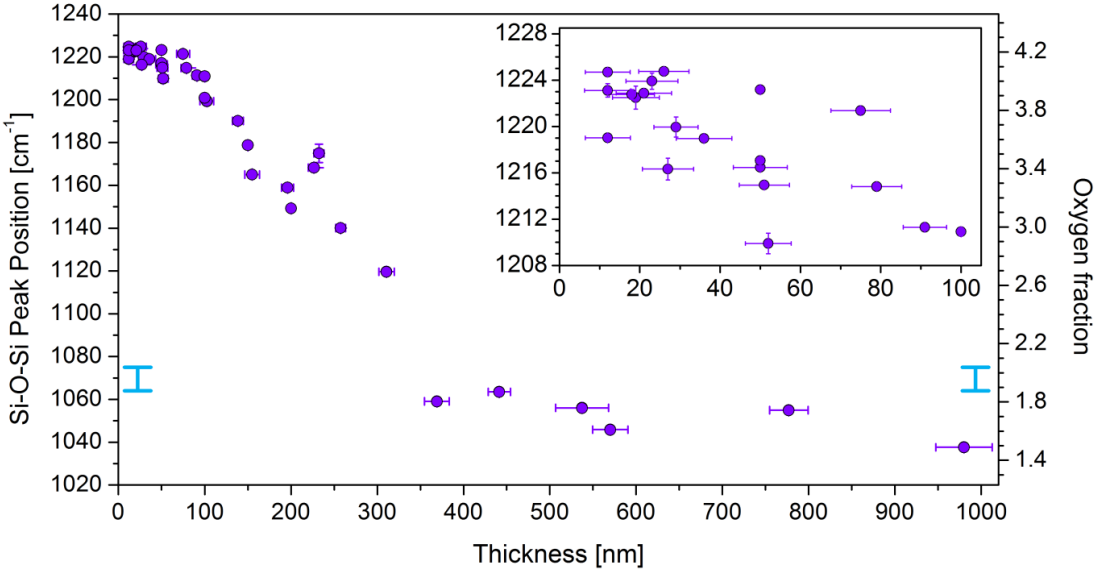

Figure 7.57: Peak positions of the main Si-O-Si band as a function of the film thickness (left) and corresponding oxygen fraction (right). In the inset, expanded view in the 0-100 nm thickness range, and reference for crystalline, stoichiometric SiO_2 (blue bars).

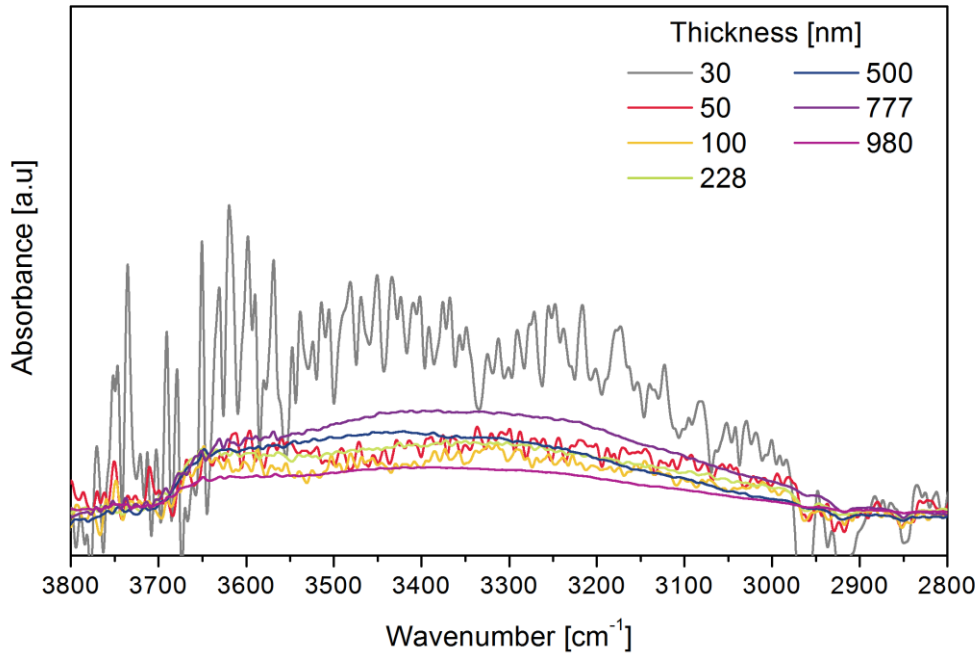

Figure 7.58: Detail of the –OH stretching band in the 3800-2800 cm^{-1} range for some of the spectra displayed in Figure 7.54 (with normalized intensities).

7.3.3 Oxygen permeation curves of barrier films with different thicknesses

The transmission rates analyses for samples of different thicknesses have been carried out according to the procedure reported in Section 6.4.1. The results are reported in Figure 7.59. For very thin films, around 20 nm or less, the evaluation of the thickness is hindered by the resolution limits of the perthometer (see also Section 6.1), which in turn at least partially affects the high dispersion shown for the OTRs. Starting already from 30 nm, however, the measured values stabilize to a minimum that remains unaltered for the rest of investigated range. The lowest and highest measured values in such stable range both occur for a 50 nm thick sample, because of the intrinsic fluctuations in the barrier performances. The range in which the OTRs are constant extends for almost two orders of magnitude and it is in direct contrast with the trends found in literature [27, 31, 38], according to which, at some point, internal stresses in the film, limits of its adhesion on the substrate and/or excessive heating induced by the prolonged duration of the deposition step cause damages and breakage in the film, and consequently a sharp increase in the corresponding OTR. This threshold, which mostly depends on the experimental conditions, can already occur, for plasma-deposited thin film, around 250 nm [239]. For very thin films, on the other hand, a less-than-optimal surface coverage, in case of an island growth mechanism, or fluctuations in the chemical composition of the first molecular layers [240] result in worse barrier performances. Poor adhesion can be ruled out, thanks to the activation of the polymeric substrate and the formation of a strong interphase with proper chemical bonds [36, 56, 57, 240] typical of a plasma-aided deposition process. For further considerations on the film morphology and growth mechanism, see also next section. The onset of the stable section for the investigated samples corresponds to significantly lower thicknesses than what achieved in RF reactors for industrial applications in PET coatings [222, 241], in which the OTRs of the deposited Al_2O_3 film remained unstable until 120 nm and the TiO_2 films, while reaching a minimum for 30 nm, too, already showed damages at 120 nm. Similarly deposited SiO_x films have shown to stabilize in the 70 to 100 nm range [35], although for radiofrequency plasmas the ionic bombardment and the associated thermal load tend to cause a retrograde increase in the OTRs because of induced cracking [27, 35].

In the current case, on the other hand, it has to be also noted that even the yet unstable films, with a thickness in the 10 to 20 nm range, already exhibit barrier improvement factors around 10 or higher. The plateau achieved at higher thicknesses is limited in the first place by the barrier properties of the substrate, which determine the amount of oxygen that permeates to the polymer-barrier interface [7], and in the second place by the presence of defects in the layer. As the latter grow together with the films, increasing the thickness does not equate to a further decrease of the OTRs, as explained in Section 3.4.

Such assumption is reinforced when looking at the shape of the oxygen concentration vs. time curves, as none of them shows a typical Fickian shape. More importantly, their rise time re-

mains fairly unaltered even when the thickness is increased, again in contrast with a diffusion driven by Fickian permeation in a defectless layer. In some cases, as the one reported in Figure 7.60, the rise in the curve shows different, progressively smaller slopes, as the O_2 permeating through the defects is detected first (with a further distribution in the transmission contribution of the defects depending on their size); the tail of the curve is instead dominated by the proper bulk diffusion and it alone is affected by an increase in the film thickness, shifting to longer times (in the case reported, a small increase in the signal is still detected after one day and a half from the start of the measurement, opposed to the steady-state value attained, for 100 nm films, usually after around 20 hours).

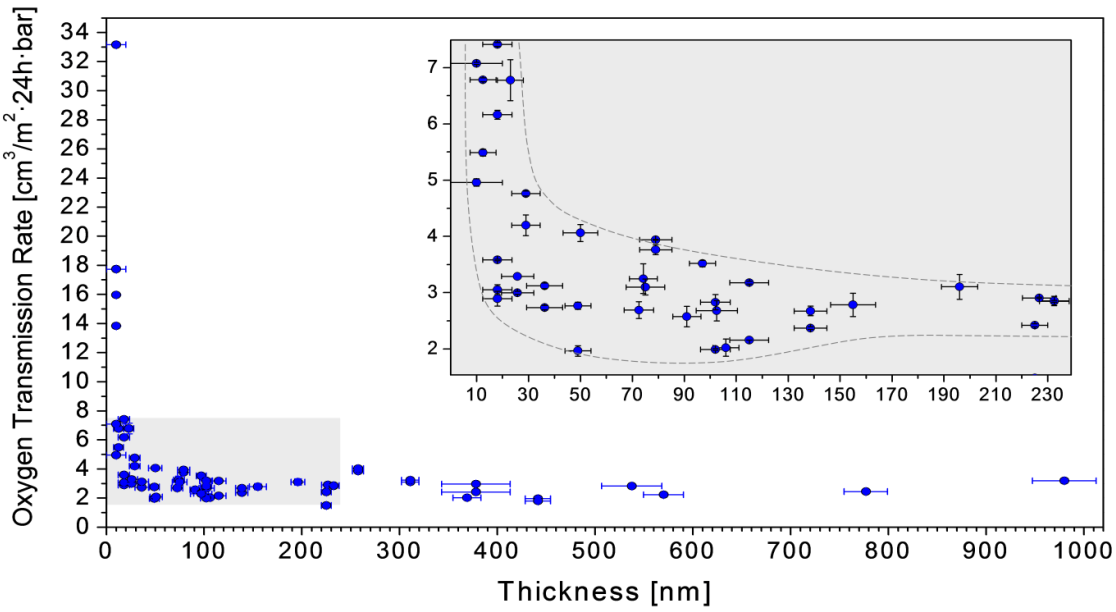

Figure 7.59: Normalized oxygen transmission rates as a function of thickness for samples deposited out of a 40/1 oxygen-to-monomer plasma feed at a power of 555 W. In the inset, details from the area shaded in grey in the main plot.

Further confirmation of the role played by defects in the overall diffusion is provided by the defects densities calculated through the pinhole test, shown in Figure 7.61. The trend as a function of the film thickness is in very good agreement with what observed for the OTRs, and the values remaining constant even for very thick film both show the lack of stress-relief cracking processes [27, 31] and the intrinsic resilience of the films, even when subjected to noticeable bending (see also Section 7.3.1). The thinner films exhibit on the other hand inhomogeneous surfaces with a great dispersion in the number of defects, hence the high errors associated with the average values. The nucleation phase associated with such thin samples shows also the same trend observed for organic films with poor barrier properties detailed in Section 7.1.5, as reported in Figure 7.62. The preponderant role played by defects on the overall permeation process, on

the other hand, causes the curves of crystals observed at the microscope in a fixed frame vs. time to show no major difference even for very different thicknesses, with the start of the nucleation phase being almost constant for all values and located between 5 and 10 minutes after the start of the test, not unlike the same effect previously observed for the oxygen permeation curves.

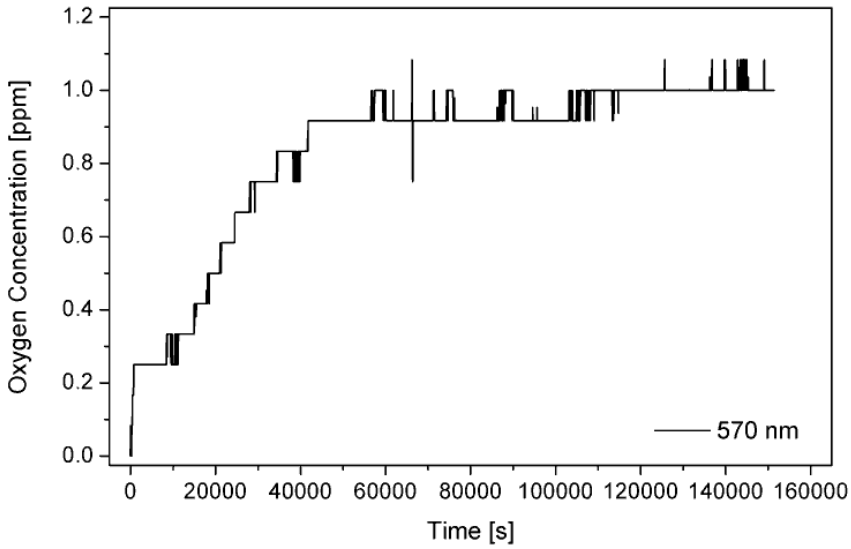

Figure 7.60: Recorded curve of the concentration of oxygen in the carrier gas versus time for a 40/1 barrier with a thickness of 570 nm. The shape of the curve is limited by the resolution of the oxygen detector. The curve up to 20000 s is dominated by diffusion through defects, followed by a mixed section and a tail controlled by pure Fickian diffusion (from 60000 s onwards).

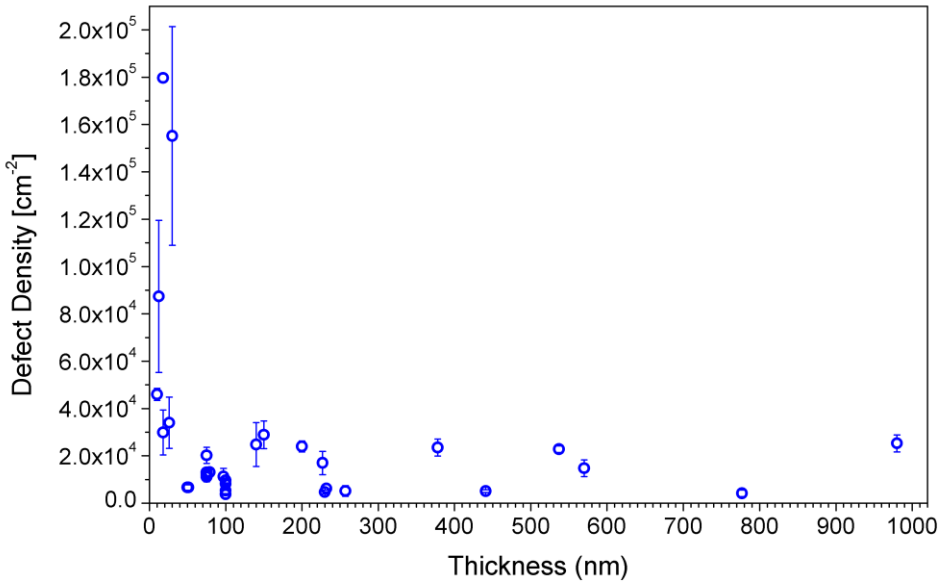

Figure 7.61: Numerical defect density for 40/1 barriers as a function of their thickness.

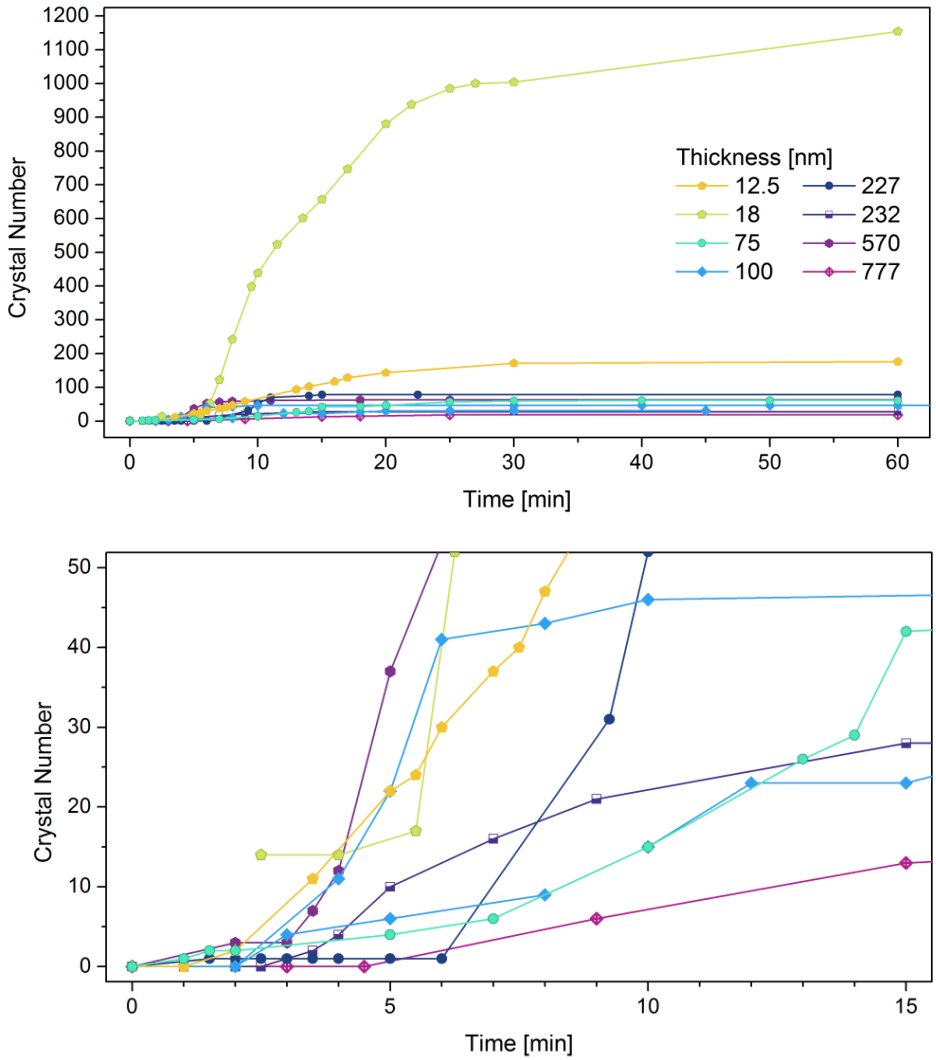

Figure 7.62: $CaCO_3$ crystals number in a fixed frame of the investigated barriers with different thickness as a function of time. t = 0 is set for the beginning of the pinhole test as described in Section 6.5.3 (top). Bottom: detail of the first minutes of the test run. Because of delays in placing the sample-holding cell under the microscope, for the 18 nm thick sample the first recorded picture already showed fully formed crystals.

When calculating the diffusion coefficients for the investigated film thicknesses, the values obtained by isolating the barrier according to the ideal laminate theory have also been normalized by their thickness. The calculated values, reported in Figure 7.63, show again great fluctuations for still unstable film up to 20 nm thick, followed by a stable region with a plateau extending up to 1 µm. The values in this stable region show not only that the PET plus thin film performanc-

es are influenced only by the barrier (hence the almost perfect correspondence between the coefficients for the bilayer and the barrier alone), but that the normalized diffusion coefficients appear to decrease linearly with the thickness. This sort of artifact highlights how the upper molecular layers in thicker films do not contribute to their barrier performances, as their volume is easily permeated by oxygen through the defects [38]. It is therefore useless to carry out longer deposition steps and increase the thickness of the barrier beyond the threshold value at which its properties stabilize. In the current case, such value could already be fixed around 40 or 50 nm, although the fluctuation related to the average values keep decreasing until a thickness of 100 nm.

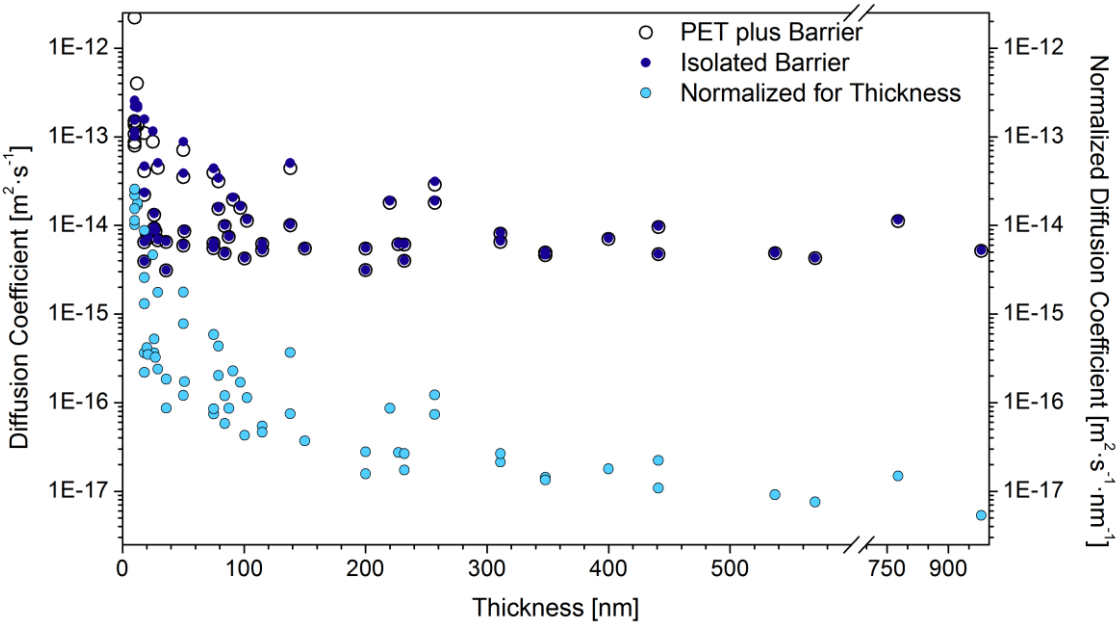

Figure 7.63: Diffusion coefficients as a function of the thickness of 40/1 films for the bilayer substrate plus barrier and for the barriers alone (left y-axis), with the latter values calculated by means of the ideal laminate model. The isolated coefficients are also reported as normalized for the barrier thickness (right y-axis).

7.3.4 Morphology at different thicknesses and growth mechanisms

Besides the calculation of surface defects densities, the pictures acquired during the pinhole test may help shed more light on the surface morphology and, when coupled with the previously commented data and results from further analyses, and to propose a tentative commentary on the growth mechanisms of the investigated films.

Figure 7.64 shows an overview of representative crystals found on samples with different thicknesses: for the thinnest barrier, either spherulites with needle-like shells or patchy, fluffy aggregates are to be found on the surface. No stars or otherwise shaped crystals resembling those for the uncoated substrate or the organic films have been spotted. It is clear how, even at such small thicknesses, the films already exhibit the same inorganic character previously found in the 100 nm counterparts. For thicker films the crystals still present the typical spherulite aspect, with structures both closed or open, much similar to those reported for a 100 nm sample in Figure 7.25. For very thin barriers, moreover, not only a very high dispersion in the average defect density – already apparent in Fig. 7.61 – but also in the size and distribution of crystals is to be observed, as shown in Fig. 7.65. All data thus far presented hint that the thinnest layers are homogeneous in their coverage of the substrate but neither in their chemical composition nor in their physical properties.

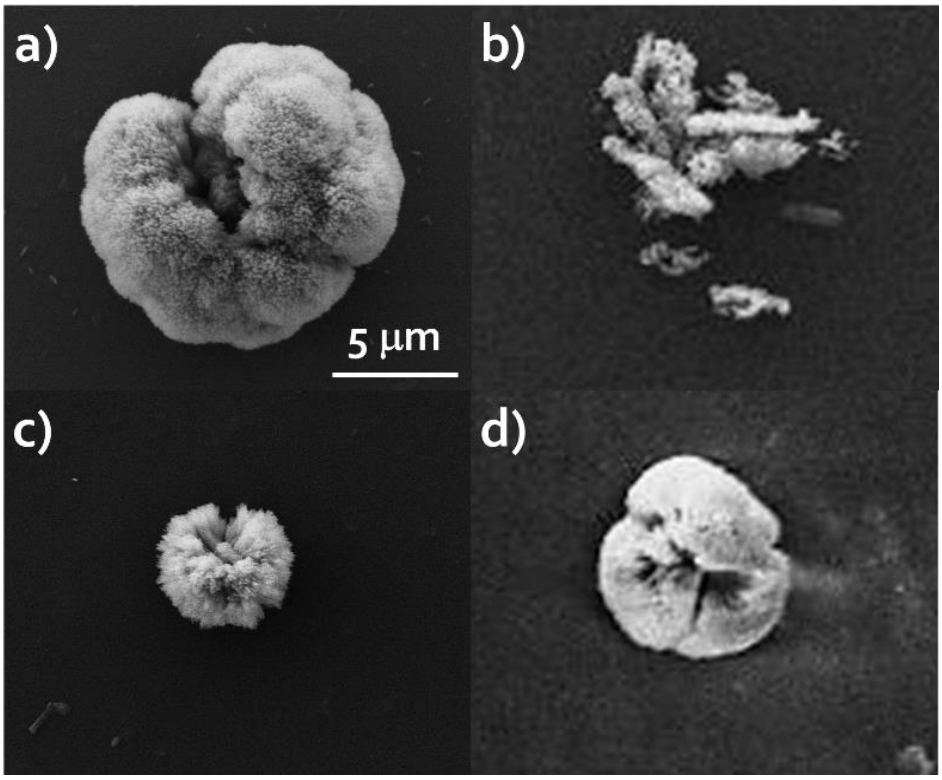

Figure 7.64: Detail of calcium carbonate crystals and other aggregates spotted on the surface of a 10 nm (a and b), of a 50 nm (c) and of a 200 nm (d) thick inorganic barrier with a 40/1 oxygen-to-monomer ratio.

In order to determine the structure of the first few tens of nanometers deposited, then, a picture of the section of such barriers via electron microscopy needed to be acquired. The sample chosen for the investigation has been deposited on a glass substrate with a significant thickness,

in order to observe also eventual variations in its physical structure. Its nominal thickness, measured by means of the perthometer, is equal to 777 nm, the second highest value among the investigated barriers. The sample has then been fractured by means of a wire cutter and a shard of suitable size has been further prepared as described in Chapter 6.3.2. The resulting pictures, acquired in two different spots along the jagged edge, are reported in Figure 7.66. The thickness of the film, measured again with the help of the in-built scale of the frames, proved to be equal to 768 nm, in excellent agreement with the average calculated through macroscopic methods.

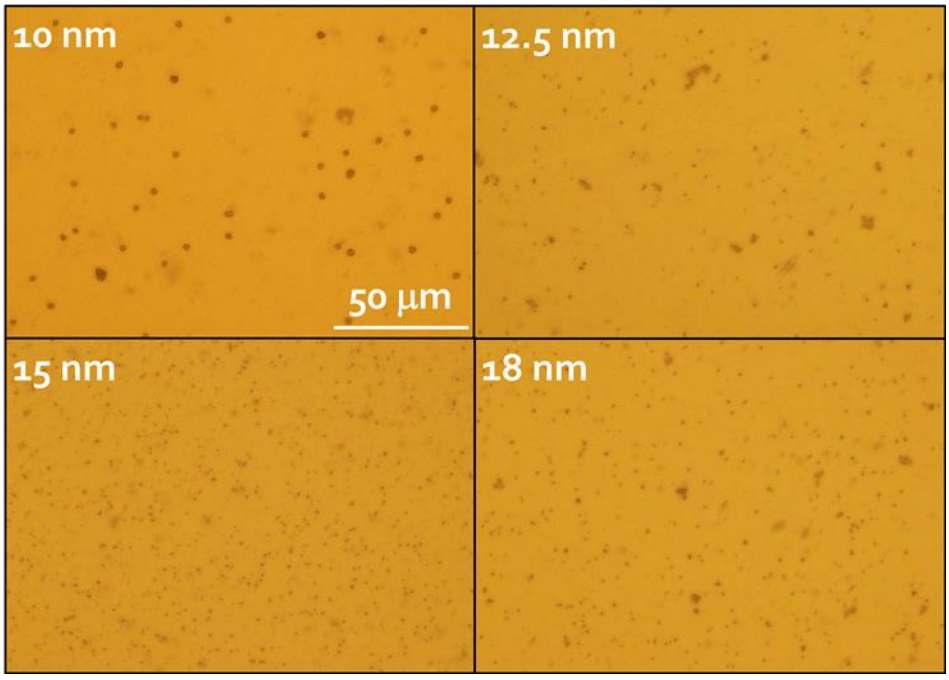

Figure 7:65: Frames from the camera connected to the optical microscope of the surface of 40/1 inorganic barriers with different thickness after one hour of pinhole test. All pictures taken with a x10 magnification.

Even at the highest magnification (100k), no discernible inhomogeneity in the first tens of nanometers of the barrier is to be found. On the contrary, as seen in Figure 7.66 c, their chemistry must already be close enough to the silica-like material detected via IR, as the small creases in the glass substrate, induced at the moment of its fracturing, easily propagate in the overlying barrier, too. The two materials, moreover, are similar enough for their color to be almost the same, and for their interface to be only faintly discernible. For films with different chemistries and consequently different colors, see also Figure 8.8 in Chapter 8.2. The first 200 nm of the films are shown to be extremely dense and homogeneous, without discernable free spaces or other disruptions of their structure. The uppermost layers of the film, on the contrary, exhibit a marked grainy structure, which also results in the gently undulated, but still uninterrupted, surface. Such

structure is particularly noticeable in Figure 7.66 c, in the small chipping exposing the columnar structures of the bulk. Some small indentures, possibly micro-cavities originating during the film growth and partially induced by the change in its bulk, can also be noticed in the upper halves of the films in Figure 7.66 b and c.

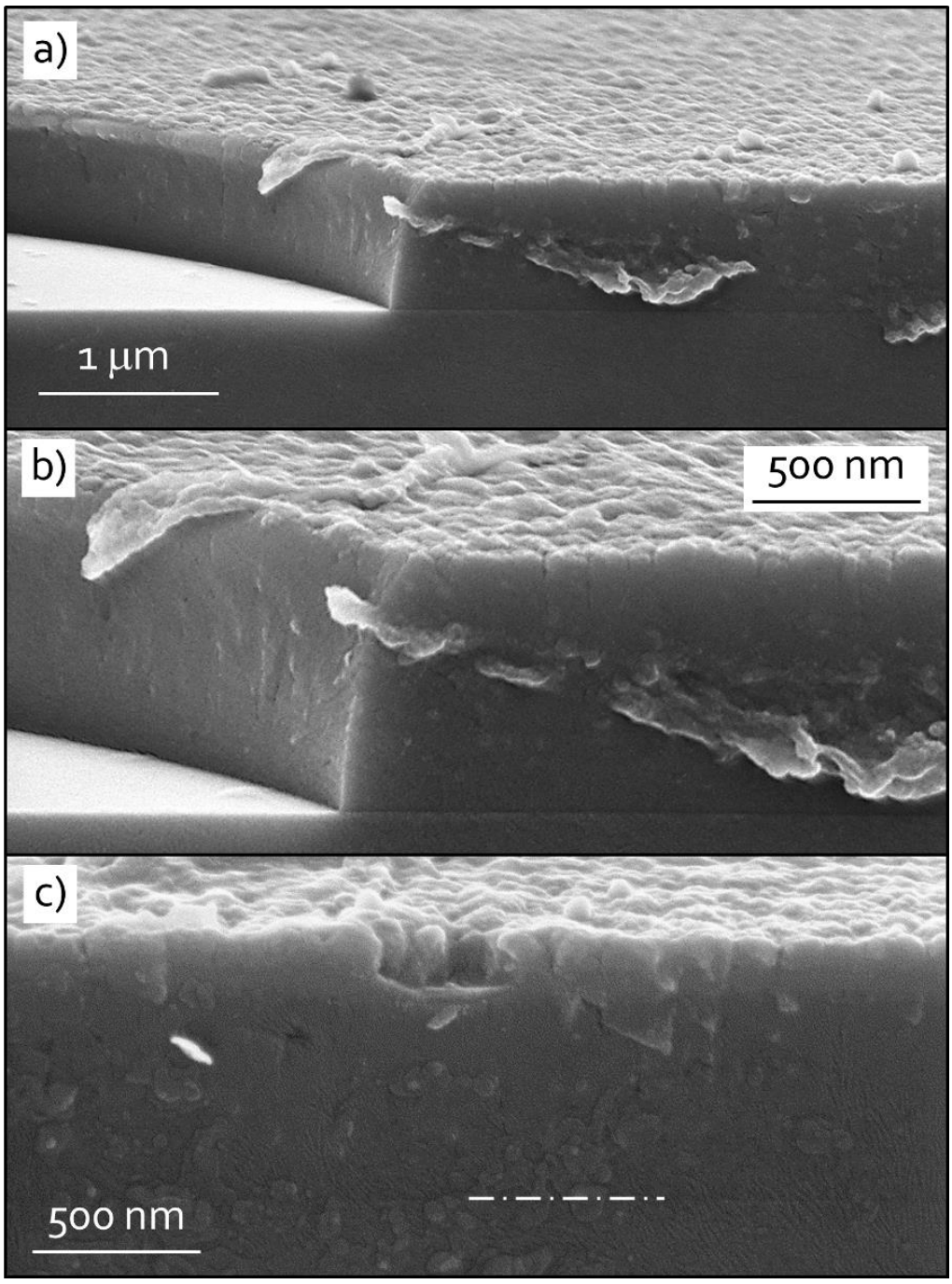

Figure 7.66: SEM pictures of a section of a 40/1 barrier layer deposited on glass, with a magnification of 50k (a) and 100k (b and c). (b) Scans performed at the Fraunhofer IGB.

The aforementioned columnar formations seem to be completely self-assembled and to originate spontaneously out of the more inchoate structure at the interface. Such suggestion is corroborated by Figure 7.67, which shows a composite picture of two SEM scans at different magnifications. As a consequence, the resolution is sub-par and no better image is available. Nonetheless, it portrays a shard of the thin film that has been chipped away when the glass has been cut. Underneath it, and partially hidden, lies the film still attached to the substrate. Its lateral section on the right side of the picture clearly shows a cliff-like structure arising from a bulk exhibiting a much finer and homogeneous grain. The columns show predictably an inverse tapered structure, with their nucleation origin being much narrower than their final width.

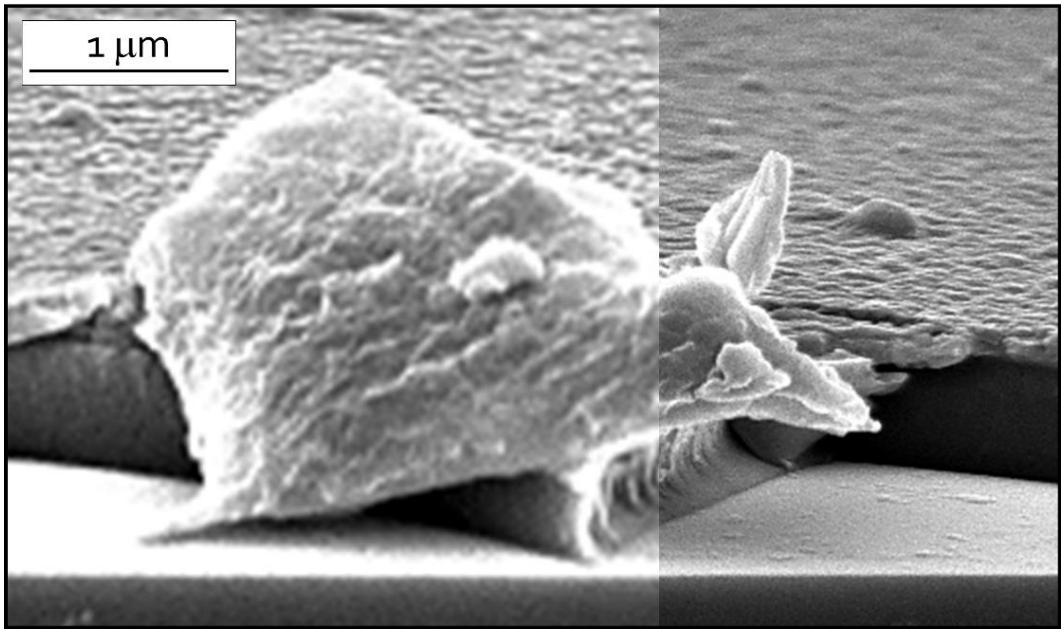

Figure 7.67: Detail of a shard of barrier being dislodged during the clipping of the glass substrate, and the underlying still attached film. The composite picture is patched from 10k (right) and 25k (left) scans of the same spot. No higher resolution available. Pictures acquired at the Fraunhofer IGB.

In light of the results thus far presented, it is now possible to at least speculate on the growth mechanisms of the investigated barriers, in the oxygen-to-monomer ratio range that ensures an inorganic chemistry to be reached in the final film, at least. The growth in the initial couple of hundreds nm of the films, most likely, follows a layer-by-layer (Frank–van der Merwe) or at worst a mixed layer-plus-island (Stranski–Krastanov) mechanism [242]. In both cases, the interactions among the incoming particles once they reached the surface are not greater than those among them and the substrate molecules. Such effect is undoubtedly reinforced by the activation of the surface caused in no small part by exposure to the VUV developed in an oxygen-rich plasma,

which however are not as destructive as those produced in RF plasmas [56]. As a consequence, the film covers mostly uniformly the surface even in the very first few tens of deposited nanometers. Diffusion of the adsorbed particles on the surface, while they still retain some mobility, plus possible coalescence effects between adjoining deposition nuclei can be inferred to take also place [243], thus resulting in a continuous and smooth film, as seen in SEM pictures, not suffering from shadowing effects and the consequent voids embedded in the bulk [92]. Such growth is in direct contrast with the one for thermally evaporated SiO_x films, which takes place almost exclusively through an island mechanism, and thus requiring at least 50 nm for the initial silica clusters to coalesce and to seal the underlying surface [215]. The almost surely present interphase among the deposited film and the substrate, which Bergeron *et al.* [57] consider to extend for several tens of nanometers, cannot be spotted in such pictures. Considering also the IR spectra in Section 7.3.2, it should be concluded that such intermediate region, in the current cases, must be relatively narrow, if present at all – at least on glass as substrate; on polymers the effect will most likely vary –. Inside such amorphous silica-like film, with a stable chemistry mostly independent on its thickness (except for, perhaps, the aforementioned very thin initial interphase), however, a nucleation of some sort of grains takes pervasively place around the 200 nm mark: it is unclear what causes such different structures to first originate, as the plasma parameters are kept fixed for the whole deposition step. A possibility could be minor changes in the film chemistry, unable to be detected by IR analyses alone, which could be in turn prompted by its growth on the eventual interphase and a readjustment of its structure, or different kinds of mechanisms for a barrier-on-PET and a barrier-on-barrier deposition. It is also unclear whether such grains are mono- or polycrystalline in structure: the formation of similar and even bigger and more defined structures in PECVD processes is well-known and has been extensively modeled [244, 245], but always considering radio-frequency plasmas with a strong ionic bombardment contribution. As the latter effect is completely lacking in microwave plasmas, and the deposition process is carried out at practically room temperature (with temperature and energy of the embedded particles being the fundamental parameters in the Anders' model [245]), it is safe to assume that a high crystalline degree in the current films would be in any case difficult to attain. Nonetheless, the precursors for the columnar structure are structurally different from the rest of the initially deposited film (as already discussed regarding Figure 7.67). As a consequence, they may also possess different growth rates, thanks perhaps to bulk diffusion inside the film [244] or, if they originate first as lumps on the growing surface, their geometrical shading and the solid angle they occupy may cause them to collect incoming particles from the plasma at a higher rate than their immediate surroundings. Both cases would result in a preferential growth of such structures at the expenses of the inchoate bulk: the columnar structure become progressively larger as the film grows, further accelerating in turn their own growth process. As a final result, the columns become the only constituent of the film. Shortly before this happens, small voids can be incorporated in the bulk, as the large columns now effectively block the incoming particles to diffuse on the surface and

reach the underlying amorphous film, as suggested by the small indentations seen in particular in Figure 7.65 c. Periodic renucleation at later stages [244], as shown in a schematic representation of the barrier's structure in Figure 7.68, cannot however be *a priori* excluded, although no direct observation of the process for the current samples is available. From a thickness of half a micron onwards, then, the columns grow in direct contact with each other, with virtually no free space among them. The coverage of the substrate will therefore still be adequately good, as partially seen on the tilted chip in Fig. 7.67. The connecting material among them, if they are assumed to possess at least a higher degree of crystallinity than the initially deposited film (but for conclusive evidence of this X-ray diffraction studies of the films would be required), could then be assimilated to some sort of grain boundaries, a much more porous and less dense structure. Contrary to what suggested in classical thin film growth mechanisms [244], however, the current structure does not exhibit poor lateral strength, nor a particular brittleness in such interstitial regions. As shown in fact by the SEM pictures, the relatively thick film still breaks evenly, without preferential directions. Furthermore, the jutting uppermost layers, left hanging after the film broke, that could be seen in Fig. 7.65a and Fig. 7.66, further show a good lateral cohesion of the investigated sample. Such complex structure proves to be very efficient in relaxing the internal stresses of the film and prevent the latter to break or to catastrophically lose its properties. Nonetheless, the interstitial material must however be less dense than the columns, as it would nicely explain the apparent decrease of the normalized BiF reported in Fig. 7.62 and previously discussed. At the same time, their properties are still close enough to those of the columns that they do not act as preferential passage for permeand gases, and as such no increase in the defect densities is to be seen. Because of the – inferred – mostly similar chemistry, on the other hand, they neither prevent the pinholes from keeping growing along the film structure.

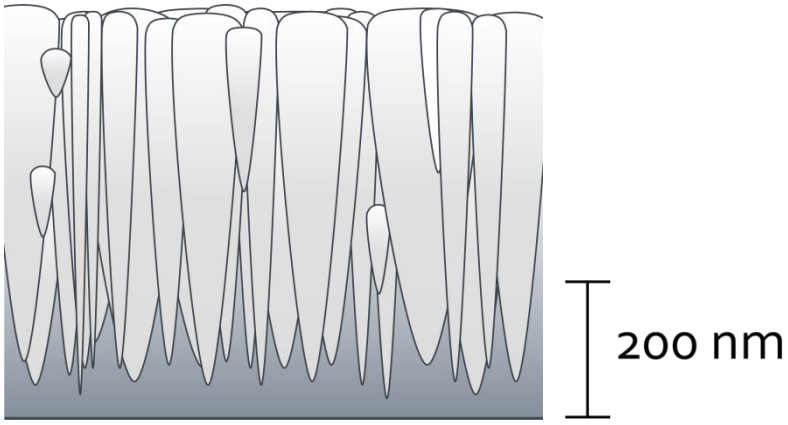

Figure 7.68: Proposed structure for a 40/1 barrier film with a thickness higher than 0.5 µm. In dark grey the initial amorphous film, in light grey the columnar structures becoming visible around approximately 200 nm of thickness. Based after [247] and [248].

In light of this, even though thicker barriers show favorable qualities that differ from most of other PECVD films, for barrier applications they are mostly useless. As standard thickness for the subsequent investigations, therefore, the chosen value has been 100 nm, which constitutes an optimum between the deposition times required and the resulting transmission rates; it also allows straightforward comparisons with previously investigated films (Chapter 7.5), knowing at the same time that it could be lowered to 75 or even 50 nm without considerable loss of its barrier performances.

7.4 Barrier films flexibility and resilience

In the following section, a selection of some of the most promising films thus far produced has been investigated in order to test their resilience: the 40/1 ratio has already resulted in the best barrier improvement factors, while the 70/1, albeit still occasionally presenting similar improvement values, as already extensively discussed in section 7.1.3 and 7.1.4, also hint at presenting a more brittle that requires further investigations. A systematical testing the film resilience becomes necessary especially in light of the barriers application for flexible electronic devices, as it will later be shown in Chapter 8, too. Some requirements for encapsulations to be suitable for OLEDs, among others, are that the barriers are both mechanically robust, and display good adhesion to the substrate, in order to remain stable for the whole lifetime of the device. For FOLEDs this also implies that the barriers must be flexible and still retain their properties, in the first place [5]. The mechanical stability and the properties of the investigated film as function of the surface morphology of the to-be-coated substrate will be finally shown in Section 7.4.2, together with the correlated effects on the films barrier properties.

7.4.1 Bending cycles

A measure of the resilience of the plasma-deposited films can be provided by calculating their oxygen transmission rates before and after one or more bending cycles. The micro- and sub-micro-damages possibly caused by the stresses thus induced in the films can be indirectly detected as a noticeable increase in the transmission rate values. Repeated bendings can in fact artificially originate micro- and sub-micro-cracks, first, and the increase their size and density, as the latter act as a stress-relieving mechanism in the thin film bulk [27, 31]. When an applied tensile stress overcomes the internal cohesive forces, a crack is originated. For compressive stress, buckling takes place, especially in films with poor adhesion, and later detachment. Cracks' propagation itself, after a certain number of cycles, can in turn also result in debonding or delamina-

tion of the coating from the underlying substrate, with large flakes of the thin film coming off the surface [249]. All these damaging processes result in smaller or bigger increases in the thin barriers' transmission rates.

The experimental steps for the bending test are listed below:

i) the selected barrier film is deposited on several 10 x 10 cm^2 PET substrates in the same PECVD process, in order to have several spares;
ii) one sample is first cut and its OTR is measured in the System I apparatus. This will provide the initial, unbent reference value;
iii) the same sample, once extracted from the permeation cell, is subjected to one or more bending cycles with a fixed curvature radius, consisting of a first bending for tensile and a second for compressive stress. The procedure is schematically illustrated in Figure 7.69. The bending is carried out by pressing the sample against a glass or metal cylinder of the appropriate radius, by means of two forceps. The anchoring points lie outside of the area tested during the OTR measurements, in order to avoid unwanted and involuntary indentation of the film. In case of damages or mishandling, the procedure is started from point i) again with a new sample;
iv) the bent sample is tested again;
v) points iii) and iv) are repeated until the desired number of cycles is reached.

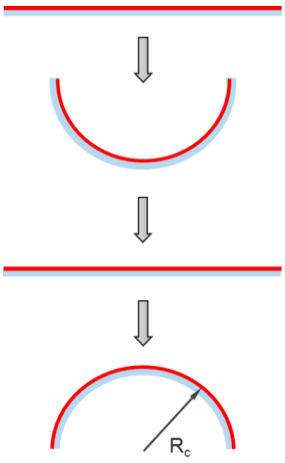

Figure 7.69: Steps in one bending cycle for a coated sample. First bending induces a compressive stress in the barrier (red) and in the substrate (blue), the second a tensile one. The radius of curvature, indicated with R_c, remains constant in both steps.

The necessary and repeated handling of the samples, and their contact (sometimes also scratching) against the cylinder surfaces are unavoidable but provide a qualitative measure of the re-

sistance of the barrier against 'being used'.

The OTR measurements have been decided to be repeated after 1, 2, 5, 10, 15, 20, 30 and 50 bending cycles (the notion that each cycle consists of a pair of bending steps will not be explicitly mentioned from now onwards, for the sake of brevity), for two curvature radii equal to 1.8 and 0.75 cm (also labelled as R_c=MAX or $R_{c,M}$ and R_c=min or $R_{c,m}$, respectively).

As briefly reasoned in the introduction to the current section, the selected samples have been produced at a fixed power of 555 W and with an oxygen-to-monomer ratio of 40/1 and 70/1, with the power value being the most investigated one and the first ratio having already provided the most promising barriers, while the second can act as a comparison. Moreover, the test can help highlight eventual differences in the fine internal structure of the two films, which could be only presumed, but not conclusively proven, based on their SEM pictures (see also Section 7.1.3). In order to exclude unlikely effects on the total OTR caused by damages in the PET substrate, an uncoated sample has been prior subjected to the same bending procedure. The results are displayed in Figure 7.70 for both curvature radii. The limited variations in the oxygen transmission rates, for both cases, do not exceed the normal range of measurement reproducibility for the same sample reported in Chapter 5.2. It is therefore possible to conclude that, predictably, the repeated bending cycles do not damage in any way the polymer foil. Eventual increases in the OTRs for the substrate plus barrier systems will therefore be ascribed to the latter's damages alone.

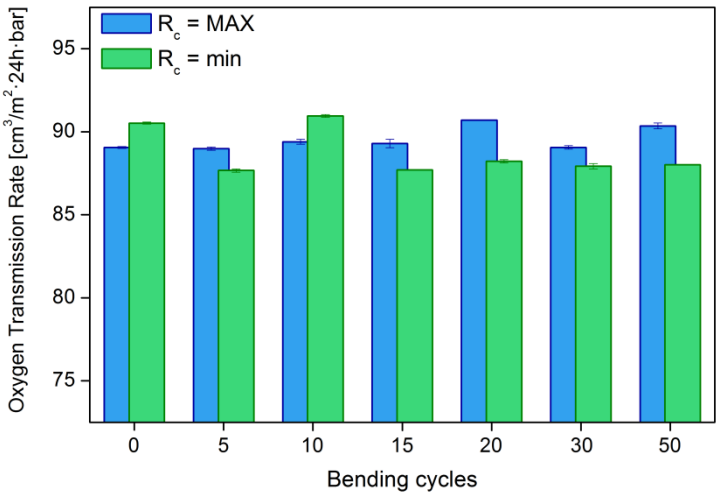

Figure 7.70: Oxygen transmission rates for an uncoated PET foil after being subjected to two cycles of bendings with a curvature radius of $R_{c,M}$ = 1.8 and $R_{c,m}$ = 0.75 cm.

Figure 7.71 reports the oxygen transmission rate values for both series of bending cycles for the 40/1 oxygen-to-monomer ratio. The initial value relative to the unbent sample has been tak-

en as reference and used to normalize all the subsequent measurements, in order to more readily display the relative variations. For the larger curvature radius, i.e. 'milder' bending, the OTRs remain unchanged even after 50 cycles, with the small fluctuation in the oxygen transmission rates never exceeding 1%. For the smaller curvature radius the normalized OTRs start increasing after two bending cycles before reaching a plateau after 15 cycles and then a final value 20% higher than the unbent reference. Such variation is still within the dispersion range obtained for unbent samples with the same operational parameters, equal to 150% (from a minimum value of 1.99 $cm^3 \cdot m^{-2} \cdot 24h^{-1} \cdot bar^{-1}$ to a maximum value of 3.59 $cm^3 \cdot m^{-2} \cdot 24h^{-1} \cdot bar^{-1}$). The micro-damage induced with the higher stress loads caused by the smaller curvature remains stable after a transient regime, between 2 and 15 bending cycles, during which it first originates. Considering the reduced increase in the OTRs, furthermore, it is also possible to exclude delamination or flaking processes, which would have resulted in much steeper increases in the transmission rates. For a further increase in the latter, then, a much higher number of cycles is first required, for the onset of other wear mechanisms.

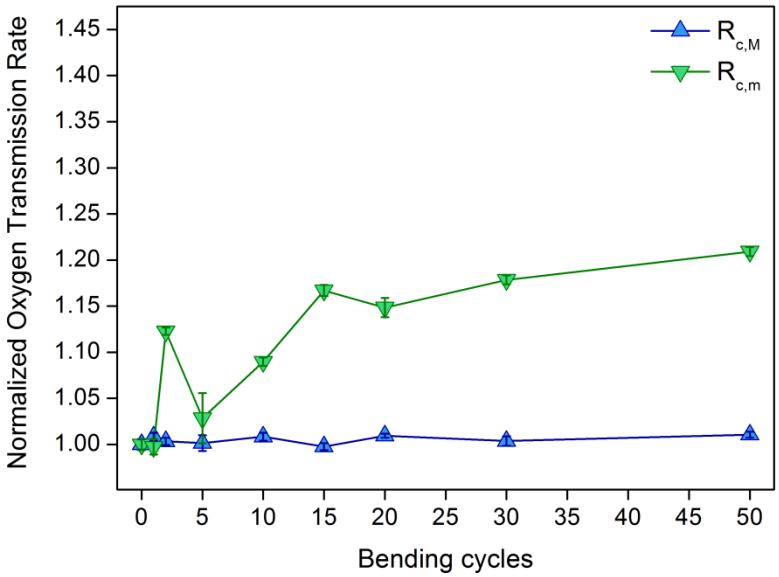

Figure 7.71: Normalized oxygen transmission rates for 0 to 50 bending cycles and the two curvature radii, $R_{c,M}$ = 1.8 and $R_{c,m}$ = 0.75 cm, for samples deposited with a gas feeding ratio of 40/1.

The normalized OTRs for bent samples with an oxygen-to-monomer ratio of 70 are reported in Figure 7.72. Here, even the bigger curvature radius is enough to damage the thin film after 5 bending cycles. The onset remains the same for the smaller R_c. The normalized OTRs remain in both cases stable in the 15 – 50 cycles range, with a final relative increase of 15%. With reduced applied stresses (i.e. the bigger curvature radius) required for damaging the films, the 70/1 ratio

samples do seem to be more brittle than the 40/1 counterparts, as already proposed in section 7.1.3. Even in this case however the damages do not propagate and result in only a moderate increase in the transmission rates.

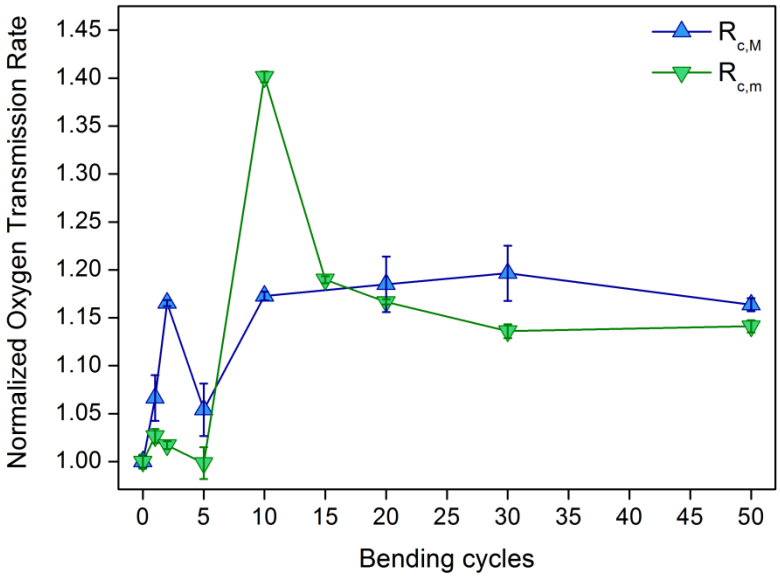

Figure 7.72: Normalized oxygen transmission rates for 0 – 50 bending cycles and the two curvature radii, $R_{c,M}$ = 1.8 and $R_{c,m}$ = 0.75 cm, for samples deposited with a gas feeding ratio of 70/1.

Finally, a selection of 40/1 films with a thickness spanning the whole range investigated in Chapter 7.3 has also undergone the full bending cycles series, for the bigger curvature radius (R_c = 1.8 cm): the test can in fact give insight on the stability of these films and on their internal stresses, where present. The results over 50 bending cycles are displayed in Figure 7.73; the 100 nm sample is the one already shown in Figure 7.71. For the thinnest film, 12.5 nm thick, the increase in the OTRs takes first place after two full bending cycles, and it never reaches a defined steady-state value, with the final OTR being twice the reference value and keeping on growing. A 32 nm thick film shows already a more similar trend to the 100 nm one, reaching an almost steady final value equal to 1.06. Subsequently thicker films, up to around 220 nm, remain unaffected by the applied stresses and show no sign of damage. The thickest investigated film, after the onset taking again place between the second and the fifth bending cycle, has a final OTR increase of only 8%.

The thinnest achievable films in the current reactor experimental configuration are shown to be still unstable, and with a poor adhesion to the underlying polymer. The 200% increase in OTR hints at surface delamination processes, with the detachment of coating flakes: such effect can be enforced by void spaces (keyholes) present in the films in the first moments of their growth

[63, 247]. The lack of direct observation at the SEM of such features may be ascribed to glass instead of PET being used as substrate for those investigated barriers.

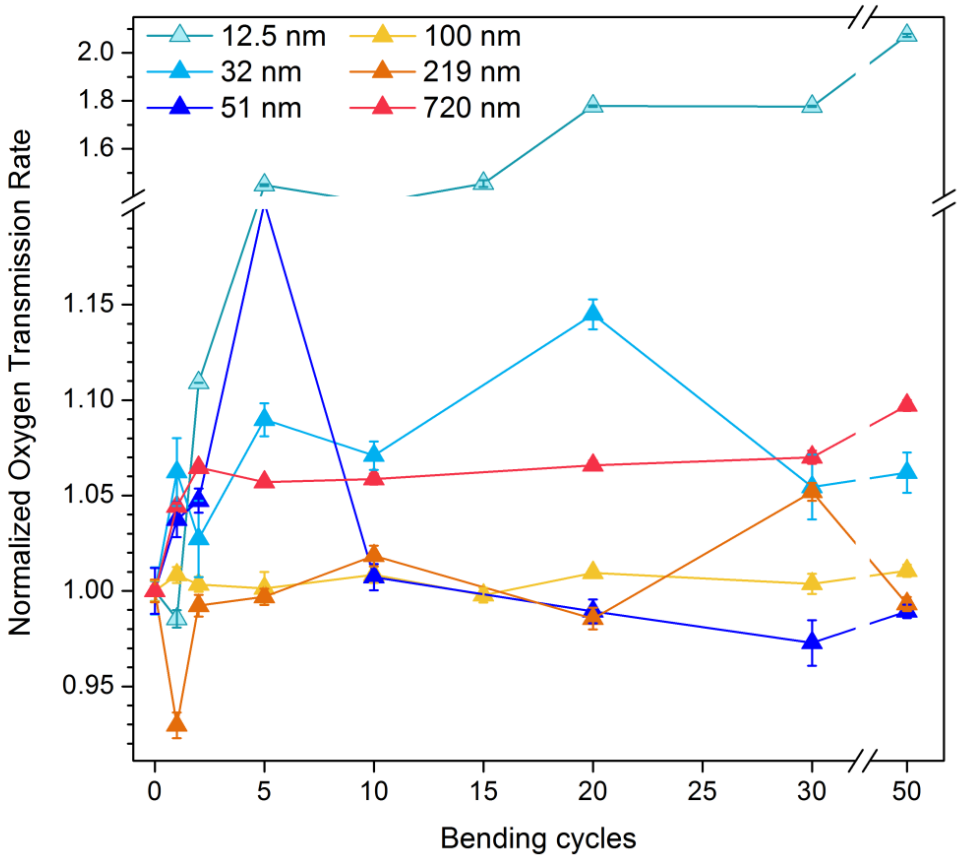

Figure 7.73: Normalized oxygen transmission rates for a 1.8 cm curvature radius over 50 bending cycles for 40/1 oxygen-to-monomer ratio samples with different barrier film thicknesses.

The steady increase in OTRs on the other hand show a propagation of cracks/continuous flaking process with further stresses applied to the film. The effect can be worsened if, as typically is the case for very thin PECVD films, their uppermost layers, which in this case coincide with the totality of their bulk volume, are richer in organic content coming from the precursor molecules [104, 108]. For such films, an increase in the coordination number of oxygen atoms to Si at the expenses of organic substituents, methyl groups in particular, corresponds to an almost linear increase in their Young's modulus [251] and a consequent better resilience against strain. The chemical instability, rather the morphological one, being the main responsible for the poor resilience [241] of the thinnest film is confirmed by the trends observed in the other samples: at 30 nm, with its bulk consisting of inorganic elements alone (see also Section 7.3.2), the film already shows a stable behavior. The test further reinforces the idea, first advanced in Chapter 7.3.2 upon

SEM investigations, that the thicker films, albeit possessing a structure which is at least partly columnar in their upper fractions, still present a lateral strength and cohesion good enough to prevent the cracking of the bulk even in case of repeated applied strains.

For these samples too, finally, the absolute final OTRs lie still in the same range of corresponding values for unbent samples. They are reported, as red circles with a black frame, in Figure 7.74.

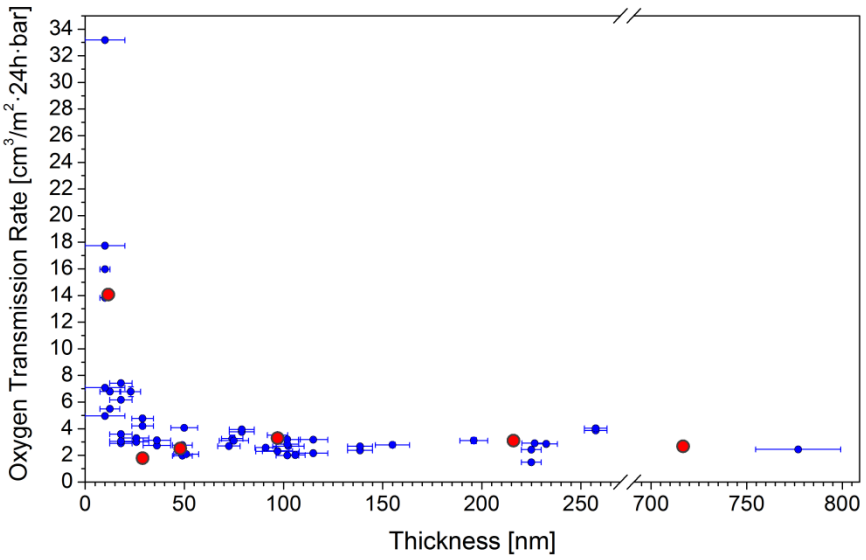

Figure 7.74: OTRs after 50 bending cycles from Figure 7.73 (red circles with black frame) compared to the unbent OTRs versus film thickness from Figure 7.59.

7.4.2 Deposition on substrates with various roughnesses

Surface roughness, especially when induced by crystalline antiblock particles, can have a dramatic effect on the barrier performances of the thin films deposited by means of PECVD [7, 251], as shown schematically in Figure 7.75. In case of a polymeric substrate with both crystalline and amorphous domains on the surface (Figure 7.75 a), in particular, the first steps in a plasma deposition process consist of a surface activation and/or etching, with a general increase in the mean roughness (Figure 7.75 b), especially in the amorphous domain, and consequently in the surface aspect ratio. The subsequent growing oxide layer presents then nanodefects scattered in its volume and pinholes extending along its whole thickness (Figure 7.75 c) [7]. The increased surface aspect ratio, depending on the growth mechanism of the film, may even result in an incomplete coverage of the substrate and much higher OTRs, or in fracturing of the barrier at the edges of the tallest surface features. Testing the performances of a barrier on a rough substrate can there-

fore provide qualitative evaluation of its flexibility, resilience and internal cohesion.

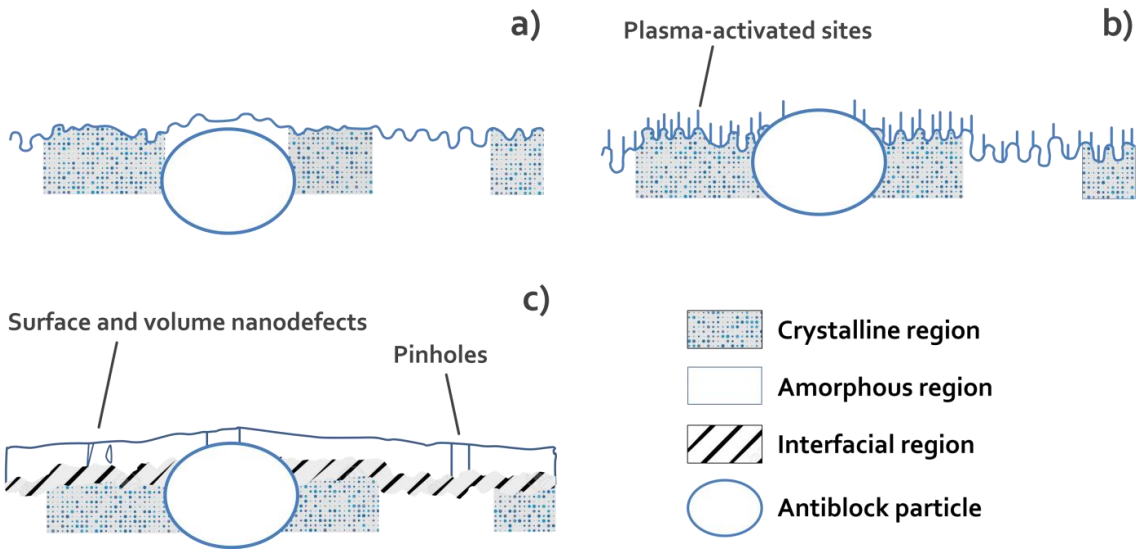

Figure 7.75: PET foil with antiblock particles prior to plasma exposure (a), after the first instant of plasma treatment, before the onset of the deposition processes, when the surface has been partially etched and otherwise activated (b), and at the end of the PECVD, with a thin film covering it that presents nanodefects in its bulk induced by the aforementioned surface roughness (picture based on [24]).

The barrier film produced with an operating power of 555 W and an oxygen-to-monomer ratio of 40/1 has been chosen for its properties in order to be tested when deposited on a substrate with a different morphology, a Melinex® 401CW PET foil from Dupont Teijin Films with antiblock particles on one side (see also Chapter 5.2 and Appendix A1 for more details on its properties, chemical composition and crystallinity degree). 100 nm of the chosen film have been coated on a piece of Hostaphan, one piece of Melinex with the 'smooth' side up and one piece of Melinex with the 'rough' side up in the same deposition step. Figure 7.76 shows the SEM pictures of the uncoated reference and the coated samples for the three surfaces.

Apart from the occasional dust particles (the white speckles in the pictures) on the surfaces, the Hostaphan foil and the Melinex on the smooth side (Melinex S) show no morphological difference. The rough side of the Melinex (Melinex R) exhibits on its surface the 50nm high antiblock particles with their preferential orientation. The deposition of the barrier film is excellently conformal, as the coated particles do not show lateral enlargements, nor the flat surface around them any inhomogeneity due to shadowing effects. Such results suggest that the particles participating in the film growth have enough time and energy to adsorb and migrate on the surface,

resulting in a continuous coverage with a homogeneous thickness. Such growth mechanism could have been at least partially inferred by observing the homogeneous and dense films reported in Fig. 7.66.

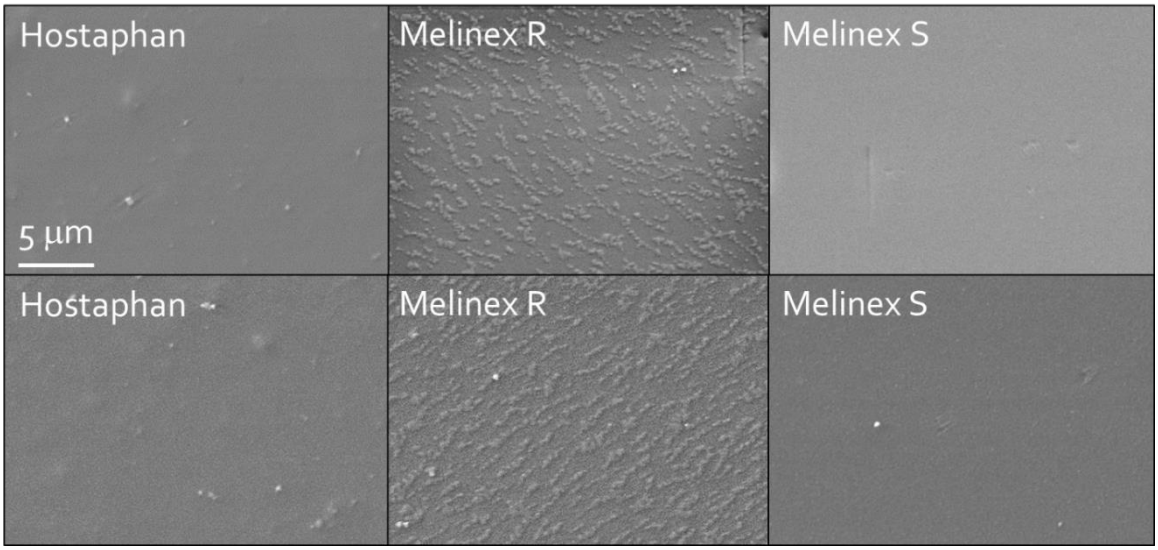

Figure 7.76: Scanning electron microscope pictures for polymer foils uncoated (top row) and with 100 nm thick inorganic film deposited with an oxygen-to-monomer ratio of 40/1.

The oxygen transmission rates measured for 100 nm films being deposited on both sides of the Melinex foil are reported in Figure 7.77, together with reference values for films Hostaphan deposited at the same operating conditions. It is possible to observe that the surface roughness bears no effect on the barrier properties of the film, as the OTR for a rough surface is in this case also the lowest value displayed. Barriers on the Melinex smooth side also result in absolute OTR values in the same range as the Hostaphan references. The barrier silica-like films are then flexible enough to coat structures with a height comparable to their own thickness without cracking. The coverage of the substrate must be complete, even in the areas possibly shadowed by the antiblock particles, otherwise a steep increase in the OTRs would have taken place. Such assumption, that the defects density is not particularly affected by the rough substrate is further confirmed by the CO_2 test pictures shown in Figure 7.78: both PET foils have been coated by a film deposited with a thickness of around 100 nm and an oxygen-to-monomer ratio of 40/1. The slightly different size in the crystals is caused by the different times having elapsed after the start of the test, one hour for the Hostaphan sample and two hours for the Melinex one. Both pictures show comparable defect densities and, in the latter case, the crystals are randomly and evenly scattered on the surface: had they been caused or enhanced by the presence of antiblock particles, they would have shown a preferential orientation that mimicked the pattern of the an-

tiblock particles themselves, such the one clearly visible in the SEM pictures in Figure 7.76. This is in strong contrast with other reports showing antiblock particles to be the main cause of defects in plasma-polymerized films, both for their densities and for their severity [7, 33], and stating that, more generally, the roughness of the PET substrate is the limiting factor for the overlying barrier films [25, 137].

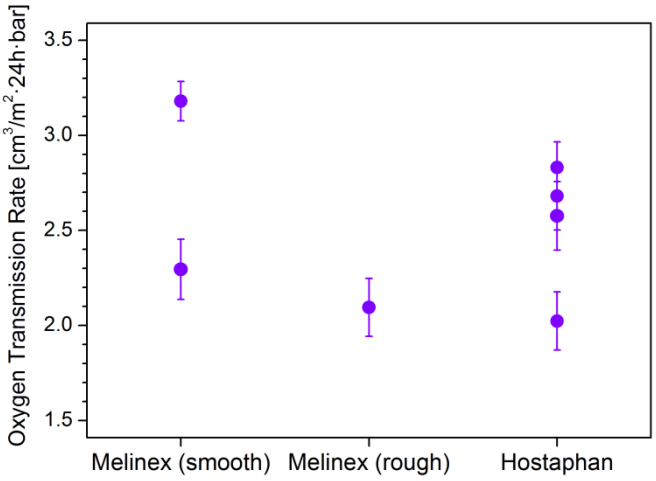

Figure 7.77: Oxygen transmission rates for 100 nm thick barriers deposited on both sides of Melinex PET foils, plus reference values for barriers on Hostaphan deposited with the same operational conditions (the latter have been previously displayed in Figure 7.15).

While the absolute OTRs measured values for the three surfaces are comparable to each other, however, as shown in Chapter 5.2 the uncoated reference values of the Melinex are half than those for the Hostaphan foil. As a consequence, in the former case the same barrier produces a BiF of less than 24 instead of more than 50. The cause of this ostensible discrepancy is the presence of defects in the barrier, which is not included in the Ideal Laminate Theory, and moreover, that the contribution of such defects to the overall transmission is dominant over purely Fickian permeation: according to the ILM, in fact, a substrate plus barrier system becomes independent on the properties of the substrate, provided the barrier has a much lower diffusion coefficient. In this case in fact:

$$D_b \gg D_{sub} \quad => \quad \frac{1}{D_b} + \frac{1}{D_{sub}} \simeq \frac{1}{D_b}. \tag{7.8}$$

Defects on the other hand offer little however to no resistance against oxygen permeation and can therefore invalidate the previous assumption, as in the current case (see also Section 7.1.4). It is therefore possible to conclude not only that the intrinsic flexibility and resilience of the investigated plasma-deposited barriers cause them not to depend on the surface roughness of the sub-

strate, even when the latter is comparable to the film thickness itself, but that their barrier performances are once again mostly limited by the presence of sub-micrometrical defects. Such intrinsic resilience, even in case of thicker coatings, is paramount if a successful encapsulation of flexible devices is to be carried out.

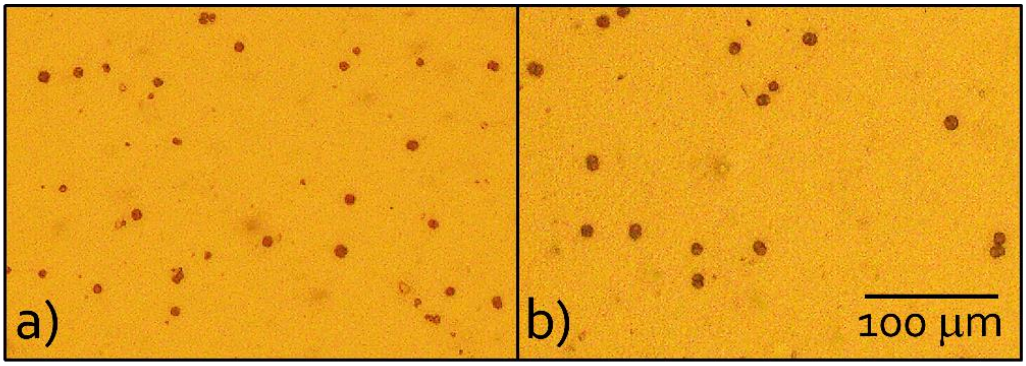

Figure 7.78: Optical microscope pictures taken for a 100 nm thick barrier layer deposited by means of an oxygen-to-monomer ratio of 40/1 on Hostaphan foil (a) after one hour of the sample-holding cell for the pinhole test and the same barrier film on the rough side of a Melinex foil after two hours.

7.5 Comparison of HMDSN- and HMDSO-based films

The starting operating conditions selected for the first studies on HDMSN-based barrier films, which ended up to be the most extensively investigated and to correspond to some of the best barrier films obtained in the current work, have been initially chosen because a previous, thorough study had been already carried out in the same reactor and at the same operating conditions for HMDSO-based films and their resulting barrier properties [52]. Organosilicon precursors as HMDSO are widely considered to be better starting materials than nitrogen-containing silanes and organosilicons, if the aim is to deposit inorganic silica-like thin films, as they already contain a starting oxygen content. HMDSO, with an O/Si ratio of 0.5, when compared to HMDSN exhibiting a null value, should then be the better choice. Tetraethoxysilane, for example, with its chemical formula $SiC_8H_{20}O_4$ and an O/Si value equal to 4 should be, according to this line of thought, an even better candidate [126]. On the other hand, considering the reactivity of atomic and excited molecular oxygen in plasma phase, most of the organosilicon precursors are considered to be good choices in order to deposit silica-like films, since their starting minor differences in chemical compositions are quickly erased by the pervasive oxidizing effect of O_2 as co-gas. With a mostly similar chemical structure, then, HMDSN and HMDSO employed for PECVD in the same reactor

were expected to yield practically indistinguishable results.

The first comparisons with the HMDSO-based films, in particular with their oxygen transmission rates, however, showed remarkable differences that prompted a more in-depth analysis and comparison of the films obtained from the two precursors. Such first comparisons are shown and discussed in Section 7.5.1, together with the resulting further investigations on film morphologies. Extensive analyses and comparison of the chemical nature of the two kinds of films, both via infrared ATR and single reflection spectroscopy, and also with XPS analyses of a chosen selection of oxygen-to-monomer ratios for both monomers, are reported in Section 7.5.2. Section 7.5.3 shortly presents and comments the normalized deposition rates for the two monomers with different oxygen dilutions, before drawing conclusions and proposing possible variations in the polymerization paths of the monomers in the plasma phase that can account for the different properties in the end films, in Section 7.5.4.

7.5.1 Barrier properties and film morphology

The first comparison has been carried out between the normalized OTRs of the two different series of films, obtained at the same operating conditions, which are listed in Table 7.7, and different oxygen-to-monomer ratios. The reference values for the uncoated PET foil for both series of measurements have been assumed to be equal to 1, thus normalizing all other values accordingly. Such supplemental step has been rendered necessary as the OTRs measurements for the HMDSO films have been carried out at a temperature of 30 ° instead of 35 °C. As shown in Section 7.1.6, however, a five degrees step in such temperature range does not cause excessive variations in the measured oxygen concentrations, while at the same time the calculated BiFs remain practically constant. It is in conclusion correct to simply compare the two series of data, once adjusted and normalized to 1.

Table 7.7: Operating conditions employed for the deposition of the HMDSN and HMDSO samples discussed in the current chapter.

Operating conditions	
Power	555 W
Pulse period	1 ms
Duty cycle	50%
Pressure	5 to 6 10^{-2} mbar

The corresponding OTRs are shown in Figure 7.79. It is possible to observe how, despite the minimum values being roughly the same for both monomers, and lying in the 40 to 45 O_2/monomer range, the dip in the transmission rates for HMDSN-based films has a much earlier onset, while good barrier properties for HMDSO arise only at higher dilution in the feed. Moreover, for very high oxygen-to-monomer ratios, the latter films quickly and severely lose their barrier properties, with the 70/1 samples showing transmission rates equal to those for the uncoated substrate, i.e. no barrier properties at all. Such trend is confirmed after carrying out pinhole tests for a small selection of newly-deposited HMDSO films, the results of which are shown in Figure 7.80 together with the data presented in Section 7.1.5 acting as reference.

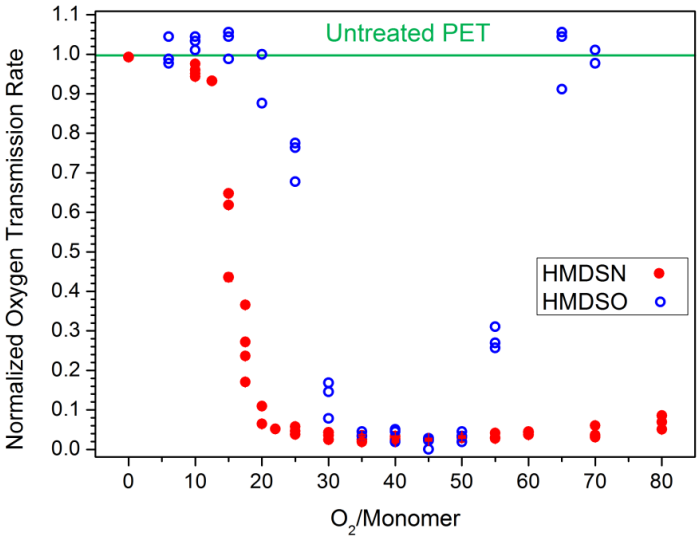

Figure 7.79: Oxygen transmission rates normalized to the uncoated PET reference for HMDSN- and HMDSO- based films 100 nm thick with different oxygen-to-monomer ratios. Results for HMDSN-based films have been previously presented and discussed in Section 7.1.4. Measurements for HMDSO-based films have been carried out at a constant temperature of 30 instead of 35 °C (see text for further details).

In this case, as previously discussed, defect density cannot be necessarily linearly correlated with the OTRs values, but still it is possible to notice how, for very high O_2/HMDSO ratios, the defect density becomes several orders of magnitude higher, and still significantly higher than the values recorded for HMDSN-based films with similar or even higher oxygen-to-monomer ratios. The pictures taken in real time and at the end of the pinhole test, while dense in defects, however, show a stochastic array of the latter, with no preferential arrangement of growth direction that could hint at fissures or other disruptions in the film structure. The rise in the defect density seems to start around a 60/1 ratio, roughly corresponding to the simultaneous increase in transmission rates. The 20/1 samples, on the other hand, show a similar defect density but the HMD-

SO-based film still lacks proper barrier properties. Nonetheless, the trend, once considering the 10/1, 40/1 and 70/1 ratios alone, is in general good accord with the one sported in Figure 7.79, as it can be better observed in Figure 7.81. The discrepancy, particularly for the high dilution ratio, is also present when comparing the OTRs measured before and after the pinhole test, as already done for the HMDSN-based films in Section 7.1.5. The results for HMDSO at the 70/1 ratio show a much smaller reduction in the transm ission rates, as shown in Figure 7.82 (to be compared with Fig. 7.28). While, with the test only been run once, i t is still possible for experimental errors to affect its results, it is however noticeable how the latter hint once again at a higher defect density, caused likely by different morphologies, chemistries or even diffusion mechanisms in the films: in the latter case, for example, a diffusion also including a large solid body contribution would then be less affected by the eventual clogging of the proper pinholes. Such results are quite surprising, as in general higher dilutions are preferable in order to oxidize and remove even the last organic remnants of the precursor, carbon atoms in particular. On the other hand, the highest attainable value for x in the SiO_x formula is 2 at best, i.e. pure silica is deposited, which is an almost perfect barrier against oxygen. Higher oxygen-to-monomer ratios should then *a priori* result in better barriers, with higher dilutions after such threshold resulting in no further improvement. Inspecting the morphology of the samples via SEM may help shed light on the matter. Figure 7.83 shows electron microscope pictures at a fixed magnification of the edges of cut coated foils for a selection of oxygen-to-monomer ratios for the two precursors. As mentioned in Chapter 7.1.3, the foils have been cut in order to induce an artificial cracking of the thin films and to analyze it.

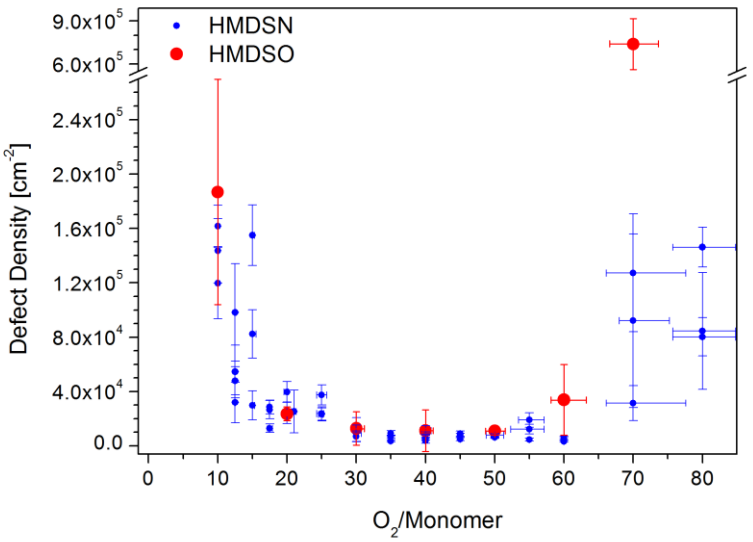

Figure 7.80: Defect densities calculated by means of the pinhole test for 100 nm thick films deposited via HMDSN and HMDSO and different amount of oxygen. The data for the former plasma feed have been already discussed in Section 7.1.4.

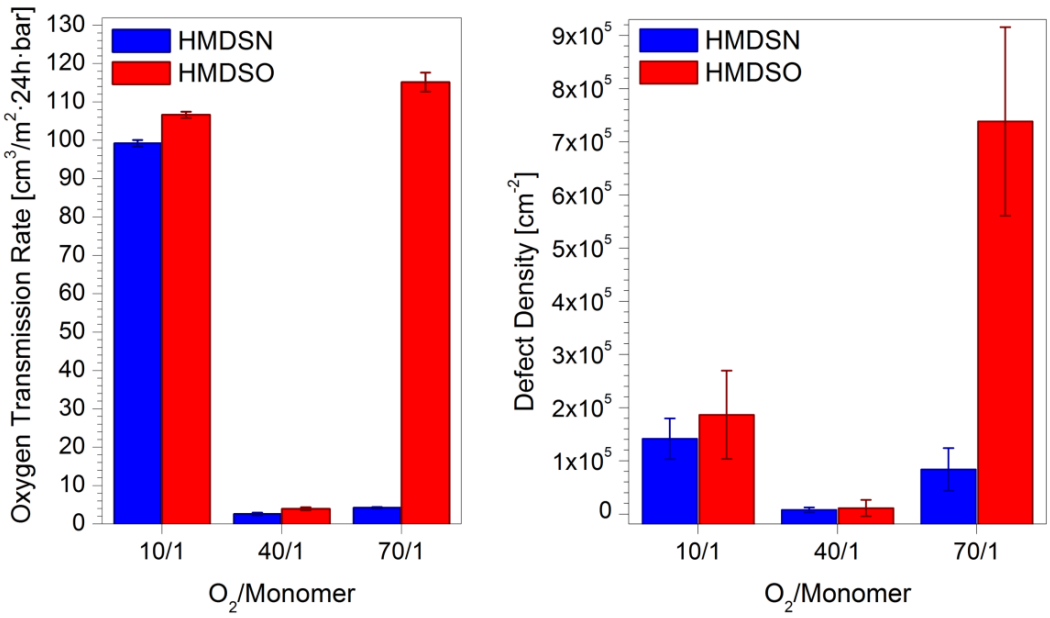

Figure 7.81: Summary of the measured OTRs and defect densities for HMDSN and HMDSO sample with 10/1, 40/1 and 70/1 oxygen-to-monomer ratios. The values for HMDSN are taken from the previously presented sets of data.

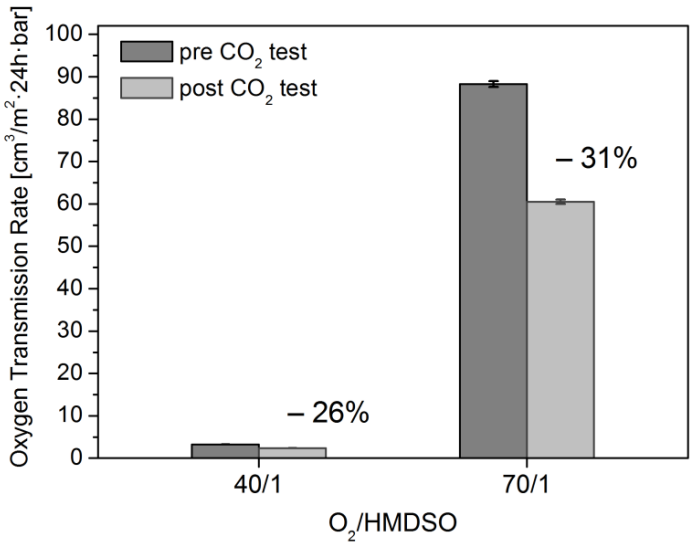

Figure 7.82: Oxygen transmission rates before and after the pinhole test for 100 nm thick HMDSO-based films with different oxygen-to-monomer ratios. The reductions in rates are reported as percentages.

It is possible to observe how the lowest ratios, corresponding to organic layers, exhibit curved, smooth fracture lines propagating from the edge. At 40/1 it is already possible to notice that the HMDSN-based film still sports the same kind of fractures, while the HMDSO barrier already presents the first straight cracks, some of them perpendicular to the others. Such behavior is preponderant for the 60/1 oxygen-to-monomer ratio, as the cracks are mostly perpendicular to each other, similar to those observed macroscopically in shattered glass, with brittle and grainy edges hinting at a granular or columnar-like inner structure of the film. In contrast to this, an even higher oxygen-to-monomer ratio for the HMDSN -based barrier shows only a minor presence of this second type of cracks, which for the most part still resemble those observed for the 40/1 case. Even the graininess at the edges is much less pronounced. Considering the already discussed tests carried out after the samples being bent and reported in the previous section, then, a first conclusion could be that the HMDSO-based films are inherently more brittle upon increasing the oxygen content in their plasma feed, their composition and morphology getting closer to those of 'real' glass. This cannot be ascribed to the presence of one oxygen in the precursor molecule, as for such high dilution such supplementary of oxygen is negligible. The oxygen in the precursor molecule, moreover, cannot explain why, in a counterintuitive way, the onset for good barriers takes places at higher dilutions than for HMDSN. Further insight in the chemical composition of both series of films is at this point needed, as it can specifically provide informations about this latter phenomenon.

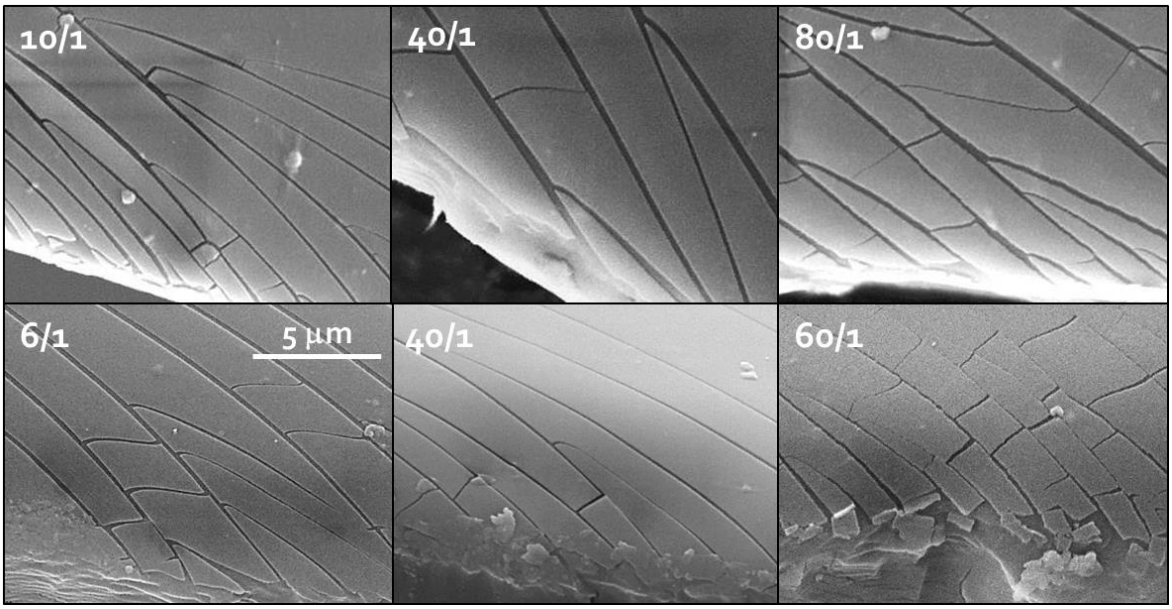

Figure 7.83: Scanning electron microscope pictures at a fixed magnification for HMDSN- (top) and HMDSO-based (bottom) films at three different plasma feed dilutions. Top row already shown in Fig. 7.14.

7.5.2 FTIR and XPS chemical analyses of HMDSN- and HMDSO-based films

The IR absorption spectra of the investigate range of O_2/HMDSO ratios previously obtained by Gaiser [52] with similar conditions than those reported for HMDSN-based films in Section 7.1.2 are reported in Figure 7.84. For the attribution of the peak, please refer to Table 7.1. It is apparent how the shape of the SiOSi main band closely resembles those previously shown for HMDSN, while the same trend of progressive oxidation with stronger dilutions of monomer in the plasma feed can be easily recognized. HMDSO spectra lack of course signals associated with the fragmentation of the amino-group in the HMDSN precursor. Similarly to what has been done in Section 7.1.2, moreover, the peak intensity of the methyl end groups signal normalized over the intensity of the SiOSi band and the peak position of the latter are also reported, together with the previously discussed data referring to HMDSN, (see Figure 7.85). For the former, the intensity is consistently higher for the HMDSO case: there is in particular no sharp abatement of the methyl signal in the 1 to 5 oxygen-to-monomer ratio range, contrary to what observed for HMDSN. In both cases the films seem to turn inorganic around the 30/1 mark, but for HMDSO a significant organic fraction is still present at 25/1, as observable also in the overall spectrum in Fig. 7.84, with a strong shoulder in the main SiOSi peak. Such prolonged presence of organic groups can be accounted for the worse barrier performances in such intermediate O_2/monomer range. It is worth of notice, on such account, that the 25/1 HMDSO sample shows the same methyl intensity than the HMDSN samples around the 15/1 dilution, and similarly, the OTRs of the former coincide with those of the latter.

As a partial counterpoint to the previous point, the SiOSi peak seems to stabilize for slightly smaller ratios in case of HMDSO as precursor. However, the final wavenumber values are practically the same for both monomers, and for HMDSO in particular they remain constant even for ratios higher than 60, where the quick failure of the barrier properties takes place. The latter does not seem to be caused then by a variation in the chemistry of the film, at least based on ATR spectra.

In order to better investigate the high-wavenumber range in which ATR spectroscopy fails to remain sensitive enough, a selection of different oxygen-to-monomer samples for both precursors has been deposited on molybdenum mirrors acting as substrates, with a fixed thickness of 100 nm, and then immediately analyzed by means of single reflectance IR spectroscopy. The procedure has been performed in the same spectrometer and with the same operating conditions described in Chapter 6, after removing the ATR unit and replacing it with a single reflectance unit in the instrument's chamber. The resulting spectra are displayed respectively in Figure 7.86 for HMDSN and in Figure 7.87 for HMDSO. The peak positions reported in Table 7.1 can be applied here too for the attribution of the signals. The poorer resolution of the spectra, when compared with ATR spectroscopy, is due to the multiple reflections in the latter that noticeably

increase the signal/noise ratio.

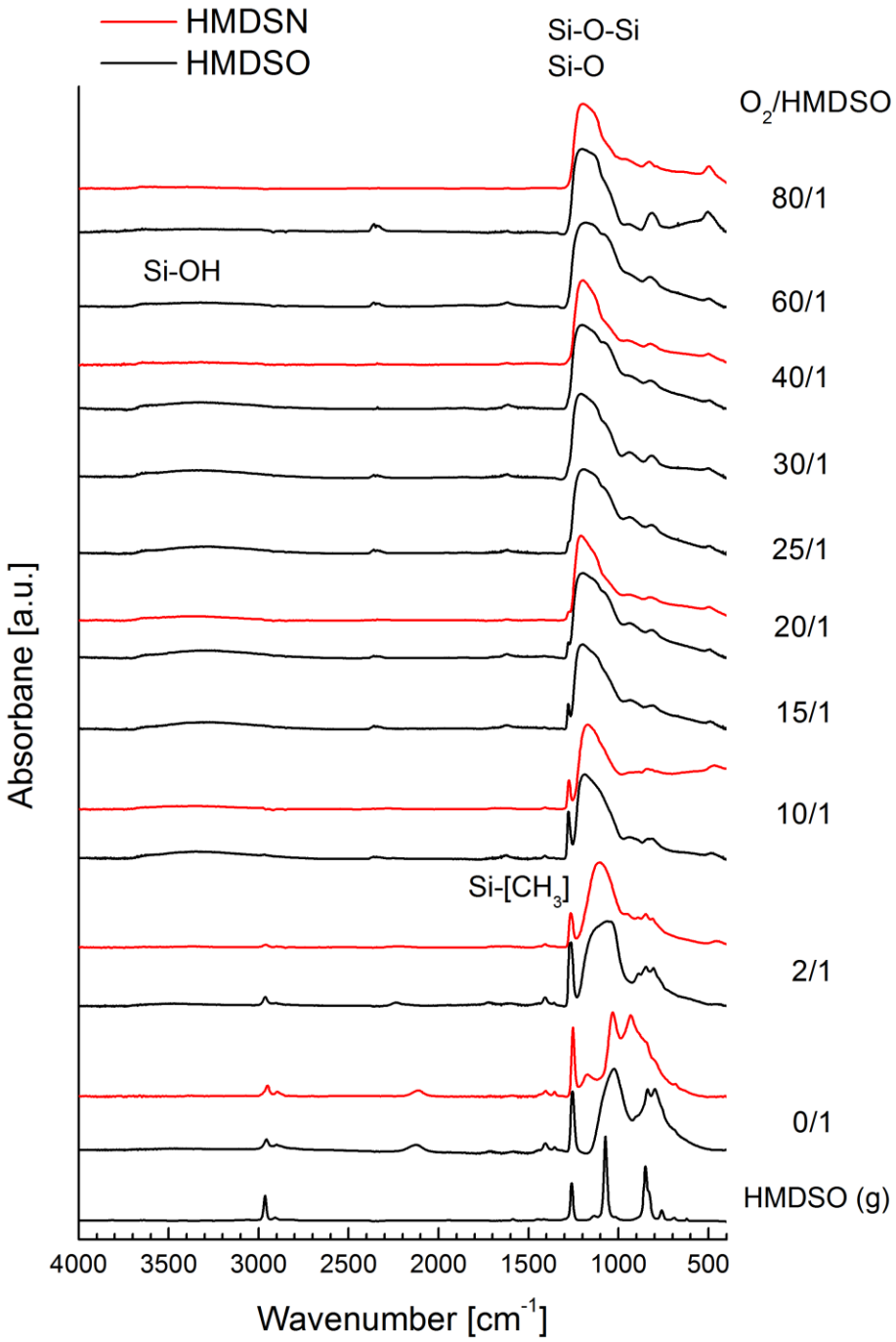

Figure 7.84: ATR FTIR normalized spectra in the 4000-400 cm^{-1} range for 100 nm thick films deposited via different O_2/HMDSO plasma feed, plus spectrum of gaseous precursor HMDSO as comparison. Data from [52]. In red, a selection of HMDSN-based samples, previously shown in Figure 7.5, for further comparison.

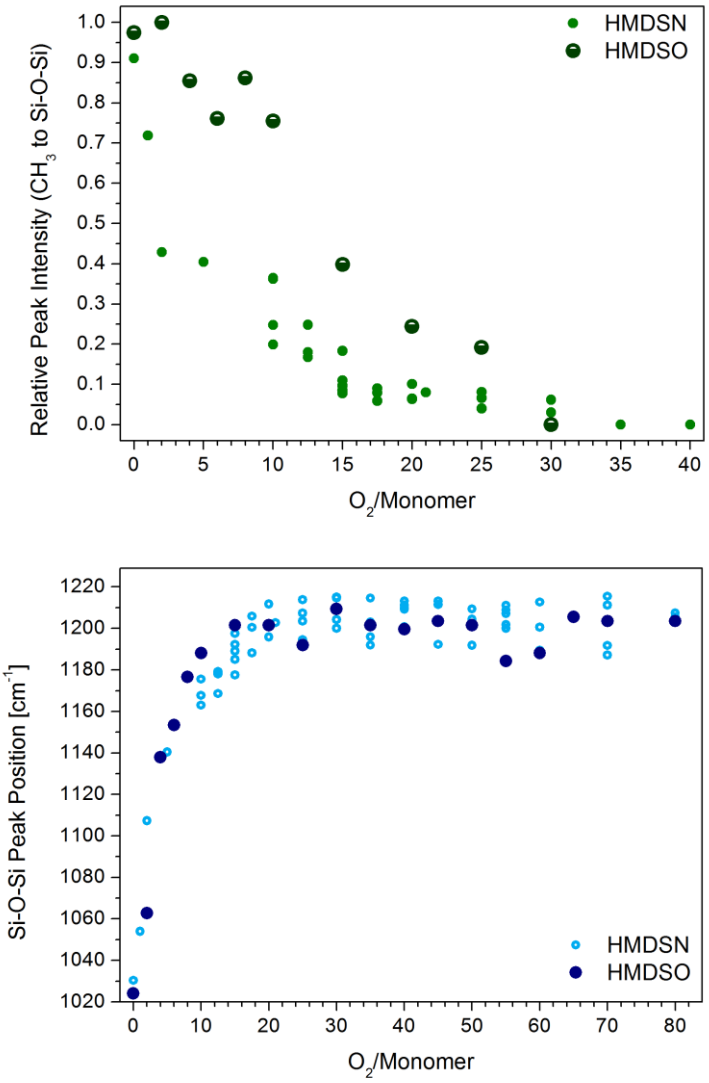

Figure 7.85: Relative peak intensity of the methyl band around 1275 cm-1 with respect to the main SiOSi band (top) and position of the main SiOSi peak (bottom) for HMDSN- and HMDSO-based films. Data for HMDSN have been previously presented in section 7.1.2. Data for HMDSO provided by [52].

The spectra still bear a close resemblance to those shown via ATR spectroscopy in Section 7.1.2. The minor deformation in the shape of the main SiOSi band and its satellite peaks at even lower wavenumbers are caused by the non-linear sensitivity of ATR spectroscopic methods. Incidentally, such phenomenon allows in this case to better discriminate the Si-O-Si, Si-CH_2-Si and Si-N-Si signals that form the main band of the spectra. For pure HMDSN, then, it is possible to observe how, even in absence of oxygen in the plasma feed, a distinct Si-O signal is present

around 1050 cm^{-1}. While it could have been originated by oxygen residuals present in the reactor chamber even after the pumping step, it has been reported [150, 252] that pure HMDSN films are extremely reactive with regard to oxygen, so much that even ESCA analyses conducted *in situ* immediately after the end of the deposition step revealed a considerable oxygen surface content, which reaches 30 % after only two hours in air [253]. In the current case, despite the small interval between the deposition step and the recording of the spectra, then, the chemistry of the pure HMDSN has already irreversibly been altered upon exposure to air.

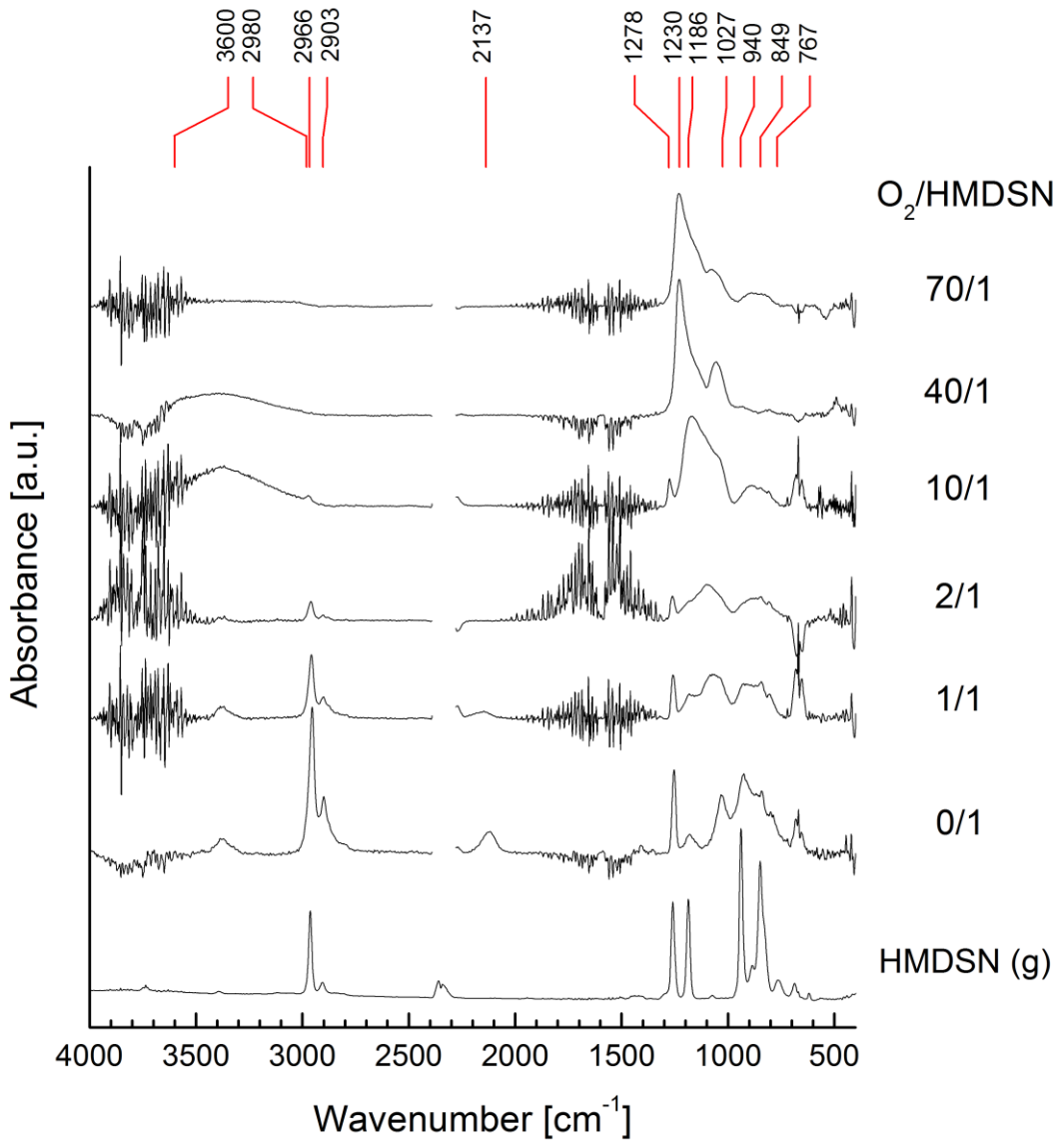

Figure 7.86: Single-reflection absorption IR spectra for a selection of samples with a thickness of 100 ± 5 nm, plus reference spectrum of the HMDSN precursor vapors. Missing data in the 2300 to 2400 cm^{-1} refer to unwanted CO_2 signals from residuals in the chamber atmosphere.

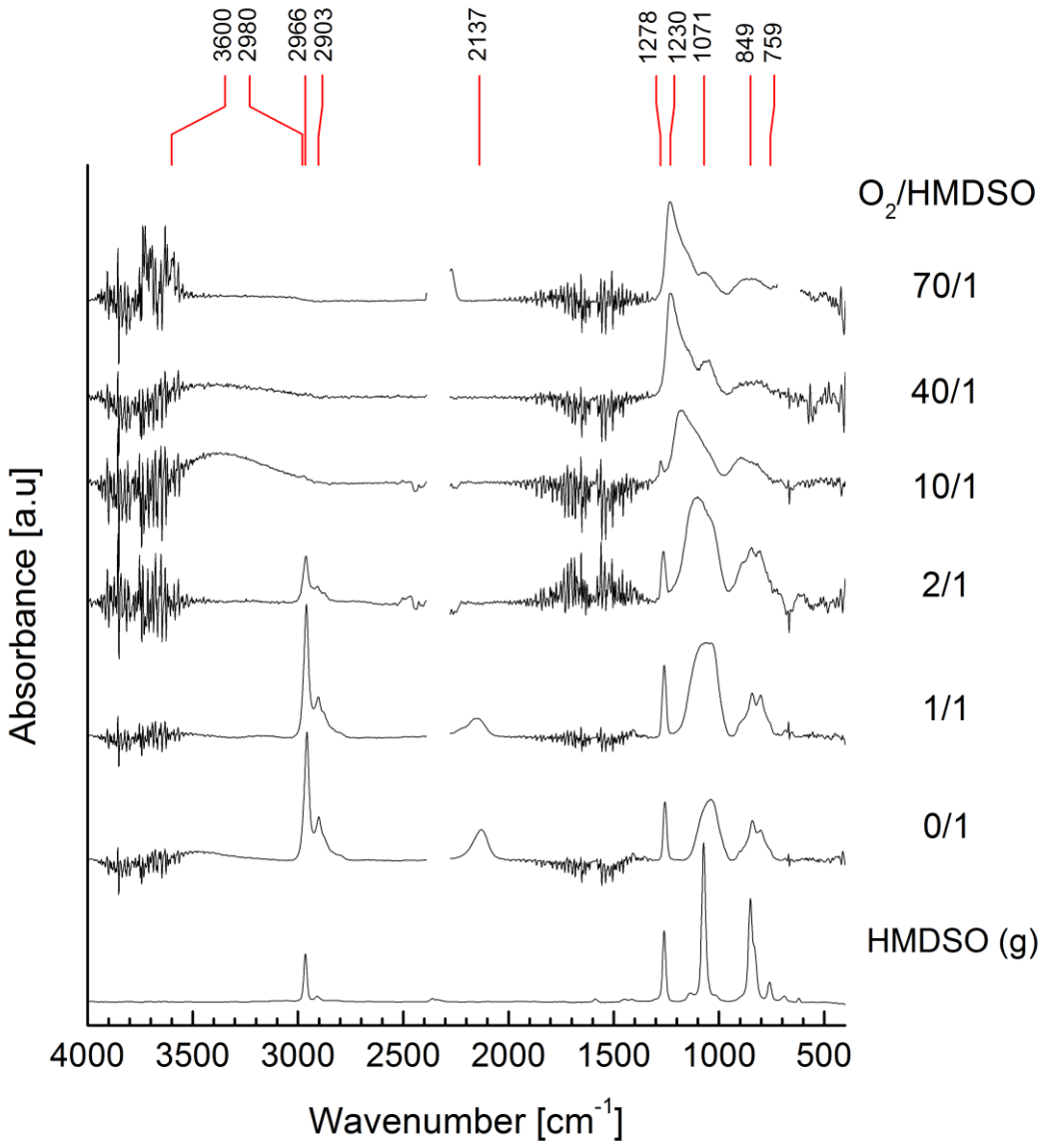

Figure 7.87: Single-reflection absorption IR spectra for a selection of samples with a thickness of 100 ± 5 nm, plus reference spectrum of the HMDSO precursor vapors. Missing data in the 2300 to 2400 cm^{-1} refer to unwanted CO_2 signals from residuals in the chamber atmosphere.

Notwithstanding the first spectrum, however, it is still possible to observe how for low dilutions in the plasma feed the Si-O peak swiftly grows at the expenses of the Si-N and, maybe, the sparse Si-H bonds [253]. Such low dilutions spectra are also the least similar to those of HMDSO-based films, which only exhibit Si-O related signals from the start. The trend is however almost the same for both precursors, with the main peak shape of the two series being in very good accord, and with other signals showing the same behavior, in particular the bell-like trend of the Si-OH broad band at high wavenumbers. The small silyl band, for example, disappears in both cases

at some point between 1/1 and 2/1. The two highest oxygen-to-monomer ratios, as better illustrated in Figure 7.88, exhibit the same shape, position and relative intensities for all their signals. The one minor discrepancy is the 40/1 HMDSN-based sample here investigated, which seems to possess a slightly higher content in hydroxyl groups. The small differences in the intensity of the signals in the lowest wavenumber range are likely artifacts caused by the background correction procedure. The spectra for the 70/1 samples in particular show, since the OH- band is even weaker than in the 40/1 case, how the pinholes originating during the growth of the films are not the source of the increased transmission rates, particularly with regard to the HMDSO-based film.

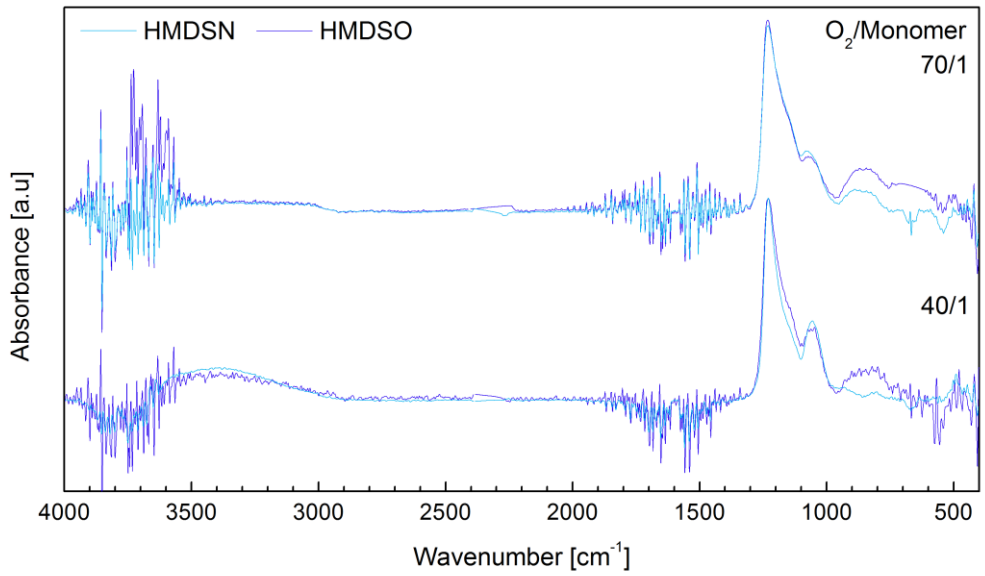

Figure 7.88: Superimposed spectra from Fig. 7.86 and 7.87 for the 40/1 and the 70/1 oxygen-to-monomer ratios. Signals normalized to the intensity of their Si-O-Si peaks at 1250 cm^{-1}.

In order to overcome the sensitivity limits of the IR analyses thus far, the same samples prepared for the single reflection spectroscopy analyses have been investigated by means of ESCA spectroscopy, around three weeks after their deposition, while in the meantime being stored in a sealed steel container purged with nitrogen atmosphere, in order to stop or at least slow down the inevitable aging process of their surfaces. The resulting relative atomic abundances, displayed as fraction of the detected Si signal (with hydrogen being too light to be detected) are displayed in Figure 7.89 for HMDSN-based films on top, and for the HMDSO-based ones on the bottom. Silicon has been chosen as a reference because, in the current deposition processes, it is the least likely element to form stable gaseous products that are pumped away. On the contrary, it is safe to assume that all the dissociated silicon is incorporated in the final film, and mostly independently on the oxygen-to-monomer ratio. As a consequence, the data thus displayed can be

interpreted at least in a semi-quantitative way. The values reported in the graphs are those measured after cleaning the surface with an ion gun, removing carbon-based and other inorganic contaminations. As, even after the cleaning step, a small amount of contaminant sodium was still to be detected on the samples (likely coming from the XPS analysis chamber self, contaminated with prior samples), the at omic percentages have been recalculated after excluding the evidently foreign element from the total. For HMDSO, N/Si ratios have been reported for the sake of comparison, in spite of nitrogen being practically completely absent from the surface.

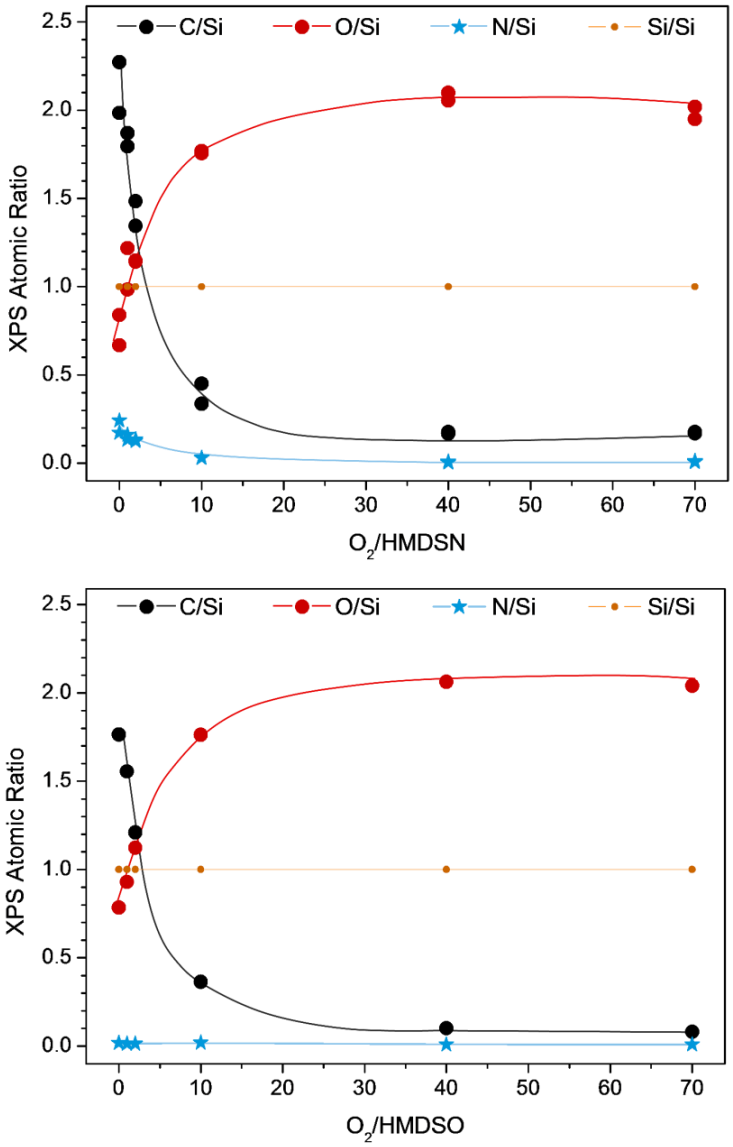

Figure 7.89: XPS atomic ratios (with Si as reference) as a function of the oxygen-to-monomer ratio for HMDSN (top) and HMDSO (bottom) as precursors. Analyses for HMDSN have been carried out for two distinct series of samples.

The general trend is similar for both precursors, with most of the changes in the chemical composition taking place in the small 0/1 to 10/1 oxygen-to-monomer range. As already hinted by the FTIR spectra, the nitrogen content for HMDSN-based films in particular is negligible from the beginning and becomes zero already for feed ratios higher than 10/1. Even the atomic percentages – data not shown – are consistent for both precursors, with the silicon percentage for example ranging from 28 to 32 % for HMDSN and from 25 to around 31 % for HMDSO. By increasing the oxygen content in the plasma feed the films turn progressively more oxidized, with the 40/1 and the 70/1 samples showing yet again the same surface chemical composition, both as ratio and as percentages. Confirming what was apparent in the single-reflection spectra, the pure HMDSN film shows already a 21% of oxygen content. As a consequence, the C/Si and N/Si ratios that can be calculated for the precursor in the gaseous form pass respectively from 3 to 2 and from 0.5 to an average of 0.2. Such increased surface reactivity seems to be a prerogative of HMDSN-based films, as the pure HMDSO sample exhibits an O/Si ratio of 0.8 instead of the 0.5 found for the gaseous molecule, a small increase that could be induced by the plasma polymerization process alone, most likely. The carbon content, although starkly reduced, remains interestingly around 5.5 % for HMDSN and 3.2 % for HMDSO at 40/1, and again 5.5 % for HMDSN and 2.5 % for HMDSO at a dilution of 70/1. As a consequence, despite what could have been surmised by the FTIR spectra alone (but hinted at after calculating the SiO_x stoichiometry after the main band position in Chapter 7.1.3.2), the films are never technically completely inorganic. The higher carbon content for HMDSN may account for the films' higher flexibility when compared to the HMDSO-based ones, similarly to the increased adhesion to the substrate that a silica-like film with a small carbon content possesses [99]. The residual carbon content also helps explain the seemingly incongruous O/Si ratios, which for the highest dilutions in the plasma phase present overstoichiometric values slightly higher than 2. This 'excess' of oxygen may then be explained as existing as bound to carbon and undetected hydrogen atoms, as carbonyl, carboxyl and hydroxyl groups, possibly.

Details about the way atoms are bond cannot be inferred by the atomic ratios alone, but can be provided by the high-resolution spectra of the investigated peaks. The latter are also useful in at least speculating on some of the reaction pathways taking place in the plasma phase, and whether or not they are the same for both precursors. The corresponding fitted high-resolution spectra of the C1s, N1s and Si2p for the HMDSN- and HMDSO-based samples are reported respectively in Figure 7.90, 7.91 and 7.92. The fitting procedure has been carried out accordingly to what explained in Section 6.2.2 and by means of the peak components listed in Table 6.1. The nitrogen band is reported for HMDSN as monomer alone, as only background noise could be recorded for HMDSO-based films. The oxygen peaks, while recorded and saved, have not been fitted, as the strong electronegativity of oxygen severely reduces the shifts in the signal caused by mutated chemical surroundings, and causes the O1s bands to remain mostly unchanged even for different dilutions in the plasma feed. It is worthy reporting, however, that O1s bands for all samples possess no symmetrical shape, hinting at several components and, consequently, at different kinds of oxygen in the films. The reported spectra refer to the samples prior the cleaning of

the surface with an ion gun. Such step results in fact in an irreversible and unquantifiable alteration of the surface chemical structure that invalidates any subsequent discussion on the latter. As a consequence, then, the C1s bands displayed in Fig. 7.90 also comprise the contributions of external contaminations. These are mostly caused by adventitious carbon in the form of short, polymeric hydrocarbon chains, with a small, variable content of CO [146]. Such peaks can be and have been employed as internal standard in order to verify and eventually correct surface charging effects that would result in the apparent shift of all recorded bands.

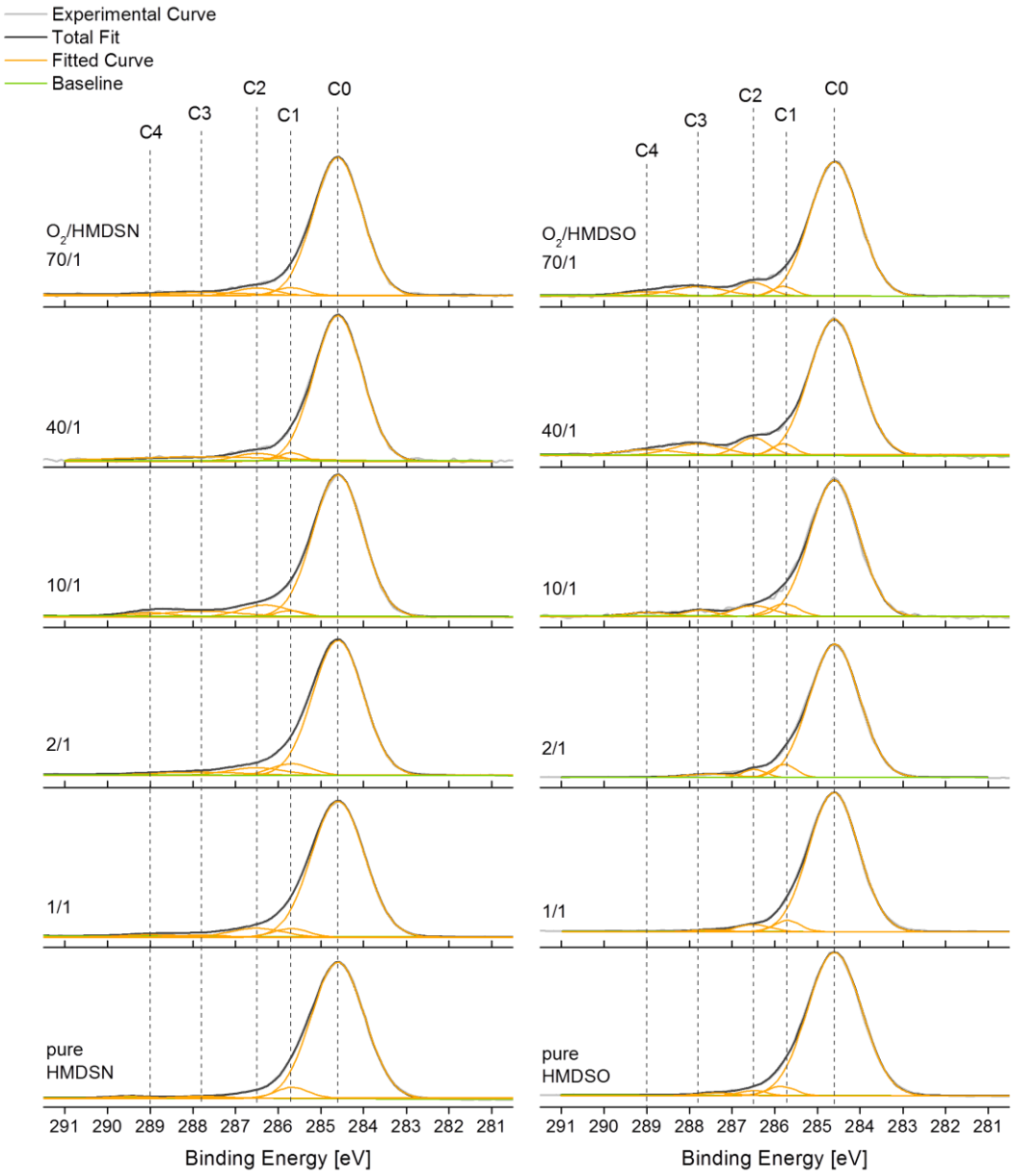

Figure 7.90: High resolution C1s spectra and relative fitting for HMDSN (left) and HMDSO (right) as precursors at different dilutions with oxygen in plasma phase. The peak attributions based on Table 6.1 are: C_0 = C-C; C_1 = C-R-O; C_2 = CO; C_3 = C=O or O-C-O; C_4 = O-C=O or O-C-O-O.

In the current case, the C-C(H) signal labelled as C0 constitute the predominant component of the band and, with a constant position at 284.6 eV, is in very good accord with the tabulated values reported in literature, equal to 284.7 ± 0.2 eV [145-148].

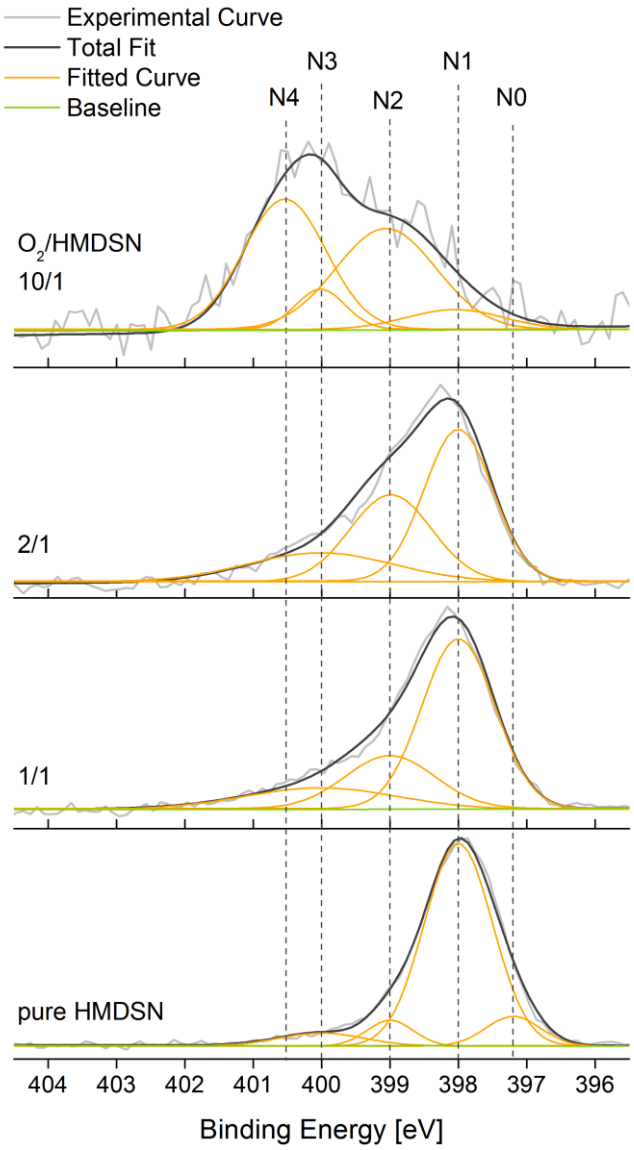

Figure 7.91: Fitted high resolution N1s spectra for HMDSN-based films up to a dilution of 10/1 in plasma phase, after which the signal is no longer detectable. The peak attributions based on Table 6.1 are: N0 = Si-NH-Si; N1 = NSi_3; N2 = NSi_2C; N3 = N-R-O; N4 = $N\text{-}(R\text{-}O)_2$.

The trend for increasingly higher oxygen content in the plasma feed appears to be the same for both monomer, with an increase in the variously oxidized carbon fractions, particularly the C-O and carbonyl groups (C2 and C3, respectively). The latter are however always more abundant

for HMDSO as precursor (more on this later). The signals coming from the various methyl groups still incorporated in the films at low dilutions (with a tabulated value in the 283.9 – 284.4 eV [108, 138, 254]) cannot be fully appreciated in the current spectra, as they are 'hidden' by the much stronger adventitious carbon signal around the same energies. For the same reasons, eventual CN bonds cannot be conclusively identified, as their relative signal (at 286.3 eV [150]) falls in too close proximity to the CO peak.

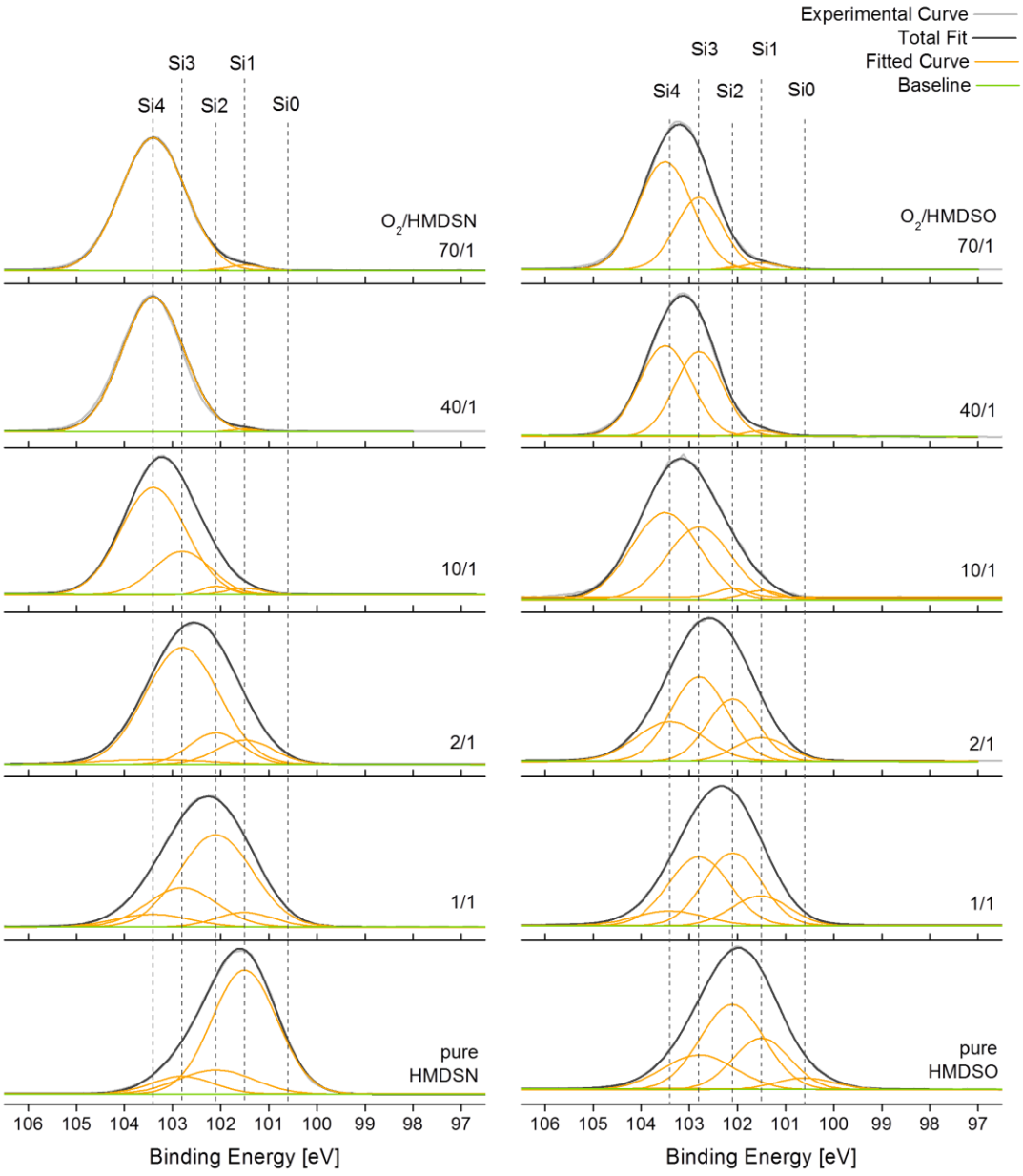

Figure 7.92: High resolution Si2p spectra and relative fitting for HMDSN (left) and HMDSO (right) as precursors at different dilutions with oxygen in plasma phase. The peak attributions based on Table 6.1 are: Si0 = Si_3-Si-C; Si1 = Si-O or Si-N; Si2 = Si-O_2; Si3 = Si-O_3; Si4 = Si-O_4.

The same general progressive oxidation is to be observed in the N1s peaks for the HMDSN-based films (Fig. 7.91). Here, at very low dilution, the nitrogen atom from the precursor's original backbone lies mostly in its original state, with possibly minor components bond to a C atom after the plasma polymerization process (peak N2) that couldn't be singled out through the C1s peaks alone. At a dilution of 10/1, however, the very faint residual nitrogen content (around 2 %) lies in a mostly oxidized state, being bound directly to an oxygen atom (N_4 component) or to, most likely, a silicon or carbon atom bond in turn to oxygen (N_3 component). Nothing but background noise can be observed for the 40/1 and 70/1 samples, indicating a complete stripping of the nitrogen component prior to the film deposition (spectra not shown). It can be concluded that, as the energies for the N-Si and the C-Si bonds are similar, both elements are homogeneously stripped/oxidized with increasing oxygen content in the plasma feed. N disappears from the final films earlier since is less abundant than C in the original monomer (C/N = 3). On the other hand, its central position in the molecule and the consequent steric hindrance render more difficult for it to be reached by oxygen, hence the relatively unaltered binding energies for low oxygen content in the plasma.

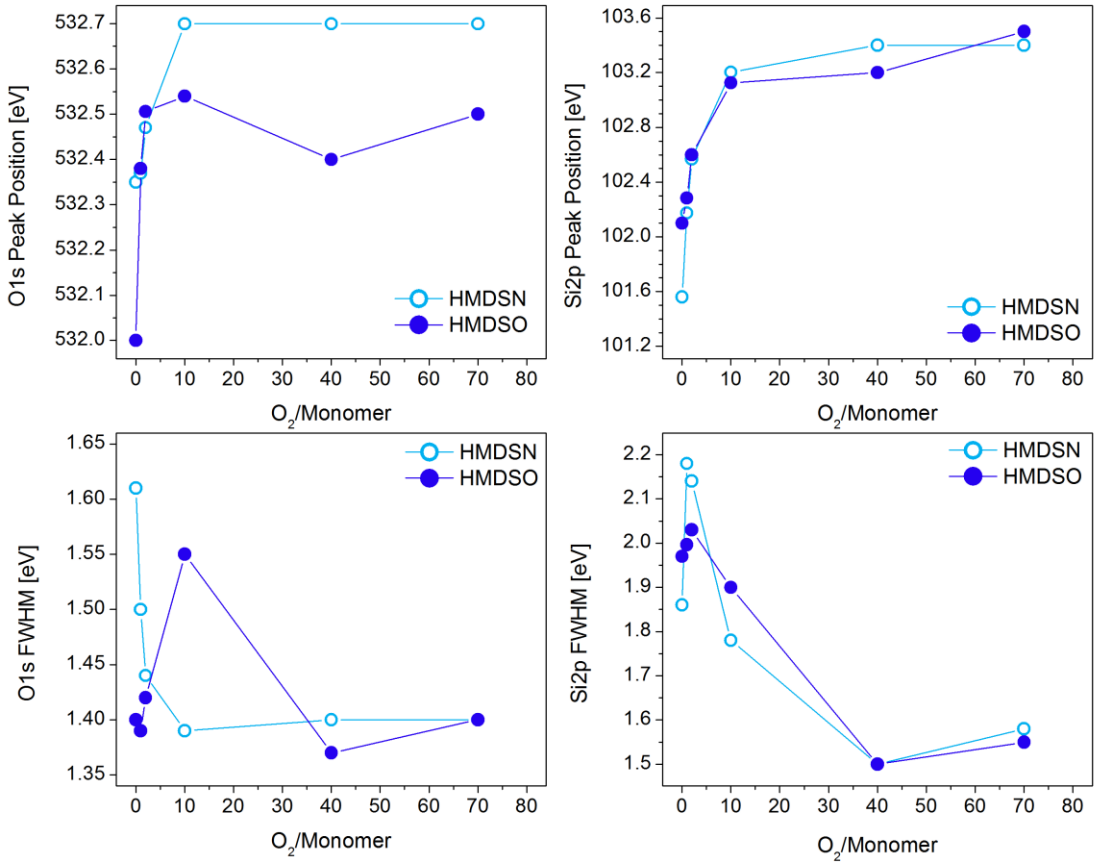

Figure 7.93: Peak positions for the experimental O1s and Si2p overall signals (top row), and their correspondent full width at half maximum (bottom row), for both precursors.

As the most abundant component in the final films, silicon is the element most affected by the progressive increase of oxygen in the plasma feed, as already shown by the position and shifts of its bands in the infrared spectra. The fitted high resolution Si2p peaks reported in Fig. 7.92 show how, for both monomers deposited without addition of oxygen in the feed, the silicon atoms are initially in a relatively reduced state, mostly. For HMDSO, already containing an oxygen atom in its backbone, the majority of Si atoms are surrounded either by one or two oxygen atoms (S1 and S2 components, respectively). As for HMDSN, as previously mentioned, post-deposition reactions with air or contaminations inside the reactor during the process still ensure an initial, albeit partial, oxidation of silicon too. The shift towards silicon atoms surrounded by three or four oxygen atoms (S3 and S4 components), while taking already place for both monomers at low dilutions, seems to be faster for the HMDSN-based films, with the 2/1 ratio of the former, in particular showing already a strong S3 contribution. From a dilution of 10/1 onwards the bands seem to stabilize. It is unclear whether the still strong S3 components for the HMDSO-based films are an artifact of the fitting procedure, or if indeed a Si-Si fraction is still present in such films, while for HMDSN the peak is composed almost only of silicon-oxygen tetrahedral, like in glass [148]. The shifts of the entire Si2p band for both monomers reported in Figure 7.93, on the other hand, show similar final values in both cases (with the pure HMDSO film exhibiting a higher initial value because of the oxygen atom already present in the monomer). A similar trend can be observed in the O1s band too, with the overall peak position for the highest dilutions almost 0.5 eV higher that the initial ones, hinting at a homogeneously more oxidized environment in the solid films. The full widths at half maximum of said bands, also reported in Fig. 7.93, are on the other hand a good indication of the degree of 'disorder' in the solid bulk. At low dilutions, with the oxygen starting to be incorporated in the film, but still not enough to guarantee a complete oxidation of the initial monomers, the silicon and oxygen atoms are surrounded by a vast range of different milieus in different oxidation states, surrounded by atomic species with different electronegativity. A distribution in bond angles and lengths, and even in Madelung values in case off ionic bonds in crystalline domain, can further be present for silicon and oxygen atoms alike [255]. As a consequence, the respective bands increase in width, reflecting such higher variance. With oxygen-rich plasma feeds, on the other hand, the final films contain fewer elements (nitrogen absent, carbon still present only in low percentages, hydrogen also supposedly strongly reduced or almost absent), and lie in a homogeneously high oxidation state: the silicon and oxygen bands will therefore shrink back to lower FWHMs [150]. For oxygen in HMDSO, in particular, the highest disorder is reached for a 10/1 ratio, while for HMDSN the trend is a constant reduction in FWHM values. This may again be explained by the post-deposition reactions with air that cause oxygen to be incorporated in an initially oxygen-free layer. Assuming, reasonably, that the highest oxygen contamination will be attained in the first molecular layer, then, surface oxygen will be surrounded by a much more electronegative milieu, while the sparse atoms penetrating more in depth will lie in a reduced environment, causing a stark broadening of the 1s peak. Final

values for both monomers lie then once again in the same range.

Overall, then, the chemical analyses performed on the samples based on both precursors highlighted that, at low oxygen-to-monomer ratios, HMDSO-based films contain a higher amount of organic bonds, which moreover lie in a more oxidized state than for HMDSN. Moreover, the threshold to inorganic films for HMDSN-based films is located at lower oxygen-to-monomer values. Once the films turn inorganic, no clear difference between monomers is to be found, neither via IR nor XPS spectroscopy. Likewise, the chemical milieus for Si and O in both cases remain fairly similar to each other, with the partial exception of the highest feed ratios for the silicon XPS spectra: in this case, HMDSN-based samples show a slightly more oxidized milieu, compatible with an exclusively Si-O_4 structure. Finally the initial small amount of incorporated nitrogen for HMDSN-based films does not seem to play a major role in their properties, and is quickly reduced to zero with increased oxygen in the plasma feed.

7.5.3 Deposition rates of HMDSN- and HMDSO-based films

While producing the HMDSO-based films for the analyses presented in the previous paragraph, since the thickness of the films has been kept constant at 100 nm for a straightforward comparison with the HMDSN-based barriers, the deposition rates as a function of the oxygen-to-monomer ratios have been easily obtained by means of the method first described in section 7.1.1. The results have been compared to the actually much more accurate values obtained with HMDSN as precursors, and are reported together with the latter in Figure 7.94. The 80/1 ratio has been left out, since a dataset wide enough to calculate an average rate was not available for the HMDSO-based films.

For very low oxygen-to-monomer ratios, up until 10/1, the rapidity of the deposition process and the subsequent high variance of the measured thicknesses cause the calculated values to not be very reliable, so prudentially the deposition rates can be assumed to be practically the same for both monomers. On the other hand, higher dilutions in the plasma phase result in much longer deposition steps, so that in this case any discrepancy between the rates for the two monomers is not likely to be due to experimental fluctuations. In such range, HMDSO seems to cause a consistently higher deposition rate, +20 % at the 40/1 oxygen-to-monomer ratio and even +30 % at the 70/1 one, when compared to HMDSN. Such effect has already been reported for microwave-powered plasmas by Wróbel *et al.* [128]. No further explanations were given in this case, however. Considering almost equal molecular weights and densities at the liquid state for both precursors (see Table 5.2), such distinct discrepancy in the deposition rates was not to be expected, assuming similar reaction pathways in both cases.

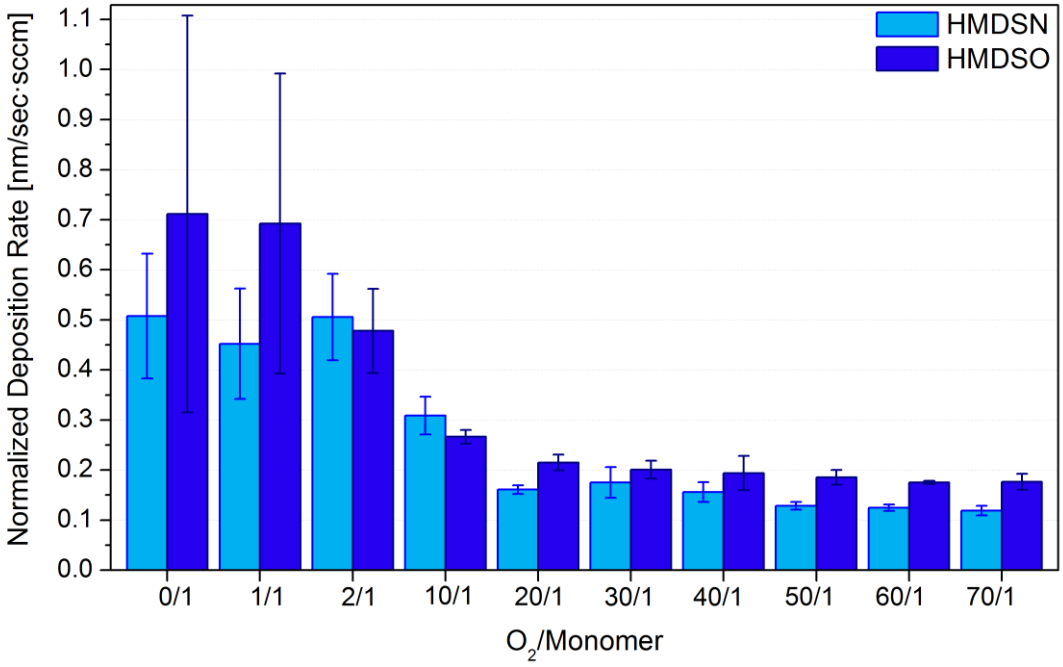

Figure 7.94: Normalized deposition rates as a function of the oxygen-to-monomer ratio for both precursors. The error bars have been equated to the standard deviation correlated to the calculated average value.

7.5.4 Polymerization reactions and pathways for HMDSN and HMDSO

In light of the data thus far presented in the current chapter, it is now at least possible to pose, as likely explanation for the different behaviors of the monomers, a partially different polymerization mechanism for the latter two. The following discussion, which can be at the current stage only qualitative in nature, is therefore to be considered strictly non-conclusive. Equally important, it is not possible to *a priori* state if and to what extent the reactions taken into account would take place in the plasma phase or on the surface of the growing film. A quantitative or even only semi-quantitative commentary would on the other hand require extensive analyses of the plasma phase by means of optical emission spectroscopy and actinometry, and of the long-living species therein by means of ion mass spectrometry. The current discussion will moreover focus primarily on the possible reactions involving the backbones of the precursors, i.e. the Si-NH-Si and the Si-O-Si groups. As already extensively proven by chemical analyses of the solid films, the methyl groups are preponderantly removed, one way or the other, at relatively low gas feed dilutions. The reaction leading to this would furthermore be the same in both cases, and cannot be therefore held accountable for the different films properties. Some pathways for the

polymerization of organosilicons involving methyl groups have been reported in Chapter 5.2. As for the oxygen radicals and anions reacting with the monomers and their fragments, they are considered to be produced in the following reaction:

$$O_2 + e^- \rightarrow 2O\cdot + e^-, \tag{7.8}$$

$$O_2 \xrightarrow{h\nu} 2O\cdot, \tag{7.9}$$

$$O_2 + e^- \rightarrow O\cdot + O^-. \tag{7.10}$$

The dissociation of molecular oxygen through radiation alone is made possible by the strong VUV emission in microwave plasmas [56].

The molecular bond energies for both employed monomers, first listed in Figure 5.10 and 5.12, are reported again here in Table 7.8.

Table 7.8: Bond energies for HMDSN and HMDSO precursor molecules. Values taken from [125, 129-131].

Molecular bond	Energy
	eV
Si–C	3.12
Si–N	3.42
N–H	4.05
Si–O	4.56
C–H	4.31

A selection of possible reactions involving HMDSN is reported in Figure 7.95. The fragmentation of the backbone, along the pathways **B** and **C**, via an excited neutral intermediate, while considered neither the first step nor preponderant for RF plasmas, can be made possible by the high-energy tail of the electrons energy distribution in microwave plasmas [89, 96-98, 100, 101]. Considering the Si-N bond being only 0.3 eV stronger than the Si-C, the cleavage of which for the here employed operating conditions is certain. Such pathway is further confirmed by the experimental data, namely the disappearance of nitrogen in the films for increasing oxygen in the plasma. It is uncertain whether the cleavage follows a homolytic or a heterolytic route, or if both processes take place in parallel. Taking into account the difference in electronegativity between nitrogen and silicon, however, in the heterolytic case the ·Si≡ fragment would retain the positive charge. Wróbel *et al.* [256] demonstrated how in RF low-pressure plasmas olygomers form

prevalently through cleavage of the Si-N bond which tends however to be a hererolytic fission. Considered the abundance of reactive oxygen species in the gaseous phase, then, it is most likely for the smaller fragment of the backbone, regardless of its eventual charge, to react with them and form a Si-O fragment that can be already considered a 'building block' of the final SiO_x film, as shown in the pathways **D** to **H**, or undergo further reactions. The **H** step, i.e. the preferential loss of a whole methyl radical, can be corroborated by its presence in the film being inverse proportional to oxygen in the plasma feed, as shown in IR spectra for both monomers. The product of the **G** pathway, however, can further react with a neutral or marginally altered HMDSN molecule and attach itself on the free electron pair of the NH group. The product would then quickly stabilize by expelling a fragment according to the **J**, **K** and **L** pathways [256]. The last one in particular, with the retention of the tertiary amino group, would result in a strong crosslinking of the solid polymer [256, 257]. Considering the bulk of the intermediate and end products, it is safe to assume that they either form directly at the surface, or do not remain long in a gaseous phase. Ultimately, however, such reaction pathways, while theoretically possible, must be fairly minor in the current polymerization process, and in particular for gas feed dilutions higher than 10/1, after which no nitrogen is to be found in the solid film. On this subject, Alexander *et al.* [258] reported the relatively little abundance in the plasma phase of species much heavier than the original monomers. The presence of unreacted HMDSN that can prompt the reaction chain, moreover, should be assumed to be unlikely, so that a significant formation of plasma polymers in the gas phase by means of radical-based chemistry should anyway be excluded. Alternatively, if such pathways do play a role in the formation of the final film, in all three cases further steps would be required in order to strip away the nitrogen central atom, as ruled by XPS results.

The ≡SiO group, whether it is charged or not, instead of depositing as it is, can also remain in the plasma phase and combine to form longer SiO_x-like chains, as illustrated in the **M** and **N** pathways. The presence of peroxy bridges has been shown in silica-like films of similar stoichiometry of those currently investigated, deposited by means of electron beam evaporation [255], and would also explain the position of the O1s band for the 10/1 to 70/1 samples.

The amino group, either ionic or radical, can lastly be reduced and expelled in the former case (pathway **O-P**), or substituted in a nucleophilic reaction in the latter (pathway **Q**). These steps, it can be safely assumed, take place exclusively in the plasma phase, as amino groups being already immobilized on the surface would have a small probability of being buried by incoming particles before being expelled, would remain embedded in the film and be detected by ESCA analyses (not the current case). Similar reactions can in principle also involve the full precursor molecule and take place in the initial moments after the plasma ignition, as HMDSN easily releases the nitrogen-bond hydrogen [256]. In both cases, a ≡SiO group is obtained, while the amino product, after an eventual further oxidation step, is to be pumped away without depositing.

As for the pathways for HMDSO as precursor, some of them are reported in Figure 7.96.

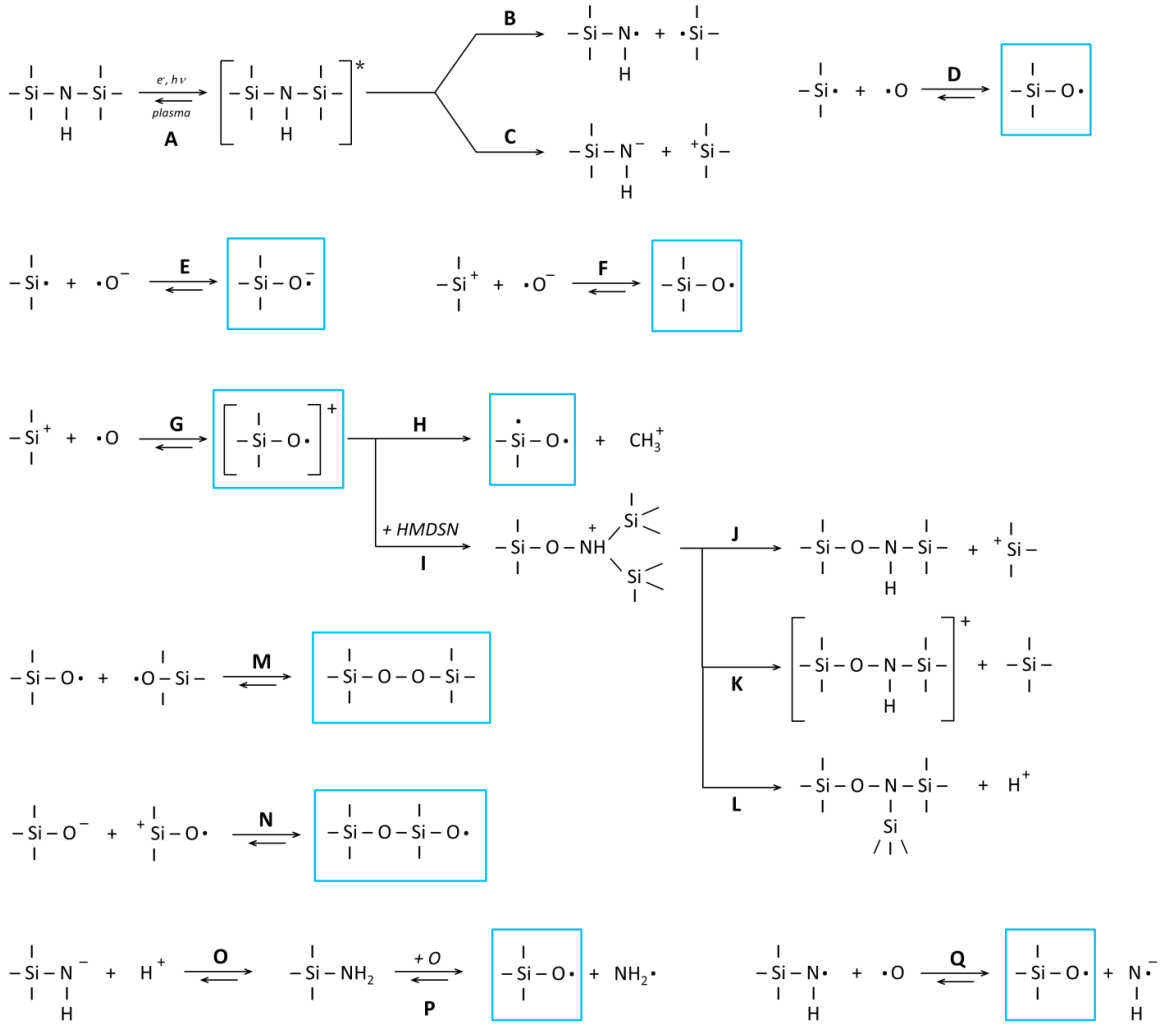

Figure 7.95: Proposed reaction pathways for the Si-NH-Si backbone of HMDSN. In light blue boxes, products that can result in the final inorganic thin films. Sources listed in the text.

Those coinciding with the reactions discussed for HMDSN have been omitted. **A'** pathway differs from the previous case as, regardless of what is bond to the silicon atoms, the Si-O-Si chain can already be considered a 'building block' for the final film, according to the definition provided at the beginning of the current discussion. The excited intermediate in particular would already be able to attach itself on an active site on the surface, and there possibly lose the eventual methyl groups still bond to the Si atoms, or not, and cause an incorporation of the latter in the final film (as shown by IR spectra, C content at low feed dilution is higher for HMDSO). Similarly, **B'** and **C'** also result in ≡SiO groups that can already form an oxidized final film. The silicon cations or radical also formed react then accordingly to the previously described **D** to **H** pathways. The previously discussed reaction branch **I** to **K**, in this case, can instead lead to the for-

mation of heavier fragments consistent with the chemistry of the obtained films (pathways **J'** and **K'** for the peroxy bridges, and **J"** and **K"** for the silicon oxide chains, respectively), regardless of how likely such mechanism could be. An eventual **L'** or **L"** variation for HMDSO is however precluded by the absence of a trivalent atom. Similarly, the **R** route can form viable oxidized products that are later incorporated in the film only in case of HMDSO as precursor.

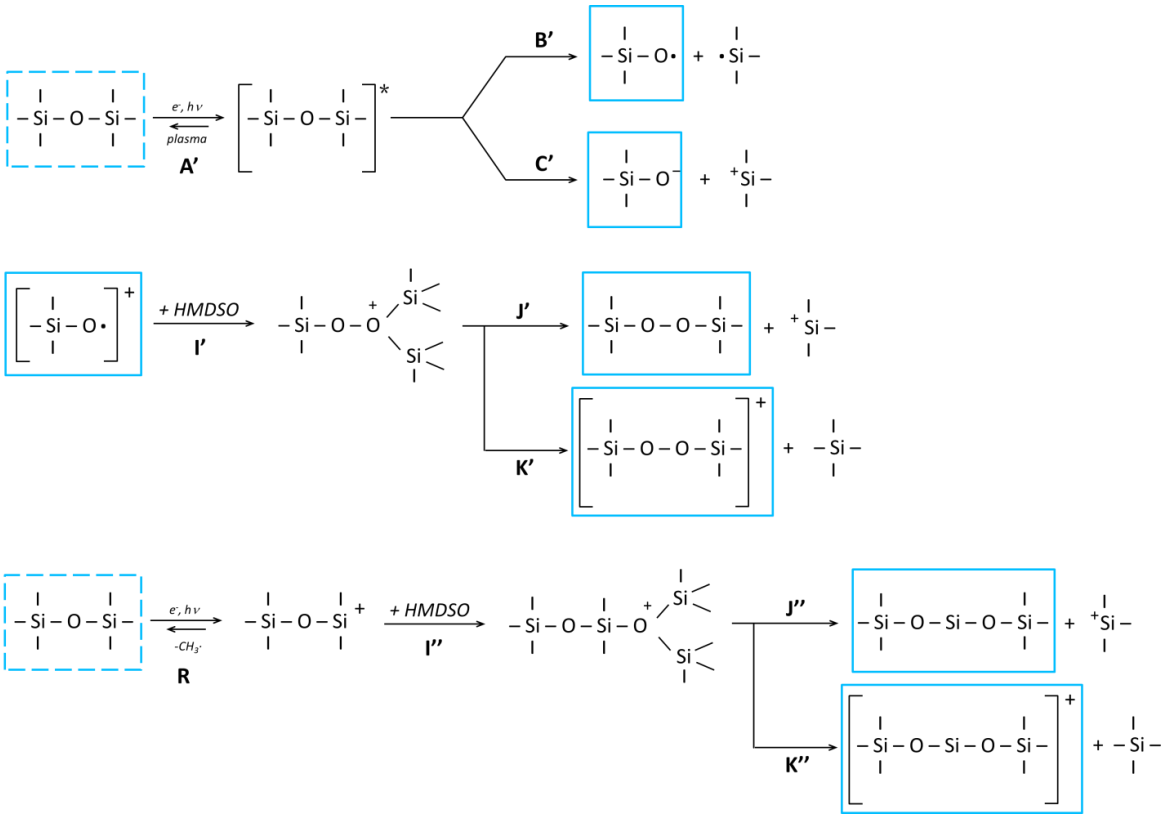

Figure 7.96: Proposed reaction pathways for the Si-O-Si backbone of HMDSO and for the resulting fragments, if not already covered for the HMDSN case. In light blue boxes, products that can result in the final inorganic thin films. Sources listed in the text.

If the proposed mechanisms for the two monomers are considered reliable, then, a very general conclusion for the pathways involving the backbone of the precursors can be reached: namely, that for HMDSN it must be invariantly be broken at the Si-N bond, and that the nitrogen must be further stripped away or substituted by oxygen, as mandated by experimental results. For HMDSO the step is not only superfluous, but even counterintuitive, as the SiOSi chain is already among the possible final products of an oxygen-enriched plasma. An extremely simplified recap is illustrated in Figure 7.97.

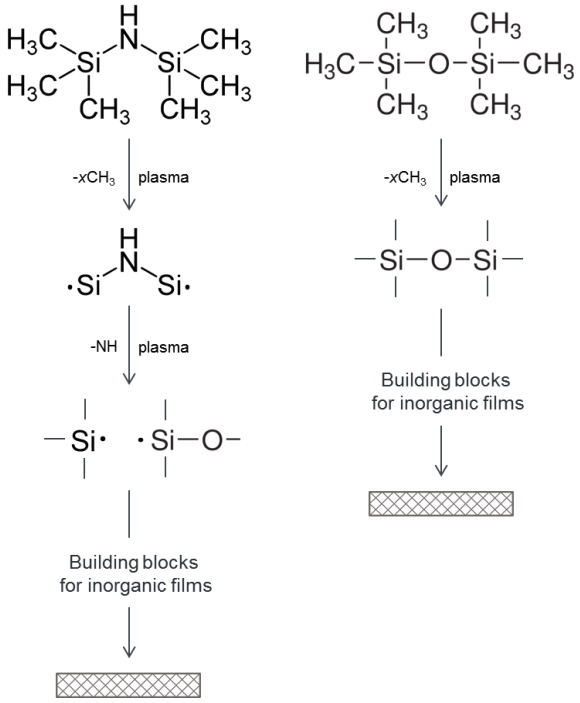

Figure 7.97: Summary of the simplified reaction pathways involving the backbones of HMDSN (left) and HMDSO (right).

It can therefore be surmised that the plasma polymerization of HMDSN includes one further step, and takes place through the recombination of smaller fragments. The discrepancy has likely no critical effect at low dilution of the gaseous feed, where the regime is still prevalently oxygen-starved and no complete oxidation and removal of the methyl groups is attained, and where the reactions for both monomers are still most likely the same (even the minor ones, as the trend for silyl groups shown in IR spectra). In environments rich enough in oxygen to result in inorganic films (i.e., mostly dilutions higher than 30), however, the discrepancy among the two processes becomes critical, and would explain not only the consistently higher deposition rates for HMDSO, but also the increased gap with HMDSN (+20 % already at 20/1 dilutions). The deposition process for HMDSO in such range, moreover, would be further sped up because of the higher concentration of oxygen radicals and ions: with the methyl groups almost completely removed and oxidized, a process that can be assumed to be the same for both precursors, a fraction of the oxygen in HMDSN-based plasmas has still to be 'spent' on oxidizing the nitrogen atoms (ideally, one sixth of the amount required by the carbon atoms per monomer molecule) and the resulting silicon fragment (one twelfth of the amount for carbon atoms). In HMDSO plasmas, on the other hand, this further excess of oxygen reagents will tend to move the equilibrium of the reactions towards the products, among which, as mentioned before, lies the stripped backbone of the precursor, in obedience to the Le Chatelier principle. The overall process is schematically

represented hereby:

$$O + monomer \underset{\leftarrow}{\longrightarrow} oxidized\ fragments\ (\uparrow) \underset{\leftarrow}{\longrightarrow} oxidized\ fragments\ (\downarrow) \qquad (7.11)$$

It also implies that, once reached the surface, the fragments have on average less time to migrate along it, before becoming anchored on a reactive site, and a smaller probability to detach and to return, even if briefly, to the gaseous phase. Such assumptions could also explain why the residual amount of carbon in the film is smaller for the HMDSO case (as a higher oxidation of C would at least partially consume the excess of oxygen), and why at the same time the incorporated carbon lies in a consistently more oxidized environment, most likely as COOH or CO with a further oxygen in α), when compared to HMDSN. Such tumultuous processes, in particular the fast precipitation of the oxidized products, would also produce film with an increased degree of microporosity: the higher percentage of free volume in the solid would then be caused in equal part by the, on average, bigger fragments forming the film, and the reduced time they have to arrange themselves in a tight, albeit still amorphous, structure. Such conclusion could be corroborated by the dramatic increase in the defects densities for very high O_2/HMDSO ratios, and the lack of pattern observed at the optical microscope during the pinhole detection test, as the entire volume of the film would be equally affected by it. The same must be true, to a much lesser extent, for the highest dilutions for HMDSN too, as the surface morphology in this case seems to become slightly more similar to the 'brittle' one observed for HMDSO-based films, and likewise the defects density too increases its value.

The sped-up kinetics of HMDSO deposition, finally, would also explain the retention of the methyl groups, as seen in IR spectra in both configurations, even at dilutions at which HMDSN-based films have already turned almost completely inorganic. In this range, this would be caused not by the lack of oxygen to react with – in fact, according to the model thus far presented, reactive oxygen species should at this stage be more readily available in HMDSO plasmas, rather than in HMDSN ones –, but rather by the lack of time for the reaction to take place, as hinted by the deposition rates, already significantly higher than in case of HMDSN. The monomer fragments, still containing some CH_3- group, once attached on the surface are quickly buried underneath new fragments before the methyl groups could be oxidized or etched away. A partial corroboration to such suggestion is once again given by the XPS spectra: up to a ratio of 10/1, in spite of the %C being slightly lower for HMDSO, the C1s high resolution band show significantly weaker contribution of oxidized species (nothing can be said on carbon in a more reduced state, unfortunately), i.e. more methyl groups in the precursor molecule consumed by oxygen, but those remaining in the final film almost still in their original state.

On the other side, HMDSN-based plasmas form more densely packed films, thanks to the overall slower and more orderly deposition mechanism induced by the presence of the NH group in the backbone. Some of the aforementioned considerations for HMDSO, in particular at very high dilution values, may still apply for HMDSN, too. The inhomogeneous areas with a much

higher defect density spotted through the pinhole test for 70/1 and 80/1 ratios could correspond to volumes with an increased, process-induced microporosity. The presence of the amino group in the precursor molecule and the possibility for it to become a branching center, moreover, may also be a factor for the increased adhesion and resilience of such films, beside the already discussed traces of incorporated carbon – and the high resolution spectra of the latter's band further reinforce such assumption, as the small contribution of oxidized groups hints at carbons in a reduced state, i.e. bond to silicon and eventually hydrogen atoms in the main chain, rather than as carbonyl *et similia* as chain-terminating or side groups that increase the porosity of the film. As XPS analyses show no N1s signals for dilution higher than 10/1, then, if such nitrogen-induced branching takes effectively place, it must be during the early stages of the deposition process and limited therefore to the first molecular layers of the barrier film. For the investigation of buried interfaces, methods like Glow Discharge Optical Emission Spectroscopy (GDOES) would then be required [259].

In summary, while the proposed polymerization mechanisms are consistent with the copious experimental data thus far collected, no conclusive evidence for them can still be presented. As previously mentioned, extensive investigations of the chemical reactions in the plasma phase need to be carried out by means of ion mass spectrometry and optical emission spectroscopy and actinometry. In order to discriminate between reactions taking place in the gaseous phase and at the surface, post-deposition plasma processes (mostly etching with a pure oxygen plasma) would need to be carried out and monitored by means of optical emission spectroscopy, in order to detect eventual organic functional groups being returned to the plasma phase. The assumed microporosity of HMDSO-based films, or better, their assumed higher microporosity when compared to HMDSN-based ones, finally, would need to be demonstrated by investigating their density, i.e. by weighting substrates of known surface before and after the deposition of thin films with known thicknesses.

Chapter 8

Multilayer barriers and encapsulation of OLEDs prototypes

Once the extensive investigations on single barriers (Chapter 7) and on the organic films to be employed as intermediate layer (Appendix A2) have been carried out, multilayer systems comprising the two kinds of films have been devised, investigated and tested, as reported in Section 8.1. Afterwards, with the aim to apply them onto OLEDs prototypes, described in Section 8.2, via a PECVD process, the ECR reactor has been accordingly modified in order to make it possible (Section 8.3). The resulting encapsulations are presented and commented, together with their further analysis, in Section 8.4

8.1 Multilayer coatings

When not explicitly stated otherwise, the thin films employed for all samples investigated in the current section are those reported in Table 8.1. The operating conditions for the barrier films have been chosen because they have been the most thoroughly investigated, and as they consistently resulted in the best barriers obtained in the current work. For the characterization of the organic intermediate layer and the choice of its composition, see Appendix A2. The thicknesses have been kept fixed at 100 nm, but a reduction up to 50 nm could still be possible without compromising the overall barrier properties.

Before starting the investigations on multilayer systems, however, samples with at least two barrier layers in them were first produced, with the aim to provide a reference for later systems. Such samples have been obtained on PET foil by coating both sides of it with the chosen barrier film. The resulting samples correspond to a double-barrier system with the substrate acting as the intermediate layer and providing the decoupling of the defects. Each barrier has been also singularly deposited on PET in the same step, in order to measure their oxygen transmission

rates as single layers. The process has been then repeated for another batch of samples. The resulting normalized OTRs and barrier improvement factors, for the single layers and for their combined effect, are reported in Figure 8.1. For the second sets of barriers, two measurements on the double-side coated substrate have been carried out, on different samples obtained through the same deposition step. It can be noticed how the transmission rates for the combined samples are starkly reduced by a factor of around 4.5 in the first case and of circa 2.6 in the second one. It is however possible, for the second batch of double-coated foils, that some damage occurred while handling it, considering its remarkably worse performances.

Table 8.1: Operating conditions and thicknesses for the films employed in multilayer systems.

Barrier layer		Intermediate layer	
Power	555 W	Power	555 W
DC	50%	DC	50%
O_2/HMDSN	40/1	H_2/HMDSN	40/1
Thickness	≃ 100 nm	Thickness	≃ 100 nm

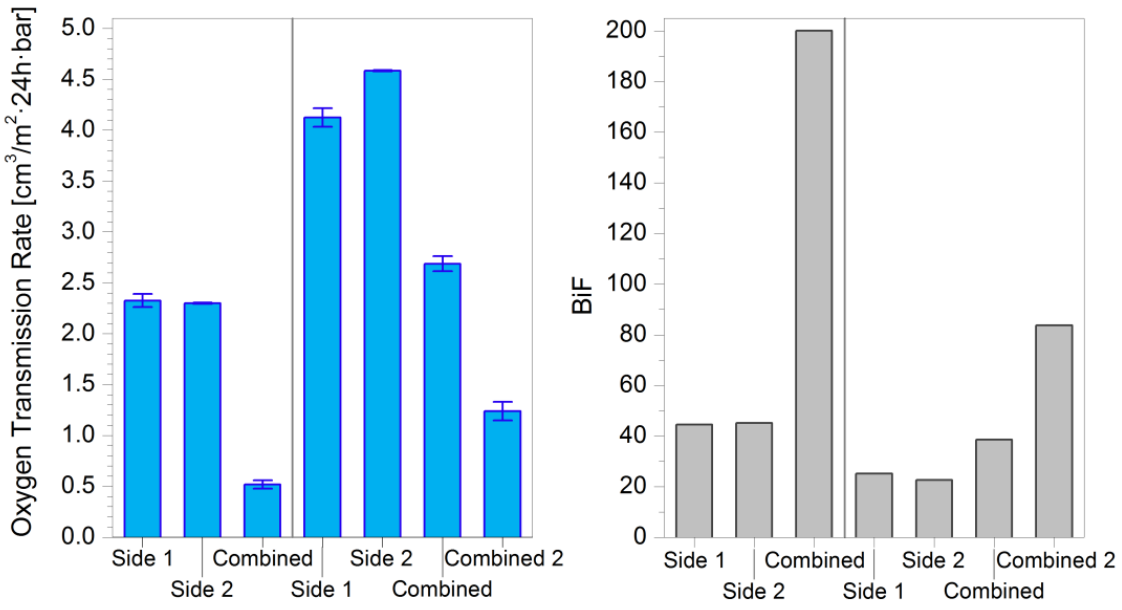

Figure 8.1: OTRs (left) and corresponding BiFs (right) for two sets of single barrier layers on PET and double-sided coated samples.

The barrier improvement factors, calculated with respect to the average PET transmission rate, show likewise a quantitatively similar increase. The improvement in the barrier performances is qualitatively further confirmed by the pinhole test for the double-sided sample, which has been let running for longer times in order to take into account the overall increased diffusion length. The before/after pictures, reported in Figure 8.2, show no crystal appearing on the surface. Assuming that the defect density in both deposited barriers is equal or consistent with the average value resulting from the same operating conditions, then, the lack of visible crystals is not due to a sudden lack of pinholes, but on the strong reduction in the flux of the permeated CO_2, which likely leads to oversaturation levels too low to start a crystallization process in close proximity of the defects.

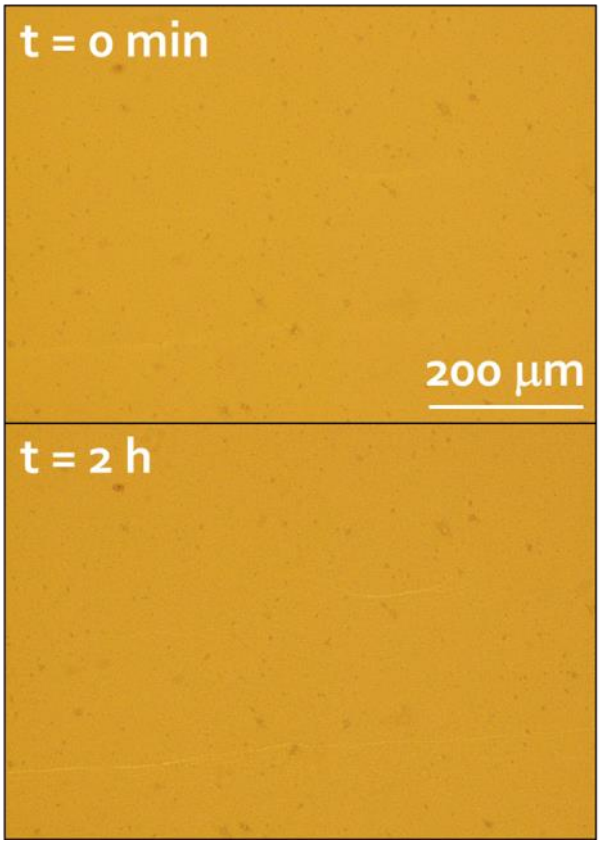

Figure 8.2: Pictures at the optical microscope for the double-sided sample before and after the pinhole test, left to run for two hours.

Finally, the corresponding diffusion coefficients, calculated by means of the typical rise time of the curves, as described in section 3.2, are reported in Figure 8.3. In this case the data refer only to the first set of measurements and, like in Section 7.1.4, they have been calculated for the substrate plus barrier(s) system and extrapolated for the barriers alone. In this case, too, the diffusion coefficient decrease is smaller than the reduction observed for the OTRs, amounting to

around 2.5 only. This is due to the deviations from the Fickian mode caused by the pinholes in the films, which result in a sharper rise of the oxygen levels in the first sections of the curves. The last pair of displayed values, labelled as 'Calculated', refers to diffusion coefficients calculated through the following equation, modelled after Eq. 3.25 and Eq. 3.26:

$$\frac{1}{D_{tot}} = \frac{1}{D_{Side1}} + \frac{1}{D_{PET}} + \frac{1}{D_{Side2}}, \tag{8.1}$$

with the first term of the equation being assumed to be the unknown variable, while the terms on the right side can be obtained through the curves for the single barriers and from the references for the uncoated PET. The diffusion coefficients for the barriers, because of the aforementioned defects, would then be still affected by an unknown error that cannot be eliminated. By noticing however how the calculated value for the double-side system is in very good agreement with the one obtained experimentally, it is possible to confirm how the PET foil acts as an effective decoupling agent. Proper bilayer systems should then exhibit transmission rates and diffusion coefficients of roughly these orders of magnitude.

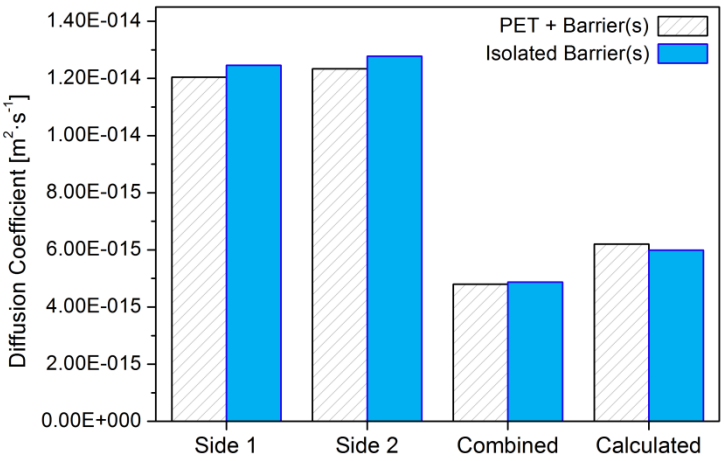

Figure 8.3: Diffusion coefficients for the first set of samples, calculated for the PET + barrier(s) system from the recorded permeation curved, and extrapolated for the barriers alone.

Regarding the multilayer systems, several possible routes for obtaining them are possible: the deposition process can take place in separate steps, with the plasma being switched off after the proper deposition time required for 100 nm, and then reignited after changing the gaseous feed composition, i.e. obtaining a stacked system of thin films, or the plasma feed can be switched during a single deposition step. In this case, as the chemistry in the plasma phase gradually and continuously changes, a similar change in the solid products takes place, which transi-

tion from a silica-like film to an organic film. The chemistry of the latter should still be different enough to provide a decoupling effect for the defects. The multilayer thus obtained is then also labelled as 'gradient' layer. Furthermore, as the multilayer are to be tested, at a later stage, for the encapsulation of OLEDs, the first layer of the system must invariably be an organic one. Its deposition, by means of an oxygen-free gas feed, does not in fact damage the exposed OLEDs; moreover, although such layers do not possess remarkable barrier properties in themselves, they can at least provide a physical separation between the devices and the plasma phase, reducing or blocking the interactions with molecular and atomic oxygen until a proper barrier film 'seals' the surface. This happens, as shown in Figure 7.59, for a thickness of around 30 nm, i.e. after around one minute with the employed operating conditions.

A first series of multilayers consisting of two dyads (intermediate plus barrier layer) has been thus deposited. For all processes, the operating conditions listed in Table 8.1 have been kept unaltered. The resulting films, with a thickness in the 350 to 500 nm range, still present a good transparency and colorlessness to the naked eye, as shown in Figure 8.4.

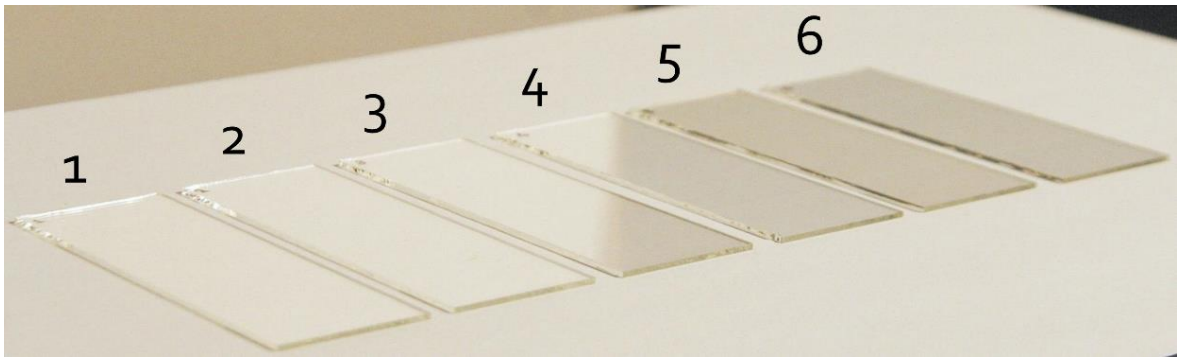

Figure 8.4: Multilayers on glass consisting of a pair of dyads, with the organic intermediate layer as the first one, deposited in different PECVD processes.

The correspondent oxygen transmission rates are reported in Figure 8.5: the red span indicates the OTR range of the corresponding single barrier layers, deposited directly on the PET, coeval to the multilayers, with a red line indicating the resulting average value. With the exception of sample n. 2, all OTRs fall in the same range of those for single barrier layers, indicating no net increase in the barrier properties. On the other hand, however, the stacking neither results in a worsening of the barrier performances, which could sometimes be induced by the augmented internal stresses in a considerably thicker PECVD film. This is in contrast with similar stack multilayers deposited by means of HMDSO at the same operating conditions, which showed stark increases in the transmission rates, sometimes comparable to those obtained for the uncoated PET reference [260]. Since, in case of breaking of the stacked multilayer, or in case of incomplete

coverage of the surface by the uppermost barrier, the transmission rates would have resulted to be much higher, such possibilities should be ruled out. Pictures of the samples after being subjected to the pinhole test reinforce such conclusion since, as it can be seen in Figure 8.6, the uppermost barrier shows defect densities comparable to those of single barriers deposited directly on PET. Furthermore, no crystal-covered crack or other surface damages akin to those shown in Figure 6.24 and Figure 6.26 are to be seen. It can be then concluded that the failure in improving the barrier properties lies in the inability of the intermediate layer to effectively decouple the pinholes in the two barriers. The relatively lower rate for sample n. 2 however seems to suggest that such failure may not be systematic. Further and thicker multilayer systems have therefore been deposited and tested. Their descriptions, together with the corresponding labels, are listed in Table 8.2. The operating parameters for the two different films are the same reported in Table 8.1.

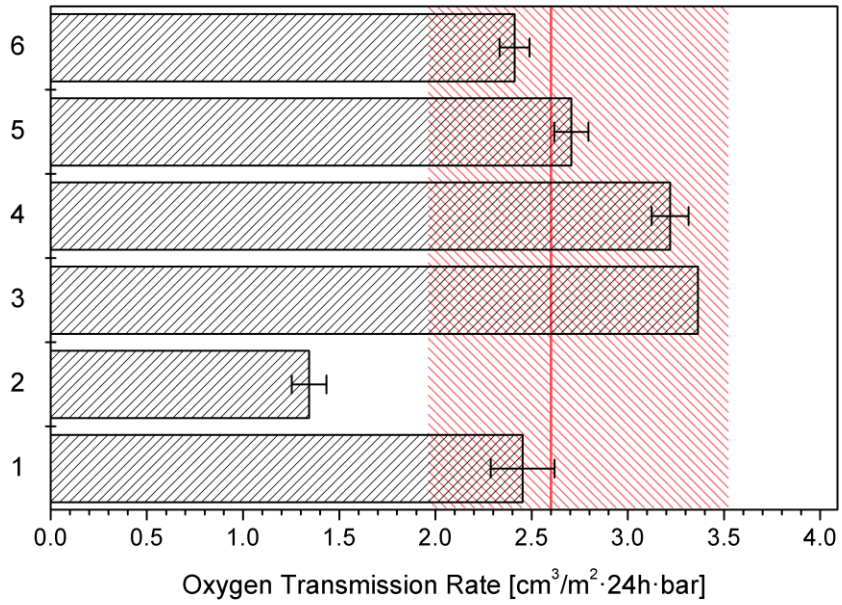

Figure 8.5: Normalized oxygen transmission rates for the first batch of multilayers, with the reference values for single barrier layers in the red range and the resulting average as a red line.

Sample IIc has been deposited with the same oxygen-to-monomer and hydrogen-to-monomer ratios but with halved fluxes in a deposition step twice longer. In sample IId the intermediate layer has been substituted by a thin liquid film of HMDSN, poured by means of a pipette after removing the sample from the reactor, in order to try a completely different chemistry from the SiO_x film that could provide a decoupling effect. The underlying assumption is that, after the evaporation of HMDSN during the pumping of the reactor, some liquid would remain trapped in the pinholes, which act as capillary, effectively 'sealing' them.

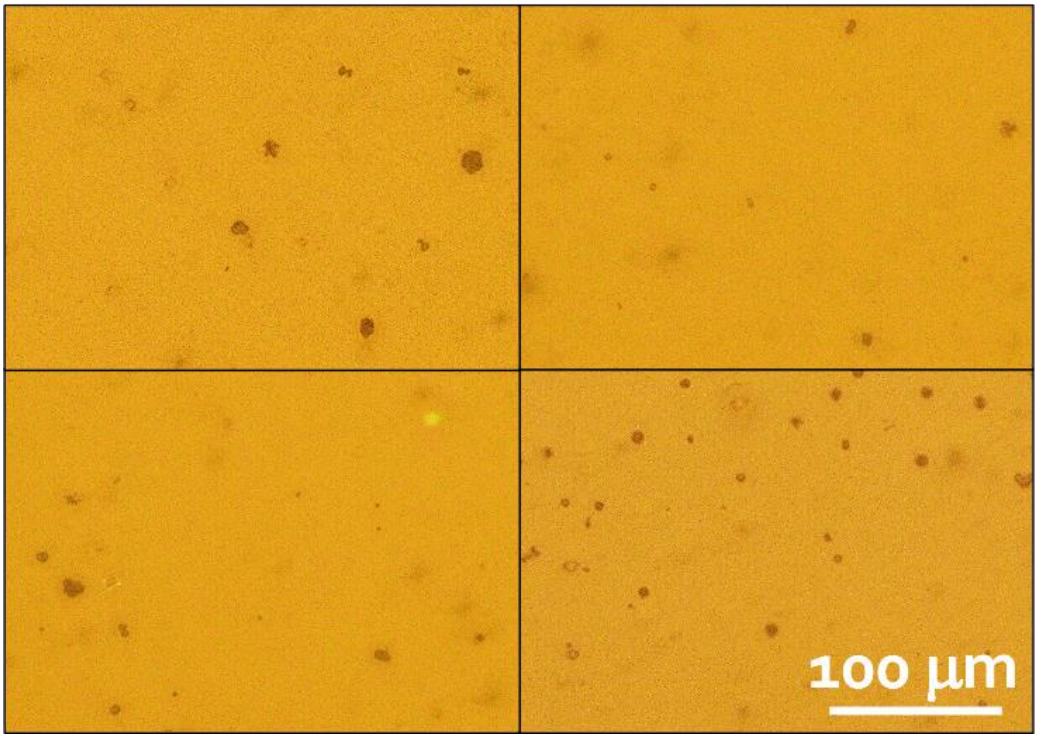

Figure 8.6: Optical microscope pictures of a selection of samples 1-6 after being subjected to the pinhole test.

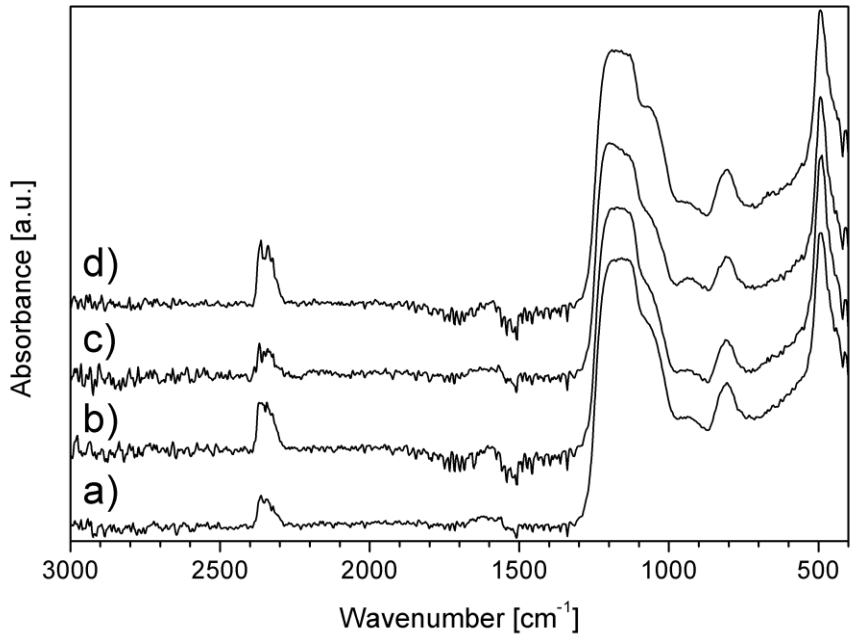

Figure 8.7: Absorbance FTIR ATR spectra of a selection of multilayers: a) = Ia; b) = IIb; c) = IIc, and d) = IId. Spectra normalized to the intensity of their main peak.

Table 8.2: Labels for the deposited multilayer samples. Roman numbers indicate the number of dyads in the multilayer. The first organic layer, when present, is excluded from the count.

Label	Stack	Gradient	Remarks
Ia	✓		first layer : organic
IIa	✓		first layer : organic
IIb		✓	first layer : organic
IIc	✓		gas fluxes : halved
IId	✓		liquid HMDSN as intermediate layer
IVb		✓	first layer : inorganic
Va	✓		first layer : inorganic
VIIa	✓		–
VIIb	✓		layers' thickness: 50 nm

A selection of such multilayers, with the uppermost film being SiO_x-based, has been investigated by means of ATR infrared spectroscopy: because of the reduced penetration depth of such method, only the chemistry of the top layer may be detected. It is therefore possible to ascertain whether the growth of the inorganic film is influenced by the chemistry of the underlying SiO_x-C_yH_z intermediate layer. The resulting absorbance spectra are reported in Figure 8.7 and show good consistency and accordance among themselves and when compared to the 40/1 spectrum in Fig. 7.5. No signal consistent with organic bonds, either from the barrier themselves or from the underlying intermediate layer, in particular the sharp methyl band around 1260 cm^{-1}, is to be appreciated.

Samples Va and IVb, deposited only on glass substrates, have been chosen as representative for both macro-categories of multilayers (stacked vs. gradient) in order to be investigated at the Fraunhofer IGB by means of electron microscopy. In order to observe a section of the films, similarly to what done for the investigations on the film thickness in Chapter 7.3.3, the samples have been cracked with a wire cutter, and only the jagged edges resulting from the fractures have been observed. The stacked multilayer Va is shown in Figure 8.8, at two different magnifications (25k and 100k, respectively). It is possible to observe how the discrete structure of the multilayer, when subjected to stresses, as those induced in this case by the cutting of the glass, results in the layers breaking singularly, with a step like structure that, in this case, slightly juts out of the substrate. The same structure can be observed on the overexposed ledge on the right border of Fig. 8.8a. The uppermost pair of layers is difficult to discern in Fig. 8.8b, because of a poor exposure of the scan. It is however possible to notice how the single layers present a clearly separated struc-

ture, attested by the thin bands of different colors (knowing that the first layers is organic, their attribution is straightforward), and grow homogeneously even on top of each other, covering the full surface. The interfaces between pairs of layers do not show a noticeable roughness, nor any punch-through or other deformation that could disrupt their structure are to be seen. The in-built scale allows to determine the thickness of the layers, which for the barriers proves to be around 95 nm, and 130 nm on average for the organic film. This confirms the values obtained by means of the profilometer, which always showed a slightly thicker than expected multilayer. The organic layers, in this case, seem to consistently grow slightly faster than usual, as their deposition time was adjusted in order to obtain a 100 nm thick film.

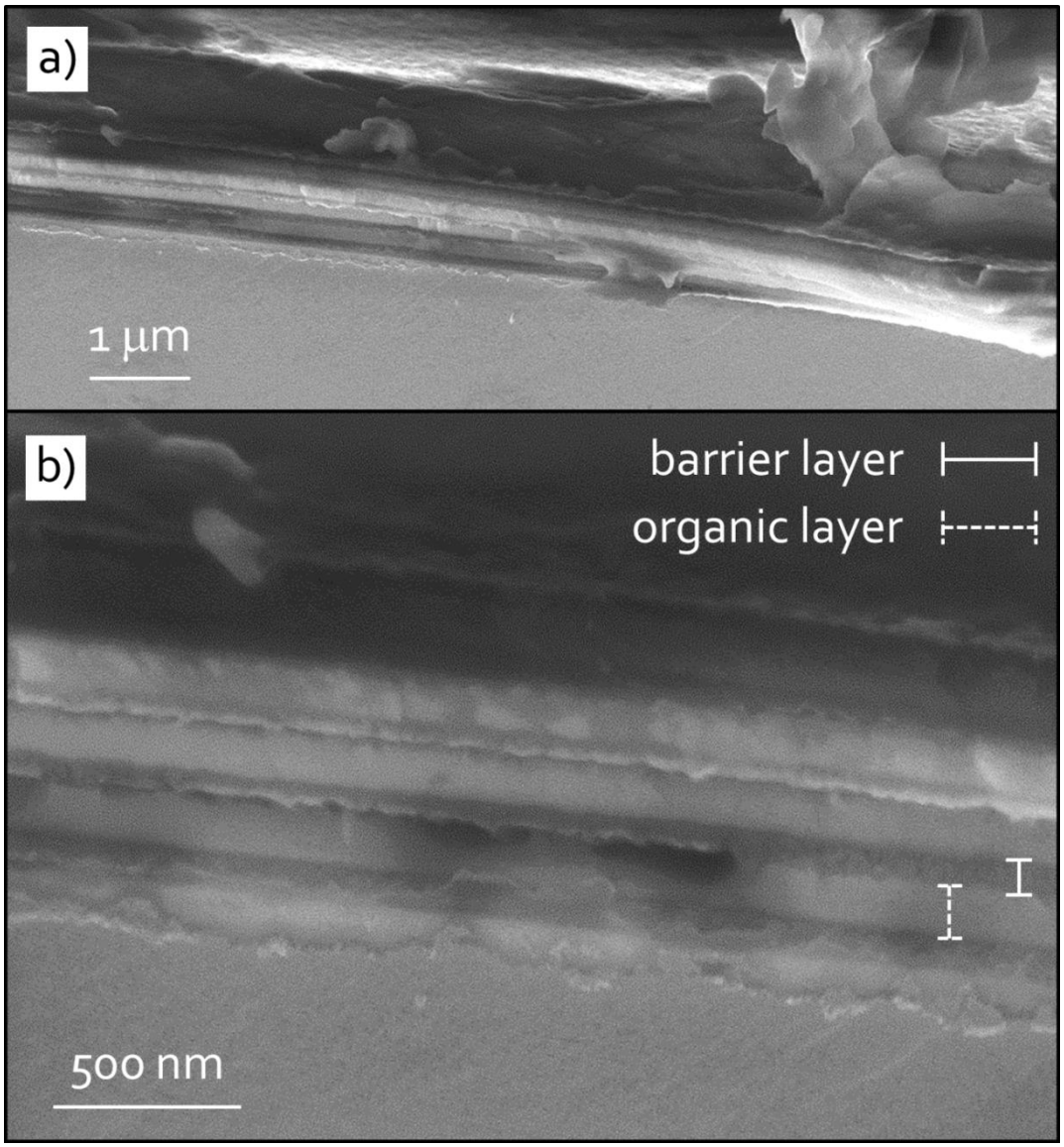

Figure 8.8: SEM pictures of the section of a stacked multilayer on glass (sample Va) at a magnification of 25k (a) and 100k (b). Picture b has been acquired at a different spot. Analyses carried out at the Fraunhofer IGB.

In contrast to this stacked structure, the gradient IVb sample, reported in Figure 8.9, shows a remarkably different structure. In this case, no bands of different colors are to be seen, but rather a homogeneous and slightly grainier composition, still however distinctly different from the underlying glass (compare this to Figure 7.66 c, with the interface being barely noticeable). Curiously, it is still possible to discern the single dyads, thanks to slight edges extending horizontally for the full length of the profile. It is unclear how such separation among dyads comes to be: as it takes place when an organic layer is deposited on top of a barrier, perhaps, as the latter has a higher deposition rate than the former, instead of slowly adapting to the silica-like substrate is more favorable – and quicker – for the system to disrupt the continuous structure. It is worth of notice, moreover, how the top bottom corner of the picture, at the interface with the glass, shows a dark spot similar to a void, where the organic layer first failed to adhere to the glass (it is not possible to conclude whether this has been induced by the presence of a foreign particle, at a further 'depth'). Immediately above the hole, however, the faint vertical growth lines in the film clearly show how the film covered the unidentified bump and later smoothed itself to a horizontal line again, which hints at a good flexibility and resilience of such multilayer systems. The four dyads, measured by means of the in-built scale, provide a consistent value of around 160 nm. This is in good accord with the choice of deposition times for each step, which have been chosen to correspond to a 200 nm (100 nm + 100 nm) bilayer on glass. Considering the transient short step ('lost time') in which the plasma feed turns from an oxygen- to a hydrogen-rich one and vice versa, then, it stands to reason that the resulting thickness of the dyad would be slightly smaller than the nominal value.

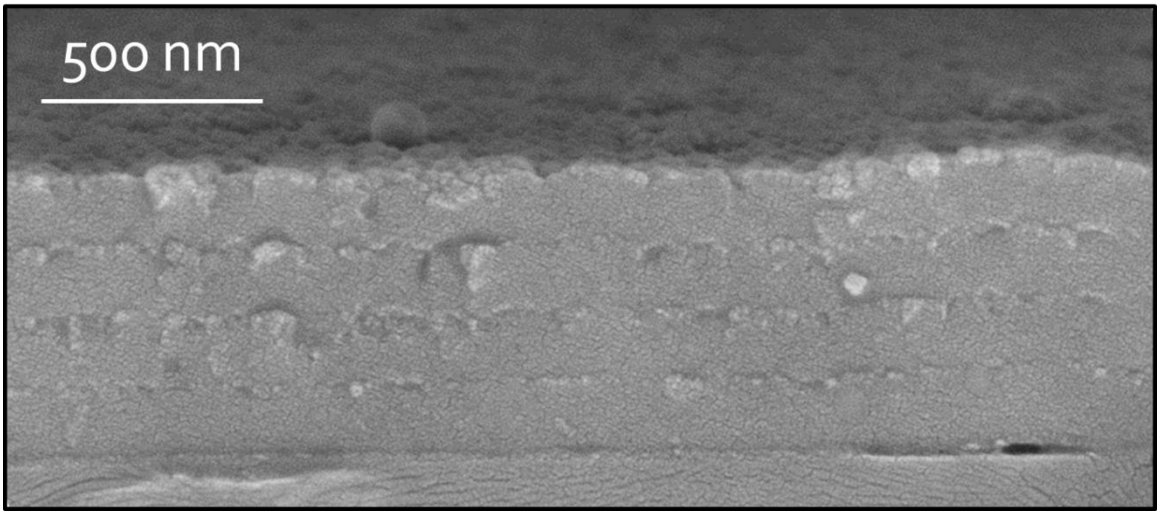

Figure 8.9: SEM pictures of the section of a gradient multilayer on glass (sample IVb) with four dyads at a 100k magnification. Analyses carried out at the Fraunhofer IGB.

The barrier properties of the samples listed in Table 8.2 – with the exception of the aforementioned samples employed for the SEM imaging analyses – have then been tested. The normalized values are reported in Figure 8.10. In case of repeated measurements for the same multilayer, only the lowest value has been displayed. This batch of samples, too, does not result in an improvement – nor however in a worsening – in the barrier performances, not even in the case of the films with the highest number of dyads, for which even one successful decoupling between two neighboring barriers would have been enough to produce a noticeable drop in the transmission rates. It is worth of notice that sample VII b, although containing barriers only 50 nm thick, shows the same performances of a layer with the same number of dyads but with twice the overall thickness.
The cause for such failure may be ascribed to at least two different phenomena:

- the chemistry of the intermediate layer is still close enough to the one of the barriers to allow the pinholes in the latter to simply keep growing throughout the additional layer, and then into the subsequent barrier layer, despite plasma being switched off – in some cases for several minutes – after each deposition step; a solution to this would then be to optimize an intermediate layer with a completely different chemical composition, perhaps not even based on HMDSN as a precursor. In this case, however, the first layer acting as a protection for the OLEDs would either still need to be based on a H_2/HMDSN discharge or on another plasma feed that still has however to be completely oxygen-free;
- the barrier properties of the intermediate layer are insufficient, as they too play a role in the overall multilayer effectiveness [9]. As shown in Appendix 2, all hydrogen-to-monomer ratios exhibit very poor barrier performances against oxygen, with the best BiF equal to only 1.2. In case of a good barrier layer, through which permeation takes place almost exclusively through defects, the underlying volumes in the intermediate layer are subjected to very strong concentration gradients that forcefully increase the overall permeated flux, almost acting as local funnels [7]. Even in the case of a successful decoupling, then, the increase in the permeation length is counterbalanced by an almost null increase in the permeation time, resulting in a permeation process still limited by the first barrier layer alone. If this is the current case, then, a completely different chemistry of the intermediate layer is still required, which should also result in improved barrier properties.

Alternatively, as suggested by Graff *et al.* [39], the diffusion path may be further increased by *reducing* the intermediate layer thickness to less than the average spacing between two neighboring defects in the barrier layer. In this case, the gradient vectors become parallel to the internal interface among layers, resulting in a much longer and arduous effective diffusion path. Nonetheless, the aforementioned multilayers, without further changes, have been chosen for

the encapsulation of OLEDs prototypes, both in a stack and in a gradient configuration, in order to at least verify whether the prolonged deposition step may cause harm to the electronic devices.

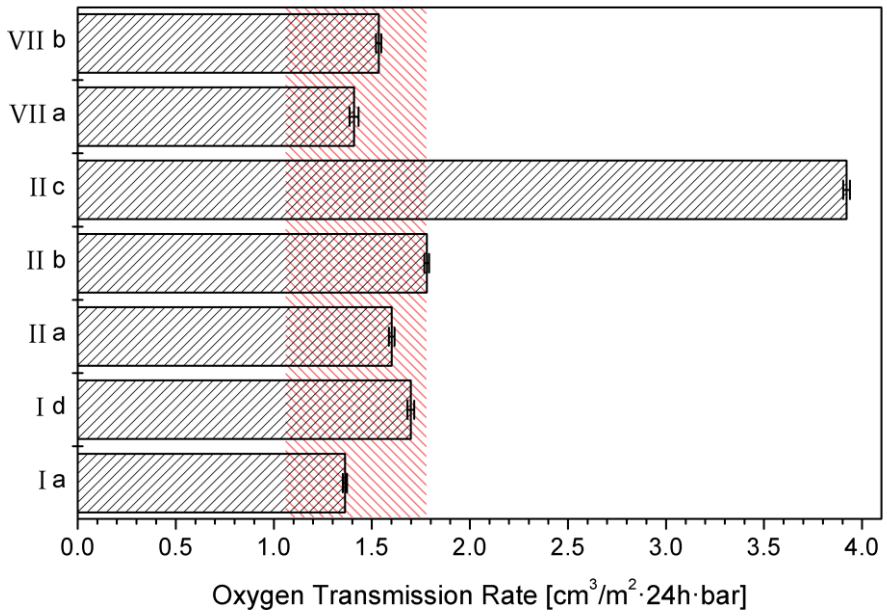

Figure 8.10: Oxygen transmission rates for multilayer systems, with the reference values for single barrier layers in the red range.

8.2 OLED prototypes

All the prototypes employed as substrates for the multilayer encapsulations consist of Bottom Emitting OLEDs (BEOLED) developed and produced at the Institute of Material Research of the University of Hasselt, Belgium, in four different colors, and in two different sizes, as reported schematically in Figure 8.11. All prototypes operate with a DC voltage of 3 to 5 V.

The design for the larger specimens includes a bottom Ag electrode in the shape of a bus bar, in order to ensure a homogeneous injection of electric charges in the emitting layer and a consequently even light emission. The structure of such larger OLEDs, together with the deposition techniques employed for each layer, is reported in Figure 8.12.

The prototypes, for both sizes, when deposited on glass acting as a rigid substrate, prove to be operational and to emit homogeneously. The same is valid, for the smaller devices, even in case of a flexible substrate (PET), as shown in Figure 8.13.

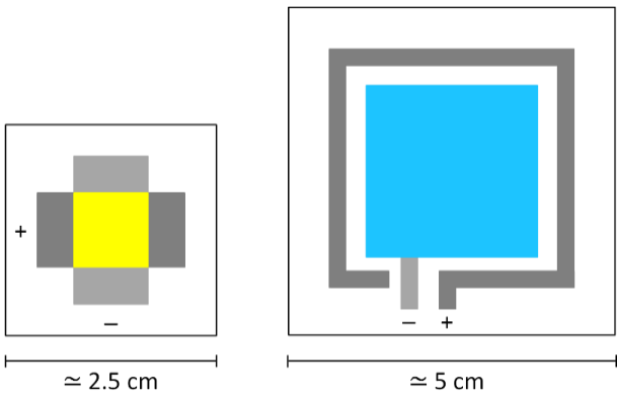

Figure 8.11: Schematic representation of the two types of BEOLEDs employed in the multilayer encapsulations.

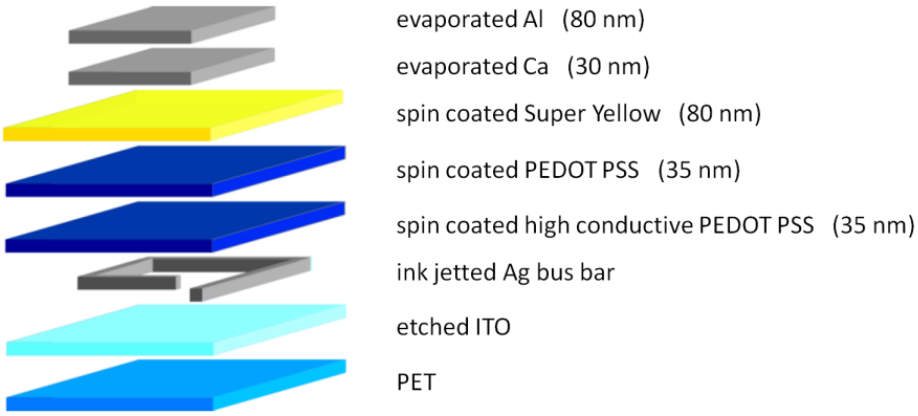

Figure 8.12: Structure of larger BEOLEDs with a total thickness of less than 500 nm [261]. ITO: indium tin oxide; PEDOT: polyethylenedioxythiophene; PSS: polystyrene sulfonate.

The prototypes printed on PET have been sent for the encapsulation in a sealed container filled with nitrogen within one week after their production. Upon arrival, they have been tested in inert atmosphere by means of a portable DC cell before the immediate encapsulation (see also next section). In most cases, however, both small and large devices showed inhomogeneous light emission, as illustrated in Figure 8.14. The cause may be delamination of the cathode [4] or detachment between cathode and emitting layer, due to a yet to-be-optimized printing process [263, 264], as some of them already presented inactive areas immediately after their completion [262], or early degradation caused by oxygen residuals in the transport box. The electrode printing and alignment, in particular, proved to be the most influential factor in determining the functioning of the devices, and in some cases their conductivity has been *a posteriori* enhanced by applying a silver-based colloidal solution on top of them.

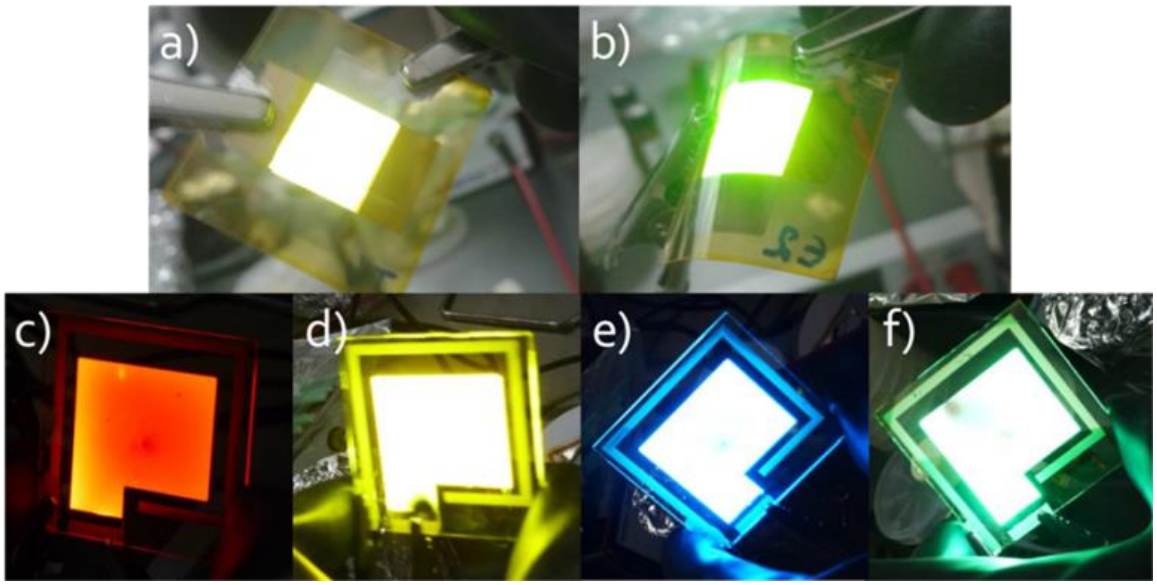

Figure 8.13: Smaller OLEDs prototypes on glass (a) and on PET 50 μm thick (b), and larger prototypes on glass in the four employed colors (c – f). Samples tested in a Glovebox flushed with nitrogen [262].

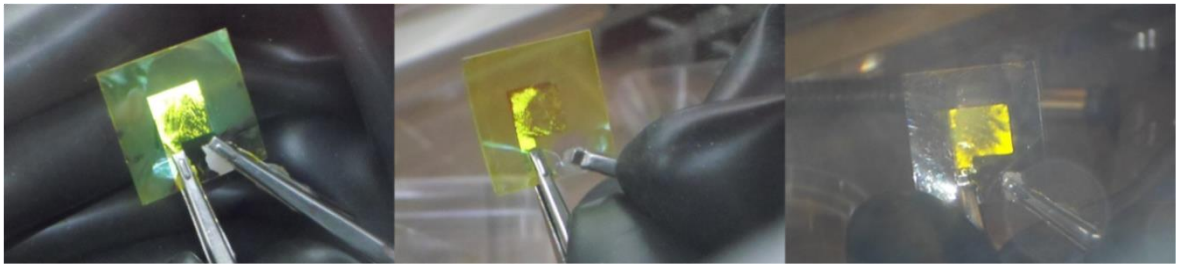

Figure 8.14: Smaller prototypes on PET tested one week after being printed and immediately before the encapsulation process, showing dark areas and inhomogeneous emission. In the first picture it is possible to observe the silver-basd solution applied on the electrodes.

8.3 Building and connection of a glovebox to the ECR reactor

The handling and the insertion of the uncoated OLEDs, transported in a sealed cylinder, must take place in an inert atmosphere devoid of oxygen and water vapor. A glovebox directly connected to the ECR reactor has been therefore rendered necessary. A schematic representation of the employed glovebox, from SylaTech Company, is reported in Figure 8.15. It consists of a trapezoidal polycarbonate box connected to a cylindrical steel airlock that allows the insertion and removal of samples.

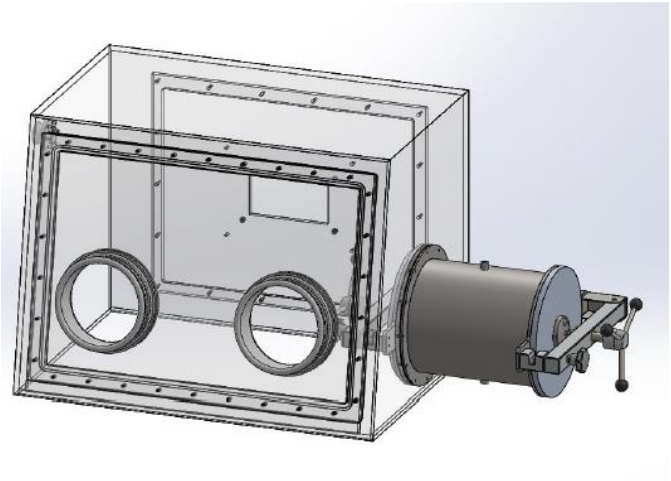

Figure 8.15: Schematic representation of the glovebox employed for handling of uncoated OLEDs. It consists of a polycarbonate main body, with walls 1 cm thick, a base of 92x65 cm^2 and a height of 67 cm. Connected to it, a stainless steel airlock with a length of 30 cm and a diameter of 27.3 cm allows the insertion of the samples [265].

The airlock is purged with nitrogen by means of a copper line and two series of valves connecting it upstream to a nitrogen bottle, and downstream to a rotary pump. A vacuum gauge allows the inner pressure to be monitored in real-time. For the glovebox, the nitrogen flux is provided by a high-pressure cylinder connected through a line with two pressure regulators and two further locks. A three-way Swagelok valve finally allows the exhaust nitrogen cylinders to be replaced while at the same time keeping the glovebox atmosphere isolated. The oxygen concentration inside the glovebox is monitored by means of a Zirox E2010 sensor, and leaks from the outside are reduced by keeping a small internal overpressure, monitored by a vacuum gauge. Backdiffusion of oxygen from the atmosphere through the gas outlet is blocked by means of a pressure relief valve. The glovebox is connected to the back of the ECR reactor through an adapter on its rear side and a windowless steel port similar to the one in front of the reactor (see also Fig 5.2). After being prepared, the samples are placed inside the reactor by fixing them with duct tape on an aluminum holding plate: the latter is handled, and then inserted in the reactor chamber, by means of a suction cup connected to a pump and to the nitrogen line that enables its suction and venting (Fig. 8.16). Before its use, the glovebox is left purging with nitrogen for at least one week. The flushing curve is reported in Figure 8.17. The main source of oxygen while operating with the box is caused by the leaks inside the ECR reactor. The latter, although its air inlet for the venting is in turn connected to a nitrogen cylinder, in order to ensure an inert atmosphere inside it, still contains significant traces of oxygen because of its relatively large volume. The level of O_2 inside the glovebox rises up to 3000 ppm every time samples are inserted in/removed from the plasma reactor. As a comparison, at the end of the first flushing step the oxygen baseline does not exceed 50 ppm (0.004 %). After isolating the glovebox from the ECR

reactor, the oxygen level then quickly subsides to around 500 to 200 ppm after around twenty minutes.

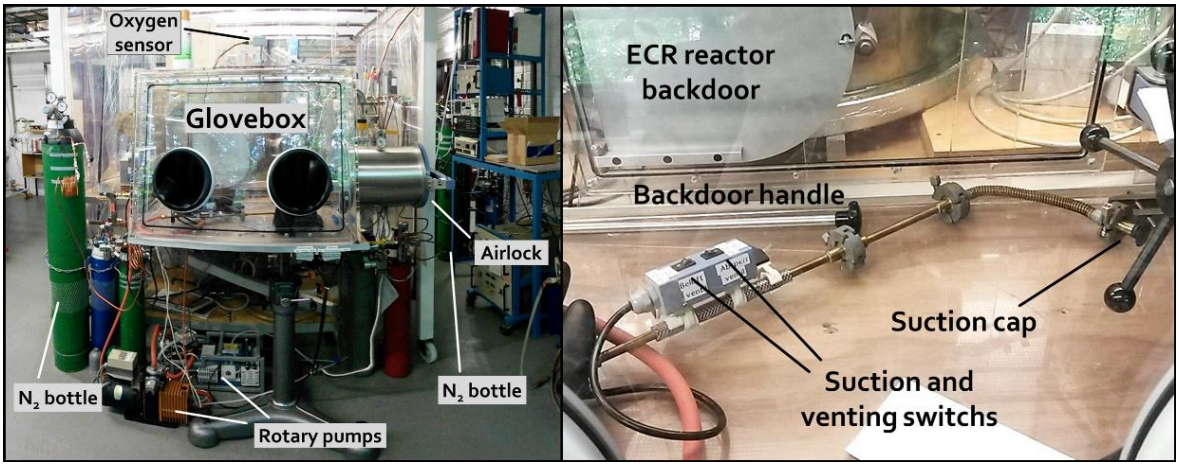

Figure 8.16: Glovebox and relative flushing system and sensors connected to the ECR reactor (left) and details of the suction cap for the insertion of samples in the vessel (right).

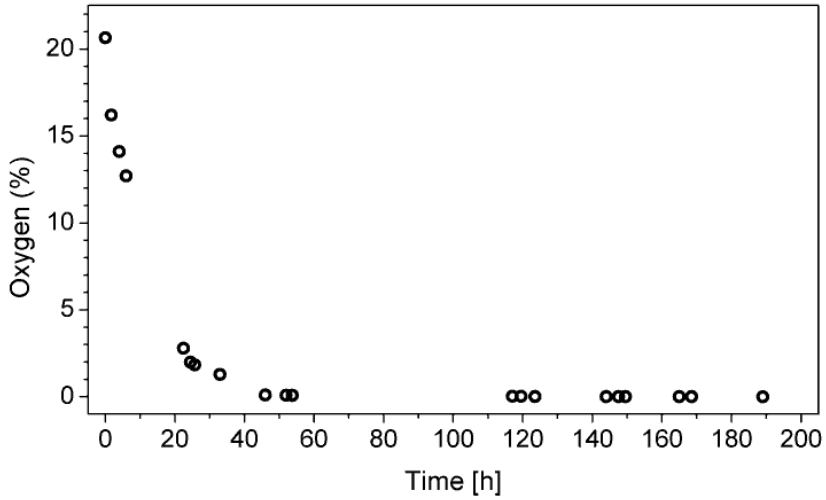

Figure 8.17: Oxygen fraction in the glovebox atmosphere as a function of time. t = 0 coincides with switching on the flushing system.

8.4 Encapsulation of OLEDs

With the prototypes being printed on a PET substrate, a two-step multilayer encapsulation is required. A multilayer system must then at first be deposited on the upper side of the devices, and

then the latter must subsequently be removed from the reactor, flipped and reinserted, for the encapsulation on their bottom side. The profile of a device encapsulated according to such approach is schematically represented in Figure 8.18.

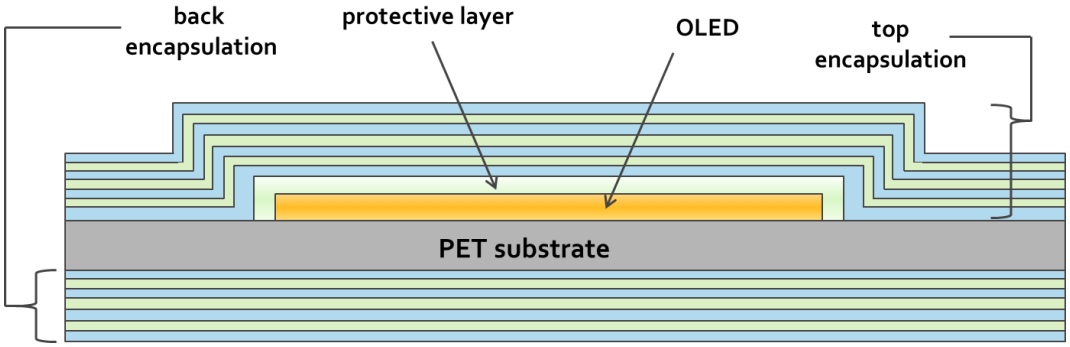

Figure 8.18: Schematics of the encapsulation strategy for OLED prototypes on PET. Picture not in scale.

The number of dyads forming the encapsulation layer has been varied from one to four, with a first film always corresponding to a protective layer deposited in an oxygen-free step. Direct exposure of the organic devices to reactive oxygen in plasma phase would in fact result in severe damages to the former's integrity [266]. Some encapsulation, in particular those with the highest and lowest number of dyads, have also been carried out at least twice for different batches of samples. The thickest barrier systems have also been deposited as gradient layers, despite the latter not being as extensively investigated as the stacked ones. The prototypes, with their lateral dimensions reported in Fig. 8.11 and amounting in total to 58, have been tested again by means of a portable DC cell, immediately prior being inserted in the reactor. When possible, each batch was constituted by one large OLED and at least six smaller ones. The samples have been fixed on the holding plate by means of small strips of duct tape, which as a side effect prevents the underlying areas, on the edges of the substrate, to be encapsulated. Furthermore, as the electrodes needed to remain exposed for subsequent testing of the devices to be possible, they too have been left masked during both encapsulation steps.

Some of the thickest multilayers, deposited at the same time also on glass substrates, with an overall thickness approaching to 1 μm, are shown in Figure 8.19. It is possible to observe how both kinds of multilayers retain their colorlessness and good transparency, when compared to an uncoated substrate. The faint rosy halos and iridescent effects observed in some samples arise from thin-film interference phenomena taking place inside the multilayers, as their thickness grows comparable to wavelengths in the visible range.

After the first encapsulation step, and once more after the back encapsulation, all samples have been electrically tested in order to observe eventual damages or failures caused to them

upon exposure on the plasma atmosphere and the associated VUV radiation. Three examples, including both small and large devices, are reported in Figure 8.20. In all cases, it is possible to observe how the emitting area, while being already far from the total active surface, especially for larger area devices, is not further reduced, nor its emission weakened. It can therefore be assumed that the first, weakly protective layer and the overlaying barrier are effective in shielding the devices for the whole duration of the deposition step, which, for the thickest multilayer, lasts up to thirty minutes. Moreover, the heating of the samples in such prolonged process is still low enough to avoid thermal damages, which for organic devices start to take place already shortly above 45°C [267]. Occasional difficulties in lighting up the devices immediately after the encapsulation are then likely to be ascribed to failures of the electrodes rather than of the organic emitting layer. As mentioned before, the conductivity of the electrodes required to be enhanced by applying a silver-based solution on them. Such supplemental layer showed poor adhesion and was easily peeled off when removing the duct tape mask from the electrodes.

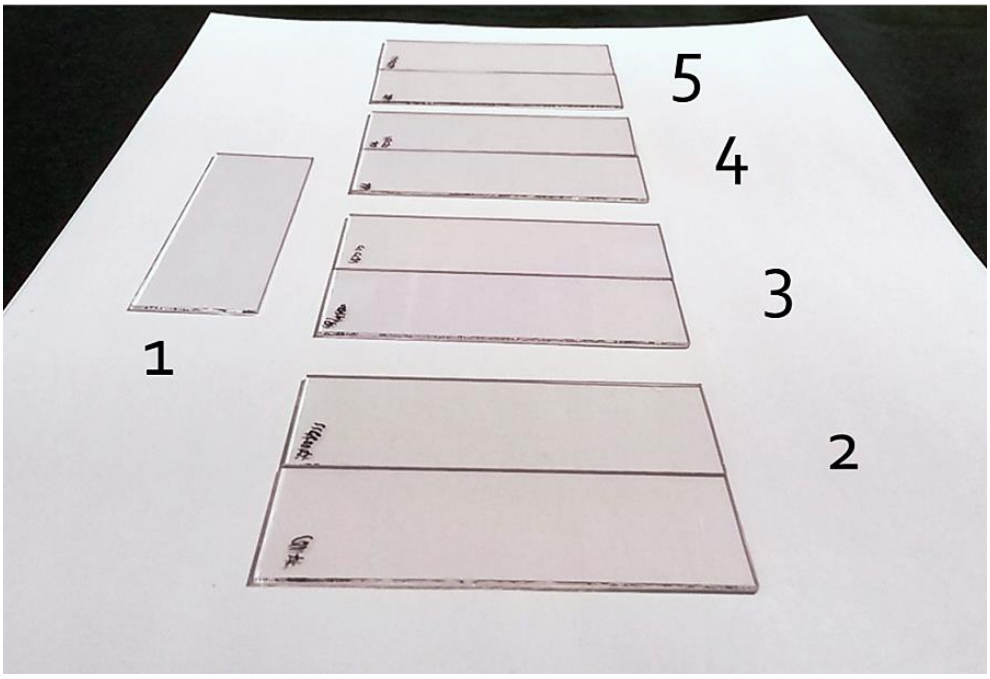

Figure 8.19: Glass substrates left uncoated for reference (1), and coated with three (2 and 4) and four (3 and 5) pairs of dyads plus a first protective organic layer. Samples 2 and 3 consist of separated, stacked barrier and organic layers, samples 4 and 5 of gradient layers gradually changing their chemistry from organic to inorganic.

The samples, repacked in the transport box with inert atmosphere, have then been brought back to the Institute of Material Research in Hasselt, Belgium, and kept in inert atmosphere for further durability tests. In some cases, after re-applying the colloidal solutions on the electrodes,

the devices were again able to function, further hinting at an electrical problem being the cause of at least some of the malfunctions. After one month, no further degradation of the still-operating OLEDs was visible. One of the best working devices, a larger yellow emitting OLED on PET, coated with the gradient layer with four dyads and an initial protective layer (the multilayer system reported in Fig. 8.10 has been simultaneously deposited during this batch of OLEDs), has then been removed from the glovebox and left in open air, while being tested at regular intervals. The pertaining pictures are reported in Figure 8.21. Fig 8.21 b, taken one month after the encapsulation process, shows unchanged performances of the emitting layer of the device, when compared to those immediately before being encapsulated (Fig 8.21 a). Fig. 8.21 c, taken 18 hours later, shows a visible degradation of the emitting layer, with worse effects around the edges of the latter. Fig. 8.21 d, taken after further 24 hours, shows the final stages of its lifetime, with only a few single spots still emitting. After little more than 40 hours in air, then, the device has ceased to operate [262]. Such survival time, when compared to the usual lifetime for similar uncoated prototypes manufactured by the same research group, which amounts to few minutes, shows an improvement factor of more than two orders of magnitudes.

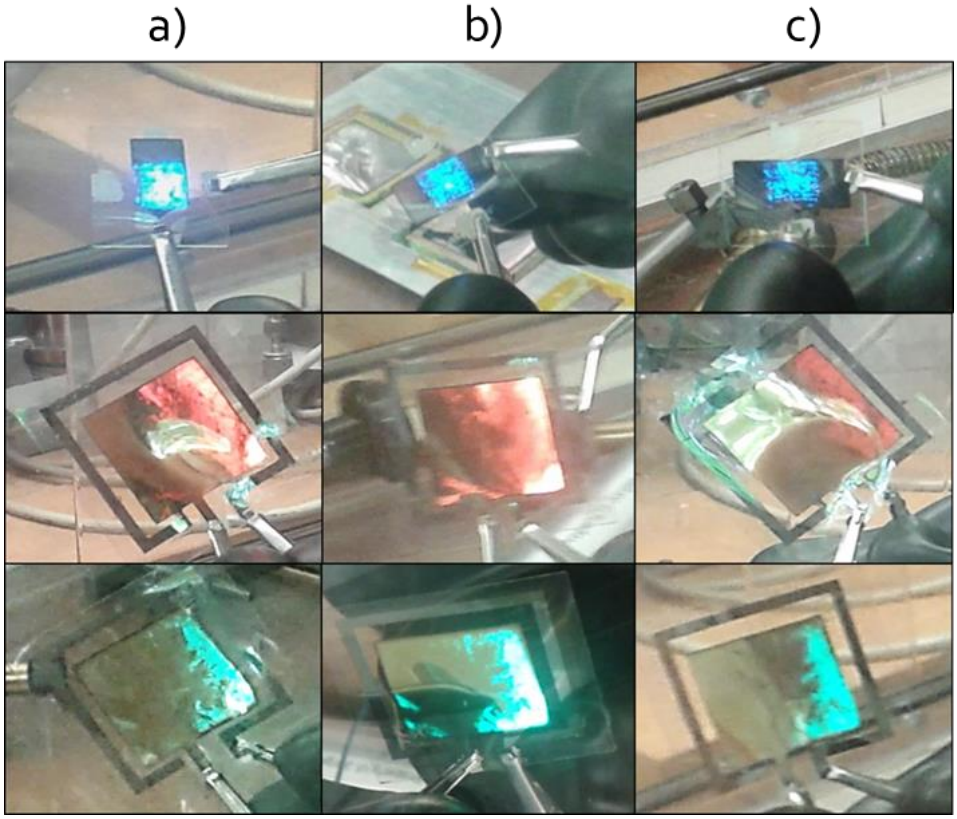

Figure 8.20: OLEDs prototypes inside the glovebox before the two-steps encapsulation (a), after the top encapsulation (b), and after the top and back encapsulation (c).

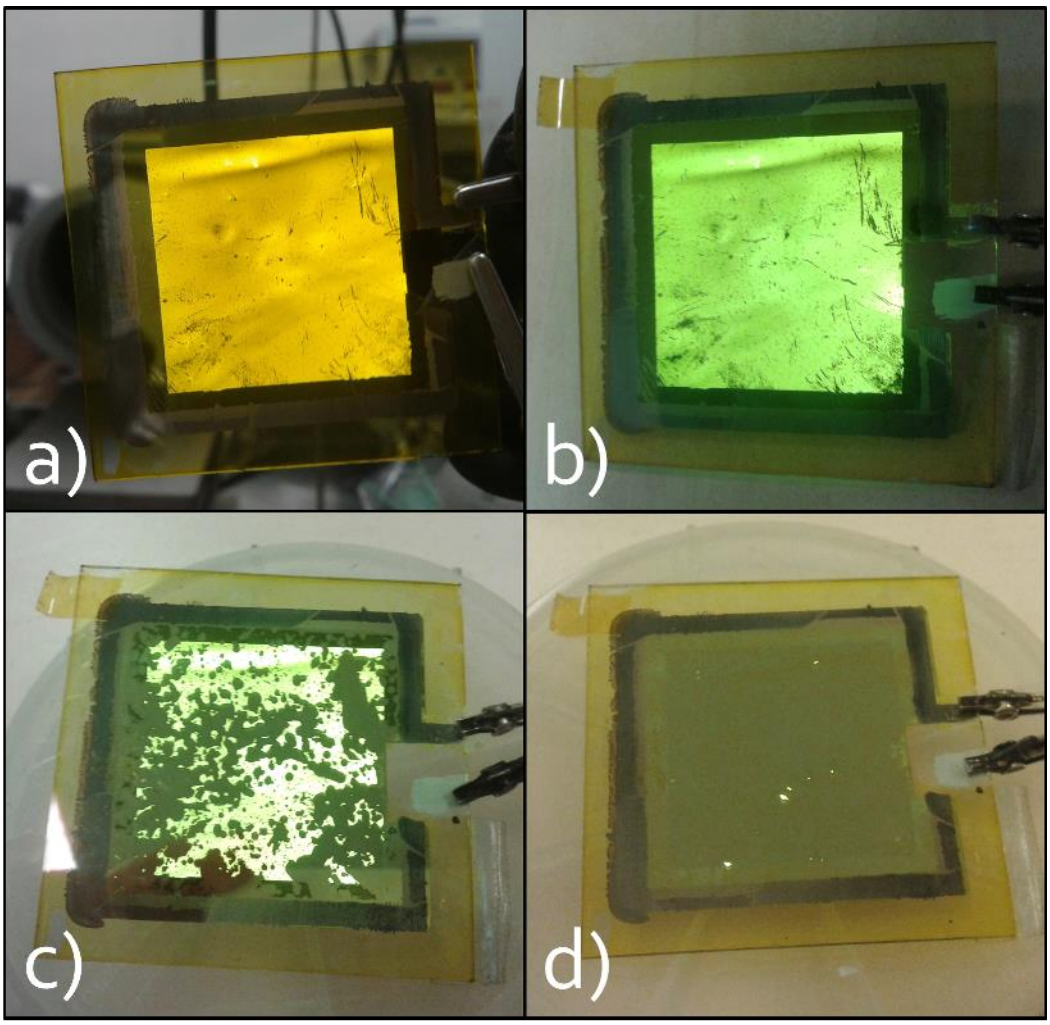

Figure 8.21: Large OLED on PET at different stages of the encapsulation and post-encapsulation process (variation in light color due to different camera settings and lightening): before being inserted in the transport box for the encapsulation process (Fig. 8.21a). The now encapsulated device, one month after remaining in inert atmosphere and immediately before being left in open air (Fig. 8.21b). The sample around 18 hours (Fig 8.21c) and 42 hours (Fig. 8.21d) after removal from the glovebox. Courtesy of Inge Verboven.

Chapter 9

Summary and outlook

9.1 Summary

In the current work, thin films with the aim to serve as barrier against oxygen for the encapsulation of sensitive devices, flexible organic LEDs included, have been investigated. The thin barriers have been obtained by means of a plasma enhanced chemical vapor deposition process carried out in a low-pressure, microwave-sustained pulsed plasma operating in an electronic cyclotron resonance configuration. The magnet in the reactor, with an area of around 0.05 m^2 and a consequent magnetic field tuned so to ensure resonance conditions with the incoming microwaves at a frequency of 2.45 GHz, through a motor connected to it can homogeneously treat a much larger surface, limited only by the size of the reactor.

The deposition process has been carried out by means of a mixture of hexamethyldisilazane (HMDSN) as precursor and oxygen as co-gas. The operating parameters investigated and optimized in the work have been oxygen-to-monomer ratio in the gas phase, operating power and deposition time.

The ensuing analyses of the chemical composition of the resulting films, carried out by means of infrared spectroscopy in different configurations and X-ray photoelectron spectroscopy showed how, by changing the gas feed composition, it is possible to gradually shift from a largely organic solid film still resembling the original precursor to an almost completely inorganic, hard film resembling amorphous silica. The threshold among the two has been found out to lie, for a power of 555 W, around a 25/1 oxygen to monomer ratio. By keeping the gas feed at a fixed composition, and by variating in turn the operating power, a similar tuning effect on the final film chemical composition has been observed. Some fixed limits in the range of operationality in the employed experimental setup have however been found. The lower range for power is limited by the inability of the plasma to ignite, and at the other end of the range the higher amount of energy injected in the plasma causes the thermally sensitive substrate to be damaged by it. Extremely low oxygen-to-monomer ratios, on the other hand (≤ 20/1), can never result in inorganic lay-

ers, regardless of the employed operating microwave power. The chemical analyses further showed how the deposition time and the resulting thickness of the films do not have an effect on their chemical composition. Small percentages of residual carbon incorporated in the films, on the other hand, proved to be beneficial to their inherent resilience and adhesion, helping them retaining their mechanical integrity.

The permeation analyses performed showed how the turn to inorganic chemistry for the films coincides almost univocally with the onset of good barrier properties, which at very high oxygen-to-monomer ratios partly degrade because of the mutated resilience of the films. The best pair of power and oxygen-to-monomer values has been found out to be equal to 555 W and 40/1, respectively. Such conditions ensure reproducible, flexible and resilient films with a barrier improvement factor up to around 100 and more. Such films have shown an optimal thickness of around 100 nm which can however be lowered to 75 and even 50 nm with only a small increase in the dispersion of the average transmission values. For higher thicknesses, the 40/1 film show excellent stability and unchanged barrier performances up to one order of magnitude more. The intrinsic growth mechanism allows the film to effectively dissipate eventual internal stresses and at the same time ensures enough lateral strength to also avoid delamination and mechanical failures. After up to 50 bending cycles performed with a bending radius of 0.75 cm, the average increase in the transmission rates for 100 nm films does not exceed 20%, i.e. still in line with the dispersion obtained for repeated depositions at the same conditions. The films also proved to remain largely unaffected by the kind of substrate, even in case of vertical structures with a height equal to 50 % of the thickness of the barriers.

A non-destructive method for the identification of defects on the macro- and on the microscale has been developed and tested, based on the local precipitation of calcium carbonate on top of the defects in the barrier layer. The assumptions on which it operates state that the precipitation process is quick and that only the immediate surroundings of a defect provide the necessary conditions to trigger a nucleation step, so that each crystal correspond to a defect underneath it. The coated sample acts as a separator between a pure CO_2 flux and saturated lime water solution inside the sample-holding cell, with the permeation of carbon dioxide into the aqueous solution above taking place preferentially through the defects in the barrier layer on top of the polymeric substrate. The thorough investigations proved the assumptions on which the test operates to be corrected, and the method to be reliable for the localization of defects on the surface. The calcium carbonate crystallites, retrievable at a later stage at the scanning electron microscope by means of markers applied on the samples surface, provide through their size and morphologies further insight about the kind of defects of the film. The applicability of such test is limited to films through which oxygen permeation takes place almost exclusively through the pinholes. The calculated numerical densities for the PECVD films lied in very good accordance with the respective oxygen transmission rates (OTRs). In this case too, 40/1 samples showed a minimal defect density. Higher oxygen-to-monomer ratios, while presenting only a minor in-

crease in the OTR values, also showed several times higher defect densities. Repeated permeation measurements after the pinhole tests confirmed that, in case of inorganic layers, the calcium carbonate crystals originate selectively on top of surface defects.

A selection of two inorganic layers and one organic one has been tested over a wide range of temperatures in order to investigate the nature of their defects. The lack of increase in the apparent activation energy for the permeation process calculated by means of Arrhenius plots proves once more the presence of defects in the films. For 40/1 barriers, further non-conclusive analyses hint at a multifactor permeation process which still includes an unknown amount of purely Fickian permeation, together with the contributions of micro- and nano-defects further sorted in different size populations.

The HMDSN-based films have been thoroughly compared with films based on hexamethyldisiloxane (HMDSO) previously obtained at the same operating conditions, showing consistently superior mechanical properties and effectiveness as barriers, in particular at high oxygen contents in the feed, for which HMDSO-based films show no barrier properties. The cause of such stark discrepancy has been tentatively found out to be most likely the different kinetic pathways taking place mainly in the plasma phase, which allow a more ordered and homogeneous growth in case of HMDSN as precursor, resulting in denser films with lesser free spaces and greater inherent resilience, better suited for practical applications.

After a brief optimization of an intermediate organic layer based on HMDSN and hydrogen ratios, multilayer systems consisting of different dyads of barriers and intermediate films have been produced and tested, with a first buffer layer being deposited in a completely oxygen-free step, in order to be readily suitable for the encapsulation of oxygen-sensitive organic devices. All of them resulted in transparent and colorless systems up to 1 μm thick. The results, on a wide range of operating conditions and combinations of the dyads, in stacked and gradient configuration alike, showed however no improvement in the barrier factors beyond those already obtained for a single barrier layer. The cause is likely to be the inability of the intermediate organic layer to effectively decouple the defects in two adjoining barriers, thus invalidating the whole multilayer approach. Such multilayers have nonetheless been employed for the encapsulation of OLEDs prototypes on flexible polymeric substrates. A readjustment of the plasma reactor, including connecting it to a glovebox in order to handle and test the prototypes in inert atmosphere has thus been rendered necessary. The ensuing deposition steps, up to 30 minutes and more long, all proved to be 'mild' enough for the devices to remain undamaged. Once the prototypes were removed from the inert glovebox atmosphere and exposed to air, their lifetime furthermore was found to increase by a factor of around 100, from few minutes to almost two days in open air.

9.2 Outlook

The barrier films produced with the best optimized operating parameters proved to perform equally or better than other PECVD films presented in literature. The partial investigations on their defects also showed their performances to be primarily limited by defects. As such, they represent the best achievable films with the current plasma reactor. A further study on the pulse duration and on its duty cycle may prove useful in determining whether a further improvement in the barrier factors is possible. With the chemistry of the barriers being optimized, any further reduction in the transmission rates is bound to a reduction in the density of defects: although no defect has been observed to be caused by foreign particles lying on the substrate and be incorporated in the film during the deposition step, the handling of substrate in a proper clean room may lead to a further increase in the barrier performances.

The CO_2-based pinhole test for the localization and identification of defects must be further developed. It can in the first place be compared with the etching test, which suffers from no limitations in its resolution, in order to determine whether the CO_2 test is able to retrieve every size of defects and, if that is not the case, where its resolution limits lie.

Furthermore, it is of great importance, after a first localization of the crystals on a barrier after the test is carried out by means of optical microscopy, to either remove them through mechanical methods or dissolve via bath in concentrated ethanoic acid (CH_3COOH), prepare the sample for scanning electron microscopy investigation and retrieve the position of the now-disappeared crystals, by means the surface markers. In this way it is then possible to directly observe the localized defects, without irreversibly altering or destroying their structure (i.e. the main advantage of such test when compared to other methods such as the etching step in oxygen plasmas). An ample enough set of observations per sample, repeated for several batches of barriers, may lead to a reliable classification of defects sorted for kinds and sizes. This can be in turn be coupled with the analyses on the dependence on temperature of the diffusion process and help develop the general model exemplified in Eq. 7.6. In order to reliably do this, however, first a much larger data set of permeation curves at different temperatures would need to be collected, both by means of repeated measurements of the same coated sample, and by testing several samples for each investigated oxygen-to-mixture ratio. With enough experimental data thus collected, it can then even be possible to model an overall permeation mechanism for the best barrier and to investigate it by means of numerical simulations.

The conclusions reached at the end of the comparison between HMDSN and HMDSO as monomers in the current setup, while being in good accordance with the presented experimental data, are far from being conclusive. Extensive investigations of the chemical reactions in the plasma phase need therefore to be carried out by means of ion mass spectrometry, optical emission spectroscopy and actinometry. Post-deposition plasma processes (mostly etching with a pure oxygen plasma) would need to be carried out and monitored by means of optical emission

spectroscopy, in order to gain a better insight on the reactions taking place exclusively in the plasma phase and those occurring at the solid surface. Studies on the densities of films obtained by both precursors and at different oxygen-to-monomer ratios also need to be performed, in order to verify the assumed microporosity of HMDSO-based films and how it correlates with the associated transmission rates.

Finally, for a multilayer approach, a completely different organic layer needs to be developed and optimized, either by changing the co-gas in the feed or the precursor molecule altogether. The aim is to obtain a chemical composition different enough to ensure an effective decoupling of the defects in the barrier layers, while at the same time retaining the current good transparency and colorlessness.

Appendix A1

Chemistry of the substrates

As mentioned in Chapter 5.2, thin inorganic layers have been deposited on two different types of PET foils in order to investigate if and to what extent a change in the substrate morphology can affect their barrier performances. In order to do so it is however necessary to exclude any other possible influence on the latter caused by, for example, small differences in the chemical composition of the substrates. A preliminary infrared analysis of the Hostaphan foil and both distinct sides of the Melinex foil has hence been carried out in the 3200-400 cm^{-1} range by means of ATR FTIR spectroscopy: the resulting spectra, with the positions of some of the most relevant bands, are shown in Figure A1.1. The complete list of main peaks and their respective attributions is reported in Table A1.1. Prior to the FTIR-spectroscopy analysis, the samples have not been washed or otherwise treated, in order to avoid external contaminations.

The complexity of the repetition unit of PET gives rise to a wide system of signals, the most intense ones relating to the carboxylate ester, like for example those at 1714 and 1245 cm^{-1}, the unresolved doublet centered around 1110 cm^{-1}, and the sharp peak at 723 cm^{-1}. By contrast the aromatic ring, thanks to its rigidity and its embedding in the main polymer chain, is less affected by the surrounding environment and produces therefore several less intense but sharper peaks, which are a common occurrence in spectra of polymers containing at least one phenylene group, like those at 1409, 1017 and 871 cm^{-1}. As reported in Table A1.1, some peak attributions remain nowadays still disputed, despite the wide investigation on spectra of polymeric materials dating back to the '60s of the last century [268-270]: for some signals a list of possible attributions is therefore provided. A further cause for the overall complexity of such spectra comes from the limited crystallinity degree of the investigated polymers [271]: with a centrosymmetric molecule in the crystalline domain, no less than 36 normal modes are IR-active [272], while conversely more modes are theoretically active for amorphous molecules. The disorder in the predominant amorphous matrix causes for a pronounced broadening of the peaks [274, 275] and, in some cases, to a splitting of the same vibrational mode in two poorly resolved peaks, as for example around 1110 cm^{-1}, with the peak at 1121 cm^{-1} pertaining to COC stretching in crystalline PET and the one at circa 1097 cm^{-1} to COC in amorphous PET. Bands related to the crystalline phase are on the other hand generally much sharper [276].

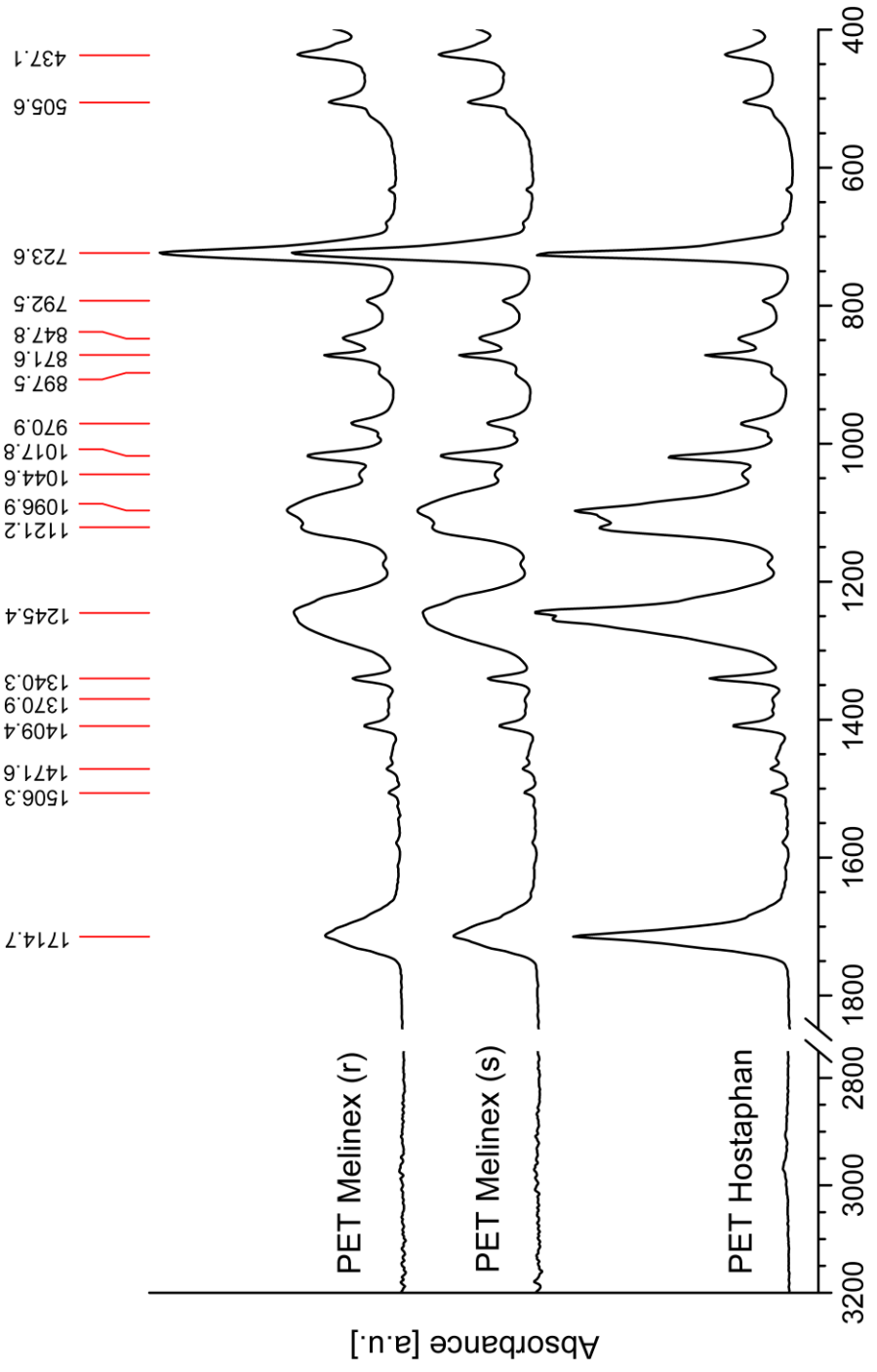

Figure A1.1: FTIR spectra of untreated PET Hostaphan (bottom), PET Melinex on the smooth side (middle), and PET Melinex on the rough side (top) in the 3200-400 cm-1 range.

Table A.1: Peak positions and vibrational mode assignments for the main absorption bands of PET.

Wavenumber cm^{-1}	Assigned group	Vibrational mode	References
2969	CH_2	ν_a	[268]
2907	CH_2	ν_s	[268]
1715	C=O	ν	[269]
1614	phenyl ring	δ	[268]
1577	C=O	ν	[269]
	C-C=O	δ	[269]
	C-C (in phenyl)	ν	[276]
1506	C-C in-plane (in phenyl)	ν	[276]
1471	CH_2 (trans)	δ	[277]
1456	CH_2 (gauche)	δ	[269]
1410	phenyl ring	ν (in plane)	[276]
1387	CH (in phenyl)	δ	[276]
1371	CH_2 (gauche)	γ	[276]
1340	CH_2 (trans)	γ	[276]
1286 1254 1245	C-O-C (unresolved triplet)	ν	[269]
1175	CH (in phenyl)	δ (in-plane)	[276]
1121	C-O-C (trans)	ν	[269]
1097	C-O-C (gauche)	ν	[269]
1045	CH_2	ν	[269]
	C-O-C (gauche)	ν_a	[276]
1018	phenyl ring	δ (in-plane)	[276]
988	CH_2 (in phenyl)		[269]
	CH_2 (trans)		[275]
971	CH_2 (in phenyl)		[268]
	C-O-C (trans)	ν_a	[276]
	O-CH_2	ν	[277]
897	CH_2 (gauche)	ρ	[276]
872	phenyl ring	γ	[277]
847	CH_2 (trans)	ρ	[269]

Table A1.1 (continued) peak positions and vibrational mode assignments for the main absorption bands of PET.

792	phenyl ring	δ (in-plane)	[277]
	C=O	ρ	[269]
	C-O-C	δ	[269]
725	H-phenyl	γ	[278]
	C-O-C	δ	[274, 278]
	C=O	γ	[275]
680	phenyl ring	δ (in-plane)	[269]
632	C-O-C	δ	[277]
523	phenyl ring	γ	[269]
505	C=O	γ	[269]
437	C-C=O	δ	[269]
377	C-O-C	δ	[269]
360	C=O	ρ	[269]
350	C=O	ρ	[269]

By comparing the spectra in Figure A1.1, it is possible to observe how the Hostaphan and Melinex foils do not show significant differences in the main IR features, apart from minor discrepancies in the shape of the unresolved triplet at 1245 cm^{-1}, which in the case of Hostaphan shows two of its components as partially resolved. All the peaks' maxima differ from each other for a couple of wavenumbers at most (differences not listed in Table A.1). Furthermore, despite the substantially different morphology, the two sides of the Melinex foil appear to possess the same chemical composition. Such spectra alone are however not enough to declare the two foils as chemically equivalent, as they do not provide informations on their respective crystallinity degrees, apart from some qualitative assumptions based on the aforementioned broadening of some spectral features. A quantification of the degree of crystallinity, usually expressed as percentage, would require differential scanning calorimetric (DSC) methods [279]. A qualitative analysis, with some limitations and *caveats*, is however possible through FTIR spectroscopy alone, and is based on the different abundance in amorphous and crystalline phase of some rotational isomers of the PET chain.

Figure A1.2 shows the two possible rotational isomers of the oxyethylene chain group: between the two, the trans one, because of steric hindrance, possesses nominally the lower energy [268]. The gauche conformer on the other hand allows the solid chains to be more closely packed [280] and is therefore the overall more favorable isomer, from an energetic point of view. Such

state of folded over, bent and coiled chains corresponds to the amorphous phase of PET [270]. The unfurled chains with trans isomers constitute instead the totality of the latter's crystal phase [268, 280, 281], but they can also exist in small domains in the amorphous phase, with a local overabundance in the first surface molecular layers [282, 283] and in the central sections of the polymer chains [281]. Even in completely amorphous films, the trans fraction has been calculated to be around 13 % [270]. It is therefore possible for two given PET foils to have the same X-ray or DSC determined degree of crystallinity, and yet different fractions of trans isomers, and vice versa [284].

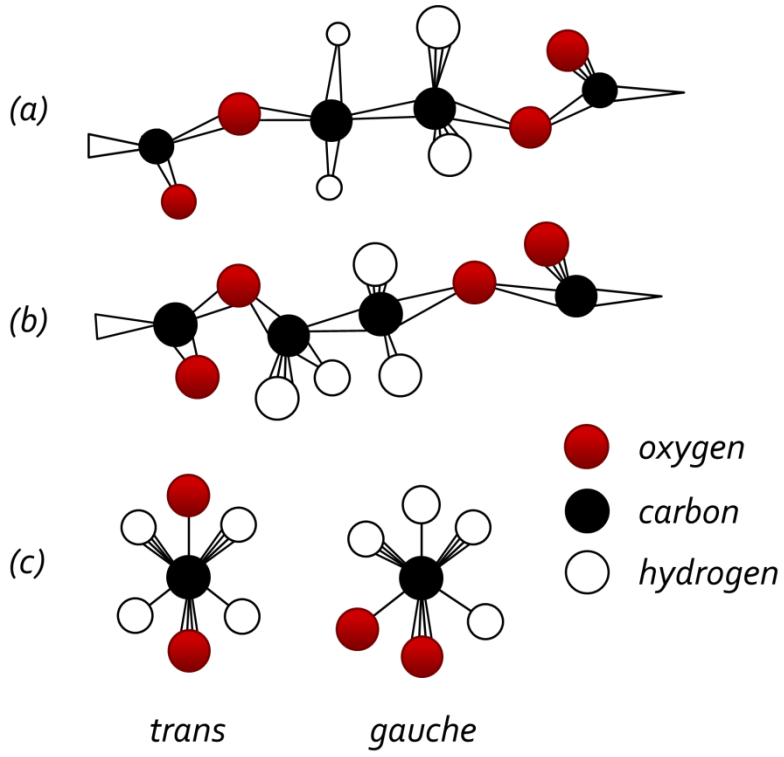

Figure A1.2: Rotational isomers of the glycolic group in PET: trans (a) and gauche (b) longitudinal view, and their respective front view (c). Based on [284].

The transition between the two forms, and therefore between amorphous and crystalline state – as polymer crystallization takes place via rotation of chain segments along their main axes, in order to form a crystalline cell [268] – can be achieved by heating the polymer, in particular above its glass transition temperature [285], in order to overcome the energy barrier ΔG between the two isomers: first the trans isomers in the amorphous phase dissolve, then their fraction starts to increase linearly at the expenses of the gauche one, by expanding the already existing crystalline domains [286, 287]. Depending on the temperature and the duration of the annealing, it is possible to reach high degrees of crystallinity even at relatively low temperatures: 1h at 130°

is already enough to ensure no residual preferential orientation [282], while 1d at 100° produces almost an equal fraction of trans and gauche isomers [280] (52 % and 48 %, respectively), after which higher temperatures must be ensured in order to obtain even higher trans fractions [281]. The crystal phase, on the other hand, never exceeds 60 %, even when the annealing is performed under tensile strain [287]. At the end of the annealing process, a quick quenching step causes the increased crystallinity degree to be 'frozen' in a non-equilibrium condition long enough to be detected by means of analytical methods. Long agings cause eventually a reversal to the original conditions [280].

As for the infrared spectra, two main kinds of changes take place together with crystallization and the concurrent gauche-to-trans rearrangement: one is caused by the newly formed (or expanded) crystalline field and the associated change in the molecular symmetry that can rule out some previously allowed vibrations: such is the case for example for the crystalline carbonyl group, that lies in the same plane of the phenyl ring, and thus creates a centrosymmetric structure, a part of whose vibrations is now no more IR active [276]. This results in an abatement of the intensity of some of the carbonyl-associated bands.

The second change is caused by the aforementioned variation in the molecular configuration: in this case, because of the different bonds angles of the two isomers and the general *milieu* surrounding them in the two phases, some of the roto-vibrational modes connected to the glycolic group shift enough to split in two different signals, corresponding univocally to one isomer or the other; a partial list is included in Table A.1. Such variation in the intensities of the coupled bands alone cannot however be converted in a quantitative analysis of the trans /gauche isomers fractions, for several reasons:

i) in PET some bands are both structure and orientation sensitive, some only orientation sensitive and some others finally depend on neither [284], i.e. the change in their intensity is at least partially caused by factors which are not easily reproduced. Trans isomers, moreover, contrary to the gauche ones, are strongly oriented and result therefore, under the same conditions, in more intense bands [288, 289];
ii) while ATR – the currently chosen IR investigation technique – has been already proved to be suited for the characterization of PET foils [290], it introduces two further sources of error: first, it is a technique extremely sensitive on bad sample-crystal contact or sample bending, which both lead to an artificial deformation of the recorded spectra. Secondly, too widely spaced bands originate from very different depth in the polymer (as an example, C=O rocking at 790 cm^{-1} and C=O stretching at 1580 cm^{-1} have a penetration depth of roughly 1.1 and 2 microns, respectively [290]), and their intensities can thus be affected by inhomogeneities in the chemistry of the film.

In light of all the previous informations, the total trans content in the investigated Melinex and Hostaphan film χ_{tot} is assumed to be thus defined:

$$\chi_{t,tot} = \chi_{t,cr} + \chi_{t,am}\,, \qquad (A1.1)$$

where $\chi_{t,cr}$ is the trans fraction in the crystalline domains and $\chi_{t,am}$ the one in the amorphous phase, their values unknown for both PET foils. During an annealing step, however, the trans content will eventually reach a steady-state value at which $\chi_{t,am}$ will have been completely dissolved in the amorphous phase, while $\chi_{t,cr}$ will have increased because of the formation of new crystalline domains and the growth of the already existing ones. The kinetic of crystal formation in amorphous phases can be safely assumed to be the same for both foils. As for the second process, it depends on the surface area of the pre-existing crystal domains, which can be roughly assumed to be directly proportional to their total volume, if their size and shape distributions are disregarded. For the current purposes, a similar numerical density in both foils is furthermore assumed. Therefore, the variation of the trans fraction after an annealing step can be rewritten as:

$$\Delta\chi_{t,tot} \sim \Delta\chi_{t,cr} \qquad (A1.2)$$

For two PET foils then a similar variation can prove that their initial crystallization degrees are in fact the same or at least lie in close proximity to each other, regardless of their initial and possibly different trans content.

Such qualitative analysis can be readily been carried out by means of ATR-FTIR spectroscopy and a suitable choice of the trans- and gauche-related bands. The trans/gauche bands chosen for the analysis are the pair related to the ethylene wagging at 1340 and 1370 cm^{-1}, respectively. Their intensities are inversely proportional to each other and the small spacing between them ensures that their penetration depth is almost the same, so that any variation in their integrated values A depends on the trans and gauche fractions alone, i.e.:

$$\frac{A_t}{A_g} \sim \frac{\chi_t}{\chi_g}\,, \qquad \frac{\Delta A_t}{\Delta A_g} \sim \frac{\Delta\chi_t}{\Delta\chi_g}\,. \qquad (A1.3)$$

A1.1 Annealing procedure

Two squares of approximately $10 \cdot 10$ cm^2 of Melinex and Hostaphan have been cut and fixed on aluminum plates with duct tape, in order to prevent unwanted curling of the foils during the heating. It is assumed that any eventual strain in the foil induced by the duct tape is negligible and has no effect on the orientation of the polymer chains or their reorientation as trans isomers [270]. The plates have been inserted separately in two polyethylene sachets, which have been then filled with deionized water and sealed, in order to prevent external contaminations. The sachets have been submerged in a bath of deionized water at 100° C for 30 hours before being removed

and opened: the plates have been pulled out and kept submerged in deionized water at room temperature for 15 minutes (quenching). The polymer foils have then been left to dry, still attached to the plates and in open air. Without further cleaning, two pair samples suitable for ATR FTIR analysis have been cut out of them. The infrared analysis took place immediately after the aforementioned steps, with the same operating parameters reported in Chapter 6.2.1. Integration of the peaks has been finally carried out by means of OPUS software (v. 6.5). During the integration procedure, the peak positions have been set by the operator and kept constant, while the FWHM and peak intensity of the fitting Gaussian curves have been kept as variables to be optimized.

A1.2 Results and discussion

Figure A1.3 shows the normalized absorbance spectra in the 3200-400 cm^{-1} range for the annealed samples (black lines) with the spectra of the native foils shown in Figure A1.1 (gray lines) as reference. Only the annealed smooth side of the Melinex foil has been investigated, as i) it provides a better and more homogeneous contact with the ATR crystal, and ii) with FTIR possessing a penetration depth far greater than the surface roughness on the antiblock particles side, and the spectra for both sides of the native Melinex being very similar to each other, it is safe to assume that the resulting spectra are more influenced by the polymer bulk than by the comparatively thin surface volume.

The overall spectra thus displayed do not show great differences after the annealing and quenching step, either in the position or intensity of the peaks, so some choice details have been reported in Figure A1.4: Figure A1.4 (a) shows the C=O stretching peak that, starting as a poorly resolved multiplet centered around 1715 cm^{-1}, shifts to higher wavenumbers after the annealing, at the same time changing shape; the same happens for the C-O-C stretching bands around 1260 (not shown) and 1100 cm^{-1}, for both Melinex (Figure A1.4b) and Hostaphan (Figure A1.4c). In the case of the latter two, the peaks are constituted by a triplet in the amorphous state and a doublet in the crystalline one: in a semi-crystalline state, as the one that can be assumed to result after the performed annealing, therefore, the overall band should consist of at least five components of varying intensity [276]. The same can be assumed true for the aforementioned C=O peak. Figure A1.4d shows the band around 725 cm^{-1}, whose attribution is still disputed (see also Table A.1). Miyake *et al.* [276], however, consider it to result from the wagging of the C=O bond and, moreover, to consist of a pair of unresolved signals, corresponding to the amorphous and crystalline phase [291], whose intensities are inversely proportional to each other: this seems to be confirmed in the current case, as after the annealing the component at lower wavenumbers increases at the expense of the other.

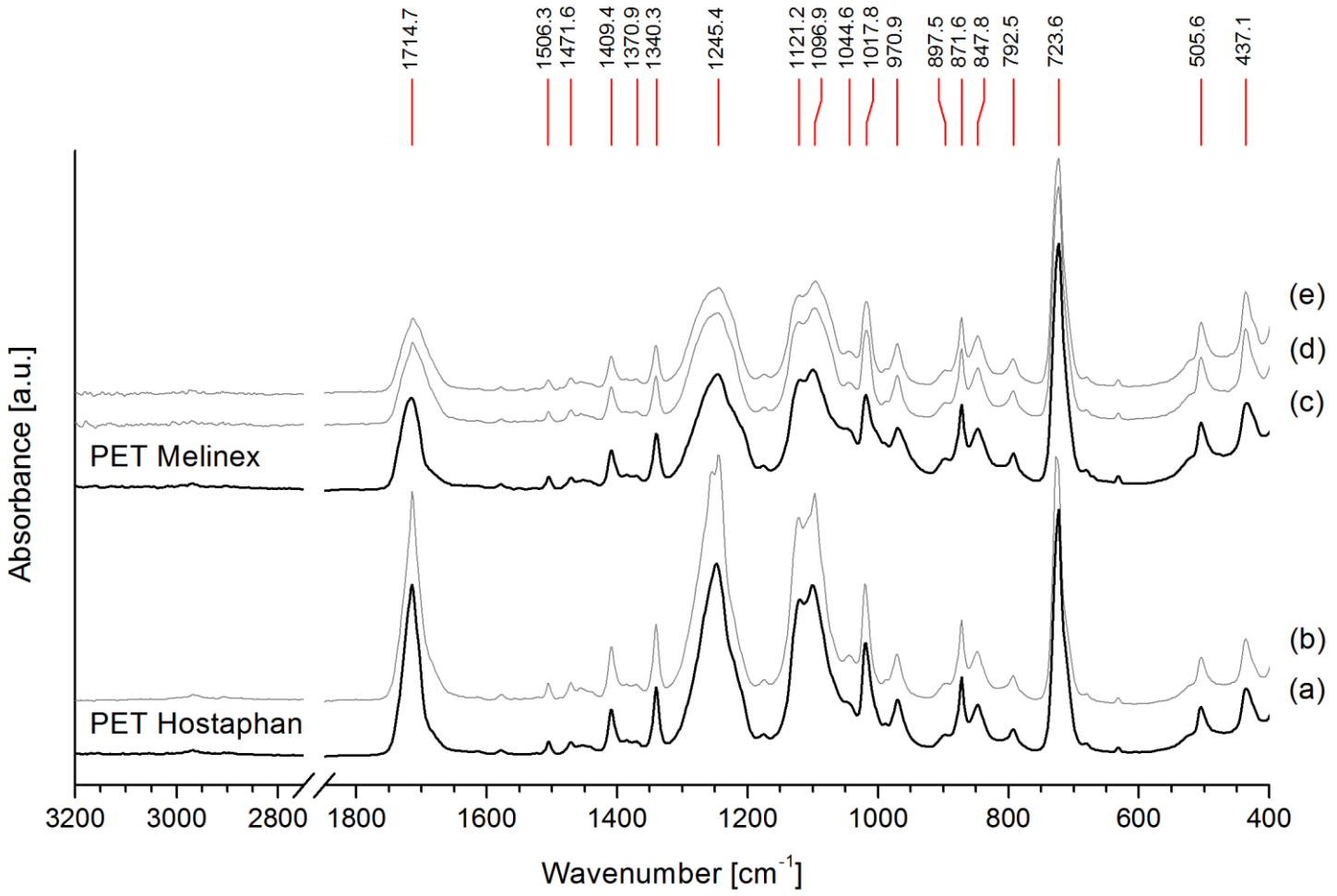

Figure A1.3: Absorbance spectra in the 3200-400 cm-1 range for annealed (a) and native (b) Hostaphan, and for annealed (c), native smooth (d) and native rough (e) Melinex foils. Spectra normalized to their respective most intense peak.

More generally, the observed increase of the FWHM of the bands (particularly evident in the whole displayed range of Figure A.4b) bespeaks of an increased dispersion in bond angles and surrounding environments (both known causes for peaks broadening), i.e. the presence of crystalline domains, or even a non-crystalline but constrained phase [292] in an amorphous matrix, which can only arise from a successful annealing recrystallization and a quick enough quenching. Thus, a direct confirmation of the validity of the chosen procedure has been given.

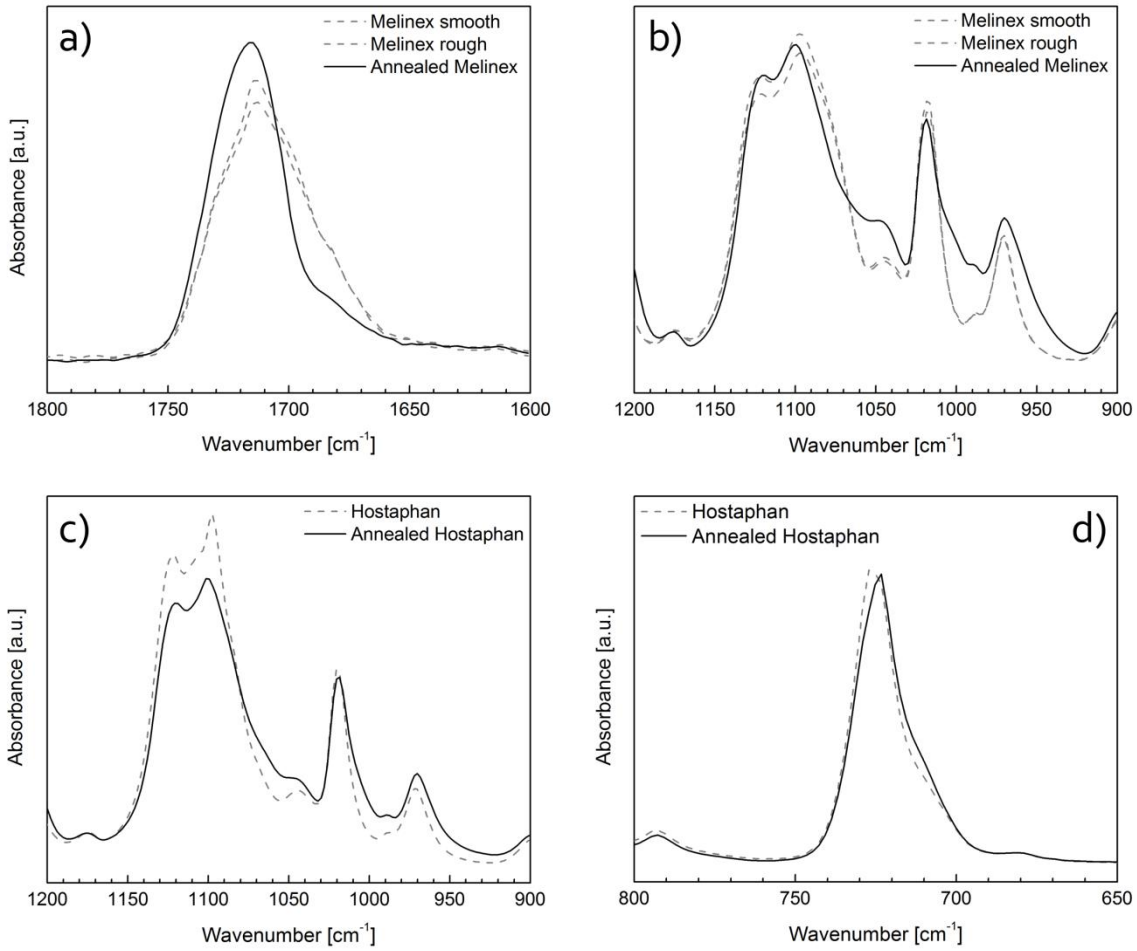

Figure A1.4: Highlights from the absorbance spectra of Figure A1.3, with variations of after-annealing peaks for Melinex (a, b) and Hostaphan (c, d) foils.

Figure A1.5 finally shows the ethylene wagging peaks chosen as indicators of the trans and gauche abundance for both investigated foils: as mentioned before, the gauche isomer, existing only in the amorphous phase, presents a considerably broader peak than the trans one. The shaded areas represent examples of the peak integrals calculated with OPUS software, whose numerical values, displayed as trans-to-gauche ratios, are reported in Figure A1.6.

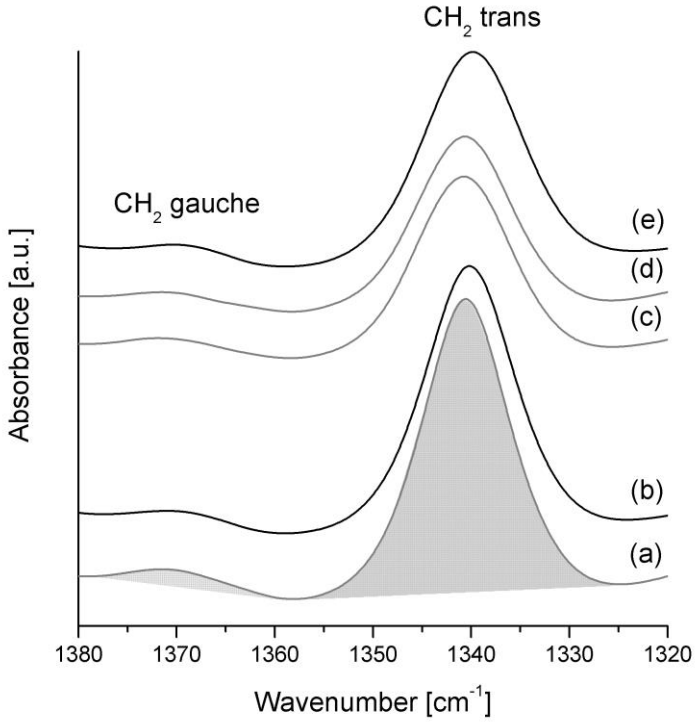

Figure A1.5: Ethylene gauche and trans bands (shaded) for: (a) native and (b) annealed Hostaphan, (C) native smooth side, (d) native rough side and (e) annealed Melinex.

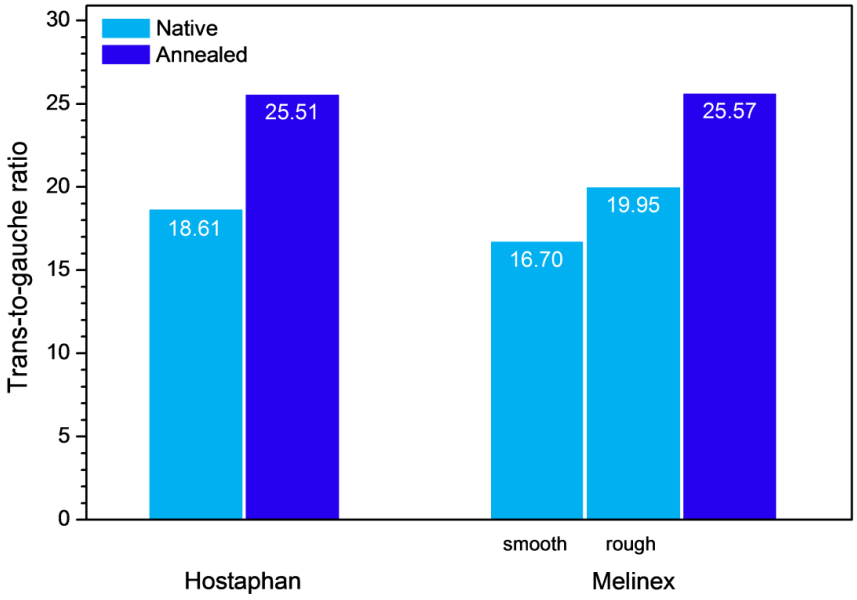

Figure A1.6: Trans-to-gauche ratios for native and annealed PET foils, based on fitting of the spectra reported in Figure A1.5.

It is possible to observe that, contrary to what appeared in Figure A1.3, the two sides of the Melinex foil do present small but significant differences in their composition. Assuming that the trans abundance in the amorphous phase is the same or at least comparable on both sides, its higher content in the rough side must be caused by the antiblock particles alone. Based on what detailed in Chapter 5.2, it is safe to assume that such particles must be highly crystalline and containing only trans isomers, therefore increasing their abundance with respect to the gauche ones. It is also to be noted that the average value of trans-to-gauche ratio for the Melinex foil, equal to 18.32, lies in close proximity to the Hostaphan's native counterpart. Regardless of the unknown distribution of trans isomers between amorphous and crystal PET, it is also possible to notice that the final trans-to-gauche ratios too are almost identical. As already mentioned, during the annealing the trans isomers in the amorphous domain first turn to gauche, and only then can the proper crystallization process take place. Close trends and final post-annealing values for both foils seem to suggest that their initial crystallization degrees should also be similar to each other (barring the slight contribution of the crystalline antiblock particles).

In order to verify the validity of these results, an alternative method has been employed, after Walls [290]: in this case, instead of a mere A_t/A_g value, a display of the single areas normalized over the integrated area of a reference peak is advocated. Such peak must not be dependent on orientation, structure or conformation of the polymer chains, and should moreover lie in the same wavenumbers range of the investigated band, for the corresponding evanescent wave to have the same penetration depth. The in-plane vibration of the phenyl ring at 1410 cm^{-1} is a very suitable choice. The normalized areas for gauche and trans isomers for all the investigated samples are reported in Figure A1.7.

Again it is possible to observe the more gauche-poor side of the Melinex foil, thanks to the crystalline antiblock particles. The general trends shown in Figure A1.6 are further confirmed, including almost identical values for the annealed foils. In light of these results, in particular the final values after the annealing step, it is possible to affirm with good confidence that the two foils not only possess comparable trans and gauche isomers' percentages, but their unknown crystallization degree is almost roughly the same. The growth of plasma-polymerized thin layer on top of the PET substrates is usually strongly dependent on the crystallinity of the latter's surface [24, 27, 57, 290], as in the crystalline domains the delocalized electrons of the phenyl rings and oxygen lone pairs lie aligned with the surface and, once activated upon plasma exposure, provide excellent anchoring points for the first radicals reaching the surface. In this case however the growth mechanism should not be influenced by the chemical differences between the two investigated foils, but only by their morphology, the increased roughness arising from antiblock particles in particular, as detailed in Chapter 7.4.2.

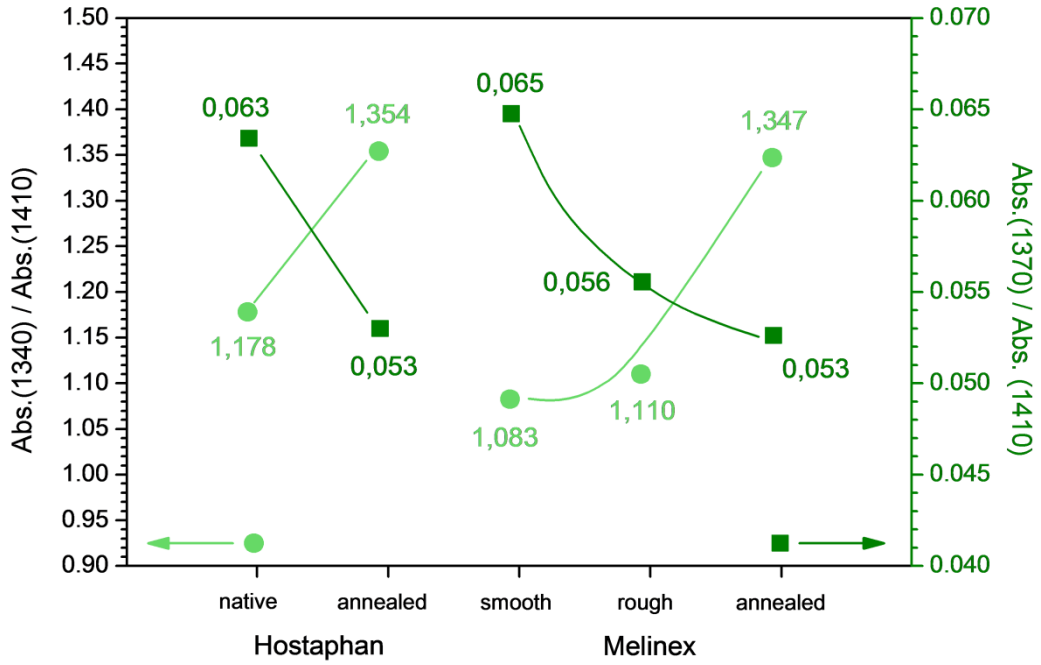

Figure A1.7: Areas of the trans (left y-axis) and gauche (right y-axis) ethylene wagging peaks normalized with respect to a phenyl stretching band at 1410 cm^{-1}.

Appendix A2

Organic intermediate layers

In the current appendix, the intermediate films for a multilayer encapsulation approach have been investigated, in order to obtain an organic buffer layer with a chemistry different enough from the barrier layers to ensure a decoupling effect for their defects, and an improvement of the overall performances against oxygen. The deposition rates, chemical composition via infrared absorption spectroscopy and oxygen transmission rates of films deposited by means of HMDSN and H_2 in different ratios will be shown.

HMDSN has been chosen as precursor for such organic films, thanks to its high starting organic content and in order to perform a full encapsulation with only one monomer, including gradient layer depositions, by only switching oxygen and hydrogen in the same deposition step. The different hydrogen-to-monomer ratio in the gas feed have been obtained by keeping the H_2 flow fixed at 100 sccm and by varying accordingly the HMDSN flux from 100 to 1.4 sccm.

A first series of PECVD processes with different durations has been performed for all the investigated gas feed ratios, in order to determine an average deposition rate and obtain 100 nm thick films. The results of these first depositions, displayed as film thickness normalized for the varying HMDSN flux versus the deposition time are displayed in figure A2.1: the trends for all hydrogen-to-monomer ratio are linear but, in contrast with the results obtained for HMDSN/O_2 feeds (see also Figure 7.2), here higher hydrogen contents in the gaseous feed result in increased thicknesses for a given deposition time. Hydrogen in plasma shows a mildly reducing effect and, thanks to its lower reactivity compared to oxygen, does not form stable volatile products by reacting with the monomer fragments; as a consequence, the amount of material deposited is increased, resulting in thicker films. It is also possible to assume that such films will show a high retention degree of the monomer original structure, whose bulky trimethyl groups will increase the film thickness and porosity. The thus calculated normalized deposition rates as a function of the hydrogen-to-monomer ratio are displayed in Figure A2.2: the values refer only to the 100 ± 5 nm thick films employed for the infrared analysis and/or the oxygen transmission rate measurements. The deposition rate increases sharply between 10/1 and 20/1 ratios, then it steadies and

seems to reach a constant value for the highest hydrogen-to-monomer ratios, as the fragments responsible for the film formation become 'saturated' with hydrogen atoms.

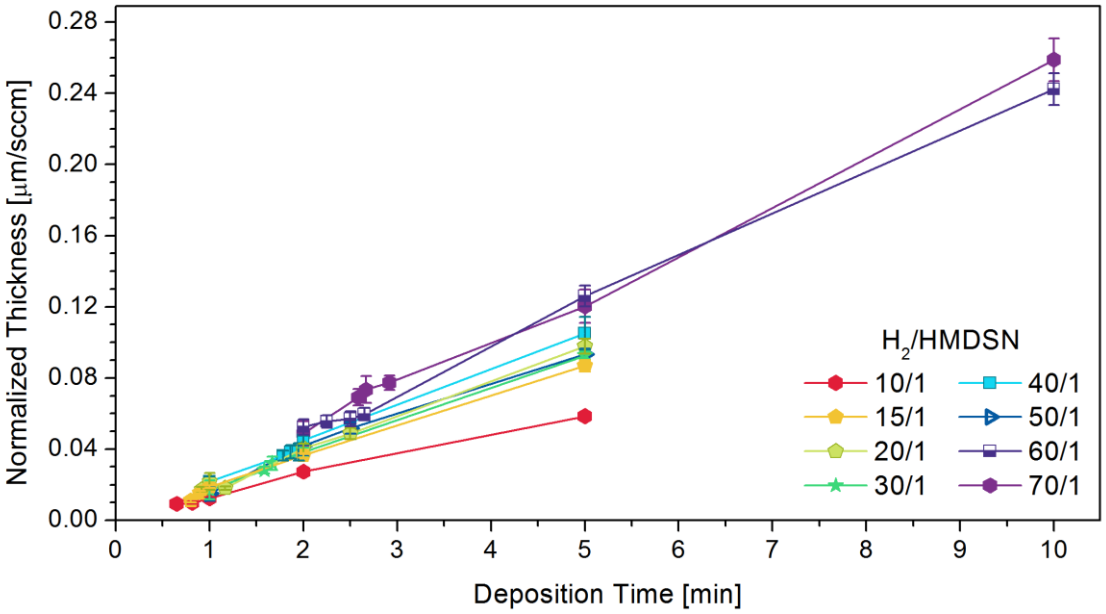

Figure A2.1: Measured thickness as a function of the deposition time for hydrogen-to-monomer ratios ranging from 10/1 to 70/1. The former is normalized for the employed HMDSN flux.

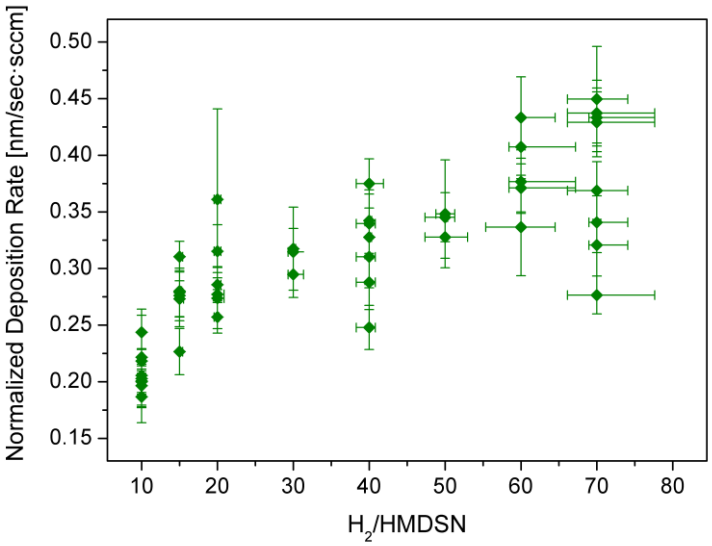

Figure A2.2: Normalized deposition rates as a function of the hydrogen-to-monomer ratio, for films with a thickness of 100 ± 5 nm.

The 100 nm films have been investigated by means of ATR FTIR absorption spectroscopy in the 4000-400 cm^{-1} range: the relative spectra, after a normalization and a baseline correction step, are reported in Figure A2.3 together with the spectrum of gaseous HMDSN as reference. A full list of the discernible peaks is reported in Table A2.1.

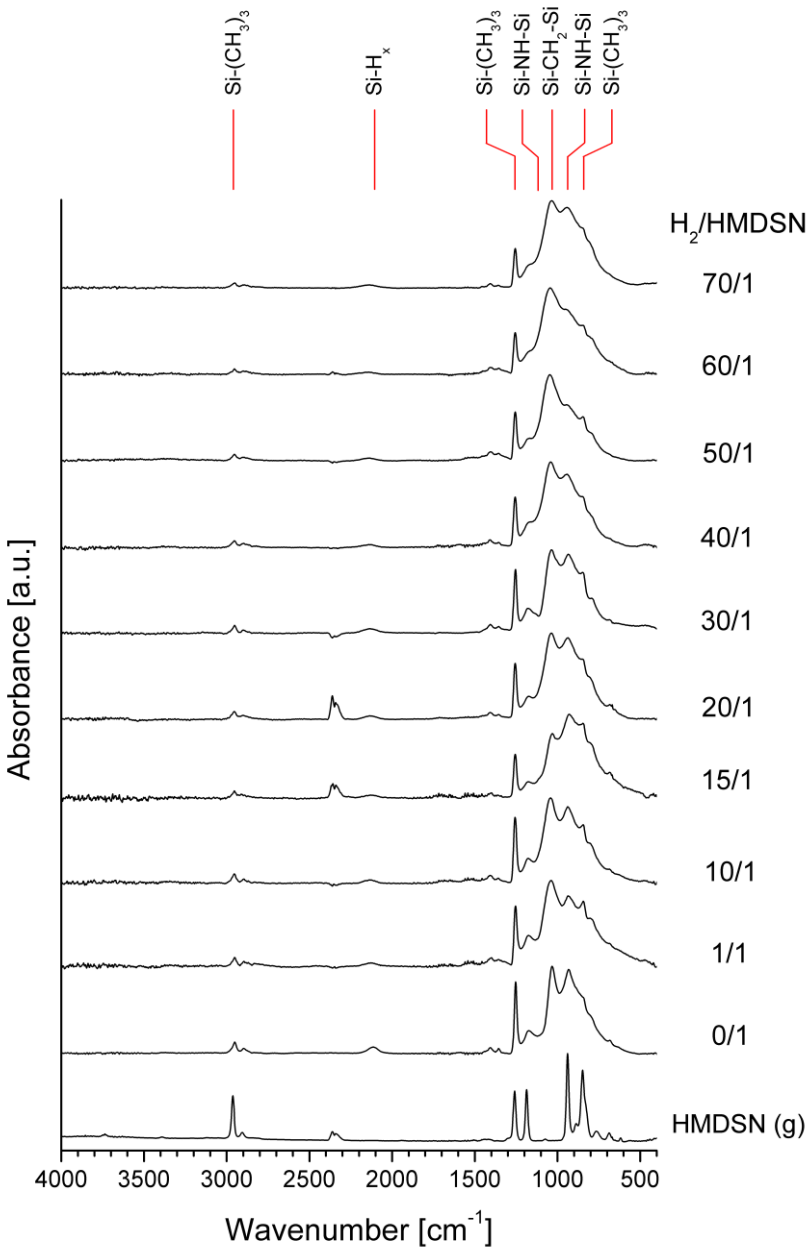

Figure A2.3: ATR infrared spectra in the 4000-400 cm^{-1} range for different hydrogen-to-monomer ratios and spectrum of gaseous HMDSN as reference, with labels for some of the most prominent signals. All spectra have been normalized for their most intense peak and their baseline has been corrected.

Table A2.1: Peak positions and vibrational mode assignments for the main absorption bands in the infrared spectra displayed in Figure A2.1.

Wavenumber cm^{-1}	Assigned group	Vibrational mode	Reference
3480	NH	ν	[202]
3380	NH_2	ν	[202]
2960	CH_x	ν_a	[151]
2900	CH_x	ν_s	[151]
2180	SiH	ν	[202]
	Si-C≡N	ν	[202]
1410	CH_x	δ_a	[151]
1260	$(CH_3)_x$	δ_s	[201, 202]
1160	Si-NH-Si	δ	[202]
	Si-N-C	ν	[202]
1090-1020	Si-CH_2-Si	δ, γ	[125, 202]
990	Si-CH_3	ρ	[125]
925-850	SiN	ν_a	[202]
860	SiH	ν	[125, 201]
840	CH_3	ρ	[151, 201]
800	SiC in $Si(CH_3)_x$	ν	[202]

All hydrogen-to-monomer ratios produce films with strong retention of the original monomer bonds, as it is possible to observe with the methyl bands at 2960, 2900, 1260 and around 850 cm^{-1}, and the precursor backbone Si-NH-Si at 1180 cm^{-1}. The spectra present furthermore new signals, like the SiH_x band, with $x \in \{1,2,3\}$ appearing already for the pure HMDSN film around 2117 cm^{-1} and then shifting continuously towards higher wavenumbers, and the wide main peak arising from the Si-CH_2-Si bonds. The films could theoretically contain residual traces of oxygen, either coming from residuals in the reactor or being incorporated in the films upon their exposure to air thanks to their residual reactivity, but no oxygen-related peak is clearly discernible. The films, all showing similar chemical compositions, consist therefore of organosilicon polymeric chains with Si atoms bond to either the original nitrogens or the dimethyl groups originated in plasma phase following the fragmentation of the precursor molecules. The overall chemical composition shows a stark contrast with the virtually inorganic silica-like films employed as barrier layers. The presence of different species acting as ending groups for such chains, such as the trimethyl and the trisilyl groups, show a poor cross-linking and an overall porous internal structure. The former's peak relative intensity to the main spectrum band and its position are reported

in Figure A2.4. With increasing hydrogen content in the plasma feed the methyl band intensity decreases linearly but never below 50 % of its original value. Such limited reduction can be explained by a minor increase in the cross-linking degree of the deposited films, as the dangling methyl groups become part of the main polymer chains. The methyl band position on the other hand remains fairly unaffected by the hydrogen-to-monomer ratio: with the trymethyl peak at 1250 cm^{-1} and the dimethyl peak at 1260 cm^{-1} [151], and the band position at 1255 cm^{-1}, most of the retained methyl groups are either end-chain groups or lateral substituents of a silicon atom in a polymer chain that prevent branching, at the same time leaving free space in the film thanks to their steric hindrance.

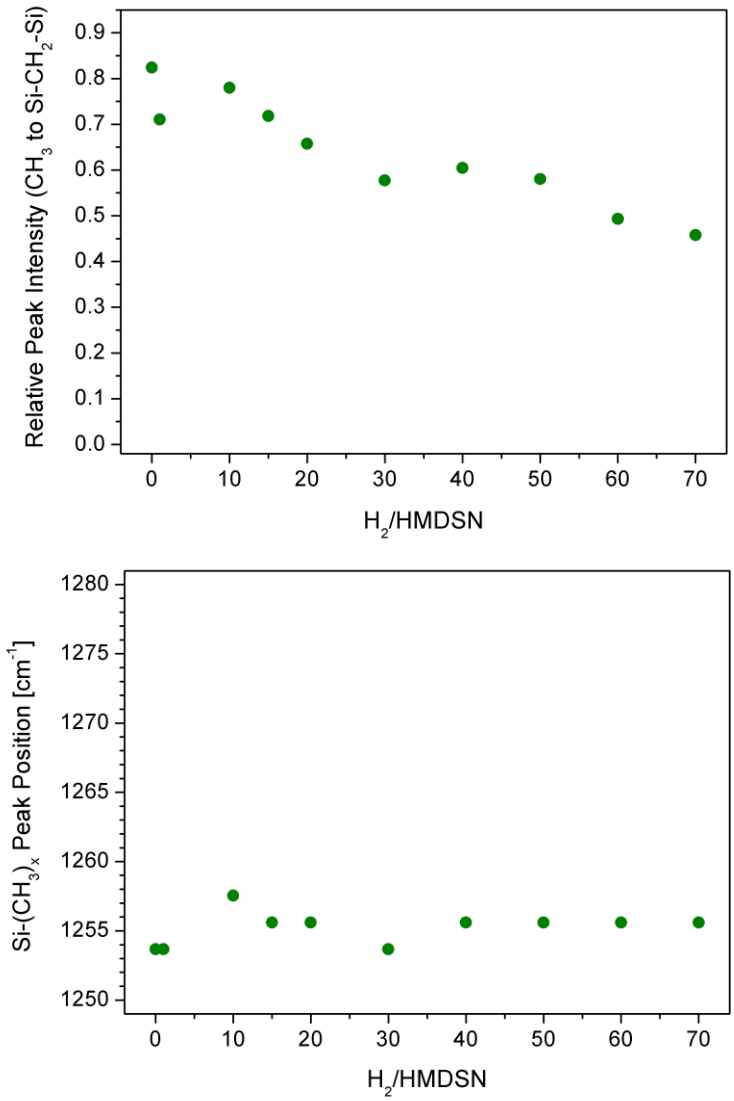

Figure A2.4: Relative intensity of the methyl peak at 1260 cm-1 compared to the main band in the 1450-1350 cm-1 range (left) and main position of the methyl band (right) as a function of the hydrogen-to-monomer feed ratio.

In order to get a better inside, the methyl band has been fitted in its three sub-peaks by means of OPUS software for the highest (70), lowest (10) and an intermediate (40) gas feed ratio. The results are displayed in Figure A2.5. The other bands originally present, as the low band around 1350 cm^{-1}, caused by residuals of water vapor in the spectrometer's chamber, and the onset of the main band starting at 1220 cm^{-1}, have been subtracted for better visual clarity. During the fitting procedure, three Gaussian peaks have been left free to vary in FWHM and intensity, with their peak positions kept fixed at the values reported in Table A2.2.

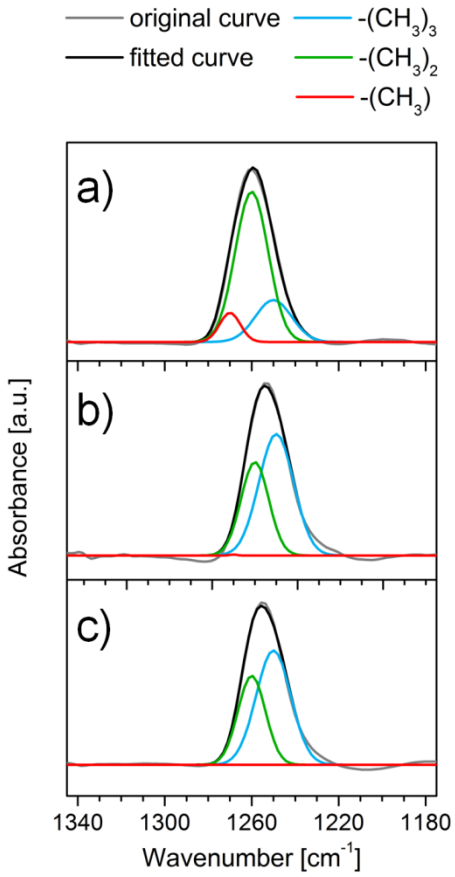

Figure A2.5: Fitted methyl bands for a hydrogen-to-monomer ratio equal to 70/1 (a), 40/1 (b) and 10/1 (c). The three components attributions and peak positions are listed in Table A2.2.

No variation in the composition of the band is observed for the two lower ratios, which form films with a methyl fraction almost equally split between trimethyl and dimethyl groups. The 70/1 ratio exhibits a reduction in the trymethyl fraction and a simultaneous appearance of a small peak for the monomethyl group, so that the overall band position remains almost unchanged. The 70/1 ratio therefore shows again a slightly increased cross-linking degree. As for the silyl substituents, the main position of the relative band around 2110 cm^{-1} for the pure HMDSN film is re-

ported in Figure A2.6; the positions of its subcomponents are listed in Table A2.2. The band shifts 20 cm^{-1} towards higher wavenumbers, in the range where the $–SiH_2$ sub-peak lies, when hydrogen is added to the gaseous feed and the excess of H^+ in the plasma phase is at least partially incorporated in the final film. The broadness of the band suggests the presence of a SiH_3 sub-peak, with the trisilyl group that, albeit much smaller than the trimethyl, still reduces the average length of the polymeric chains in the film, while the disilyl, similarly to the dimethyl substituents, prevents their branching and cross-linking.

Table A2.2: Peak positions and band intervals for the sub-components of the methyl band at 1260 cm^{-1} (left) and the silyl band around 2120 cm^{-1} (right).

Assigned group	Wavenumber	Assigned group	Wavenumber
	cm^{-1}		cm^{-1}
$–(CH_3)_3$	1250	$–SIH_3$	2163-2142
$–(CH_3)_2$	1260	$–SIH_2$	2138-2117
$–(CH_3)$	1270	–SIH	2113-2092

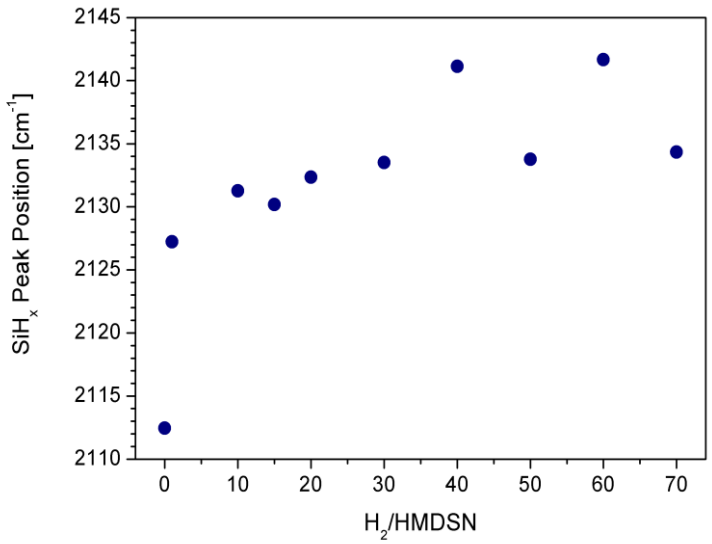

Figure A2.6: Silyl band position as a function of the hydrogen-to-monomer ratio.

The expected poor performances of the films when acting as barrier against oxygen are confirmed by their OTR values, reported in Figure A2.7: all measured values, largely independent on the hydrogen-to-monomer ratio, result in at best a barrier improvement factor of 1.2: such value

may itself be an overestimation, as uncoated PET foils show fluctuation in their intrinsic OTR (see also Chapter 5.2). Such films are however transparent and colorless, despite their nitrogen content. A 10/1 sample with a thickness of around 100 nm is shown in Figure A2.8 together with a SiO_x-like barrier and a sample of similar thickness produced with a gaseous feed of HMDSN and nitrogen. In the latter case, the incorporation of nitrogen causes the film to turn distinctly yellow (color more visible at the edges of the glass substrate, highlighted by the brackets). Such kind of films was the first choice for the intermediate layer, and has been thoroughly investigated (data not shown) in a similar fashion to the hydrogen-based films, but the yellow hue visible for most nitrogen-to-monomer ratios caused it to be eventually discarded.

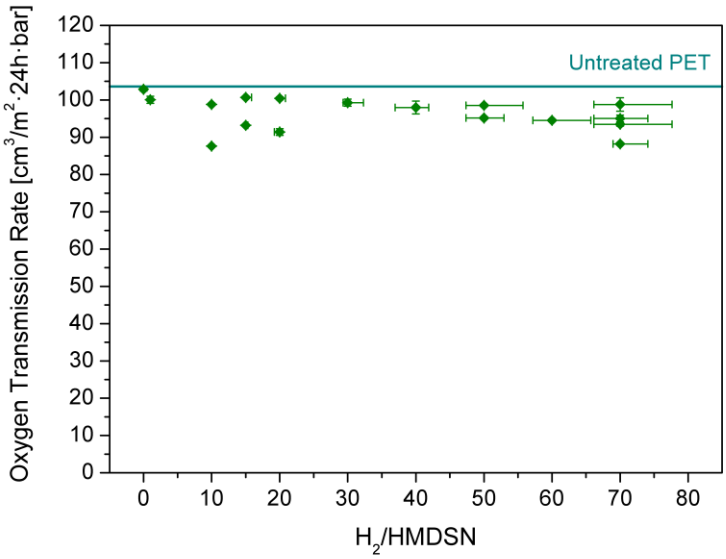

Figure A2.7: Oxygen transmission rates as a function of the hydrogen-to-monomer ratio, for 100 ± 5 nm thick films. The horizontal error bars derive from the fluctuations of the precursor flux and the sensitivity limits of the mass flow controllers.

Because of the predominant organic nature of such SiC_xH_y films, after their deposition in a multilayer encapsulation process, the following step, i.e. the deposition of a barrier layer by means of an oxygen-based plasma, may damage them to an extent: the methyl and silyl groups are particularly prone to react with oxygen [104]. More generally, the hydrogen, carbon and nitrogen atoms in the films can all react with oxygen and form volatile products, resulting in a thinning of the layer. Silicon atoms form oxidized products but remain in the films. If the etching is too severe, the organic layer may be fully consumed and provide no decoupling effect between two barrier layers. As such, a small study over the minimum thickness required for the organic layers has been performed, on films with a hydrogen-to-monomer ratio equal to 10, 40 and 70. The optimization of the buffer layers' thickness causes also a reduction in the multilayer overall thickness, which ensures better flexibility and resilience against cracking [292].

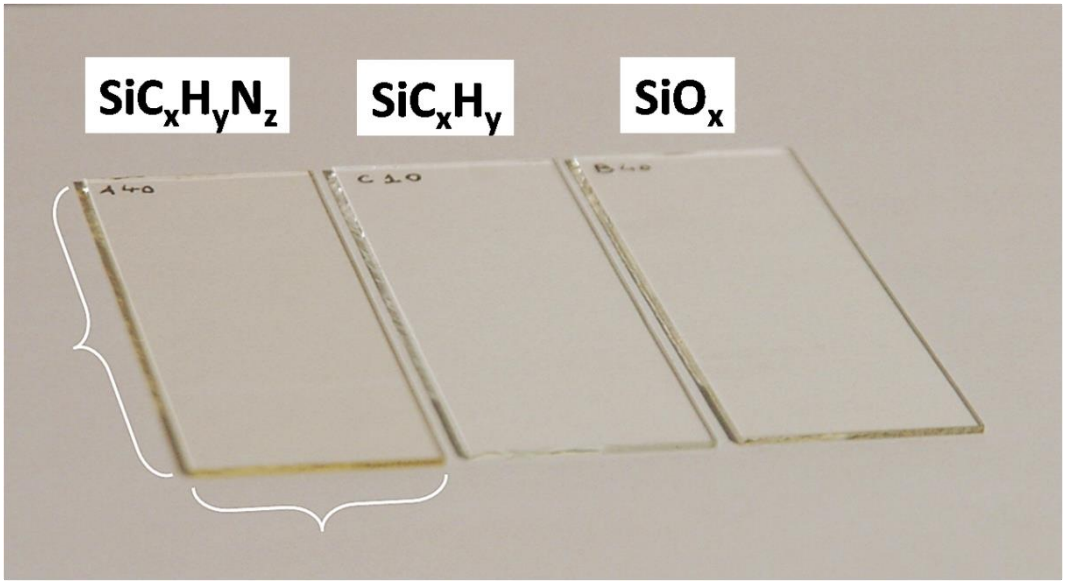

Figure A2.8: 100 nm films deposited with HMDSN as precursor and nitrogen (left), hydrogen (center) and oxygen (right). The brackets highlight the edges of the glass substrate, where the yellow hue of the silicon-nitride-like film is more apparent.

A 100 nm film for each of the gas feed ratios has first been deposited on glass substrates. The same samples have been then exposed to a pure oxygen plasma (with 100 sccm O_2) for 5, 10, 15, 30, 60 and 90 seconds: after each step, their thickness has been measured. The determination of the etching rate by means of such procedure will be overestimated, as in 'real' cases part of the oxygen in the plasma phase will react with HMDSN to form the barrier layer. Moreover, such barrier will start to immediately cover progressively larger areas of the underlying organic layer, dampening its etching. As 30 nm of barrier layers are deposited after 90 seconds of treatment, and as shown in section 7.3.3 the films at this point are completely sealed, it has been assumed that after one minute and a half the organic layer would be completely protected from the plasma. The results for the three investigate hydrogen-to-monomer ratios are reported in Figure A2.9: the 10/1 organic film is severely affected by exposure to oxygen, as its thickness is quickly reduced to a residual value already after 30 seconds of treatment. The 40/1 film shows a higher resistance against it while the 70/1 is barely affected, thanks to its higher cross-linking degree and, probably, because of smaller free spaces in its bulk that hinder to a small extent the oxygen permeation through its bulk. For all data, longer etching times cause an increase of the surface roughness and therefore a bigger error on the measured thickness. Each series of data has been fitted by means of an exponential equation:

$$y(t) = A \cdot e^{-t/\tau} + y_0 \,, \qquad (A2.1)$$

where *y* is the film thickness, dependent on the etching time *t*, *A* is a coefficient depending on the chemical and structural composition of the etched film (i.e. a measure of how prone the film is to

be etched), τ is the time required for the original thickness to decrease to 0.37 of its original value, provided that A = 1, and y_o is the residual, 'unetchable' thickness. For very long etching times it can in fact be assumed that:

$$y(t = \infty) = A \cdot e^{-\infty/\tau} + y_0 \simeq y_0 \; ; \qquad (A2.2)$$

the residual thicknesses calculated by means of the fitting for the three ratios are listed in Table A2.3, together with the thickness variation percent induced by the full etching process.

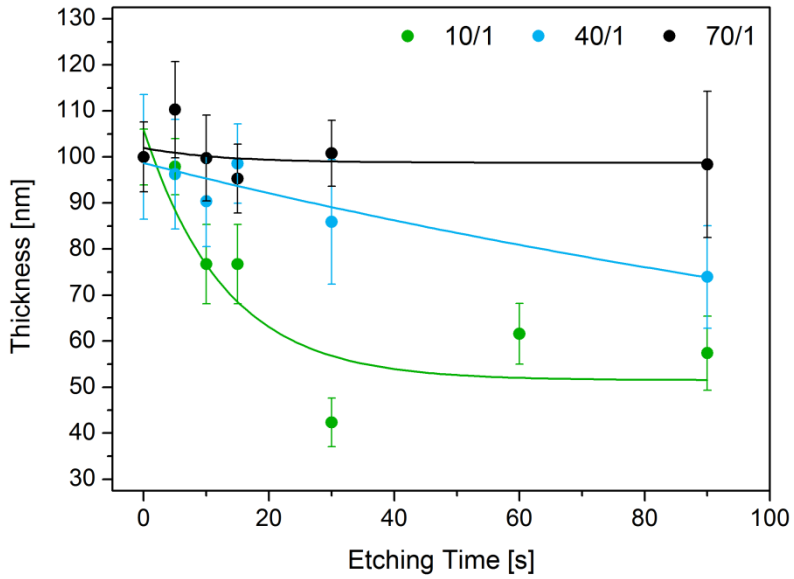

Figure A2.9: Residual thickness of organic layers with a hydrogen-to-monomer ratio of 10, 40 and 70 after being exposed to a 100 sccm pure oxygen plasma for different etching times.

Table A2.3: Calculated residual thicknesses as absolute and relative values for the three etched films.

H_2/HMDSN	y_0	Δy
10/1	52 nm	48%
40/1	61 nm	39%
70/1	98 nm	2%

The 10/1 film is too soft to be a reliable buffer layer, unless its deposited thickness is considerably increased. This is however highly undesirable. 40/1 films on the other hand would require a starting thickness of around 50 nm in order to have a final value of at least 30 nm, which can be

assumed to correspond to a continuous film, similarly to what observed for the silica-like layers, and still provide a full separation between barriers. For a 70/1 ratio the initial value is further reduced to 31 nm. Both higher hydrogen-to-monomer ratios have been therefore employed, at different stages, as buffer layers in the encapsulations of OLEDs prototypes reported and discussed in Chapter 8.

Bibliography

[1] A. R. Duggal *et al.*: *Organic light-emitting devices for illumination quality white light*, Appl. Phys. Lett. 80, 3470 (2002)

[2] A. R. Duggal *et al.*: *Fault-tolerant, scalable organic light-emitting device architecture,* Appl. Phys. Lett. 82, 2580 (2003)

[3] M. S. Weaver *et al.*: *Organic light-emitting devices with extended operating lifetimes on plastic substrates*, Appl. Phys. Lett. 81, 2929 (2002)

[4] A. B. Chwang *et al.*: *Thin film encapsulated flexible organic electroluminescent displays*, Appl. Phys. Lett. 83, 413 (2003)

[5] J. S. Lewis and M. S. Weaver: *Thin-Film Permeation-Barrier Technology for Flexible Organic Light-Emitting Devices*, IEEE Journal of selected topics in quantum electronics 10, 1 (2004)

[6] J. W. Jones US Patent 3, 442, 686 (1969)

[7] H. Chatam, *Oxygen diffusion barrier properties of transparent oxide coatings on polymeric substrates*, Surface and Coatings Technology 78, 1 (1996)

[8] European Parliament and Council Directive 94/62/EC of Dec. 20, 1994, O*n Packaging and Packaging Waste*, Official J. L 365, 365/10 (1994) 0010

[9] C. Charton *et al.*: *Development of high barrier films on flexible polymer substrates*, Thin Solid Films 502, 99 (2006)

[10] R. Ragni *et al.*: *Organic and Organometallic Fluorinated Materials for Electronics and Optoelectronics: A Survey on Recent Research*, Eur. J. Org. Chem. 27, 3500 (2018)

[11] C. W. Tang and S. A. VanSlyke: *Organic electroluminescent diodes*, Appl. Phys. Lett. 51, 913 (1987)

[12] C. W. Tang *et al.*: *Electroluminescence of doped organic thin films,* J. Appl. Phys. 65, 3610 (1989)

[13] G. M. Farinola and R. Ragni*: Electroluminescent materials for white organic light emitting diodes*, Chem. Soc. Rev. 40, 3467 (2011)

[14] https://www.sony.co.uk/electronics/oled-tv-display, Retrieved on 05/05/2018

[15] https://www.samsung.com/global/galaxy/what-is/super-amoled/, Retrieved on 05/05/ 2018

[16] https://www.energy.gov/eere/ssl/iesna-lm-80-08-overview-test-procedure-and-how-it-used-

energy-star, Retrieved on 10/06/2018

[17] Illuminating Engineering Society, *Projecting Long Term Lumen Maintenance of LED Light Sources*, Illuminating Engineering Society (2011)

[18] J. S. Park, *Thin film encapsulation for flexible AM-OLED: a review*, Semicond. Sci. Technol. 26, 034001 (2011)

[19] P. E. Burrows *et al.*: *Reliability and degradation of organic light emitting devices*, Appl. Phys. Lett. 65, 2922 (1994)

[20] G. Gustafsson *et al.*: *Flexible light-emitting diodes made from soluble conducting polymers*, Nature 357, 477 (1992)

[21] A. Sugimoto *et al.*: *Flexible OLED Displays Using Plastic Substrates*, IEEE Journal of selected topics in quantum electronics 10, 107 (2004)

[22] A. N. Krasnov, *High-contrast organic light-emitting diodes on flexible substrates*, Appl. Phys. Lett. 80, 3853 (2002)

[23] D. Affinito, US Patent 6268695 (2001)

[24] Y. Leterrier, *Durability of nanosized oxygen-barrier coatings on polymers*, Progress in Materials Science 48, 1 (2003)

[25] A. G. Erlat *et al.*, *SiO_x gas barrier coatings on polymer substrates: morphology and gas transport considerations*, J. Phys. Chem. B 103, 6047 (1999)

[26] G. Czeremuszkin *et al.*: *Ultrathin Silicon-Compound Barrier Coatings for Polymeric Packaging Materials: An Industrial Perspective*, Plasmas and Polymers 6, 107 (2001)

[27] J. T. Felts and A. D. Grubb, *Commercial scale application of plasma processing for polymeric substrates: From laboratory to production*, Journal of Vacuum Science & Technology A 10, 1675 (1992)

[28] T. Tanaka *et al.*: *Diamond-like carbon deposition on plastic films by plasma source ion implantation*, J. Vac. Sci. Technol. A 20, 625 (2002)

[29] S. Kho *et al.*: *Passivation of organic light-emitting diodes by the plasma polymerized paraxylene thin film*, Japan. J. Appl. Phys. 41, L1336 (2002)

[30] Y. G. Tropsha and N. G. Harvey: *Activated rate theory treatment of oxygen and water transport through silicon oxide/poly(ethylene terephthalate) composite barrier structures*, J. Phys. Chem. B 101, 2259 (1997)

[31] M. Yanaka *et al.*: *How cracks in SiO_x-coated polyester films affect gas permeation*, Thin Solid Films 397, 176 (2001)

[32] A. S. da Silva Sobrinho *et al.*: *Defect-permeation correlation for ultrathin transparent barrier coatings on polymers*, Journal of Vacuum Science & Technology A 18, 149 (2000)

[33] A. S. da Silva Sobrinho *et al.: A study of defects in ultra-thin transparent coatings on polymers*, Surface and Coatings Technology 116, 1204 (1999)

[34] M. Deilmann *et al.: Permeation mechanisms of pulsed microwave plasma deposited silicon oxide films for food packaging applications*, J. Phys. D: Appl. Phys. 41, 135207 (2008)

[35] A. G. Erlat *et al.: Morphology and gas barrier properties of thin SiO_x coatings on polycarbonate: Correlations with plasma-enhanced chemical vapor deposition conditions*, J. Mater. Res. 15, 704 (2000)

[36] A. S. da Silva Sobrinho *et al.: Plasma-deposited silicon oxide and silicon nitride films on poly(ethyleneterephthalate): A multitechnique study of the interphase regions*, Journal of Vacuum Science & Technology A 16, 2021 (1998)

[37] J. Crank: *The Mathematics of Diffusion*, Clarendon Press, Oxford, 2nd edn. (1975)

[38] B. M. Henry *et al.: Characterization of transparent aluminium oxide and indium tin oxide layers on polymer substrates*, Thin Solid Films 382, 194 (2001)

[39] G. L. Graff *et al.: Mechanisms of vapor permeation through multilayer barrier films: Lag time versus equilibrium permeation*, J. of Appl. Phys. 96, 1840 (2004)

[40] J. Brill *et al.: A flexible ferroelectric liquid-crystal display with improved mechanical stability for smart-card applications*, J. Soc. Inform. Display 10, 189 (2002)

[41] J. D. Affinito *et al.: A new method for fabricating transparent barrier layers,* Thin Solid Films 290, 63 (1996)

[42] J. Greener *et al.*: *Moisture permeability through multilayered barrier films as applied to flexible OLED display*, J. Appl. Polym. Sci. 106, 3534 (2007)

[43] H. Fujita: *Diffusion in polymer-diluent systems*, Fortschritte Der Hochpolymeren-Forschung, Springer (1961)

[44] M. Walker: *Permeation von Toluol durch plasmapolymerisierte Barriereschichten auf Polyethylen hoher Dichte*, PhD Universität Stuttgart (1996)

[45] M. E. Glicksman, *Diffusion in Solids*, Wiley-Interscience, Hoboken (1999)

[46] W. R. Vieth, *Diffusion in and through polymers*, Carl Hanser Verlag, München (1991)

[47] J. Comyn, *Polymer permeability*, Springer, Dordrecht, (1985)

[48] A. Einstein, *Über die von der molekularkinetischen Theorie der Wärme geforderte Bewegung von in ruhenden Flüssigkeiten suspendierten Teilchen*, Annalen der Physik 17, 549 (1905)

[49] W. Sutherland, *A dynamical theory of diffusion for non-electrolytes and the molecular mass of albumin*, Philosophical Magazine 9, 54, 781 (1905)

[50] M. von Smoluchowski, *Zur kinetischen Theorie der Brownschen Molekularbewegung und der Suspensionen*, Annalen der Physik 326, 756 (1906)

[51] D. Tu: *Permeation, Diffusion, Plastifizierung und Permselektivität von flüssigen Kohlenwasserstoffen durch reine und gefüllte Thermoplasten (PE und PP)*, PhD Universität Stuttgart, (1978)

[52] S. Gaiser, *Vergleichende Untersuchung zur Abscheidung quarzähnlicher Schichtsysteme aus Siloxanen in einem ECR-Plasma*, Bachelor Universität Stuttgart (2012)

[53] H. Rauscher *et al.*: *Plasma technology for hyperfunctional surfaces: food, biomedical and textile applications*, John Wiley & Sons, Weinheim (2010)

[54] A. P. Roberts *et al.*: *Gas permeation in silicon-oxide/polymer (SiO_x/PET) barrier films: role of the oxide lattice, nano-defects and macro-defects*, Journal of Membrane Science 208, 75 (2002)

[55] M. Hanika, *Zur Permeation durch aluminiumbedampfte Polypropylen- und Polyethylenterephtalatfolien*, PhD Technische Universität München (2004)

[56] E. M. Liston *et al.*: *Plasma surface modification of polymers for improved adhesion: a critical review*, Journal of Adhesion Science and Technology, 7:10, 1091 (1993)

[57] A. Bergeron *et al.*: *Structure of the interfacial region between polycarbonate and plasma-deposited $SiN_{1.3}$ and SiO_2 optical coatings studied by ellipsometry*, Journal of Vacuum Science & Technology A 16, 3227 (1998);

[58] D. Kirchheim *et al.*: *Transport mechanisms through PE-CVD coatings: influence of temperature, coating properties and defects on permeation of water vapour*, J. Phys. D: Appl. Phys. 50 085203 (2017)

[59] D. Kirchheim *et al.*: *Temperature-dependent transport mechanisms through PE-CVD coatings: comparison of oxygen and water vapour*, J. Phys. D: Appl. Phys. 50 395302 (2017)

[60] A. S. da Silva Sobrinho, *Defect-permeation correlation for ultrathin transparent barrier coatings on polymers*, Journal of Vacuum Science & Technology A 18, 149 (2000)

[61] W.G. Perkins *et* al.: *Diffusion and permeation of He, Ne, Ar, Kr, and D_2 through silicon oxide thin films*, J. Chem. Phys. 54, 1683 (1971)

[62] V. Stannett in: J. Crank (Ed.), *Diffusion in polymers*, Academic Press, London, 1968 (Chapter 2)

[63] A. Singh and W. J. Koros: *Significance of entropic selectivity for advanced gas separation membranes*, J. Ind. Eng. Chem. Res. 35, 1231 (1996)

[64] M. Orzinski: *Untersuchung der Permeation von anorganischen Gasen und organischen Verbindungen durch barriereverbesserte Kunststoffflaschen und ihre messtechnische Erfassung*, PhD Technische Universität Berlin (2007)

[65] R. Doremus, *Glass science,* Wiley Interscience, 2nd edn. (1994)

[66] C. Schenk *et al.*: *Theoretische und Experimentelle Untersuchungen an Ebenen Aerostatischen Gaslagerelementen unter Hochvakuumbedingungen*, Cuvillier, Göttingen (2007)

[67] L. W. McKeen: *Permeability properties of plastics and elastomers*, Elsevier, 3rd edn. (2011)

[68] H. L. Frisch: *Fundamentals of membrane transport,* Polymer Journal 23, 445 (1991)

[69] S. A. Stern and H .L. Frisch: *The selective permeation of gases through polymers*, Annu. Res. Mater. Sci. 11, 523 (1981)

[70] J. Fahlteich, Transparente Hochbarriereschichten auf flexiblen Substraten, PhD Technischen Universität Chemnitz (2010)

[71] S. Kanehashi, *Analysis of dual-mode model parameters for gas sorption in glassy polymers*, Journal of Membrane Science 253, 117 (2005)

[72] R. M. Barrer *et al.*: *Sorption and diffusion in ethyl cellulose. Part III. Comparison between ethylcellulose and rubber*, J. Polym. Sci. 27, 177 (1958)

[73] A. S. Michaels *et al.*: *Solution of gases in polyethylene terephthalate*, J. Appl. Phys. 34, 1 (1963)

[74] S. Roualdes *et al.*: *Gas separation properties of organosilicon plasma polymerized membranes*, Materials, Interfaces, and Electrochemical Phenomena 45, 1566 (1999)

[75] M. Knudsen: *Die Gesetze der Molekularströmung und der inneren Reibungsströmung der Gase durch Röhren*, Annalen der Physik 12, 75 (1909)

[76] A. Einstein and M. von Smoluchowski: *Brownsche Bewegung*, Reihe Ostwalds Klassiker Bd. 199, Verlag Harri Deutsch, Frankfurt (1997)

[77] W. Kast and C.-H. Hohenthanner, *Mass transfer within the gas-phase of porous media*, International Journal of Heat and Mass Transfer 43, 807 (2000)

[78] M. H. Abbasi *et al.*: *Diffusion of gases in porous solids: Monte Carlo simulations in the Knudsen and ordinary diffusion regimes*, AlChE Journal 29, 617 (1983)

[79] E. H. H. Jamieson and A. H. Windle, *Structure and oxygen-barrier properties of metallized polymer film*, Journal of material science 18, 64 (1980)

[80] G. Rossi and M. Nulman: *Effect of local flaws in polymeric permeation reducing barriers*, Journal of Applied Physics 74, 5471 (1993)

[81] M. Hanika *et al.*: *Inorganic layers on polymeric films – Influence of defects and morphology on barrier properties*, Chem. Eng. Technol. 26, 605 (2003)

[82] W. Prins and J.J. Hermans: *Theory of permeation through metal coated polymer films,* J. Phys. Chem. 63, 716 (1959)

[83] S. Glasstone *et al.*: *The theory of rate processes*, McGraw-Hill, New York 1st edn. (1941)

[84] R. J. Goldston and P. H. Rutherford: *Introduction to to plasma physics,* Institute of Physics Pub. (1995)

[85] A. Schulz, private communication

[86] M. Leins, *Development and spectroscopic investigation of a microwave plasma source for the decomposition of waste gases*, PhD Universität Stuttgart (2010)

[87] F. F. Chen: *Introduction to plasma physics and controlled fusion, Vol 1: Plasma physics*, Springer, Cham 3rd ed. (2015)

[88] Bergmann-Schäfer, *Lehrbuch der Experimentalphysik, Band 5: Vielteil-chensysteme,* Gruyter, Berlin (1992)

[89] M. Geisler *et al.*: *Elongated microwave electron cyclotron resonance heating plasma source*, Journal of Vacuum Science & Technology A 8, 908 (1990)

[90] U. Schumacher: *Fusionsforschung – Eine Einführung,* Wissenschaftliche Buch-gesellschaft, Darmstadt (1993)

[91] N. A. Krall and A. W. Trievelpiece: *Principles of Plasma Physics*, McGraw-Hill, New York (1973)

[92] J. A. Thornton: *Magnetron sputtering: basic physics and application to cylindrical magnetrons,* J. Vac. Sci. Technol. 15, 171 (1978)

[93] A. Artsimowitsch and S. Sagdejew, *Plasmaphysik für Physiker*, B. G. Teubner Stuttgart (1983)

[94] F. Cap: *Einführung in die Plasmaphysik, Band 1*, Vieweg & Sohn (1975)

[95] M. Troia: Realizzazione di superfici nanostrutturate via plasma e loro caratterizzazione tribologica, Master Università degli Studi di Bari (2012)

[96] M. R. Wertheimer and M. Moisan, *Comparison of microwave and lower frequency plasmas for thin film deposition and etching*, Journal of Vacuum Science & Technology A 3, 2643 (1985)

[97] C. M. Ferreira and J. Loureiro: *Electron energy distributions and excitation rates in high-frequency argon discharges*, J. Phys. D: Appl. Phys. 16, 2471 (1983)

[98] C. M. Ferreira and J. Loureiro: *Characteristics of high-frequency and direct current argon discharges at low pressures: a comparative analysis*, Phys. D: Appl. Phys. 17, 1175 (1984)

[99] M. N. Hirsh and H. J. Oskam, *Gaseous Electronics*, Academic, New York, p. 211. (1978)

[100] R. Claude *et al.: Comparison of microwave and lower-frequency discharges for plasma polymerization*, Plasma Chemistry and Plasma Processing 7, 451 (1987)

[101] L. Paquin *et al.*: *Amorphous silicon for photovoltaics produced by new microwave plasma-deposition techniques*, Can. J. Phys. 63, 831 (1985)

[102] R. d'Agostino, private communication

[103] S. Merli: *Hochrateabscheidung von Siliziumoxid- und Zinkoxidschichten mittels Mikrowellenplasma-unterstützter chemischer Gasphasenabscheidung auf Polycarbonat*, PhD Universität Stuttgart (2015)

[104] R. d'Agostino *et al.*: *Plasma deposition, treatment, and etching of polymers*, Academic Press Inc., San Diego (1990)

[105] E. Ramisch: *Influence of the ion energy on generation and properties of thin barrier layers deposited in a microwave plasma process*, Phd Universität Stuttgart (2011)

[106] J. Leiber *et al.: Plasmapolymerisation-Ein Verfahren für viele Anwendungen*, Vakuum in der Praxis 1, 22 (1992)

[107] D. Hegemann *et al.*: *Macroscopic description of plasma polymerization*, Plasma Process. Polym.4, 229 (2004)

[108] I. Tajima and M. Yamamoto: *Spectroscopic study on chemical structure of plasma-polymerized hexamethyldisiloxane,* J. Polym. Sei., Polym. Chem. 23, 615 (1985)

[109] H. K. Pulver: *Characterization of optical thin films*, Appl. Optics 18, 1969 (1979)

[110] W. J. Schrenk and T. Alfrey, Jr.: *Some Physical Properties of Multilayered Films*, Polymer Engineering and Science 9, 393 (1969)

[111] J. E. Klemberg-Sapieha *et al.*: *Effect of interface on the characteristics of functional films deposited on polycarbonate in dual-frequency plasma*, J. Vac. Sci. Technol. A 15, 985 (1997)

[112] S. Vallon *et al.: Adhesion mechanisms of silica layers on plasma-treated polymers. Part I. Polycarbonate,* J. Adhes. Sci. Technol. 10, 1287 (1996)

[113] Tridelta Magnetsysteme: SECOLIT - der temperaturbeständige Werkstoff für hochwertige Dauermagnete.
www.tridelta.de/ viomatrix/imgs/download/secolit-d.pdf, retrieved on 30.5.2018

[114] R. Nabenhauer: *Verpackungslexikon: Fachbegriffe und Anwendungsbeispiele von Experten erklärt*, Nabenhauer Verlag, 2. Auflage (2010)

[115] A. K. van der Vegt: *Polymeren, van keten tot kunstof*, Delft University Press (2005)

[116] Dupont Teijin Films: Datasheet Melinex 401CW,
http://www.cadillacplastic.co.uk/wp-content/uploads/2013/10/Melinex_4011.pdf Retrieved on 06.04.2018

[117] Mitsubishi Polyester Film Datasheet: Hostaphan RNK, Edition 10/11,
www.m-petfilm.com/upload/Europe_182GER.pdf, retrieved on 01.02.2018

[118] G. Abts: *Kunststoff-Wissen für Einsteiger*, Carl Hanser Verlag, München (2014)

[119] Packaging Materials. 1. *Polyethylene terephthalate (PET) for food packaging applications,* Report Series. International Life Sciences Institute (ILSI) (2002)

[120] S. Peterson: *Funktionalisierung von Polymeroberflächen zur Mediation der Biosystem-Biomaterial-Interaktion*, Hochschule Osnabrück, V2017, Dresden, 26th October 2017

[121] K. S. Miller and J. M. Krochta: *Oxygen and aroma barrier properties of edible films: A review*, Trends in Food Science &Technology 8, 228 (1997)

[122] © Wikimedia Commons User: Jü/CC-BY-SA-3.0, retrieved on 15.01.2018

[123] H. Bahre *et al.*: *Surface pre-treatment for barrier coatings on polyethylene terephthalate,* J. Phys. D: Appl. Phys. 46 084012 (2013)

[124] Dr. Klaus Noller and Stanislav Dribinskiy, private communication

[125] M. T. Kim and J. Lee: *Characterization of amorphous SiC:H films deposited from hexamethyldisilazane*, Thin Solid Films 303, 173 (1997)

[126] K. Schmidt-Szalowski *et al.*: *Thin films deposition from hexamethyldisiloxane and hexamethyldisilazane under dielectric-barrier discharge (DBD) conditions*, Plasmas and Polymers 5, 173 (2001)

[127] A. M. Wróbel and M. Kryszewski: *Effect of glow discharge conditions, structure and thermal properties of polysilazane thin films*. J. Macromol. Sei.-Chem. A 12, 1041 (1978)

[128] A. M. Wróbel *et al.: Polymerization of Organosilicones in Microwave Discharges*, Journal of Macromolecular Science- Chemistry 14, 321 (1980)

[129] T. L. Cottrell, *The strength of chemical bonds,* Butterworths Scientific Publications, London (1954)

[130] J. Kupčík *et al.: IR laser-induced decomposition of hexamethyldisiloxane for chemical vapour deposition of nano-structured hydrido(methyl)silicone powders,* Journal of Analytical and Applied Pyrolysis 57, 109 (2001)

[131] S. S. Zumdahl and S. A: Zumdahl, *Chemistry*, Brooks Cole, Belmont, 9th edn. (2014)

[132] J. M. Tibbit *et al.: A model for the kinetics of plasma polymerization,* Macromolecules 14, 647 (1977)

[133] A. T. Bell: *Fundamentals of plasma polymerization*, J. Macromol. Sci.-Chem. 10, 369 (1976)

[134] A. M. Wróbel *et al.: Thermal Decomposition of Plasma-Polymerized Organosilicon Thin Films*, Journal of Macromolecular Science—Chemistry 17, 433 (1982)

[135] C. Eaborn, *Organosilicon Compounds*, Butterworths Scientific Publications, London (1960)

[136] H. Sakurai in *Free Radicals, Vol. 2* (J. K. Kochi, ed.), Wiley-Interscience, New York (1973)

[137] A. A. Miller: *Radiation chemistry of polydimethylsiloxane. I. Crosslinking and gas yields*, J. Am. Chem. Soc. 9, 3519 (1960)

[138] M. R. Alexander *et al.: A study of HMDSO/O_2 plasma deposits using a high-sensitivity and -energy resolution XPS instrument: curve fitting of the Si 2p core level,* Applied Surface Science 137, 179 (1999)

[139] M. R. Alexander *et al.: Radio-frequency hexamethyldisiloxane plasma deposition: a comparison of plasma- and deposit-chemistry,* Plasmas and Polymers 2, 277 (1997)

[140] Perthen GmbH: *Bedienungsanleitung für Perthometer C5D*

[141] A. S. da Silva Sobrinho *et al.*: *Transparent barrier coatings on polyethylene terephthalate by single and dual-frequency plasma-enhanced chemical vapor deposition*, Journal of Vacuum Science & Technology A 16, 3190 (1998)

[142] H. Günzler and H.-U- Gremlich: *IR-Spektroskopie - Eine Einführung. Wiley-VCH*, Weinheim, 4th edn. (2003)

[143] Bruker: *Vector 22 FT-IR spectromenter user manual*

[144] N. J. Harrick: *Internal Reflection Spectroscopy*, Interscience, New York (1967)

[145] P. Swift: *Adventitious carbon – The panacea for energy referencing?*, Surface and interface analysis 2, 47 (1982)

[146] T. L. Barr and S. Seal: *Nature of the use of adventitious carbon as a binding energy standard,* Journal of Vacuum Science & Technology A 13, 1239 (1995)

[147] C. D. Wagner and A. Joshi: *Developing trends in the application of XPS in the USA*, Surf. Interface Anal. 6, 215 (1984)

[148] C. D. Wagner *et al.: Handbook of X-ray photoelectron spectroscopy,* Perkin-Elmer Corporaton, Eden Prairie (1979)

[149] G. Beamson and D. Briggs, *High resolution XPS on organic polymers,* John Wiley and sons Ltd., Chichester (1992)

[150] F. Fracassi *et al.: Thin film deposition in glow discharges fed with hexamethyldisilazane-oxygen mixtures*, Plasma Sources Sci. Technol. 2, 106 (1993)

[151] E. Vassallo *et al.: Structural and optical properties of amorphous hydrogenated silicon carbonitride films produced by PECVD*, Applied Surface Science 252, 7993 (2006)

[152] J. Schäfer *et al.*: *Carbon-free SiOx films deposited from octamethylcyclotetrasiloxane (OMCTS) by an atmospheric pressure plasma jet (APPJ)*, Eur. Phys. J. D 54, 211 (2009)

[153] Tescan: *VEGA Plus TS 5135 MM - Bedienungsanleitung*

[154] Cressington Scientific Instruments Ltd.: *Bedienungsanleitung 'cool' Sputter Coater, Cressington 108auto*

[155] Zirox Sensoren & Elektronik GmbH: *Schutzgasmessgerät zur Messung der Sauerstoffkonzentration in Gasen, SGMT 1/SGMS Gerätehandbuch*

[156] Zirox Sensoren & Elektronik GmbH: *Schutzgasmessgerät zur Messung der Sauerstoffkonzentration in Gasen, SGM5 Gerätehandbuch*

[157] G. Nisato *et al.*: Proceedings Asia Display/IDW01, Nagoya, Japan, 16–19 October 2001

[158] R. S. Kumar *et al.*: *Low moisture permeation measurement through polymer substrates for organic light emitting devices*, Thin Solid Films 417 120 (2002)

[159] H. Kim *et al.: Experimental investigation of defect-assisted and intrinsic water vapor permeation through ultrabarrier films*, Review of Scientific Instruments 87, 033902 (2016)

[160] H. Klumbies et al.: *Thickness dependent barrier performance of permeation barriers made from atomic layer deposited alumina for organic devices*, Organic Electronics 17, 138 (2015)

[161] H. de Vries *et al.*, PT-18, Goettingen, 20th-22th March 2017

[162] B. A. Banks and S. K. Rutledge, *Proceedings of the 4th International Symposium on Spacecraft Materials in Space Environment*, Toulouse, France (1988)

[163] S. Willski *et al.*: *Mechanisms of oxygen permeation through plastic films and barrier coatings*, J. Phys. D: Appl. Phys. 50, 425301 (2017)

[164] C.-N. Liu *et al.*: *Combined in situ FTIR-spectroscopic and electrochemical analysis of nanopores in ultra-thin SiOx-like plasma polymer barrier films*, J. Phys. D: Appl. Phys. 46 084015 (2013)

[165] B. Ozkaya *et al.*: Inhibition of interfacial oxidative degradation during siox plasma polymer barrier film deposition on model organic substrates, Plasma Process. Polym. 12, 392 (2015)

[166] M. Hanika *et al.:* 45th Annual Tech. Conf. Proceedings, Society of Vacuum Coaters, Germany (2002)

[167] M. Hanika *et al.*: 46th Annual Tech. Conf. Proceedings, Society of Vacuum Coaters, Germany (2003)

[168] A. G. Erlat, *Mechanism of Water Vapor Transport through PET/AlO_xN_y gas barrier films*, Journal of Vacuum Science & Technology A 18, 149 (2000)

[169] T. Ogino *et al.*: *The formation and transformation mechanism of calcium carbonate in water*, Geochimica et Cosmochimica Acta 51, 2757 (1987)

[170] F. C. Meldrum: *Calcium carbonate in biomineralisation and biomimetic chemistry,* International Materials Reviews 48, 187 (2003)

[171] R. M. Smith and A. E. Martell, *Critical Stability Constants, vol. 3*, Plenum, New York (1976)

[172] H. S. Harned and R. Davies Jr.: The ionization constant of carbonic acid in water and the solubility of carbon dioxide in water and aqueous salt solutions from 0 to 50°, J. Am. Chem. Soc.65, 2030 (1943)

[173] H. S. Harned and S. R. Scholes: *The Ionization Constant of HCO_3- from 0 to 50°* J. Am. Chem. Soc. 63, 1706 (1941)

[174] A. J. Ellis: *The solubility of carbon dioxide in water at high temperatures* Am. J. Sci. 257, 217 (1959)

[175] D. Langmuir: *Aqueous environmental chemistry,* Prentice Hall, Upper Saddle River, (1997)

[176] L. M. Dabb, *Calcium carbonate dissolution and precipitation in water: factors affecting the carbonate saturometer method*, PhD, Utah State University (1971)

[177] ILO, International Chemical Safety Cards http://www.ilo.org/dyn/icsc/showcard.display?p_version=2&p_card_id=1193 retrieved on 29/06/18

[178] J. A. Wojtowicz: *Factors affecting precipitation of calcium carbonate,* Journal of the Swimming Pool and Spa Industry 3, 18 (2001)

[179] J. J. De Yoreo and P. G. Vekilov: *Principles of crystal nucleation and growth*, Reviews in Mineralogy and Geochemistry 54, 27 (2003)

[180] W. Stumm and J. J. Morgan: *Aquatic chemistry,* Wiley Interscience, Hoboken (1996)

[181] D. Kralj *et al.*: *Vaterite growth and dissolution in aqueous solution III. Kinetics of transformation,* Journal of Crystal Growth 177, 248 (1997)

[182] A. Navrotsky: *Energetic clues to pathways to biomineralization: Precursors, clusters, and nanoparticles*, PNAS 133, 12096 (2004)

[183] D. Gebauer *et al.*: Stable Prenucleation Calcium Carbonate Clusters, Science 322, 1819 (2008)

[184] J. Rieger *et al.*: *Precursor structures in the crystallization/precipitation processes of $CaCO_3$ and control of particle formation by polyelectrolytes*, Faraday Discuss. 136, 265 (2007)

[185] J. Johnston *et al.*: *The several forms of calcium carbonate,* Amer. J. Sci. 41, 473 (1916)

[186] J. H. Magill: *Spherulites: A personal perspective*, Journal of materials science 36, 3143 (2001)

[187] H. D. Keith and F. J. Padden: *A phenomenological theory of spherulitic crystallization*, Journal of Applied Physics 34, 2409 (1963)

[188] R. Beck and J.-P. Andreassen: *Spherulitic growth of calcium carbonate*, Crystal Growth & Design 10, 2934 (2010)

[189] L. Gránásy *et al.*: *Growth and form of spherulites*, Physical Review E 72, 011605 (2005)

[190] J.-P. Andreassen *et al.: Investigations of spherulitic growth in industrial crystallization*, Chemical Engineering Research and Design 88, 1163 (2010)

[191] F. C. Frank: *Growth and Perfection of Crystals*, John Wiley & Sons, Inc., New York (1958)

[192] R. Kniep and S. Busch: *Biomimetic growth and self-assembly of fluorapatite aggregates by diffusion into denatured collagen matrices,* Angew. Chem. Int. Ed. Engl. 108, 2623 (1996)

[193] S. L. Tracy *et al.*: *The growth of calcite spherulites from solution II. Kinetics of formation*, Journal of Crystal Growth 193, 382 (1998)

[194] R. B. Williamson: *Constitutional supersaturation in Portland cement solidified by hydration,* Journal of Crystal Growth 3, 787 (1968)

[195] M. B. Tomson and G. H. Nancollas: *Mineralization kinetics: a constant composition approach*, Science 200, 1959 (1978)

[196] M. Faatz *et al.*: *Amorphous calcium carbonate: Synthesis and potential intermediates in biomineralization*, Adv. Mater. 16, 996 (2004)

[197] P. Schmitz and S. Janocha: *Films*, Ullmann's Encyclopedia of Industrial Chemistry, Wiley Interscience, Weinheim (2012)

[198] S. Payne *et al.: Formation of thin calcium carbonate films on chitosan biopolymer substrates*, Crystal Growth & Design 7, 1262 (2007)

[199] F. Manoli and E. Dalas: *Spontaneous precipitation of calcium carbonate in the presence of ethanol, isopropanol and diethylene glycol*, Journal of Crystal Growth 218, 359 (2000)

[200] A. Declet *et al.: Calcium carbonate precipitation: A review of the carbonate crystallization process and applications in bioinspired composites*, Rev. Adv. Mater. Sci. 44, 87 (2015)

[201] F. Meermann: *Charakterisierung von plasmapolymerisierten SiO_x-Schichten aus den Arbeitsgasen Hexamethyldisiloxan und Sauerstoff*, Bachelor Universität Stuttgart (2004)

[202] R. di Mundo *et al.: A novel organosilicon source for low temperature plasma deposition of silicon nitride-like thin films,* Plasma Processes and Polymers 2, 612 (2005)

[203] F. Fracassi and R. Lamendola: *PECVD of $SiO_xN_yC_zH_w$ thin films from hexa-methyldisilazane containing feed. Investigation on chemical characteristics and aging behavior,* Plasmas and Polymers 2, 25 (1997)

[204] D. V. Tsu *et al.: Local atomic structure in thin films of silicon nitride and silicon diimide produced by remote plasma-enhanced chemical-vapor deposition*, Physical Review B 33, 7069 (1986)

[205] L. J. Bellamy: *The Infra-red spectra of complex molecules*, Springer Nature (1954)

[206] R. Ashokan *et al.*: *IR absorption spectra of SiO_x films grown by Photo-CVD*, Phys. Stat. Sol. (a) 121, 533 (1990)

[207] G. Feliciano: Infrared properties of the Si-Sio_2 interface from first principles, PhD École Polytechnique Fédérale de Lausanne (2005)

[208] J. E. Olsen and F. Shimura: *Infrared spectroscopy of thin sincon dioxide on silicon,* Appl. Phys. Lett. 53, 1934 (1988)

[209] W. Bensch and W. Bergholz: *An FT-IR study of silicon dioxides for VLSI microelectronics*, Semicond. Sci. Technol. 5, 421 (1990)

[210] I. W. Boyd: *Deconvolution of the infrared absorption peak of the vibrational stretching mode of silicon dioxide: Evidence for structural order?*, Appl. Phys. Lett. 51, 418 (1987)

[211] H. Rinnert *et al.: Strong visible photoluminescence in amorphous SiO_x and SiO_x:H thin films prepared by thermal evaporation of SiO powder*, Journal of Luminescence 80, 445 (1999)

[212] NIST https://webbook.nist.gov/cgi/cbook.cgi?ID=C7631869&Mask=80 retrieved on 22.04.2015

[213] D. W. Berreman, *infrared absorption at longitudinal optic frequency in cubic crystal films*, Phys. Rev. 130, 2193 (1963)

[214] G. N. Kuznetsova *et al: ATR spectra of thin SiO_2 and GeO_2 layers on germanium,* J. App!. Spectrosc. 30, 215 (1979)

[215] L. Agres *et al.: Oxygen barrier efficiency of hexamethyldisiloxane/oxygen plasma-deposited coating*, Journal of Applied Polymer Science 61, 2015 (1996)

[216] K. T. Queeney *et al.: Infrared spectroscopic analysis of an ordered Si/SiO_2 interface*, Appl. Phys. Lett. 84, 493 (2004)

[217] R. S. McDonald: *Surface functionality of amorphous silica by infrared spectroscopy*, Journal of Physical Chemistry 62, 1168 (1958)

[218] X. Landreau *et al.: A thorough FT-IR spectroscopy study on micrometric silicon oxide films deposited by atmospheric pressure microwave plasma torch*, Eur. Phys. J. D 66, 160 (2012)

[219] J. Schäfer *et al.: Complex analysis of $SiO_xC_yH_z$ films deposited by an atmospheric pressure dielectric barrier discharge*, Surface & Coatings Technology 205, S330 (2011)

[220] H. Coelfen and L. Qi: *A systematic examination of the morphogenesis of calcium carbonate in the presence of a double-hydrophilic block copolymer,* Chem. Eur. J. 7, 106 (2001)

[221] P. J. Mohr *et al.: CODATA recommended values of the fundamental physical constants: 2014*, Journal of Physical and Chemical Reference Data 45, 043102 (2016)

[222] J. Fahlteich *et al.*: *Permeation barrier properties of thin oxide films on flexible polymer substrates*, Thin Solid Films 517, 3075 (2009)

[223] E. Schmachtenberg *et al.*: *Microwave assisted HMDSO/oxygen plasma coated polyethylene terephthalate films: effects of process parameters and uniaxial strain on gas barrier properties, surface morphology, and chemical composition*, J. Appl. Pol. Sci. 99, 1485 (2005)

[224] R. M. Barrer: *Diffusion in and Through Solids*, Cambridge University Press, New York, (1941)

[225] F.J. Norton: *Permeation of gaseous oxygen through vitreous silica*, Nature 191, 701 (1961)

[226] E. W. Sukov: *Diffusion of oxygen in vitreous silica*, Journal of the American Ceramic Society 46, 14 (1963)

[227] A. B. Shelekin *et al.*: *Theory of gas diffusion and permeation in inorganic molecular-sieve membranes*, AIChE Journal 41, 58 (1995)

[228] V. T. Stannett *et al.*: *Recent advances in membrane science and technology*, AdV. Polym. Sci. 32, 69 (1979)

[229] D. Chirakkal: *Untersuchung zur Abscheidung polymerartiger Schichten für die Anwendung in der Medizintechnik*, Bachelor Universität Stuttgart (2018)

[230] E. Häberle *et al.*: *Deposition of barrier layers for thin film solar cells assisted by bipolar substrate biasing*, Plasma Processes and Polymers 6, s282 (2009)

[231] G. Scarel *et al.*: *Berreman effect in infrared absorption spectroscopy of ionic oxide coatings formed by atomic layer deposition on three-dimensional structures*, Journal of Applied Physics 104, 094314 (2008)

[232] M. K. Gunde: *Vibrational modes in amorphous silicon dioxide*, Physica B 292, 286 (2000)

[233] V. P. Tolstoy *et al.*: *Handbook of infrared spectroscopy of ultrathin films*, Wiley Interscience, Hoboken (2003)

[234] H. Shirai and R. Takeda: *Determination of thickness of thin thermal oxide layers on Czochralski-grown silicon wafers from their longitudinal optical vibrational mode*, Jpn J. Appl. Phys 35, 3876 (1996)

[235] C. Martinet and R. A. B. Devine: *Analysis of the vibrational mode spectra of amorphous SiO_2 films*, Journal of Applied Physics 77, 4343 (1995)

[236] B. C. Trasferetti *et al.*: *Observation of the Berreman effect in infrared reflection-absorption spectra of amorphous titanium oxide thin films deposited on aluminum*, Applied Spectroscopy 54, 687 (200)

[237] I. P. Lisovskii *et al.*: *IR spectroscopic investigation of SiO2 film structure,* Thin Solid Films, 213, 164 (1992)

[238] A. Lehmann *et al.*: *Optical phonons in amorphous silicon oxides*, Phys. Stat. Sol. (b) 121, 505 (1984)

[239] A. Morlier *et al.*: *Gas barrier properties of solution processed composite multilayer structures for organic solar cells encapsulation*, Solar Energy Materials & Solar Cells 115, 93 (2013)

[240] G. Dennler *et al.*: *Growth and structure of hyperthin SiO_2 coatings on polymers*, Journal of Vacuum Science & Technology A: Vacuum, Surfaces, and Films 19, 2320 (2001)

[241] J. Fahlteich *et al.*: *Characterization of reactively sputtered permeation barrier materials on polymer substrates*, Surface & Coatings Technology 205, S141 (2011)

[242] N. Kaiser: *Review of the fundamentals of thin-film growth*, Applied Optics 41, 3053 (2002)

[243] P.Barna in: *Diagnostics and Application of thin films*, p. 295, Ed. L. Eckertova, (1992)

[244] J. A. Thornton: *High rate thick film growth,* Ann. Rev. Mater. Sci. 7, 239 (1977)

[245] A. Anders: *A structure zone diagram including plasma-based deposition and ion etching,* Thin Solid Films 518, 4087 (2010)

[246] J. A. Thornton: *Influence of apparatus geometry and deposition conditions on the structure and topography of thick sputtered coatings*, Journal of Vacuum Science and Technology 11, 666 (1974)

[247] R. Messier: *Toward quantification of thin film morphology*, Journal of Vacuum Science & Technology A: Vacuum, Surfaces, and Films 4, 490 (1986)

[248] J. E. Yehoda and R. Messier: *Are thin film physical structures fractals?*, Appl. Surf. Sci. 22/23, 590 (1985)

[249] B. Bushan: *Nanotribology & Nanomechanics*, Wear 7, 1507 (2005)

[250] K. W. Gerstenberg and K. Taube: *Measurement of the Young's modulus for structural characterization of amorphous Si: C: N: H-films*, Fresenius Z Anal Chem 333, 313 (1989)

[251] A. Patelli *et al.*: *SiOx-based multilayer barrier coatings produced by a single PECVD process*, Plasma Process. Polym. 6, S665 (2009)

[252] F. Kraus *et al.*: *Plasmapolymerized silicon organic thin films from HMDSN for capacitive humidity sensors*, Sensors and Actuators B 88, 300 (2003)

[253] F. Fracassi *et al.*: *Plasma deposition of silicon nitride-like thin films from organosilicon precursors*, Plasmas and Polymers 1, 3 (1996)

[254] M. R. Alexander *et al.*: *An X-ray photoelectron spectroscopic investigation into the chemical structure of deposits formed from hexamethyldisiloxane/oxygen plasmas*, Journal of materials science 31, 1879 (1996)

[255] Y. N Sun *et al.: X-Ray photoelectron spectroscopy of O1s and Si2p lines in films of SiO_x formed by electron beam evaporation*, Thin Solid Films 157, 351 (1988)

[256] A. M. Wróbel *et al.: Oligomeric products in plasma = polymerized organosilicones*, Journal of Macromolecular Science - Chemistry 20, 583 (1983)

[257] F. Arefi-Khonsari, private communication

[258] M. R. Alexander *et al.: Mass spectral investigation of the radio-frequency plasma deposition of hexamethyldisiloxane*, J. Phys. Chem. B 101, 3614 (1997)

[259] K. Rokosz *et al.*: *GDOES, XPS, and SEM with EDS analysis of porous coatings obtained on titanium after plasma electrolytic oxidation*, Surface and Interface Analysis 49, 303 (2017)

[260] S. Gaiser, private communication

[261] I. Verboven in: POLEOT Masterclass, Radisson Blu Scandinavia Hotel, Düsseldorf, 23.06.2015

[262] I. Verboven, private communication

[263] L. S. Liao *et al.*: *Bubble formation in organic light-emitting diodes*, Journal of Applied Physics 88, 2386 (2000)

[264] L. Ke *et al.*: *Bubble formation due to electrical stress in organic light emitting devices*, Applied Physics Letters 80, 171 2002

[265] SylaTech GmbH, https://www.sylatech-glovebox.de/ retrieved on 12.10.2014

[266] A. Hofrichter*et al.: Plasma treatment of polycarbonate for improved adhesion*, Journal of Vacuum Science & Technology A: Vacuum, Surfaces, and Films 20, 245 (2002)

[267] W. Deferme, private communication

[268] W. W. Daniels and R. E. Kitson: *Infrared spectroscopy of polyethylene terephthalate*, Journal of Polymer Science 23, 161 (1958)

[269] C. Y. Liang and S. Krimm: *Infrared spectra of high polymers Part IX: Polyethylene terephthalate*, Journal of Molecular Spectroscopy 3, 554 (1959)

[270] C. J. Heffelfinger and P. G. Schmidt: *Structure and properties of oriented polyethylene terephthalate films*, Journal of Applied Polymer Science 9, 2661 (1965)

[271] R. F. Boyer: *Glassy transitions in semicrystalline polymers*, J. Polym. Sci.: Symposium 50, 189 (1975)

[272] D. I. Bower and W. F. Maddams: *The vibrational spectroscopy of polymers*, Cambridge University Press, Cambridge (1992)

[273] W. H. Cobbs Jr. and R. L. Burton, *Crystallization of polyethylene terephthalate*, J. Polymer Sci. 10, 275 (1953)

[274] R. G. J. Miller and H. A. Willis: *An independent measurement of the amorphous content of polymers*, J. Polymer Sci. 19, 485 (1956)

[275] A. Miyake: *The infrared spectrum of polyethylene terephthalate I*: *The effects of crystallization*, Journal of Polymer Science 28, 479 (1959)

[276] K. C. Cole *et al.*: *Characterization of surface orientation in poly(ethylene terephthalate) by front-surface reflection infrared spectroscopy*, Applied Spectroscopy 48, 1513 (1994)

[277] F. J. Boerio and S. K. Bahl: *Vibrational analysis of polyethylene terephthalate and its deuterated derivatives*, Journal of Polymer Science 14, 1029 (1976)

[278] M. C. Tobin*: The infrared spectra of polymers. II. The infrared spectra of polyethylene terephthalate*, The Journal of Physical Chemistry 61, 1392 (1967)

[279] C. Bach *et al.*: *Characterization of poly(ethylene terephthalate) used in commercial bottled water*, IOP Conference Series: Materials Science and Engineering 5, 12005 (2009)

[280] J. R. Atkinson *et al*: *An investigation of glass formation and physical ageing in poly(ethylene terephthalate) by FT-IR spectroscopy*, Polymer 41, 6965 (2000)

[281] J. M. Huang *et al.*: *Conformational changes and molecular motion of poly(ethylene terephthalate) annealed above glass transition temperature*, Polymer 41, 1741 (1999)

[282] I. M. Ward: *The molecular structure and mechanical properties of polyethylene terephthalate fibers*, Textile Research Journal 31, 650 (1960)

[283] B. J. Factor *et al.*: *Surface-induced ordering of an aromatic polyimide*, Physical Review Letters 66, 1181 (1993)

[284] P. G. Schmidt: *Polyethylene terephthalate structural studies*, Journal of Polymeric Science A 1, 1271 (1963)

[285] K. H. Illers and H. Breuer: *Molecular motions in polyethylene terephthalate*, Journal of Colloid science 18, 1 (1963)

[286] A. Ajji *et al.*: *Orientation and structure of drawn poly(ethylene terephthalate),* Polymer 37, 3707 (1995)

[287] P. Boulanger *et al.*: *XPS study of polymer chain conformation in amorphous and crystalline poly(ethylene terephthalate) samples*, Journal of Electron Spectroscopy and Related Phenomena 63, 53 (1993)

[288] C. Duchesne *et al.*: *Molecular Orientation and Relaxation of Poly(ethylene terephthalate) by Polarization Modulation Infrared Spectroscopy*, Macromolecules 38, 8768 (2002)

[289] J. Guèvremont *et al.*: *Orientation and conformation in poly(ethylene terephthalate) with low raw ratios as characterized by specular reflection infra-red spectroscopy*, Polymer 36, 3385 (1995)

[290] D. J. Walls: *Application of ATR-IT to the analysis of surface structure and orientation in uniaxially drawn poly(ethyleneterephthalate),* Applied Spectroscopy 45, 1193 (1991)

[291] R. S. Stein and G. B. B. M. Sutherland: *Effect of Intermolecular Interactions between CH Frequencies on the Infrared Spectra of N-Paraffins and Polythene*, The Journal of Chemical Physics 22, 1993 (1954)

[292] J. R. Havens and D. L. Van der Hart: *Morphology of poly (ethylene terephthalate) fibers as studied by multiple-pulse proton NMR*, Macromolecules 18, 1663 (1985)

[293] K. Bahroun *et al.*: Influence of layer type and order on barrier properties of multilayer PECVD barrier coatings, J. Appl. Phys. D: Applied Physics 47 (2014)

Acknowledgements

First and foremost I would like to thank Prof. Dr. Thomas Hirth for the opportunity to join the IGVP as a PhD student and for his continued guidance even from Karlsruhe, and for his comments and suggestions on the several drafts of the current thesis. I would also like to thank (in strictly alphabetical order) my supervisors, Dr. Andreas Schulz and Dr. Matthias Walker, for the constant guidance and assistance throughout the PhD. Similarly, I would like to thank all the colleagues, present and past, from the Plasmatechnology group and the whole IGVP, particularly Heinz Petto for the continuous technical assistance in the lab and Sandra Gaiser and Martina Leins for helping me in several ways, not all of them strictly work-related. In addition I would like to thank Burkhard Plaum for the computer-related support in the initial stages of my PhD.

The initial core of my work was directly related to the *Printing Of Light-Emitting Devices On Textile* (*POLEOT*) project and as such I thank all the project partners, particularly Wim Deferme and Inge Verboven for producing, optimizing and bringing the OLEDs prototypes employed as samples all the way from Hasselt and back, and for the ongoing stimulating discussion and company.

I would also like to thank Dr. Jakob Barz and Dr. Joachim Mayer for all the help for the ESCA analyses for my samples, and for providing me the much needed raw data, too.

I am very grateful to Dr. Andreas Holländer for the useful inputs kindly provided over the course of the years and to Pr. Michael Wertheimer and Pr. Farzaneh Arefi-Khonsari, whose effortless insight and suggestions helped me bringing together some of the most arduous parts of my work.

I am grateful to Ruth Edelmann-Amrhein, and Ingeborg Wagner for their help in administrative matters. In particular I am deeply indebted to Ingeborg Wagner for her thorough and ongoing help, even as I write this, in setting up the defense committee and in submitting my PhD.

Finally, I would like to remember my late professor, Dr. Riccardo d'Agostino, whose kind, down-to-heart and caring nature always helped and encouraged me both as a student attending his lectures and as I was working in his lab as a part of my Bachelor and Master theses. This PhD is also undoubtedly due to him and I consider it to be the goodbye I never managed to say to him in person.

Eidesstattliche Erklärung

Hiermit erkläre ich an Eides Statt, dass ich die vorliegende Arbeit selbstständig verfasst und keine anderen als die angegebenen Quellen und Hilfsmittel verwendet habe. Alle wörtlichen oder sinngemäßen Zitate aus anderen Arbeiten sind durch Angabe der Quellen kenntlich gemacht worden.
Ich erkläre dazu, dass ich die vorliegende Arbeit nur in diesem und keinem anderen Promotionsverfahren eingereicht habe und dass diesem Promotionsverfahren keine endgültig gescheiterten Promotionsverfahren vorausgegangen sind.

Stuttgart, den 5. Juli 2019 _____

Mariagrazia Troia